Friction in Long Bearing Channels During Multi-hole Extrusion of Aluminum Alloy: Experimental and Numerical Investigations

von

Mech.-Eng. Vidal R. Sanabria Rosas

aus Porlamar, Bolivarische Republik Venezuela

von der Fakultät III – Prozesswissenschaften

der Technischen Universität Berlin

zur Erlangung des akademischen Grades

Doktor der Ingenieurwissenschaften

- Dr.-Ing. -

genehmigte Dissertation

Promotionsausschuss:

Vorsitzender:	Prof. Dr. J. Banhart
Gutachter:	Prof. Dr. W. Reimers
Gutachter:	Prof. Dr. H. Valberg

Tag der wissenschaftlichen Aussprache: 27.06.2016

Berlin 2016

D83

Acknowledgements

I would like to thank to the German Academic Exchange Service (DAAD), the Venezuelan Scholarship Foundation (Fundayacucho) and the Extrusion Research and Development Center of the TU Berlin for the financial support during my doctoral studies.

I wish to express my gratitude to my supervisor Prof. Dr. Walter Reimers for his remarks and the challenging discussions through my research work. Furthermore, I want to thank Prof. Dr. Henry Valberg from the Norwegian University of Science and Technology NTNU for his interest in my investigations and his enriching contributions through the application of a grid pattern technique. In addition, I would like to thank Prof. Dr. John Banhart for chairing the examination committee.

Especial thanks to Dr. Soeren Mueller for his confidence in me and for making my research work possible at the Extrusion Research and Development Center of the TU Berlin. Moreover, I would like to thank Dr. Sven Gall for his support and help in proof-reading my publications and thesis. Further, I would like to thank Dr. H.-M. Mayer for his invaluable contribution during the development of the new friction device and support during all the experimental tests.

I am thankful to Prof. Dr. Pavel Hora, Dr. Longchang Tong and Dr. Christoph Becker for their helpful contributions to the experimental and numerical friction investigations at the Institute of Virtual Manufacturing IVP ETH Zurich. Moreover, I express my thanks to Dr. Dong-Zhi Sun from the Fraunhofer Institute IWM for the helpful discussions about his friction investigations. Furthermore, I would like to thank my colleagues Dr. W. Thedja, M. Negendank, F. Gensch, R. Nitschke, A. Nitschke, S. Quander, H. Kauker, J. Nissen and I. Driehorst for their support. Furthermore, I would like to thank all the students who made any contribution to this investigation, especially to Laurenz Radtke for his useful collaboration during the development phase of the new friction device and his efficient metallographic work.

I thank my family and friends for their prayers and support. Very special thanks to my wife Claudia and children Daniel and Andres for the unconditional understanding and love during the last years.

"The horse is made ready for the day of battle, but the victory belongs to the LORD".
Proverbs 21:31.

Abstract

The friction behavior between the aluminum alloy EN AW-6060 and the hot working steel AISI H13 was investigated under extrusion conditions. The visco-plastic response of the EN AW-6060 was determined by means of hot compression tests at high different temperatures and strain rates. The Garofalo or Zener-Hollomon relationship was applied to model the flow stress $\bar{\sigma}(T,\dot{\varepsilon})$. Furthermore, tribo-torsion-tests (IVP ETH Zurich) were carried out at low pressures to study the slipping friction behavior. In addition, a new friction device was developed to reproduce full sticking conditions. Thus, the sticking friction as well as the microstructural changes of the friction boundary layer could be analyzed. Full sticking conditions could be reproduced by the new friction device applying a normalized normal stress of 3.5. Simulations validated applying intern grid pattern technique showed high strains values (8 mm/mm) in the friction boundary layer. The experimental and numerical results suggest that the EN AW-6060 experiments a softening effect (>10%) during large deformation at high temperature (400 °C – 500 °C) and low strain rate ($\dot{\varepsilon}$<10 1/s). Based on the slipping and sticking friction results as well as the thermo-mechanical response of the EN AW-6060 a new friction model was developed. The new empirical formulation models not only the friction as a function of the pressure and temperature, but also introduces a physical boundary (maximal friction) related to the material model $k\{T, \dot{\bar{\varepsilon}}(T,v)\}$.

Multi-hole extrusion trials were carried out applying -0.5° relief, 0° parallel and +0.5° and +1° choked bearing channels. Moreover, evaluations of the bearing appearance and the microstructure of the friction boundary layers allowed the identification of the friction mechanisms and their interaction length inside the bearing channels. Thus, sticking friction at the inlet of the channels generated a grain refinement in the subsurface, resulting from the strong shearing. Slipping zones were also detected at the end of the bearing channels due to the reduction of the normal pressure. Multi-hole extrusion simulations applying the FEM-based software DEFORM^{TM} were performed. A similar experimental product speed distribution could be numerically predicted applying the new friction model.

Kurzfassung

Das Reibungsverhalten zwischen der Aluminiumlegierung EN AW-6060 und dem Warmarbeitsstahl AISI H13 wurde unter Strangpressbedingungen untersucht. Das viskoplastische Verhalten der EN AW-6060 wurde mittels Warmdruckversuchen bei hohen Temperaturen und unterschiedlichen Verformungsgeschwindigkeiten bestimmt. Darüber hinaus wurde die Garofalo oder Zener-Hollomon Beziehung verwendet, um die Fließspannung $\bar{\sigma}(T,\dot{\varepsilon})$ zu modellieren. Außerdem wurden Versuche mit dem Tribo-Torsion-Test (IVP ETH Zürich) bei niedrigen Drücken durchgeführt, um das Gleitreibungsverhalten zu untersuchen. Zusätzlich wurde ein neuer Reibprüfstand entwickelt, um eine vollständige Haftreibung reproduzieren zu können. Somit konnten Haftreibungswerte bestimmt sowie mikrostrukturelle Veränderungen in der Reibungsgrenzschicht analysiert werden. Vollständige Haftreibung konnte durch den neuen Reibprüfstand mit einer normalisierten Normalspannung von 3,5 reproduziert werden. Numerische Simulationen der Haftreibungsversuche, die mit visioplastischen Experimente validiert wurden, zeigten hohe Dehnungswerte in der Scherzone (8 mm/mm). Die experimentellen und numerischen Ergebnisse der Haftreibung lassen vermuten, dass die EN AW-6060 in der Reibungsgrenzschicht bei hohen Temperaturen (400 °C - 500 °C) und niedrigen Verformungsgeschwindigkeiten ($\dot{\varepsilon}$<10 1/s) signifikant entfestigen (>10%). Basierend auf den Gleit- und Haftreibungsergebnissen sowie dem thermomechanischen Verhalten der EN AW-6060 wurde ein neues Reibmodell für die Modellierung der Pressreibung beim Strangpressen entwickelt. Die neue empirische Formulierung modelliert nicht nur die Reibung als Funktion des Drucks und der Temperatur, sondern führt auch eine physikalische Grenze (maximaler Reibungswert) in Abhängigkeit von dem Materialmodell $k\{T, \dot{\bar{\varepsilon}}(T,v)\}$ ein.

Strangpressversuche mit EN AW-6060 unter der Verwendung einer Mehrlochmatrize mit erweiternden (-0,5°), parallelen (0°) und verengenden (+0,5°, +1°) Presskanälen wurden durchgeführt. Hieraus konnten durch die Analyse der Presskanaloberfläche und der Mikrostruktur in den Reibungsgrenzschichten die Reibungsmechanismen und ihre Wechselwirkungslänge identifiziert werden. Die Haftreibung am Presskanaleingang führte zu einer Kornfeinung in der Reibungsgrenzschicht infolge der starken Verformung. Am Ende der Presskanäle wurden Gleitreibungszonen beobachtet, die durch den abnehmenden Normaldruck erzeugt wurden. Das Strangpressen über die Mehrlochmatrize wurde mittels der FEM Software DEFORM^{TM} simuliert. Durch das Implementieren des neu entwickelten Reibmodells in der

Simulation konnten Strangaustrittsgeschwindigkeiten, die den realen Ergebnissen entsprechen, vorhergesagt werden.

Table of contents

List of symbols

Latin symbol	Comment
a	Temperature variable to modify the average strain rate
a_o	Constant of the new friction model
a'	Constant
A	Constant
A	Constant of Garofalo or Zener Hollomon relationship
A_a	Apparent contact area
A_o	Container cross section
A_f	Product cross section
A_m	Measured contact area of a contact patch
A_r	Real contact area
A_1	Minimum value of the logistic function
A_2	Maximum value of the logistic function
b	Constant
b'	Constant
b	Constant of the new friction model
B	Constant
c	Constant of the new friction model
c_1	Constant of the new friction model
c'	Constant
d	Internal diameter of the hollow cylinder
d'	Constant
d_o	Initial diameter of the friction specimen
dS	Surface differential
dV	Volume differential
D_e	External diameter
D_i	Internal diameter
f	Constant of the new friction model
f_{hk}	Interfacial shear factor
f_v	Function of the exit speed
F	Force
F_a	Axial force
F_f	Friction force
F_{fa}	Friction force at the beginning of the relative movement
F_{fb}	Friction force at quasi-steady state
F_i	Surface traction
F_l	Friction length
F_n	Normal force
F_s	Stroke of the axial friction test
h	Height of the friction specimen after upsetting
h	Thickness of the friction boundary layer
h_o	Initial height of the friction specimen
H	Hardness of the soft surface
H_{eff}	Effective hardness

Latin symbol	Comment
I_1	First invariant
I_2	Second invariant
I_3	Third invariant
J_1	First deviatoric stress invariant
J_2	Second deviatoric stress invariant
J_3	Third deviatoric stress invariant
k	Constant
k	Shear flow stress
k_p	Surface constant
K	Penalty constant
L_i	Relative product length
l_b	Length of the bearing channel
l	Constant
m	Friction factor
m'	Constant
m_0	Constant
M	Torque
n	Constant
n	Normal unit vector
n	Constant
n'	Constant
P	Pressure
P_o	Constant
P_s	Initial normal pressure
q	Constant
R	Gas constant
R_z	Mean roughness depth
R_a	Average roughness
s	Slope average of the curves ln(sinh($\alpha\bar{\sigma}$)) vs. ln($\dot{\varepsilon}$)
S_{ij}	Deviatoric stress tensor
t	Time
T	Temperature
$\boldsymbol{T}$	Stress vector
T_o	Constant
T_k	Absolute temperature
u_o	Constant
v_f	Product speed of the extrusion
v_s	Stem speed
v_i	Relative product speed
v	Sliding velocity
v_o	Constant
v'	Reference sliding velocity
x_i	Distance from the die entry
Z	Zener-hollomon Parameter

Greek symbol	Comment
α	Stress multiplier
β	Constant of the new friction model
β'	Slope average of the curves $\bar{\sigma}$ vs $\ln(\dot{\varepsilon})$
β_e	Effective attack angle of the representative elliptical paraboloid
γ	Temperature variable to modify the form and slope of the friction curve
$\dot{\gamma}$	Shear deformation rate
γ_1	Constant of the new friction model
γ_2	Constant of the new friction model
$\delta\dot{\bar{\varepsilon}}$	Infinitesimal change of average strain rate
$\delta\dot{\varepsilon}_V$	Infinitesimal change of volumetric strain rate
δ_{ij}	Kronecker delta
δu_i	Infinitesimal change of displacement
ε	Strain
$\dot{\varepsilon}$	Strain rate
$\dot{\bar{\varepsilon}}$	Average strain rate
$\dot{\varepsilon}_V$	Volumetric strain rate
η	Factor of proportionality
λ	Magnitude of the stress vectors
ΔH	Deformation activation energy
Δx	Thickness of the boundary layer
ΔF_f	Additional friction force due to contact between punch and Al layer
μ	Coefficient of friction
π	Constant
$\boldsymbol{\sigma}$	Stress tensor
$\bar{\sigma}$	Effective or flow stress
σ_a	Axial stress
σ_{ij}	Component of the stress vector applied on plane *i* and in the direction *j*
σ_n	Normal stress
$\sigma_n{}'$	Normalized normal stress
σ_y	Yield strength
σ_1	First or maximum principal stress
σ_2	Second principal stress
σ_3	Third or minimum principal stress
τ	Shear stress or friction stress
τ_a	Friction stress at the beginning of the relative movement
τ_b	Friction stress at quasi-steady state
τ_B	Bingham friction
τ_e	Constant friction at the outlet of the bearing channel
τ_i	Friction stress at the extrusion die entry
τ_{max}	Maximal friction stress calculated at $\dot{\varepsilon}$ =1000 and ε=0.2
τ_{min}	Minimum value of the friction
τ_o	Minimum friction stress
τ_{sl}	Friction stress at the slipping zone of the bearing channel
τ_{st}	Friction stress at sticking conditions
τ_y	Shear yield stress

Greek symbol	Comment
ϕ	Inclination angle of the tribo-torsion-test
φ	Die angle
φ'	Deflection angle of the bearing channel
ψ'	Slope average of the curves $\ln(\bar{\sigma})$ vs $\ln(\dot{\varepsilon})$

1 Introduction

Extrusion of aluminum alloy is extensive applied in the field of construction, health, sport and transport. The 6000-serie are the most used alloys due to the attractive extrudability, mechanical properties, corrosion resistance and surface quality. The increasing demand of light extrudates brings new challenges to the industry, such us production of single and multiple profiles at higher speed and with complex cross sections. Unfortunately, there are several factors that limit the product velocity and thus the productivity. Approximately 90 % of the plastic deformation work is transformed in heat during the extrusion. Since the generated heat cannot be transferred to the surroundings with the same generation rate, places with large deformations experiment a local temperature increase. As a result, the material in the bearing channel acquires a higher temperature than the rest of the workpiece and in the case of overheat unacceptable defects appear on the product surface. Therefore, an adequate billet temperature and ram speed must be combined to achieve the best compromise between productivity and good surface finish [BAK12].

On the other hand, a demanding die design is required to produce a uniform material flow through asymmetric bearing channels and a good synchronization applying multi-hole dies. Usually this task is achieved changing the position and geometry of the pockets [LI03, SHE03, ZHO09], as well as modifying the length and inclination angle of the bearing channels [AKE85, BAU06]. Both methods seek the alteration of the local friction conditions to control the profile speed distribution. In the practice it is an iterative correction process that induces significant production costs. Virtual production techniques applying numerical simulations could be an effective alternative to reduce the trial and error process. Commercial FEM-based softwares are available to simulate the extrusion process, nevertheless a precise prediction is not always easy to achieve. In the last years, numerical benchmarks have been carried out to reproduce multi-hole extrusions evaluating the influence of different length and inclination angle of the bearing channels [HOR05, DON15]. Inaccurate prediction of the extrusion force, relative product speed and temperature has demonstrated the complexity of this task. Incorrect modelling of the constitutive relation, heat transfer and friction can cause important deviations of the numerical solution. Nonetheless, it is accepted that the wrong friction assumptions are the responsible for most of these differences. Despite the numerous efforts the friction phenomena has not been fully understood since the combination of the pressure, temperature, speed and surface

conditions generate different chemical and mechanical interactions difficult to describe and quantify. Conventional test methods such as pin-on-disc or rotating-disc are not convenient to reproduce similar friction under extrusion conditions [HOR12]. More sophisticated testing devices have been developed for this purpose [HOR12, OCK12, WID12]; however the imitation of sticking friction and the posterior evaluation of its subsurface layers is still a difficult task.

Extrusion investigations have proved the presence of different friction mechanisms between the workpiece and tools. Inside the container both surfaces remains fixed producing a severe shearing under the contact surface [VAL96, FLI05, SCH07]. Moreover, along the bearing channels a more complicated behavior takes place depending on the inclination angle. Using choked bearing channels a sticking zone is formed at the inlet, which is followed by slipping contact [VAL94, ABT96]. In parallel channels the friction decreases considerably and the bearing land is covered by a thin layer during the slipping friction [AKE85, THE92, MUE96]. Hence, a suitable friction model should predict not only the right contact mechanism but also the length of its action. These scenarios cannot be analyzed applying the classic friction models. *Amontons-Coulomb* established the proportionality to the normal force what produce over estimated friction under high pressures. In addition, *Tresca* suggested scaling the shear stress with a constant factor, with the disadvantage that the friction remains constant even at low contact stress. Based on experimental tests numerous friction models have been formulated [LEV97, OCK12, HOR14], but their particular application and complicated implementation in commercial codes difficult their general use.

Thence, new investigation methods of the friction behavior and its proper estimation by means of simply models, as well as flexible numerical codes could improve the numerical prediction of the extrusion process.

2 Literature review

2.1 Continuum mechanisms

2.1.1 Stress tensor

When a body is subjected to multiple forces (Fig. 2.1a) stresses are induced in all the three dimensions. The whole body could be studied as a point where all forces are concentrated (center of mass), but thus only an average stress could be calculated considering a particular application surface. However, when the stress distribution in the body has to be calculated another method must be used. Augustin Cauchy considered an infinitesimal stress element in equilibrium, which consists of 6 faces in the three dimensions and where a stress vector $\boldsymbol{T}^{(\mathbf{n})}$ acts on each face (Fig. 2.1b). Each stress vector contains a normal stress and 2 shear stresses. This concept gave rise to a multidimensional array with 9 stress components; 3 normal stresses ($\sigma_{11}, \sigma_{22}, \sigma_{33}$) and 6 shear stresses ($\sigma_{12}, \sigma_{13}, \sigma_{21}, \sigma_{23}, \sigma_{31}, \sigma_{32}$) also called 3D stress tensor $\boldsymbol{\sigma}$ [CHA06], which defines the stress at any point in a three dimensional space (Eq. 2.1).

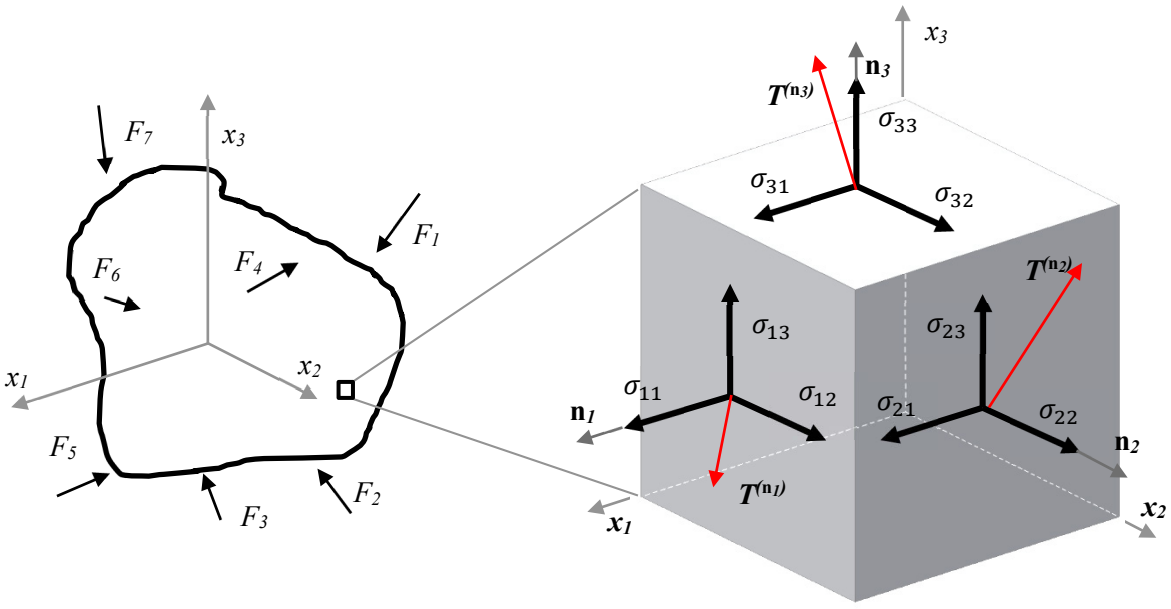

a) b)

Fig. 2.1. Stress element in three dimensions.

$$\boldsymbol{\sigma} = \begin{bmatrix} \boldsymbol{T}^{(\mathbf{n1})} \\ \boldsymbol{T}^{(\mathbf{n2})} \\ \boldsymbol{T}^{(\mathbf{n3})} \end{bmatrix} = \begin{bmatrix} \sigma_{11} & \sigma_{12} & \sigma_{13} \\ \sigma_{21} & \sigma_{22} & \sigma_{23} \\ \sigma_{31} & \sigma_{32} & \sigma_{33} \end{bmatrix} \equiv \begin{bmatrix} \sigma_{xx} & \sigma_{xy} & \sigma_{xz} \\ \sigma_{yx} & \sigma_{yy} & \sigma_{yz} \\ \sigma_{zx} & \sigma_{zy} & \sigma_{zz} \end{bmatrix} \quad \text{(Eq. 2.1)}$$

The stress vector $\boldsymbol{T}^{(\mathbf{n})}$ is parallel to the normal unit vector **n** according to the Cauchy's second law [HIL50]. Eq. 2.2 shows the general relation, where λ is an unknown scalar quantity that corresponds to the magnitudes of the stress vectors σ_{ij}.

$$T_i^{\mathrm{n}} = \sigma_{ij}\mathrm{n}_j = \lambda \mathrm{n}_i \qquad \text{(Eq. 2.2)}$$

Applying the Kronecker delta function $\mathrm{n}_i = \delta_{ij}\mathrm{n}_j$ a homogeneous system is obtained (Eq. 2.3).

$$\mathrm{n}_j\left(\sigma_{ij} - \lambda\delta_{ij}\right) = 0 \qquad \text{(Eq. 2.3)}$$

In order to have a non-trivial solution ($\mathrm{n_j} = 0$) for the Eq. 3, the determinant of the matrix has to be equal zero (Eq. 2.4).

$$\left|\sigma_{ij} - \lambda\delta_{ij}\right| = \begin{bmatrix} \sigma_{11}-\lambda & \sigma_{12} & \sigma_{13} \\ \sigma_{21} & \sigma_{22}-\lambda & \sigma_{23} \\ \sigma_{31} & \sigma_{32} & \sigma_{33}-\lambda \end{bmatrix} = -\lambda^3 + I_1\lambda^2 - I_2\lambda + I_3 = 0 \qquad \text{(Eq. 2.4)}$$

The terms I_1, I_2 and I_3 of the Eq. 2.4 are independent to the orientation of the coordinate system and are known as the first, second and third invariants of the stress tensor respectively. The invariants represent the physical content of the stress tensor. For instance, the first invariant I_1 represents the pressure in all directions ($\sigma_{11} + \sigma_{22} + \sigma_{33}$). Furthermore, λ has three possible solutions meaning the three principal normal stresses ($\sigma_1, \sigma_2, \sigma_3$).

Additionally, the Cauchy stress tensor can be also written as the sum of the deviatoric stress tensor S_{ij} and the hydrostatic stress tensor $\frac{I_1}{3}\delta_{ij}$ [ROW91]. The deviatoric component of the stress tensor produces changes of the shape and size of the body, while the hydrostatic component modifies the volume. The deviatoric stress tensor is expressed in Eq. 2.5.

$$S_{ij} = \sigma_{ij} - \frac{I_1}{3}\delta_{ij} = \begin{bmatrix} \sigma_{11}-\frac{I_1}{3} & \sigma_{12} & \sigma_{13} \\ \sigma_{21} & \sigma_{22}-\frac{I_1}{3} & \sigma_{23} \\ \sigma_{31} & \sigma_{32} & \sigma_{33}-\frac{I_1}{3} \end{bmatrix} \qquad \text{(Eq. 2.5)}$$

The deviatoric stress tensor has also invariants which can be obtained with the same procedure applied to calculate the invariants of the stress tensor. Moreover, the principal directions of the stress deviator tensor S_{ij} are the same as the principal directions of the stress tensor σ_{ij}, thus the characteristic equation can be written as (Eq. 2.6).

$$\left|S_{ij} - \lambda\delta_{ij}\right| = \lambda^3 - J_1\lambda^2 - J_2\lambda + J_3 = 0 \quad \text{(Eq. 2.6)}$$

The Eq. 2.7, 2.8 and 2.9 show the deviatoric stress invariants J_1, J_2 and J_3 respectively, expressed as function of the Cauchy stress tensor. Because the first invariant J_1 is cero the stress deviator tensor is in pure shear.

$$J_1 = 0 \quad \text{(Eq. 2.7)}$$

$$J_2 = \frac{1}{6}[(\sigma_{11} - \sigma_{22})^2 + (\sigma_{22} - \sigma_{33})^2 + (\sigma_{33} - \sigma_{11})^2] + \sigma_{12}{}^2 + \sigma_{23}{}^2 + \sigma_{31}{}^2 \quad \text{(Eq. 2.8)}$$

$$J_3 = \frac{2}{27}I_1{}^3 - \frac{1}{2}I_1I_2 + I_3 \quad \text{(Eq. 2.9)}$$

2.1.2 Yield criterion

A metal subjected to stress responds elastically until a limit at which the material begins deforming plastically. This particular stress state is known as the yield strength or yield point σ_y. There are many theories applied to define the yield strength, however the most used in metal forming are the *maximum shear stress* proposed by Tresca and the *distortion energy theory* suggested by von Mises [VAL10]. Tresca proposed that yielding occurs when the shear stress τ exceeds the shear yield strength τ_y (Eq. 2.10).

$$\tau = \left|\frac{\sigma_1 - \sigma_3}{2}\right| \geq \tau_y = \frac{\sigma_y}{2} \quad \text{(Eq. 2.10)}$$

Alternatively, von Mises set that in ductile materials yielding occurs when the distortion energy reaches a critical value. This is also true for a uniaxial test such as tensile test where the maximum principal stress σ_1 is equal to the yield stress σ_y while $\sigma_2 = \sigma_3 = 0$. Considering this criterion and rewriting the second deviatoric stress invariant J_2 (Eq. 2.8) in function of principal stress the Eq. 2.11 is obtained.

$$J_2 = \frac{1}{6}[(\sigma_1 - \sigma_2)^2 + (\sigma_2 - \sigma_3)^2 + (\sigma_3 - \sigma_1)^2] = \frac{\sigma_y{}^2}{3} \quad \text{(Eq. 2.11)}$$

The above indicate that the material flows plastically when the yield strength is equivalent to $\sqrt{3J_2}$. Thus, combining the Eq. 2.11 and Eq. 2.8 a general expression for calculating yield strength or also called effective stress $\bar{\sigma}$ can be obtained (Eq. 2.12).

$$\bar{\sigma} = \frac{1}{\sqrt{2}}[(\sigma_{11} - \sigma_{22})^2 + (\sigma_{22} - \sigma_{33})^2 + (\sigma_{33} - \sigma_{11})^2 + 6(\sigma_{12}{}^2 + \sigma_{23}{}^2 + \sigma_{31}{}^2)]^{1/2} \quad \text{(Eq. 2.12)}$$

Both hypotheses are well accepted for isotropic materials; however the von Mises criterion has shown better agreement to the experimental results [SHE99].

2.2 Extrusion of aluminum alloy

2.2.1 Extrusion process

During the extrusion process a preheated billet is pushed through a die with an opened cross section or bearing channel. This manufacturing process allows the production of single or multiple solid and hollow profiles with complex cross-sections [BAU06]. When the billet is pushed by a dummy block while the container and die remain static, the method is called direct or forward extrusion (Fig. 2.2a). The relative movement between billet and container generates usually high friction that increases considerably the total extrusion force [MUE04]. On the other hand, in the indirect extrusion the dummy block and container move together generating almost no friction between them. In this case the product passes through a hollow stem which limits the maximal diameter of the extruded profile (Fig. 2.2b) [AVI83].

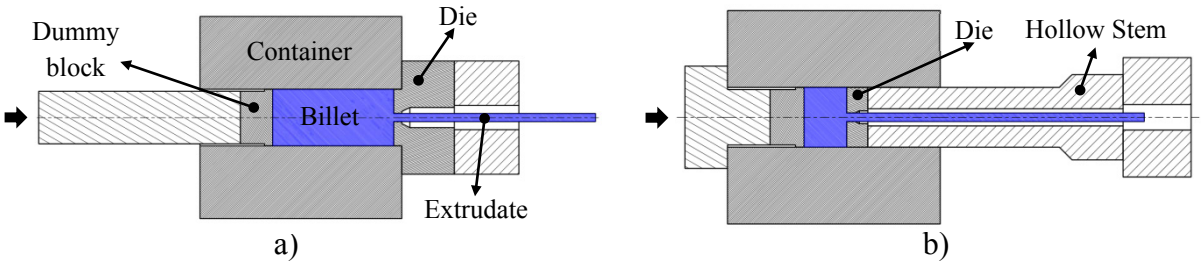

Fig. 2.2. Schematic representation of a) direct and b) indirect extrusion.

According to the extrusion type, initial billet temperature and lubrication conditions, the billet can experiment different intern deformation patterns [PEA60, DUE68]. Several experimental investigations applying grinding and internal grid pattern techniques have revealed the real metal flow inside the billet during extrusion process [VAL88, FLI05]. However, in the case of aluminum alloys two main flow patterns characterize the unlubricated direct and indirect extrusion (Fig. 2.3) [VAL96]. In direct extrusion the internal area of the profile is formed with the material coming from the primary deformation zone, while the extrudate surface is formed with the material that flows between the dead zone and shear zone [VAL88, LEF92]. Moreover, the peripheral skin of the billet remains stick at the container wall and is scraped off by the moving dummy block during the extrusion. This material accumulates in the rear end corner of

the billet which later flows radially toward the center also known as the secondary deformation zone (Fig. 2.3a) [VAL10].

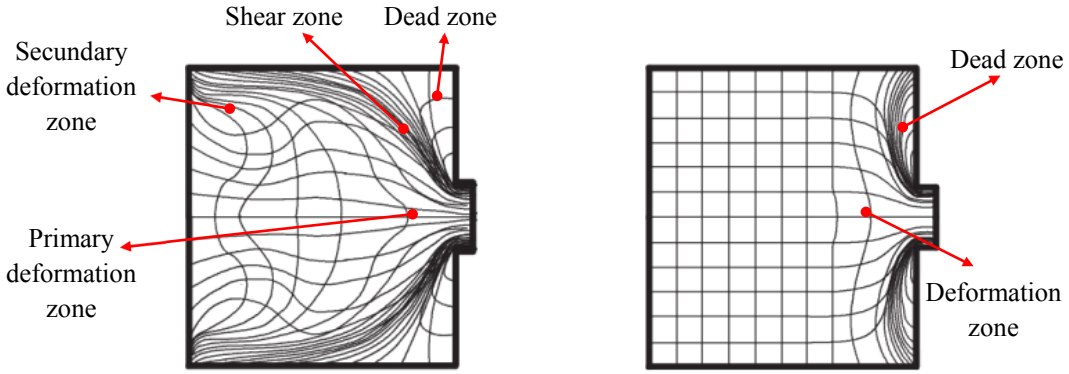

Fig. 2.3. Flow patterns of a) direct and b) indirect extrusion of aluminum alloys [VAL10].

During indirect extrusion only the front part of the billet suffers plastic deformation as is seen in Fig. 2.3b. The front surface of the billet remains stick to the flat-face die creating a dead zone. Furthermore, the billet surface is forced to flow between the dead zone and the deformation zone, to posteriorly enter in contact with the bearing channel and create the extrudate surface (Fig. 2.3b) [SAH00]. Multiple profiles can be simultaneously extruded using dies with several holes. The extrusion with multi-hole dies is an efficient way to increase productivity, because several extrudates with the same or different shapes can be manufactured at the same time. However, in the practice, an iterative and complicated die design process is needed to control the material flow and the relative speed of the products. When dies with single bearing channels are used, the product speed v_f can be easy calculated relating the stem speed v_s to the ratio between the initial A_o and final A_f cross section (Eq. 2.13) [MUE04]. However accurate friction models have to be used to predict the final product speed in multi-hole extrusion [HOR14].

$$v_f = \frac{A_o}{A_f} v_s \qquad \text{(Eq. 2.13)}$$

Experimental investigations have shown the internal deformation patterns with multi-hole dies [VAL96, SHE04]. Fig. 2.4a and 2.4b depict the flow pattern of partial direct extruded billets using two and three bearing channels respectively. These micrographs show the formation of dead zones not only at the corner of the billets but also between bearing channels [SHE04]. The position of the holes will influence the size of the dead zones, therefore the length of the shear zone and thus the material flow and product speed [HOR05, KAR05].

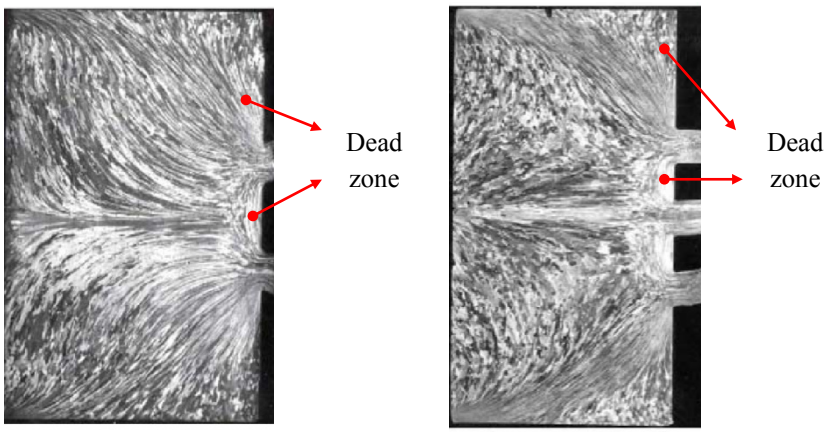

Fig. 2.4. Flow patterns of direct extrusion with a) two holes and b) three holes [SHE04].

Considering equidistant positioned holes, the extrudate relative speed will depend on the resistance that experiment the material to flow through the bearing channels. In other words, the relative product speed will be related to the contact area, cross section and inclination angle of the bearing channels [AKE85, AKE88, VAL94, MUE96, HOR05, KAR05]. Additionally, several investigations demonstrated that the pocket geometry also plays an important role on the material flow and product speed [LI03, SCH08, ZHO09, LIB10].

2.2.2 Aluminum alloy EN AW-6060

The EN AW-6XXX series alloys are the most used in the extrusion industry, mainly due to the high formability, medium strength and good corrosion resistance, making them suitable for decorative and structural applications [SHE99]. In this series alloy the elements magnesium and silicon are combined to form magnesium silicide Mg_2Si being the primary hardening phase (β). Since a quantity of magnesium silicide exceeds the equilibrium solid solubility limit at room temperature, precipitates in form of plates or cubes (β - Mg_2Si) will appear in the aluminum matrix. However, this phase will be dissolved into solid solution if the temperature exceeds the solvus temperature (Fig. 2.5). An increase of Mg_2Si content improves the tensile properties, but reduces the extrudability [GAR04]. Medium strength alloys or for general propose contain around 0.8 % of Mg_2Si, while 1 % correspond to high strength alloys used for structural applications. On the other hand, the alloys with high extrudability such as EN AW-6060 contain circa 0.7 % of Mg_2Si, and are used for applications where the shape has more relevance than the strength [SHE99].

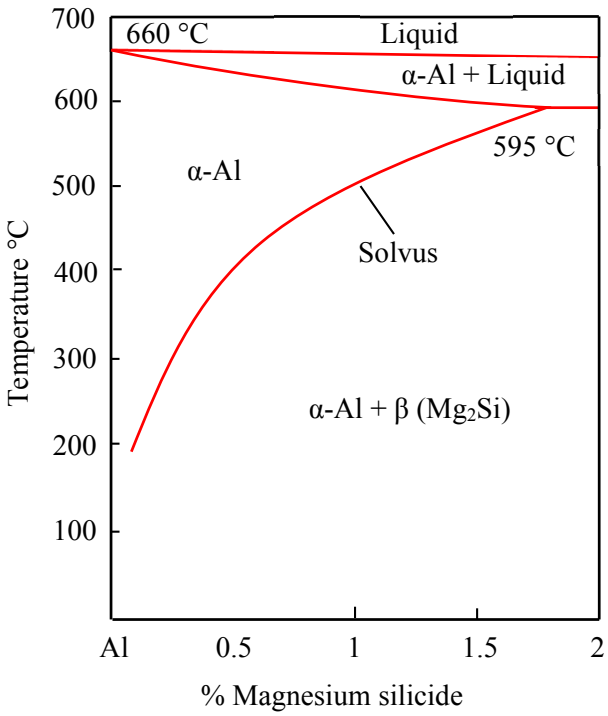

Fig. 2.5. Al-Mg_2Si phase diagram [SHE99].

The typical chemical composition of the aluminum alloy EN AW-6060 is resumed in the table 2.1.

Table 2.1. Typical composition of aluminum alloy EN AW-6060 [Wt%][SHE99].

Al	Si	Fe	Cu	Mn	Mg	Cr	Zn	Ti
Balance	0.30-0.60	0.10-0.30	0.10	0.10	0.35-0.60	0.05	0.15	0.10

During extrusion it is desired that the Mg_2Si dissolves into solution when the material passes through the deformation zone. Thus the Mg_2Si can be retained in solution after extrusion through quenching and important improvement of the mechanical properties can be achieved by means of additional heat treatments (ageing). However, a complete dissolution is only possible when the cast billet is homogenized before extruding to achieve precipitates (Mg_2Si) with small size (0.25 µm-0.50 µm) and uniform distribution.

2.2.3 Plastic deformation and restoration during aluminum extrusion

In aluminum alloys the atoms are arranged in unit cells forming a face-centered cubic lattice FCC (Fig. 2.6a). Each unit cell has 12 different atomic planes which can slip over each other when external forces exceed the atomic bonds. Additionally, the crystal lattices are unevenly distributed generating linear defects in the arrangement called dislocations (Fig. 2.6b).

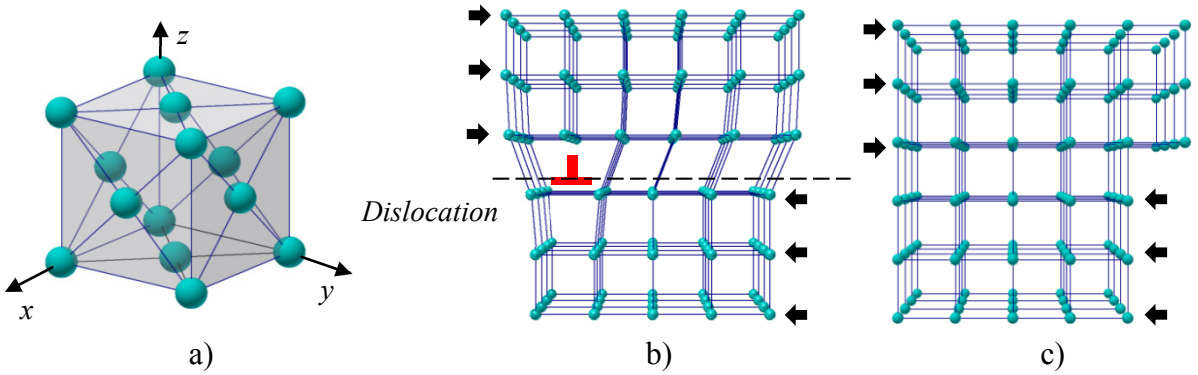

Fig. 2.6. Lattice structure a) unit cell FCC, b) dislocation c) moved dislocation.

The dislocations make easier the plastic deformations because only the bonds of an individual row of atoms have to be broken before springing to another lattice place (Fig. 2.6c). Multiplication and interaction of dislocations occur during plastic deformation, increasing thus the stored energy. At low temperature (T<350 °C) this process generates grain refinement and increase of the flow stress (strain hardening). In metals with high stacking fault (HSF) energy such aluminum alloy, dislocation movements are facilitated at high temperature. Since the mobility of dislocations increases at higher temperatures, they can be rearranged in a more stable configuration with a minimum energy. When a critical strain is achieved the dislocations tend to arrange themselves in walls which are roughly equi-spaced forming subgrains (polygonization). The occurrence of this phenomena and eventually the annihilation of dislocations during the plastic deformation is called dynamic recovery (DRV). Both processes occur simultaneously, thus the flow stress is increased by the strain hardening, but reduced by the dynamic recovery. Hence, during extrusion of aluminum alloy strain hardening and dynamic recovery compete until reaching a steady state with a constant flow stress.

Although stored energy decreases during dynamic recovery, it is not completely removed. The remained stored energy accompanied by a minimum deformation can generate new strain-free grains. This thermally activated process is known as recrystallization, and can occur during (dynamic recrystallization DRX) or after the deformation (static recrystallization SRX). The dynamic recrystallization is divided into discontinuous dynamic recrystallization (DDRX) and continuous dynamic recrystallization (CDRX). DDRX occurs mainly in materials with low stacking fault energy, involving nucleation at the old grain boundaries and grain growth. On the other hand, during CDRX occur subgrain formation through DRV, consequently progressive misorientation of the subgrain boundary and transformation into high angle grain boundary.

Finally, the subgrains and grain boundaries are eliminated due to boundary migration. According to the literature CDRX can be classified into geometric dynamic recrystallization (GDRX) and dynamic recrystallization by progressive lattice rotation [HUM04]. The geometric dynamic recrystallization GDRX also known as grain dividing (gDRV) [MCQ10], generate an equiaxed microstructure with a high number of high angle boundaries. The origin of this microstructure is the grain impingement, which occurs when the grains are elongated and its thickness becomes equal to the subgrain size [HUM04]. Furthermore, the dynamic recrystallization by progressive lattice rotation involves a gradual rotation of subgrains adjacent to pre-existing grain boundaries.

When the deformation process is finished, static recrystallization can take place if the stored energy as well as the temperature overcome the critical values. Subsequent to the recrystallization the energy remained in the high angles grain boundaries is the driving pressure to produce grain growth.

The literature reports mixed opinions about the occurrence of restoration during extrusion of aluminum EN AW-6XXX alloys. On one hand it is reported that the metal suffers only DRV in the deformation zone and the recrystallization takes place when the extrudate leaves the die (SRX) (Fig. 2.7a) [BAU06]. On the other hand, other extrusion investigations revealed that DRX not only occurs for low stacking fault energy materials (Fig. 2.7b), but also for aluminum alloys EN AW-6XXX [PAR04, OCK12]. Hence, fibrous and unrecrystallized cross section was observed using low ram speed (2 mm/s) regardless the temperature. Contrary fully recrystallized cross section was detected at high ram speed (30 mm/s). Extrusions trials carried out with an intermediated ram speed showed fibrous core structure and recrystallized in the outer band. This effect is also called peripheral coarse grain (PCG) also investigated in [KIK88, DUA03, GEE04]. Hence, the extrusion operating parameters are often controlled to obtain fibrous structures due to the associated higher strength [PAR04].

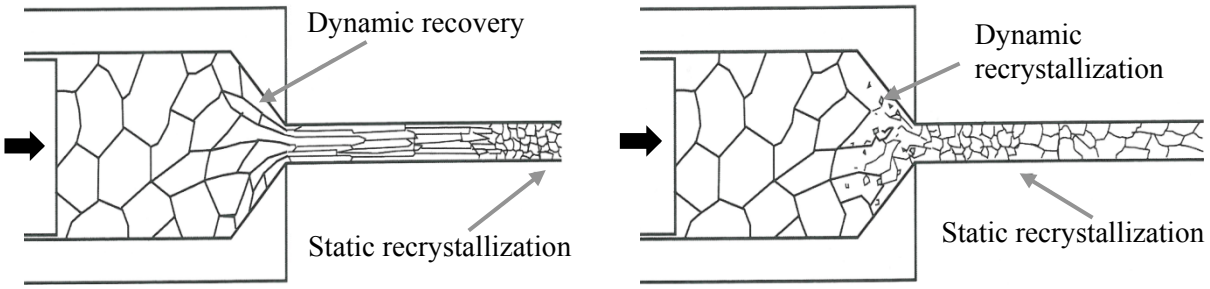

Fig. 2.7. Dynamic recovery and recrystallization during extrusion using material with a) high stacking fault energy and b) low stacking fault energy [MCQ75].

2.2.4 Constitutive equations

The von Mises yield criterion (Eq. 2.12) allows relating any state of stress of a material to its yield strength, which is obtained from a simple unidirectional mechanical test, such as compression or tensile test. From the mechanical point of view, the yield strength of a specific material is influenced by the temperature T, strain ε and also at different strain rates $\dot{\varepsilon}$ in viscoplastic materials such as aluminum alloy [SHE99]. Moreover, the microstructure also changes during deformation because it is allowed through dislocations movements. Under certain conditions of temperature, strain and strain rate the grain size is also changed affecting thus the local mechanical response. This indicates that there must be a relation between the yield strength or effective stress with the temperature, strain, strain rate and the current microstructural structure. Additionally, another relation must quantify the changes of the state variables (dislocation density, grain size, etc.) produced at different temperature, strain, strain rate and also the previews state of the microstructure. These physical relations are called constitutive equations and are used in plasticity to predict the effective stress at any condition of temperature and deformation. Unfortunately, the time evolution of the metallurgical structure has not been fully understood and therefore the phenomenon is usually highly simplified. Thus, the effective stress is usually related only the temperature, strain and strain rate.

Unfortunately, the available laboratory experiments such as hot compression and tension tests are not able to reproduce the larger strains generated during extrusion process. Although the torsion test reproduces high strains, important radial gradients of strain and strain rate cannot be avoid [MCQ02, MIS06]. Since, the strain does not change the flow stress at high temperatures during aluminum extrusion; the strain effect can be neglected in the constitutive equation [SHE99]. The Zener-Hollomon parameter Z (Eq. 2.14) allows relating the temperature and the

strain rate dependence in hot working [ZEN44]. Thus, ΔH is the deformation activation energy, R the gas constant and T_k the absolute temperature. Based on this relation, Sellars and Tegart proposed a constitutive equation [SEL72] which was modified later by Sheppard and Wright [SHE79] to calculate the flow stress in extrusion process (Eq. 2.15). This equation estimates the effective stress at steady state depending on the temperature T and the strain rate $\dot{\varepsilon}$ (Eq. 2.14), where α, A and n are constants.

$$Z = \dot{\varepsilon} e^{(\Delta H / RT_k)} \quad \text{(Eq. 2.14)}$$

$$\bar{\sigma} = \frac{1}{\alpha} sinh^{-1} \left(\frac{Z}{A}\right)^{1/n} \quad \text{(Eq. 2.15)}$$

2.3 Friction in extrusion processes

2.3.1 Friction Phenomena

The friction can be defined as the force that opposes the relative movement between two surfaces in contact. In an intuitive way this concept is well known because it allows carrying out simple tasks such as walk or shake hands, however there are multiple factors that influence this complex phenomena. According to the literature, the first friction principles were suggested by Leonardo da Vinci in 1495 [DOW97], who established that the friction force F_f is proportional to the normal force F_n and independent to the contact area. Almost two hundred years later Amontons confirmed da Vinci's idea and proposed the proportionality between normal and friction force. Although the mathematician Leonard Euler introduced the friction coefficient μ, was Charles Coulomb who in 1785 postulated the law of dry friction or Coulomb's law. Coulomb carried out numerous experiments evaluating the effect of the material pair, surface composition, lubrication, temperature, sliding speed, and humidity. According to his results, the sliding friction is independent to the sliding speed. Additionally he defined the friction response at static and dynamic conditions and its dependence to the contact time.

In 1882 Heinrich Hertz presented a new concept to study the contact area generated when two spheres are pressed elastically against each other. His work gave rise to the classical contact mechanism allowing the calculation of contact stress as a function of the normal force, the elasticity modulus and the radius of the spheres [JOH85]. Later in 1950, Bowden and Tabor emphasized the importance of the roughness in the contact mechanisms [POP10]. They concluded that the real contact area is much smaller than the apparent area, and suggested that

the sliding friction is produced through the formation and shearing of cold weld junctions [BOW50]. Posteriorly, Greenwood and Williamson combined the Hertz's theory and the new knowledge about roughness to calculate the real contact area. They observed that the real contact area of rough surfaces is proportional to the normal force, because more asperities become in contact at higher normal load [WUT87]. In 1943, Orowan suggested that under low normal force the friction stress is proportional to the normal pressure, but it is equal to the shear yield stress at high pressures [ORO43]. This new friction approach was later refined by Wanheim and Bay [WAN73, WAN78]. Additionally, it has been emphasized the roll of the local shear instabilities that develop large plastic strains accumulated in the surface [BLA81, GLA81, RIG84, CHE85]. They also suggested that both adhesion and contact geometry influence the sliding friction.

Even though the friction phenomenon has been investigated for more than five hundred years and a deep knowledge in this field has been developed, there are still difficulties to predict accurately the friction force in real operational conditions. There are many variables involved in this subject defining thus the nature of the process; but researchers agree that the contact mechanisms is one of the most important aspect to be taken into account specially in the case of metal sliding. As was mentioned above, only the asperities become in contact during friction, hence the number of contacts increases with the normal force and thus the friction. However, friction reaches a maximum values at high normal pressure.

In general, three main contact scenarios are present during sliding dry friction between a softer material and a harder material under different normal forces ($F_{n1} < F_{n2} < F_{n3}$) (Fig. 2.8). In the first scenario (Fig. 2.8a) a low normal force F_{n1} produces only elastic deformation of the asperities creating the proportionality mentioned by Coulomb (slip condition). In this case the roughness characteristic plays and important role and the Hertz theory is the basis used to estimate the real contact area and the friction stress.

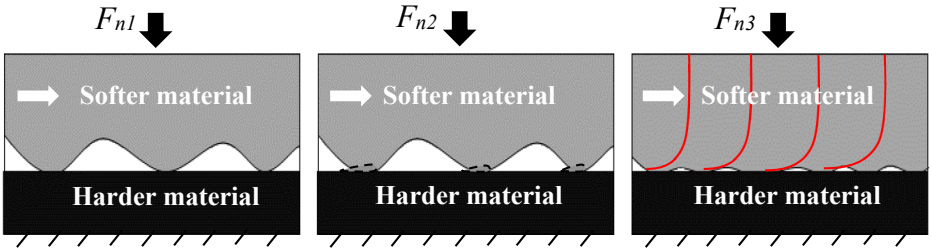

Fig. 2.8. Mean contact mechanisms at dry metal sliding.

a) Slip, b) slip-stick and c) stick friction.

On the other hand, a more complicated situation is produced when at higher normal forces or at higher temperatures the yield strength of the asperities is reached, producing significant plastic deformations (Fig. 2.8b). This situation modifies permanently the roughness creating wear and in some cases discontinuous thin layers between the contact pair (slip-stick) [WAN78]. Under these conditions it is not convenient the use of the classical contact theories and phenomenological approaches have to be used. In addition, it is also known that the friction is caused not only by mechanical interactions, but also by chemical adhesion. The adhesion role in metal friction is still object of study, however it is accepted that intermolecular forces play a role at high temperature. When the asperities are subjected to plastic deformations the superficial oxide layer is broken and metal-metal contact is produced. Furthermore, the asperity plastic deformation increases its local dislocation density and vacancy density activating the superficial layer and contributing with the formation of intermolecular bonds [WUT87].

In the third scenario the real and apparent contact areas become similar because of the high plastic deformation of the asperities (Fig. 2.8c). Strong junction forces occur remaining together both contact surfaces, whereas the sublayer of the softer material experiences a severe shearing [DAU73, DAU80].

2.3.2 Friction nature in extrusion process

In direct extrusion friction occurs mainly in the dummy block, container, shear zone and the bearing channel [MUE04]. The dummy block transfers a high normal pressure against the rear of the billet; however the friction in this zone is less studied due to its minor importance during this process. On the other hand, the friction force generated at the container is relevant for the total power estimation, because it represents a great portion of the extrusion force. According to experimental investigations, the high friction occurs due to peripheral shear deformation of

the billet surface under sticking conditions [SAH98]. The thickness of this region can vary from 100-300 µm [FLI00] to circa 10 mm [KAM12]. In this region the friction is equivalent to the shear flow stress of the workpiece adjacent to the billet surface. Moreover, friction is also generated at the interface between the death zone and the flowing material called the shear zone. It plays also an important role because in this region begins the formation of the extrudate surface [SHE88, VAL88]. The friction in the shear zone is related directly to the local temperature, strain and strain rate defining thus the material shear flow stress. Furthermore, it is also associated with the billet-container and billet-die friction conditions, because they are responsible for the form of the dead zone and therefore for the length of the shear zone [FLI03]. Under high temperature and severe metal forming in the shear zone, local dynamic recrystallization have been also observed for different aluminum alloys such as Al-Zn-Mg-(Cu) [KIK88], $AlCu_4Mg$ [LIB92], AA6063 [CLO92] and EN AW-6060 [SCH07, KAY10]. Theses microstructural changes may change the flow stress or effective stress of the material that posteriorly will interact with the bearing channel to give the final product shape. The friction in the bearing channel normally represents a small portion of the total extrusion force, however it has a strong influence on the material flow, the final profile temperature and product quality [LAN84]. The contact mechanisms between workpiece and bearing land has been systematic investigated during the last 40 year, however it has not been fully understood. According to Akeret it is “a mechanism based on dynamic equilibrium between adhesion and removal of adhered aluminum particles” [AKE81]. He also observed that in spite of the adhesive characteristic of hot aluminum, using nitrided dies a significant area of the bearing channel remains always free of adhesive layer [AKE83]. However, other investigations reported that a total or partial aluminum layer will cover the bearing channel during aluminum extrusion [TOK76, MER77, SHE88, TOK88, CLO90, THE92, THE93]. Additionally, the adhesion layer is unstable and it can be detached from the die bearing by the extrudate [KEM67, MER77, TOK88].

2.3.3 Friction behavior in long bearing channels

Experimental investigations have shown the strong influence of the bearing channel angle on the contact mechanisms between the workpiece and the die land, observing significant changes in the range from 0.5° chocked to 0.5° relief [AKE83, AKE85, AKE88]. The influence of many geometrical configurations and bearing angles have been also studied [AKE83, PAR96], thus they can be grouped in three main types: chocked, parallel and relief channels (Fig. 2.9).

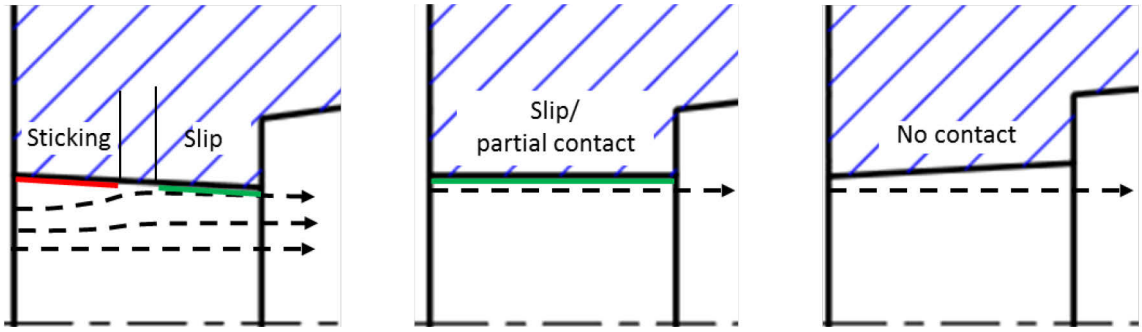

Fig. 2.9. Contact mechanisms present in a) choked, b) parallel and c) relief bearing channels.

Using choked bearing channels (Fig. 2.9a) a high contact pressure takes place between the workpiece and the die land producing intimate interaction and thus sticking friction. Under these conditions a thin layer sticks on the die land while a subsurface suffers a severe shear deformation. As a result the magnitude of the friction stress is in the order of the material shear flow stress [AKE85]. Experiments carried out with short and long chocked dies showed sticking conditions at the beginning of the channel but sliding conditions toward the outlet [VAL94, ABT96]. Using contrast material Valberg demonstrated that in the transition stick-slip the subsurface layers of aluminum situated over the sticking contact flow with a lower axial speed than the material in the middle of the channel. Thus, the material flows radially outwards toward die land at the end of the sticking layer (Fig. 2.9a) [VAL96]. The stick-slip behavior could explain the friction variation along chocked channels. Die inspections after extrusion trials have revealed a dark color area in the sticking zone, which is possible due to oxide created through chemical reaction between aluminum and the die land [VAL96]. Likewise, the extrudate surface will be generated at the end of the sticking zone; but it may be altered as it slides along the bearing. At the end of the die land an adhesive layer of aluminum is formed, as a consequence of the interaction between the extrudate and bearing channel [SHE88, CLO90].

In parallel dies (fig. 2.9b) the friction stress decreases considerably [AKE85, MUE96]. According to the literature, the shear stress transferred to the bearing channel is around 0.2 times the flow shear stress of the extrusion material [TOK76, LAN84, TOK88]. In order to explain the friction decrease, it is assumed that the extrudate has a partial loss of the contact with the bearing channel caused by tool bending [VAL94]. On the other hand, the strong reduction of friction can also be caused due to the low contact pressure between the extrudate surface and the die land or the adhesive layer, which only interact with their asperities. Additionally, surface

defect formation could favor a low to medium pressure level between the extrudate surface and the bearing channel or adhesive layer modifying also the length of the slipping zone [ROO12]. Experimental results have demonstrated that the parallel bearing channels are cover by an adhesive layer, which starts at the entry of the bearing channel and progressive covers the whole bearing area [ABT96]. The form of the aluminum layer correspond to the scheme of lamellar current and its formation is a random process, thus it can be partial detached and ones again formed [THE92, THE93]. Moreover, the product surface topology continues changing during the extrusion due to interaction to the adhesion layer. Extrusion experiments carried out with parallel channels and aluminum alloy AA6063 at 450 °C, revealed the composition of the adhesion layer [TOK88]. A thicker layer of about 10 µm was found, rich in Fe, Si and O and depleted with respect to Mg. Similar investigation was done using nitrided dies observing a thickness around 6 µm composed by two thin layers. Adjacent to the steel the aluminum layer was reach in Mg and O, but in the outer layer high content of Si was observed [THE92, THE93]. During extrusion with relief bearing channels (Fig. 2.9c) the extrudate surface is generated in the shear zone adjacent to the death metal zone and in theory it does not have any contact with the die. In this case the friction force generated at the bearing channel is zero.

2.3.4 Factors affecting the friction under slipping contact conditions

Temperature. At high temperature the asperities in contact are plastic deformed allowing a more intimate contact and increasing the tendency to develop the adhesive layer [SAH98, SAH04]. Extrusion of aluminum alloy AA6063 carried out with parallel and smooth bearing channels, concluded that the nature of the adhesion layer on the bearing channel also is influenced by the temperature [TOK76, TOK88]. At 450 °C the extrudate asperities adhere to the die land creating a homogeneous white spot-like adhesion layer which generates a good product surface quality. Moreover, at 500 °C the lower deformation resistance favors the increase of contact area. Under these conditions the contacts will be spread in the extrusion direction producing a white stripe-like adhesion layer and therefore bad product surface quality.

Billet alloy. Twist-compression experiments with different aluminum alloys (1050, 5182, 6061-T6 and 2024-T351) were carried out using hard steel O1 prepared with diverse roughness (Ra= 0.05 µm, 0.15 µm and 0.30 µm). The main friction variations were not influenced by the roughness, but by the thickness, continuity and stability of the adhesion layer. Thus it was concluded that the sliding friction and metal transfer were governed by alloy composition. For

ductile materials (1050) there are heavy transfer and retransfer, and strong attachment that suggests adhesion [NAU91].

Surface topography of the bearing channel. It is general accepted that smooth surfaces reduce the friction [STA73]. Usually the surface topography is associated to the average roughness R_a and the mean roughness depth R_z, however studies have demonstrated that it is not sufficient to characterize a functional characteristic like friction [LUN95]. Hence, two surfaces with the same roughness *Ra* but different texture (lay pattern) can have different friction response [KAI03, MEN06]. According to friction tests between aluminum and steel using the pin on plate apparatus, the adhesion and plowing and even the average coefficient of friction are controlled mainly by the directionality of the grounding marks and are independent of the roughness [MEN06, KAI09]. The surface texture has been also studied in extrusion experiments using parallel dies. On the bearing surface ground vertically to the extruding direction, the ground grooves are filled with the adhesion material and the bearing surface becomes smooth. When the bearing surface is grounded parallel to the extrusion direction ridged stripe of adhesion grows on the bearing surface, producing rougher product surfaces [TOK88]. Frequently a polished bearing channel is related with a gut product quality, nevertheless buffed bearing surfaces generates poor adhesion which makes the product surfaces rough.

Surface coating of the bearing channel. Extrusion dies with nitrided or vapor deposited CVD coated bearing channels are usually used to improve the surface product obtained with plain steel (without coating). The different adhesion behavior between aluminum alloys and the coated surfaces influence the formation of the adhesion layer, wear and friction behavior. The adhesion generated with nitrided surfaces is significant lower than those produced without coating [TOK88, THE93, SAH98, SAH04]. This statement was also confirmed through friction tests, observing lower friction forces using coated surfaces [KAR10]. Additionally, similar friction experiments concluded that nitrided and vapor deposited CVD coated (Al_2O_3 and TiCN) have similar friction response especially at high normal pressure [BEC14]. However, CVD coating by TiC + TiN has a superior wear resistance compared to the nitrided dies [BJO99].

2.3.5 Methods for friction investigation

A tribological investigation requires evaluating the influence of many variables associated to the process (speed, temperature, and pressure), tools (coating, surface roughness and texture), workpiece material and transfer process (adhesive layer), wear, lubrication, etc. Since the nature of this phenomenon can change according to a specific process and its working conditions, an

investigation in situ would be the ideal manner to study the specific friction response. However in the practice this study is very complicated and expensive, therefore the friction is usually investigated using apparatus and scaled deformation methods that simulate similar operative conditions.

2.3.5.1 Friction evaluation during extrusion trials.

The friction in extrusion process can be investigated by means of multiple methods:

- The friction generated between billet and container is usually estimated from the difference of the total direct and indirect extrusion force maintaining constant the other extrusion parameters. Some extrusion machines are equipped with special measuring technique that enables measuring not only the total extrusion force, but also the friction force between billet and container [MUE96, MUE12].
- The friction attributed to the bearing channel can be also calculated comparing the total friction forces measured in different extrusion trials, but changing only a die characteristic such as: contour of the cross section, bearing length, surface coating, surface roughness and texture, bearing angle, etc. [LAN84]. Since the friction force in the bearing channel is small compared with the total extrusion force, long channels and changes of the die angle are used to generate a higher friction difference [AKE83, AKE85].
- A modular type die equipped with a load measuring technique was used to compute the friction in the bearing channel [ZIE77]. However, the measured force was considerably higher than expected. Recently, a similar technique has measured the pressure distribution on extrusion die surface [MOR02]. In this method, a small load sensor is placed into the die allowing the measurement of the local pressure [TUN88, LUP05].
- Extrusion experiments using multi-hole dies have been used to evaluate the influence of the bearing channel characteristics, specially the bearing angle and length, on the relative product speed [AKE85, MUE96, VAL96, HOR05, MUE12].

Using multi-hole dies the product velocity depends not only on the stem velocity and cross section of each profile, but also on the resistance generated at each bearing channel. Thus, more material flows through the bearing channel where less friction is generated, affecting simultaneously the local temperature and the flow distribution through the other channels. Fig. 2.10 shows the simultaneous extrusion of two profiles.

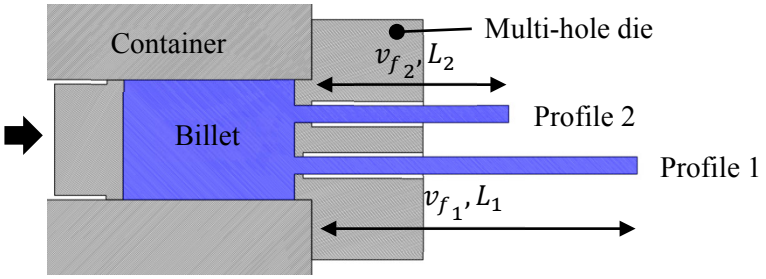

Fig. 2.10. Direct extrusion using a multi-hole die.

Although the billet is forced to pass simultaneously through the two bearing channels, the profile 1 flows faster than the profile 2 because of the lower friction in bearing channel. As a consequence, the profile 1 is longer than profile 2 because more material flows through the bearing channel 1 in the same extrusion time t (Fig 2.10). The product speed can be calculated by means of the product length and the extrusion time. Additionally, the percentage of the relative product speed $\%v_i$ can be also calculated with the product length L_i (Eq. 2.16).

$$\%v_i = \frac{100\%\ v_i}{\sum_{i=1}^{n} v_i} = \frac{\frac{100\%\ L_i}{t}}{\frac{\sum_{i=1}^{n} L_i}{t}} = \frac{100\%\ L_i}{\sum_{i=1}^{n} L_i} \qquad \text{(Eq. 2.16)}$$

2.3.5.2 Friction tests based on rotational movement

Many tests have been developed to simulate the friction; only in the 60's there were more than 100 test devices [BEN66]. In these methods usually two surfaces are subjected to rotational or translational relative movement, while the speed, normal load and temperature are varied. Fig. 2.11 shows schematically the more common rotational friction tests. The *pin on disc test* is a standard method to measure friction and wear. In this test a stationary small cylinder is pressed against a rotating disc with a controlled force (Fig. 2.11a). According to the hardness difference the disc or pin can suffer important plastic deformation changing thus the contact conditions. Microstructural changes of the friction boundary layer have been observed in pins [DAU73, DAU80], while a wear track can be observed on the disc surface. Multiple pins can also be used as reported in [MAH84]. The *ball on disc test* (Fig. 2.11b) is a variation of the pin on disc test but in this case a small hard sphere rubs against a softer disc. It has been used to study friction conditions for extrusion process [WAN09, WAN10]. Additionally, *the block on cylinder test* was developed to reproduce friction condition in extrusion process [BJO99]. In this test a small block is pressed against the lateral surface of a hard steel cylinder to simulate the tribological conditions at the bearing channel (Fig. 2.11c). A variant of this method is the *block on disc test*

which uses a bigger and hard block (die) to increase the friction contact area against a softer disc (Fig. 2.11d) [PEL07]. In another configuration called the *twits-compression test* a flat plate (specimen) is placed between two hardened steel.

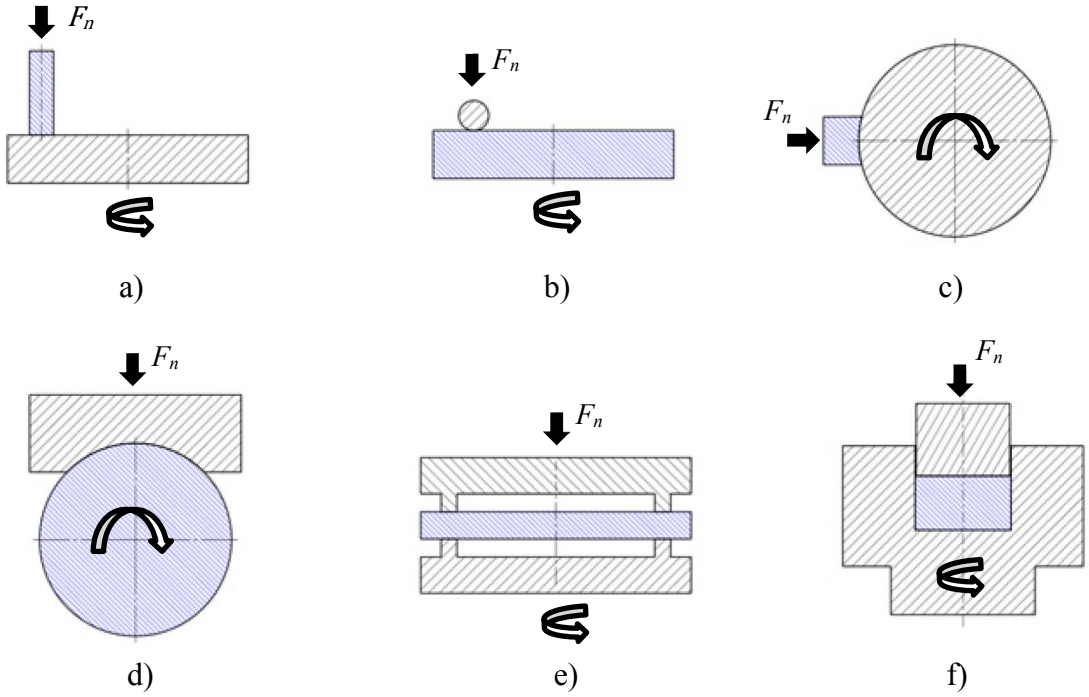

Fig. 2.11. Friction tests based on rotational movements.
a) Pin on disc, b) ball on disc, c) block on cylinder, d) block on disc, e) twits-compression test and f) compressive compressional method.

A new configuration based on this method uses two dies with annular shaped edges which press a softer disc (Fig. 2.11e). One die rotates and the other rotationally fixed controls the normal load. The measured torque is due to frictional resistance transferred from the upper to the lower die [TAJ06]. The similar principle was applied by Buch to develop the *rotary forging tribometer* [BUC08].

In order to analyze thermo-mechanical condition required for sticking conditions, higher normal load has to be applied, usually in the order of the material yield strength. Under this high pressure the above mentioned friction tests (Fig. 2.11a-2.11e) have a poorly perform and new methods have to be used [HOR12]. Recently, the slip-stick conditions between aluminum alloy EN AW-6060 and hardened steel was studied at different temperatures using a *compressive rotational method* [WID12]. Thus an aluminum disc is compressed in a lower die with a cup-

shape by an upper die with the same internal diameter, filling thus the lower cavity (Fig 2.11f). The normal load is applied by the upper die, while the lower die rotates with the sample at a specific speed. Using aluminum disc with inserted contrast material the deformed subsurface was revealed to identify the depth of deformation.

Additionally the *tribo-torsion-test* is a new prototype designed at the Institute of Virtual Manufacturing of ETH Zurich suitable for friction investigation at high pressure, temperature and speed conditions [BEC14]. Fig. 2.12a shows an improved version of this setup based on the tribo-cone and tribo-cylinder [KAR10, HOR12]. This setup is placed in a torsion machine (Baehr STD 810) with tension-compression capabilities allowing simultaneously axially and rotationally loading.

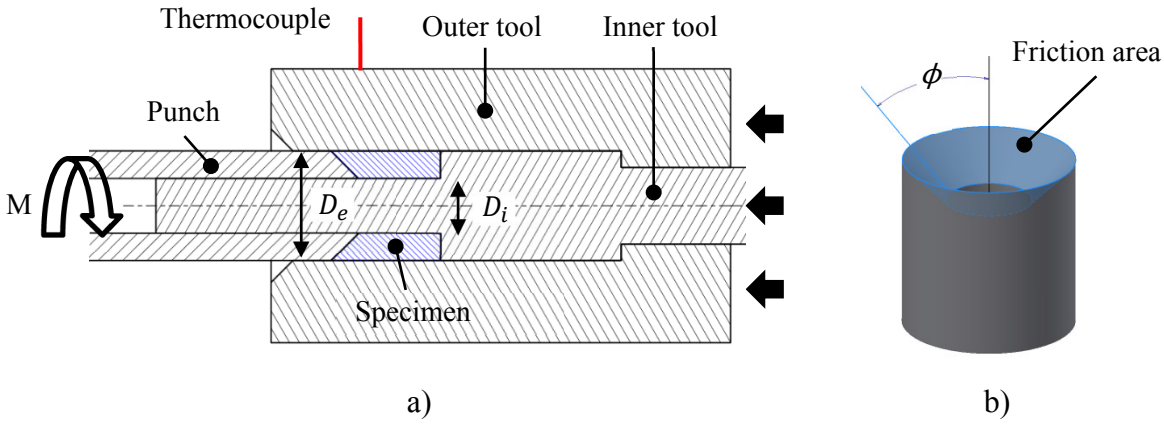

Fig. 2.12. Schema of the tribo-torsion-test.

a) Assemble of the tools and specimen, b) specimen.

The specimen is constrained between the outer and inner tools using radial screws, while the whole system is pushed against a rotating conic punch. The friction is generated on the conic contact area between the punch and the specimen (Fig. 2.12b). The system is heated by an inductive heat coil and the temperature is measured and controlled using a thermocouple placed on the outer tool.

Using the torque M measured by the device and the geometrical characteristics of the specimen such as: apparent contact area A_a, internal and external diameter (D_i, D_e) and inclination angle (ϕ) an average of the friction stress can be calculated (Eq. 2.17).

$$\tau = M\frac{16}{\pi}\frac{\sin(\phi)}{({D_e}^2 - {D_i}^2)(D_e + D_i)} \qquad \text{(Eq. 2.17)}$$

2.3.5.3 Friction tests based on translational movement

Few friction tests based on translational movement are available, possible because only a short friction length can be investigated through this method. Using the same friction principle of the ball on disc friction test a prototype test apparatus with translational movement was developed [STO05]. In this method two small hardened balls with vertical constrain are pressed against a softer flat sheet as indicated in Fig. 2.13a. The friction force is the force required to move vertically the specimen with a constant speed v, and easily measured with load cells.

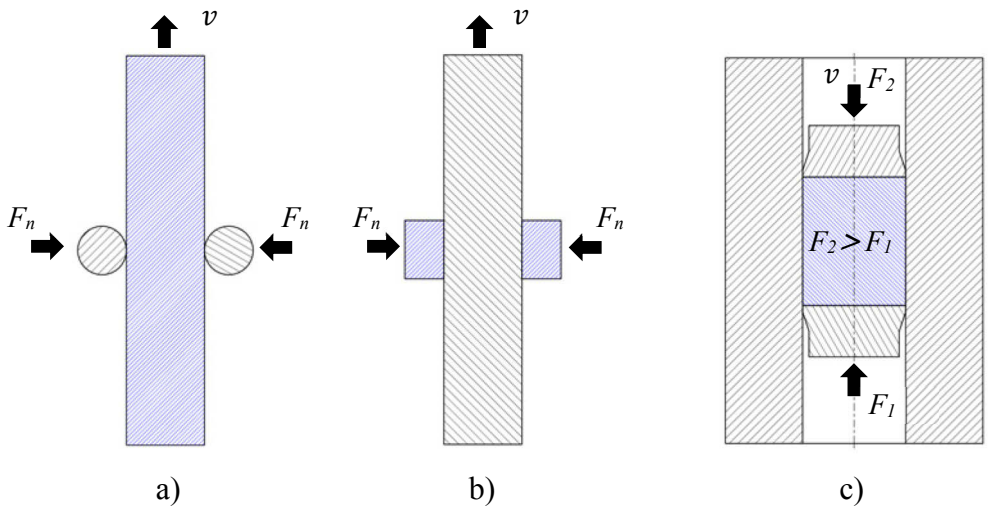

Fig. 2.13. Friction tests based on translational movement. a) Low load using hard ball indenter, b) low load using soft blocks, c) high pressure friction test.

A similar approach is used to measure the friction between soft blocks and a hardened steel bar (Fig. 2.13b) [SUN12]. On the other hand, friction tests under high normal pressure were carried out using a new two-step friction device [OCK12]. In the first step a small cylindrical specimen is set up in a steel hollow cylinder by two counteracting stems (Fig. 13c). Posteriorly, the force of one stem is kept constant F_1 while the other is forced to move the cylinder with a constant speed v. The friction force generated between the specimen and the internal wall of the hollow cylinder is calculated from the difference of both punch forces (F_2-F_1).

2.3.5.4 Friction testing methods through bulk metal forming.

Other alternative methods used to investigate the friction phenomena in bulk metal forming involve the high plastic deformation of a sample, based on two basic practices: the compression test (Fig. 2.14a,b) and the other on the backward extrusion technique (Fig. 2.14c-h). Thus, the final dimension can be for instance related directly with the friction conditions as is the case of

the *cylindrical compression test* (Fig. 2.14a) and the *ring compression test* (Fig. 2.14b). The first one is the typical compression test which produces a barrel effect in the sample due to friction effect. The higher the radius difference between top/bottom and middle, the higher the constant friction factor between the specimen and compression plates [NAJ04]. Moreover, the *ring compression test* developed by Male [MAL64] allows evaluating the friction factor through compression of a ring. Fig. 2.14b1 and Fig. 2.14b2 depict examples of ring compression tests at high and low friction respectively. The friction factor can be calculated either by means of analytical calculations related with the sample dimensions (internal and external diameter and height) [WAN92] or trough numerical simulations [SOF01, CAM13]. Friction parameters can be also indirectly investigated using the backward extrusion technique. Thus high temperature and normal pressure can be reproduced at small scale. By means of numerical simulations and applying adequate material models, different friction factors are evaluated until reproducing similar experimental shape. The *open-die backward extrusion* proposed by Sofuoglu [SOF02] is similar to a compression test but using an opened top die (Fig. 2.14c). A more complicated configuration was suggested by Kang [KAN11] allowing the simultaneous extrusion of a rib and boss (Fig. 2.14d).

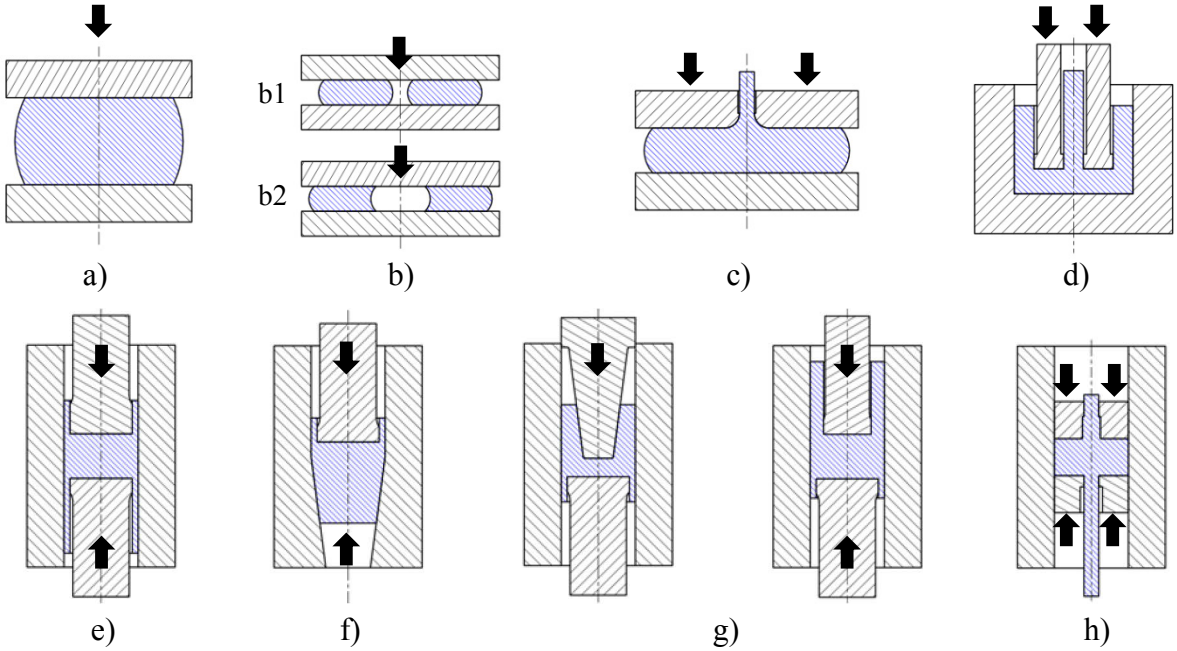

Fig. 2.14. Friction testing methods by bulk metal forming. a) cylindrical compression test, b) ring compression test, c) open-die backward extrusion, d) boss and rib test, e) combined forward conical can-backward straight can extrusion, g) combined for forward rod-backward can extrusion h) double backward extrusion, i) double action extrusion.

Additionally, Busch [BUS92] applied two stems in the backward extrusion to create the *double back extrusion test* (Fig. 2.14e). Based on this method *the combined forward rod-backward can* (Fig. 2.14f) and the *combined forward conical can-backward straight can extrusion* (Fig. 2.14g) were designed by Nakamura [NAK97, NAK98]. Recently, Wang developed the *double action extrusion test* (Fig 2.14h) to highlight the effect of the friction at the die bearing in aluminum extrusion [WAN10, WAN12].

2.3.6 Friction modeling in bearing channel

This section summarizes the models used in extrusion process to determine the friction force and the friction stress in the bearing channel.

2.3.6.1 Coulomb based friction model

The proportionality or *Coulomb friction law* (Eq. 2.18) is a classical friction model that considers the friction force proportional to the normal force F_n using the friction coefficient μ, which is mainly related to the surface contact conditions [POP10].

$$\mu = \frac{F_f}{F_n} \approx \frac{\tau}{P} \qquad \text{(Eq. 2.18)}$$

The implementation of the Coulomb friction model in FE simulations can cause convergence problems due to a sharp transition of the friction force direction at neutral points, where sliding velocity changes its direction. To overcome this problem a *smoothing function* was proposed [CHE78], and a modified coulomb equation was constructed (Eq. 2.19). Where v and u_o ($u_o < v$) are the sliding velocity and a positive constant respectively.

$$F_f = \mu F_n \left[\frac{2}{\pi} arctan\left(\frac{|v|}{u_o}\right)\right] \frac{v}{|v|} \qquad \text{(Eq. 2.19)}$$

The simplicity of this model allows its easy application in numerous processes, however only a single friction coefficient μ is unable to reproduce the complex contact friction conditions. Therefore, equations have been developed to calculate the friction coefficient in dependence to other physical variables such as roughness, hardness, lubrication, etc. Using the *slip-line friction model* developed by Challen and Oxley [CHA79], Ma calculated the total friction force (Eq. 2.20) and the normal force (Eq. 2.21) acting on all the asperities in contact per unit area

[MA10]. Thus he could estimate the variation of the friction coefficient μ at different contact conditions applying coulomb friction law.

$$F_n = \sum_{i=1}^{n} A_{m_i} H_{eff} \quad \text{(Eq. 2.20)}$$

$$F_f = \sum_{i=1}^{n} \mu_i(\beta_e, f_{hk}) A_{m_i} H_{eff} \quad \text{(Eq. 2.21)}$$

In this formulation the extrudate is considered as smooth and perfectly plastic surface while the bearing surface is modelled as rigid rough surface. The equations are based on the measured contact area A_m, effective hardness of the softer material H_{eff}, interfacial friction factor f_{hk}, and effective attack angle of the representative elliptical paraboloid β_e.

2.3.6.2 Shear based friction model

In the *shear friction model* (Eq. 2.22) the friction stress is considered as the shear resistance of the surface in contact and therefore it is usually denoted as shear stress τ. Eq. 2.22 shows how the friction stress is proportional to the shear yield strength τ_y (initial yielding) or shear flow stress k (at any plastic state) and scaled through the friction factor m [WUT87]. The friction factor can vary from m=0 to m=1 when no friction and sticking conditions are considered respectively. This model is very simple and is widely used in extrusion and processes where the high normal pressure generates intimate contact between the workpiece and tool.

$$\tau = m\tau_y = mk \quad \text{(Eq. 2.22)}$$

According to the von Mises yield criterion (Eq. 2.23) and assuming pure shear in one direction ($\sigma_{11} = \sigma_{22} = \sigma_{33} = 0$, $\sigma_{23} = \sigma_{31} = 0$) an expression for the shear flow stress k in function of the effective stress ($\bar{\sigma}$) can be made.

$$k = \frac{\bar{\sigma}}{\sqrt{3}} \quad \text{(Eq. 2.23)}$$

Wanheim and Bay proposed a friction model that combined the coulomb and shear friction models [WAN73, WAN78]. In Practical terms it considers that the friction factor (m= τ/k) is proportional to the normal pressure when $\sigma_n/\bar{\sigma} < 1.5$, but it will be a constant at higher normal

pressure ($\sigma_n/\bar{\sigma} > 3$). The Wanheim-Bay friction model is based on the shear friction model and additionally incorporates a relation between the real A_r and apparent A_a contact area (Eq. 2.24).

$$\tau = m\frac{A_r}{A_a}k \qquad \text{(Eq. 2.24)}$$

As was explained above for the Coulomb friction law, the Wanheim-Bay friction model has also convergence problems during FE simulations. In order to solve these problems the smooth function developed by the Chen and Kobayashi [CHE78, KOB89] was applied to modify the original Wanheim-Bay friction mode. A final version of this equation was presented by *Lin* [LIN03] (Eq. 2.25). Where v and u_o are the relative slipping velocity and the arbitrary positive constant respectively.

$$\tau = -\frac{2}{\pi}m\frac{A_r}{A_a}\frac{\bar{\sigma}}{\sqrt{3}}arctan\left(\frac{|v|}{u_o}\right) \qquad \text{(Eq. 2.25)}$$

Abtahi developed and *empirical friction model* [ABT95, ABT96] based on his friction experiments. He observed sticking and slipping areas at the entry and outlet of the bearing channel respectively. Using the Eq. 2.26 the friction stress at sticking conditions τ_{st} can be related to the friction stress at the extrusion die entry τ_i, the function of the exit speed f_v and the distance from the die entry x_i. Additionally, he proposed also an equation to estimate the friction stress at the slipping zone of the bearing channel (τ_{sl}) (Eq. 2.27). Thus the die angle φ, the deflection angle and length of the bearing channel (φ', l_b), the extrusion speed v_f and some constants (m and m') are taken into account.

$$\tau_{st} = \tau_i + f_v x_i \qquad \text{(Eq. 2.26)}$$

$$\tau_{sl} = m\ln\left(\frac{\varphi - \varphi' + m'}{v_f}\right)(l_b - x) + \tau_e \qquad \text{(Eq. 2.27)}$$

Furthermore *Saha* developed another friction model based on the Abtahi's experimental results [SAH98]. Saha's model calculates separately the friction due to sticking contact and due to slipping contact mechanism (Eq. 2.28). Where A_r is the real contact area and the subscripts 1 and 2 represent the sticking and slipping zones respectively.

$$F_f = m_1 k A_{r_1} + m_2 k A_{r_2} \qquad \text{(Eq. 2.28)}$$

Levanov [LEV97] proposed an exponential equation (Eq. 2.29) to reproduce the friction increase as function of the normal stress σ_n at the beginning of the curve. At high normal stress the friction tends to rich the maximal value or the material shear flow stress k.

$$\tau = k_p k \left[1 - exp\left(-1.25\frac{\sigma_n}{\bar{\sigma}}\right)\right] \quad \text{(Eq. 2.29)}$$

Hora and Gorji [HOR12] created an equation to calculate the friction factor m in function of the normal pressure P and the relative friction speed v (Eq. 2.30). According to the experimental observations, the friction factor increases at higher normal pressure and higher friction speed. Additionally, the temperature T and strain rate $\dot{\varepsilon}$ are indirectly evaluated by the yield function $\bar{\sigma}(\dot{\varepsilon}, T)$ (Eq. 2.31). In the Eq. 27 m_0, q, A, B, n, P_o, v_o and k are constants.

$$m = m_0 + \left\{\mathrm{A} - [\mathrm{A} - \mathrm{B}]e^{\left(-\mathrm{q}\frac{P}{\mathrm{P_o}}^{\mathrm{n}}\right)}\right\}\left(\frac{v}{v_o}\right)^{\mathrm{k}} \quad \text{(Eq. 2.30)}$$

$$\tau(\dot{\varepsilon}, T, P, v) = m(P, v) \cdot \bar{\sigma}(\dot{\varepsilon}, T) \quad \text{(Eq. 2.31)}$$

Furthermore, *Ockewitz and Sun* modified a theoretical model [BEH09] to describe the influence of the normal stress (σ_n) and friction speed (v) on the friction stress [OCK12]. The flow stress $\bar{\sigma}(\dot{\varepsilon}, T)$ and shear flow stress ($k = \bar{\sigma}/\sqrt{3}$) are also incorporated in the equation (Eq. 2.32). The reference sliding velocity (v') and the constants a', b', c', d' and n' were fitted with friction experimental data.

$$\tau = k\left[1 - exp\left(-a'\frac{\sigma_n}{\bar{\sigma}}\right)^{d'}\right]\left[b' c'^{\frac{v}{v'}}\left(\frac{v}{v'}\right)^{n'}\right] \quad \text{(Eq. 2.32)}$$

Karadogan and Hora proposed that during extrusion the workpiece experiments a large deformation in the bearing channel which results in a locally extreme heating. The high heat can melt the metal and contaminate the die land. Under these conditions the friction model should include the adhesion force which should remain even for tensile forces [KAR07]. Thus, this phenomenon was treated as a Bingham material, which is a viscoplastic material that behaves as a rigid body at low stresses but flows as a viscous fluid at high stress [BIN22]. Contrarily to Coulomb approach, in the *Bingham model* the friction will be greater than zero when the normal pressure is zero and even the same when it is negative. The Bingham friction model (Eq. 2.33) is a function of the material, temperature and strain rate. The shear yield stress (τ_y) will define

the minimum friction value, which will be proportional increased by the shear deformation rate ($\dot{\gamma}$). The profile speed (v_f) and the boundary layer thickness (Δx) will be multiplied by the corresponding factor (η).

$$\tau_B = \tau_y + \eta\dot{\gamma}_{Boundary} \approx \tau_y + \eta\frac{v_f}{\Delta x} \qquad \text{(Eq. 2.33)}$$

The Eq. 2.34 combines the classical Coulomb and shear friction models with the Bingham model, introducing a higher ($m\bar{\sigma}$) and a lower limit (τ_B).

$$\tau = \begin{cases} \mu P & if \quad \tau_B \leq \mu P \leq m\bar{\sigma} \\ \tau_B & if \quad \mu P \leq \tau_B \\ m\bar{\sigma} & if \quad \mu P > m\bar{\sigma} \end{cases} \qquad \text{(Eq. 2.34)}$$

Becker and Hora [BEC14] proposed an equation to describe directly the shear friction as function of the normal pressure, temperature and friction speed (Eq. 2.35). The maximal friction value (τ_{max}) is incorporated in the equation assuming that the shear flow stress is reached at a high strain rate ($\dot{\varepsilon} = 1000\ s^{-1}$) (Eq. 2.36). Moreover, the adhesion minimum friction value is 20 % of the maximum friction stress ($\tau_o = 0.2 \cdot \tau_{max}$). The constants q, n, k, l, P_o, v_o, *and* T_o are fitted to reproduce experimental friction data.

$$\tau = \left\{\tau_{max} - [\tau_{max} - \tau_o]e^{\left(-q\frac{P}{P_o}^n\right)}\right\}\left(\frac{v}{v_o}\right)^k\left(\frac{T}{T_o}\right)^l \qquad \text{(Eq. 2.35)}$$

$$\tau_{max}(T) = \frac{\bar{\sigma}(T, \dot{\varepsilon} = 1000, \varepsilon = 0.2)}{\sqrt{3}} \qquad \text{(Eq. 2.36)}$$

The friction factor used during the simulations (Eq. 2.37) is calculated dividing the experimental friction stress (Eq. 2.35) by the maximal friction stress (Eq. 2.36).

$$m(T, v, P) = \frac{\tau(T, v, P)_{exp}}{\frac{\bar{\sigma}(T, \dot{\varepsilon} = 1000)_{exp}}{\sqrt{3}}} \qquad \text{(Eq. 2.37)}$$

2.4 Finite element method in extrusion process

Analytical formulations such as the upper-bound and slip-line field techniques were initially applied for analyzing the extrusion process [HIL50, VAL10]. Two dimensions approaches of single and even symmetric multi-hole extrusion were also achieved [JOH58]. However, these

analytical methods were replaced by numerical methods which allow an easier calculation and more accurate results when complex geometrical models have to be analyzed. The Finite Element Method (FEM) is the numerical method most used for extrusion simulations involving three main steps: pre-processing, solve and post-processing. During the pre-processing step the geometrical model is constructed, material and process characteristics as well as the boundary conditions are applied. Additionally, the continuum is replaced for a subdomain composed by a finite number of elements generated by means of a discretization process known as meshing (Fig. 2.15a) [HIN79, ZIE00]. Thus each element represents a portion of the whole material and is connected to other elements by nodes which contain the spatial position (Fig. 2.15b).

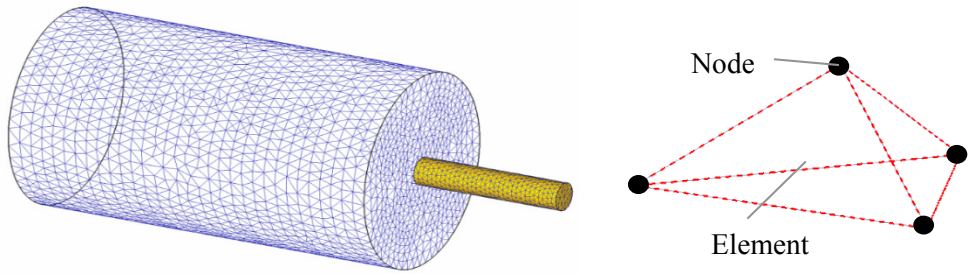

Fig. 2.15. Discretization in FEM. a) free meshed extrusion billet and b) tetrahedron 4-noded.

In the solving step a set of partial differential equations are simplified in a set of algebraic and ordinary differential equations for steady state and transient problems respectively [ROW91]. Posteriorly, the set of equations are recombined in a global system of equations for the final calculation. The evaluation of the simulation results can be done in the post-processing part.

There are different approaches that govern the elements response during plastic deformations. In the Euler approach the mesh and the nodal positions remain static (Euler approach) during the simulations [BIR07], while in the updated Lagrangian approach the mesh is deformed with the material and remeshed in cases of large deformations [DEF12]. Deform 3D was the software selected to carry out all the extrusion simulations analysis, which is based on the updated Lagrangian approach. The whole extrusion simulation is divided into many steps to minimize the calculation error generated at large deformations. Based on the minimum work rate principle (Eq. 2.38), the velocity distribution is calculated such a way that the lowest work rate can be achieved [DEF12].

$$\int_V \bar{\sigma}\,\delta\dot{\bar{\varepsilon}}dV - \int_S F_i\,\delta u_i dS + K\int_V \dot{\varepsilon}_V\,\delta\dot{\varepsilon}_V dV = 0 \qquad \text{(Eq. 2.38)}$$

The first term corresponds to the plastic work due to deformation. The second term takes into account the work due to surface traction F_i or friction force. The last term maintains the volume constant (incompressibility). This is done by integrating the volumetric strain rate $\dot{\varepsilon}_V$ and multiplying by a large constant K (penalty constant). After determining the nodal velocities and integrating with the time step, the new spatial coordinates of each node is updated before beginning the next simulation step.

3 Objective of the Study

The excellent extrudability of the aluminum alloys 6000-serie allows the production of profiles with asymmetric and complex cross sections. To this purpose, the die must be carefully designed to generate a uniform material flow through the single or multiple bearing channels. This is not an easy task, since the local velocity depends not only on the ram speed and extrusion ratio, but also on the yield stress and friction behavior [VAL10]. Besides, the variation of the temperature, strain and strain rate during the large deformations modifies the yield stress. In addition, the internal flow distribution is highly influenced by the friction conditions between the workpiece and the die. As a result, the geometric configuration, extrusion parameters, constitutive behavior and boundary conditions have to be taken into account to achieve a proper material balance through the bearing channel. Due to the complexity of this multi-physic process, analytical approaches only provide a general and imprecise calculation. Hence, in the practice the die is subjected to a manual correction which involves a long and iterative trial and error process. The numerical analysis based on the finites element methods FEM represents a suitable alternative to estimate a more accurate and detailed solution, reducing thus the number of prototypes and the development investment. However, numerical investigations of multi-hole extrusion of aluminum alloy [HOR05, MUE12, DON15] have confirmed the necessity of a better modelling of the friction boundary conditions to predict a more precise product speed.

The objectives of the present work include the development of a friction model, based on experimental investigations between the aluminum alloy EN AW-6060 and the hot working steel AISI H-13 at different conditions of temperature, pressure and speed. Moreover, the flow stress is also considered in the new mathematical approach, since it is closely related to the friction phenomena [WUT87]. To this purpose, the constitutive behavior of the alloy EN AW-6060 is determined by means of hot compression tests. Due to the presence of slip and stick friction in the bearing channel [VAL96, FLI05, SCH07] similar conditions are reproduced during the experimental investigation. Tests are performed with the *tribo-torsion-test* [HOR12] at low pressure to study the slipping friction. Friction investigations at high hydrostatic pressure can be performed by means of the *tribo-torsion-test* and the *high pressure friction test* [OCK12], however evidences of sticking conditions applying these methods have not been published. On the other hand, stick friction could be identified applying specimens with internal contrast material by means of the *compressive compressional method* [WID12]. Nevertheless, the

dissimilar radial velocity of the contact surface generates a variation of the local friction stress, which reduces the accuracy of the measure. In order to be able to reproduce stick friction at high temperatures and high speed a new testing device is developed. Additionally, the new testing method alloys the investigation of the friction boundary layer and its relation with the friction parameters.

This investigation also includes the direct extrusion of the aluminum alloy EN AW-6060 applying multi-hole dies with different bearing channel configurations. Thus, massive rods are extruded simultaneously through different arrangements of relief, parallel and choked bearing channels. According to the literature different inclination angles of the bearing channel generate dissimilar friction mechanisms and therefore a variation of the relative product speed [AKE85]. For that reason, the appearance of the bearing land is also examined after each extrusion trials. Finally, the new friction model is integrated in a FEM-based software to simulate the multi-hole extrusion trials. The numerical results are validated with the experimental data with focus on the relative product speed.

4 Development of a new friction testing device

4.1 General concept

During extrusion of aluminum alloy single and multiple profiles with complex shapes are produced, thus demanding on an accurate design of the die bearing channel. Numerical simulations are used to improve the die design process, but it can only be realized if correct friction boundary conditions are applied. Although, a wide variety of devices and tests allow the friction investigation, similar extrusion conditions are difficult to reproduce. Since the workpiece is pressed against the container and die with a high pressure usually higher than the flow strength, sticking contact conditions are generated between them. Therefore, friction stresses similar to the shear flow strength occurs even in the bearing channel controlling thus the material flow distribution during the process. The new friction device was designed to allow friction investigation especially at high hydrostatic pressure, high temperature and high relative speed. Additionally, the friction surface and the microstructure of the friction boundary layer can also be investigated posterior to the friction test. Fig. 4.1 illustrates the three main steps carried out during the friction investigation. First, an aluminum block is heated and set up inside a steel hollow cylinder until a certain axial force (F_a) is achieved (Fig. 4.1a). Then the hollow cylinder is pulled down with a constant velocity (v) producing a relative movement (F_l) with respect to the aluminum cylinder, while the friction force (F_f) is directly measured and the axial force is kept constant (Fig. 4.1b).

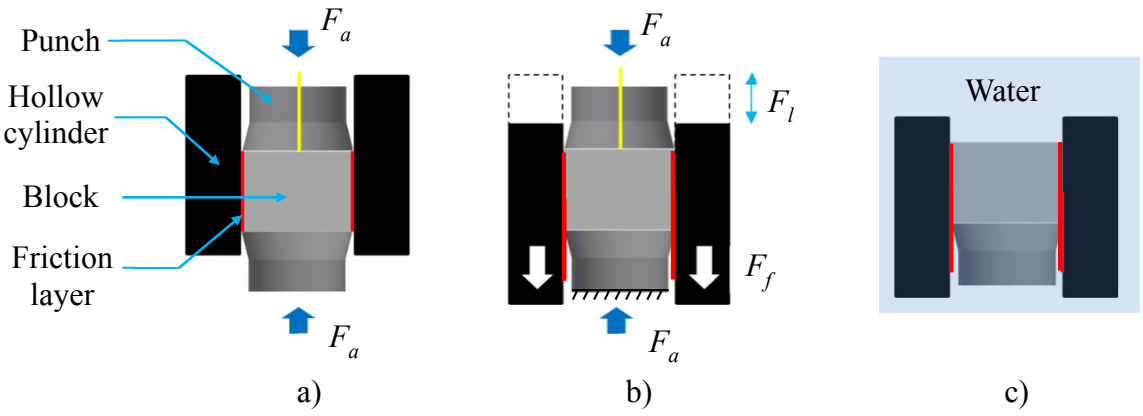

Fig. 4.1. Schematic representation of the axial friction test [SAN15].
a) Set up, b) friction test, c) quenching.

Finally, the friction pair is quenched in water to avoid static alteration of the microstructure by recovery or recrystallization (Fig. 4.1c). Thus the friction stress is calculated dividing the friction force by the contact area.

During the compression step the specimen is completely set up increasing its initial diameter d_o until a maximal value equivalent to the internal diameter of the hollow cylinder (d final diameter). Simultaneously, the specimen's height is reduced from an initial value h_o to a magnitude h which will be the height of the friction area (Fig. 4.2a).

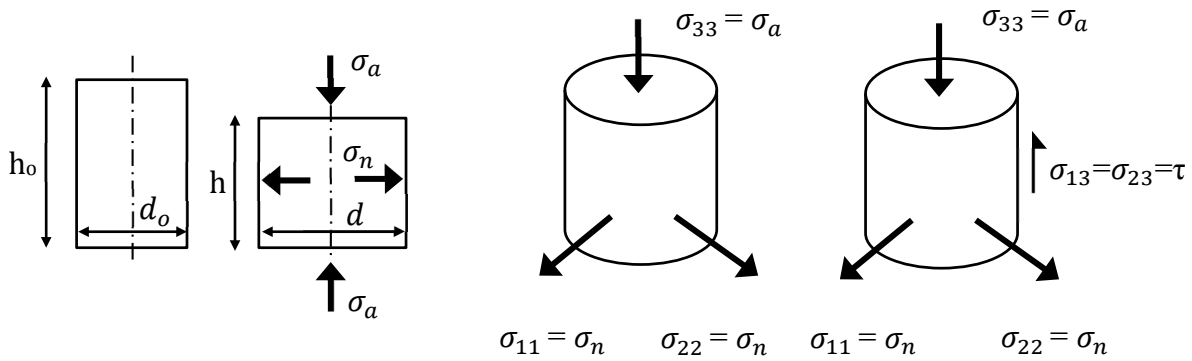

a) b) c)

Fig. 4.2. Schematic stress state of the specimen. a) Initial and compressed state, b) combined state of stress during compression and c) combined state of stress during friction.

Considering mass and volume conservation during compression, the height h and the friction area A_a can be calculated using the Eq. 4.1 and 4.2 respectively.

$$h = \frac{{d_o}^2 h_o}{d^2} \quad \text{(Eq. 4.1)}$$

$$A_a = \pi\, d\, h \quad \text{(Eq. 4.2)}$$

If the specimen is introduces as a Gauchy stress element (Fig. 2.1b), the combined state stress can be analyzed with the von Mises yield criterion (Eq. 2.12). Thus a relation between the axial stress (σ_a), the normal stress (σ_n) and flow strength can be constructed. Eq. 4.3 is derivated from the Eq. 2.12 to calculate the normal stress during the compression step, neglecting the friction with the punches and hollow cylinder (Fig. 4.2b). Posteriorly, the friction stress (τ) is incorporated in the Eq. 4.4 to calculate the normal stress during the friction test (Fig. 4.2c).

$$\sigma_n = P = \sigma_a - \bar{\sigma} \quad \text{(Eq. 4.3)}$$

$$\sigma_n = P = \sigma_a - \sqrt{\bar{\sigma}^2 - 3\tau^2} \qquad \text{(Eq. 4.4)}$$

As indicated in the Eq. 4.3 and Eq. 4.4, a well estimation of the flow stress ($\bar{\sigma}$) is also necessary to calculate the normal stress (σ_n) or the normal pressure P. For this, the called Garofalo or Zener-Hollomon equation (Eq. 2.14) is applied, which requires the definition of the temperature (T_k) and the strain rate ($\dot{\varepsilon}$). Assuming uniform radial deformation, the strain rate during compression step is calculated dividing the strain by the time of compression (Eq. 4.5).

$$\dot{\varepsilon} = \frac{\varepsilon}{t} = \frac{(h_o - h)}{h_o} \cdot \frac{1}{t} \quad ; \ (h < h_o) \qquad \text{(Eq. 4.5)}$$

During the friction test at high hydrostatic pressure, sticking conditions are achieved and under these conditions the shear flow strength is equivalent to the friction stress ($\bar{\sigma}^2 - 3\tau^2 = 0$), therefore the normal stress is equal to the axial stress (Eq. 4.4).

4.2 Description of the new friction device

The new axial friction device consists of multiple components which are listed and illustrated in the Table 4.1 and the Fig. 4.3 respectively. The set-up is installed in a universal testing machine (MTS 810), which governs and records the tension and compression force, displacement as well as the speed (Fig. 4.3a). The friction pair is heated using an electric furnace (#4). Fig. 4.3b shows in details the internal component arrangement.

Table 4.1. Main components of the friction device.

#	Description	#	Description	#	Description
1	Upper support rod	8	Nut	15	Upper stem
2	Upper cross block	9	Coupling nut	16	Punch
3	Block	10	Lower support rod	17	Thermocouple channel 1
4	Furnace	11	Load cell	18	Housing cylinder
5	Lower stem	12	Belleville springs	19	Hollow cylinder
6	Cotter plate	13	Bushing	20	Slotted cylinder
7	Lower cross block	14	Axle load	21	Thermocouple channel 2

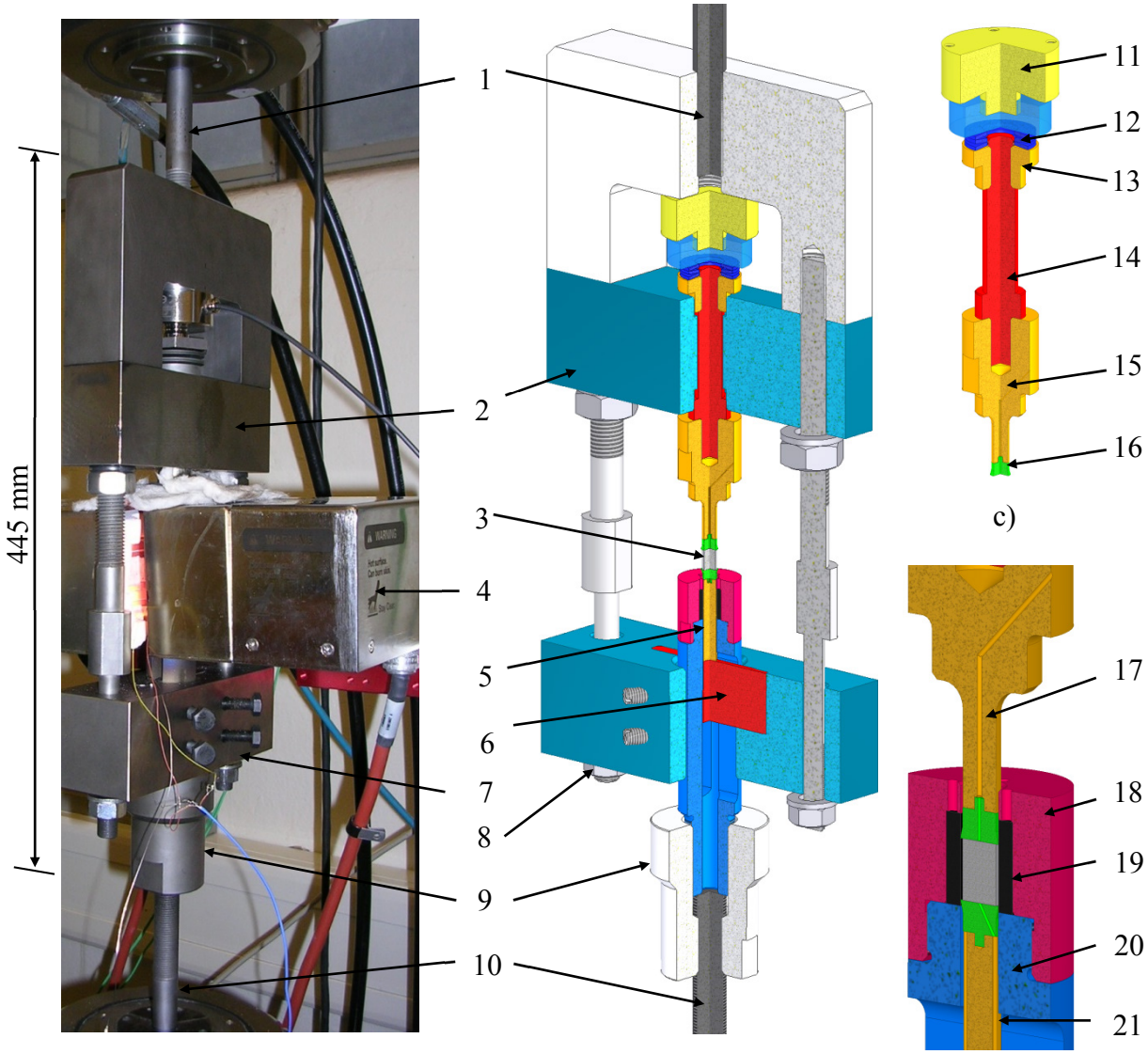

Fig. 4.3. General description of the axial friction test. a) Constructed assembly, b) designed assembly, c) floating upper stem and d) set-up specimen into the hollow cylinder.

The upper support rod (#1) is fixed in the superior clamp and remains stationary, while the lower support rod (#10) is fixed in the inferior clamp which is able to move vertically. When the block is compressed, the floating upper stem (Fig. 4.3c) is moved upwards due to the elastically compression of a set of Belleville springs (#12) accumulating a potential energy. This energy (axial force) can be kept in the system tightening the lateral nuts (#8). After that, the compression force is not controlled by the MTS, but by the compressed springs. Thus, small elastic deformations during the friction test can be compensated to maintain the initial axial

compression force. Under these conditions the lower moving assembly (#9, #10, #18, #19, #20) can be pulled down to generate the friction between the block and the hollow cylinder (#19). Moreover, an additional data acquisition system (DAQ) is used to register the axial compression force measured by the load cell (#11) as well as the temperature of the specimen. The block temperature is measured using thermocouples that are placed directly on the top and bottom side of the block. That is possible because thin thermocouples (0.5 mm diam.) pass through channels (#17, #21) placed in the upper (#14) and lower stem (#5) as well as in the punches (Fig. 4.3d). The specimen, punch and hollow cylinder have a diameter 7.80 mm, 7.99 mm and 8.00 mm respectively. The small tolerance between liner and stem (5 μm) reduces their friction, and also is enough to avoid the material flow in between them during the compression step.

4.3 Experimental procedure

For each friction experiment unused aluminum cylinders (specimen) and steel hollow cylinders were applied. Specimens with diameter 7.8 mm and height 10.5 mm were extracted from billets of aluminum alloy EN AW-6060 (cast and homogenized) by means of wire erosion. Applying the same method, the hollow cylinders were extracted from hardened hot working steel AISI H-13 (HRC 48-52) with height 15 mm and 8 mm and 14 mm of internal and external diameter respectively.

After the friction device is fixed in the MTS, thermocouples are installed and a new steel hollow cylinder is introduced. A new specimen is positioned between both punches and the set-up is positioned for heating (Fig. 4.4). Graphite paper is used between the specimen and the punches to reduce the friction during compression. A small gap of around 0.6-1 mm should be allowed between specimen and punch to avoid axial compression due to thermal expansion during heating. Fig. 4.5 depicts the temperature evolution of the specimen during the heating step, applying 12 min to 15 min to heat from room temperature to 300 °C and 500 °C respectively. When the block temperature is achieved the specimen is compressed with a constant strain rate of 5E-04 1/s approximately. Since the springs set is also compressed during this step, the displacement measured by the MTS corresponds to the specimen's plastic deformation as well as the elastic deformation of the elements situated on the compression path, specially the lower stem due to its small transversal area. For that reason, the displacement during compression is defined by controlling the final compression force F_a and compression time t and not by the displacement.

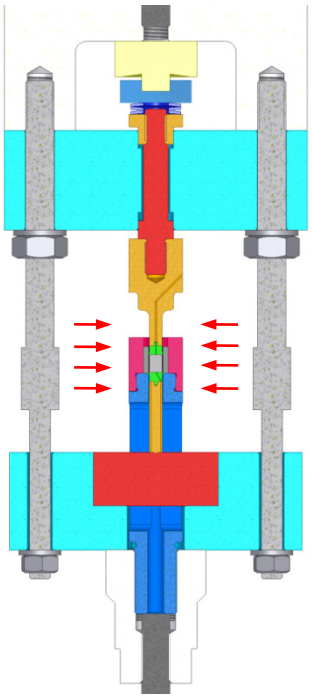

a)

Fig. 4.4. Set-up arrangement for heating.

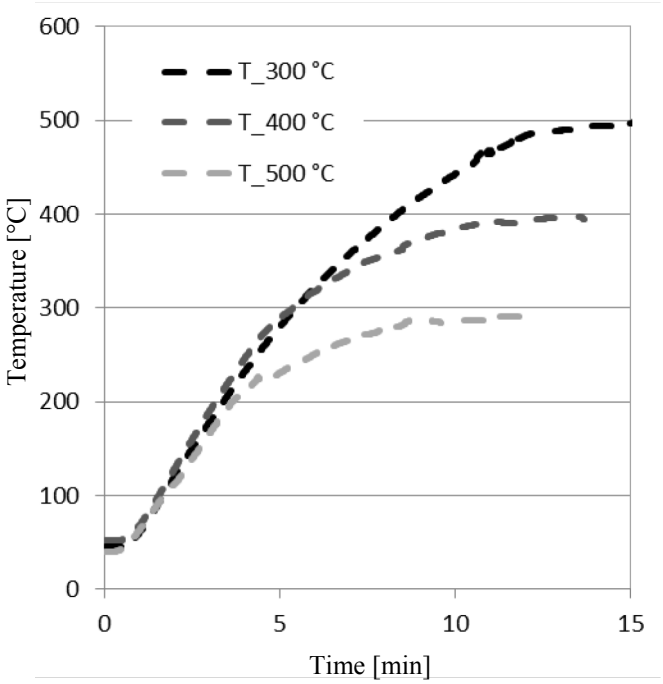

b)

Fig. 4.5. Specimen temperature during heating step.

The final compression force F_a is calculated (Eq. 4.3), so that the axial stress (σ_a) is higher than the flow stress ($\bar{\sigma}$) and the specimen can be plastically compressed in the hollow cylinder. Since, the specimen is compressed approximately a height h (Eq. 4.1) the compression time can be calculated to obtain an average strain rate (Eq. 4.5). Thermocouple placed on the top and bottom of the specimen (Fig. 4.6) allow measuring the temperature during heating, compression and friction test. Additionally to the MTS measure system, a small load cell placed on the compression path records the axial force variation during compression and friction test. Fig. 4.7 depicts the evolution of the temperature and the compression force during the specimen compression at 12825 N, 3395 N and 1700 N at 300 °C, 400 °C and 500 °C respectively. The compression procedure is controlled by the MTS and riches the maximal force in 82 s approximately. After the specimen is compressed and kept during 20 s at the final force (Fig. 4.8, zone a), the lateral nuts are light tightened by hand. Posteriorly the initial compression force applied by the MTS is reduced to zero (Fig. 4.8, zone b). From this moment the compression of the specimen is produced by the stored energy of the Belleville springs, thus the MTS is programed to move in the other direction to carry out the friction test at a constant velocity.

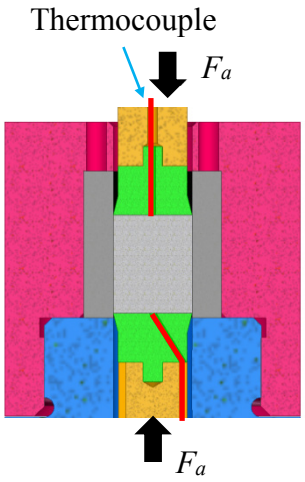

Fig. 4.6. Set-up of the compressed specimen in the hollow cylinder.

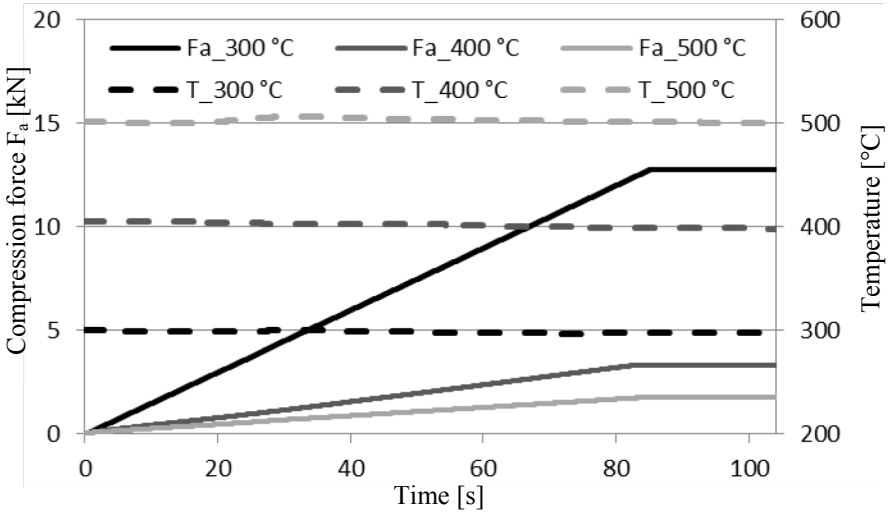

Fig. 4.7. Compression force and temperature during the compression of the specimen.

Posterior to the friction test, the specimen and hollow cylinder are removed from the set-up without extra plastic deformation to be quenched in water (Fig. 4.8, zone c). This step takes 60 s approximately but it can be reduced to 30 s. The MTS can reproduce low speeds with a very high precision, however at speeds higher than 50 mm/s deviations were observed. Fig. 4.9 displays the real velocity reproduced by the MTS traveling 3.4 mm in almost 100 ms. Instead of a nominal speed of 50 mm/s the average of the real speed was about 40-42 mm/s. A perfect constant speed cannot be obtained due to the inertia that must be overcome starting and ending the movement at a very high velocity. Additionally, Fig. 4.9 depicts also a typical friction force measured by the MTS. The first part of the curve (I) represents the elastic elongation, while the second part (II) represents the necessary force to separate the block and the hollow cylinder.

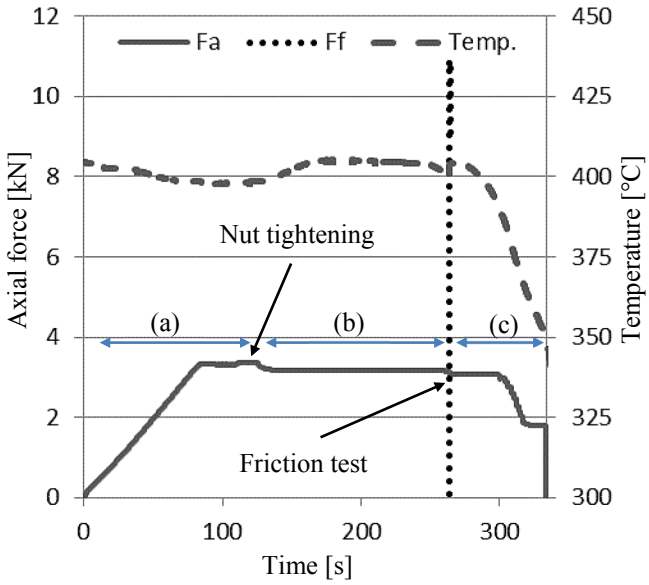

Fig. 4.8. Axial force and temperature evolution during compression and friction test (F_a=3395 N and T=400 °C).

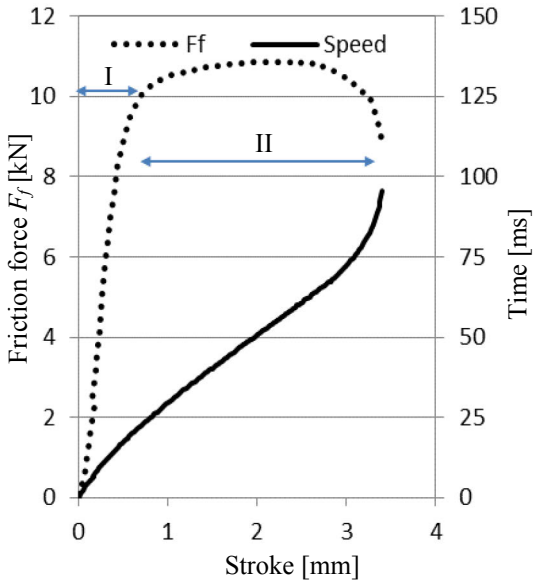

Fig. 4.9. Friction force and real speed (F_a=3395 N, T=400 °C, v=50 mm/s).

5 Experimental procedure and fundamental techniques

Multiple experiments were accomplished in order to investigate the friction phenomenon in extrusion processes (Fig. 5.1). Hot compression tests, friction experiments and extrusion trials were carried out applying aluminum alloy EN AW-6060. The stress-strain curves were obtained by means of hot compression tests to describe the constitutive model. Furthermore, the friction at low pressure was investigated with the tribo-torsion-test to evaluate the relation between friction and normal pressure at different temperature and speed. Moreover, the first experiments applying the new axial friction test (A and B) allowed improving the punch configuration and the procedure to extract the tested specimen. Thus, the best practices were implemented in the friction test C to obtain the friction response at sticking conditions. The results acquired with the tribo-torsion-test and the axial friction test C were used to define a new friction model. Additionally, friction tests (D) were also developed using small specimens of a similar aluminum alloy (AA6063) with internal contrast material (grid pattern). For these experiments the specimens were extracted from extruded profiles, therefore no dendritic structure was observed, as in friction tests A, B and C (cast and normalized). Furthermore, extrusion trials with multi-hole dies were also performed. Microstructural changes were analyzed using light optical microscope (LOM) and electron backscatter diffraction (EBSD). The influence on mechanical properties was investigated by hardness mapping.

Mech. Test	Hot compression test	Hardness and microstructural analysis (LOM)
Friction Experiments	* Tribo-torsion-test	
	Friction test (A)	Microstructural analysis (LOM)
	Friction test (B)	Microstructural analysis (LOM)
	* Friction test (C)	Hardness and microstructural analysis (LOM + EBSD)
	Friction test (D)	Analysis of intern grid pattern
Forming	Direct extrusion	Microstructural and contact analysis in the bearing channel

* Friction test applied to define the new friction model.

Fig. 5.1 Summary of experiments carried out to investigate the friction in extrusion process.

5.1 Sample analysis techniques

5.1.1 Metallographic sample preparation

Usually the samples are embedded in a polymer resin to facilitate the handling during grinding, etching and posterior microstructure analysis techniques or even during hardness measurements. After the sample is embedded, the study surface must be progressive ground depending on the following method of analysis. Using different SiC abrasive grinding papers (320 µm, 800 µm, 1200 µm) and water as lubrication, the samples were prepared to macro etching. In order to prepare the samples to electrolytic polishing, they were additionally ground with SiC abrasive papers (2500 µm, 4000 µm) and lubricated with ethanol, followed by mechanical polishing using polishing discs (MD-Dur and MD-Mol) and diamond suspension (3 µm and 1µm). Using a Struers LectroPol-5 machine the samples were electrolytic polished according to the parameters described in the Table 5.1. The electrolytic polishing was the last surface preparation step carried out before performing the anodization according to Barker and the analysis by EBSD.

Table 5.1. Electrolytic polishing parameters.

Electrolyte	Temperature [°C]	Time [s]	Voltage [V]
10 % Perchloric Acid ($HClO_4$)			
7 % Glycerol ($C_3H_8O_3$)	-35 °C	30-45	40-45
83 % Ethanol (C_2H_5OH)			

5.1.2 Macroetching techniques

Two different macroetching solutions were prepared according to the Poulton and Tucker specifications (Table 5.2) [ASM93].

Table 5.2. Ingredients for sample macroetching.

Macroetching (Poulton)		Macroetching (Tucker)	
12 ml	HCl (37 %)	45 ml	HCl (conc.)
6 ml	HNO_3 (conc.)	15 ml	HNO_3 (conc.)
1 ml	HF (48 %)	15 ml	HF (conc.)
1 ml	H_20 (dest.)	25 ml	H_20 (dest.)

The Poulton etchant was applied on the prepared surfaces of the aluminum alloy EN AW-6060 by swabbing during 10 s approximately. Moreover, the intern grid pattern was revealed by

immersion in Tucker etchant during circa 10 s. In order to obtain a dark color of the grid pattern the sample was heated in hot water immediately before etching.

5.1.3 Anodization with Barker agent

Anodization is an etching process performed in presence of an electrolyte allowing the deposition of an oxide film on the sample surface. During this process the growth of the thin oxide film depends on the grain orientation of the substrate crystal structure. Due to the different orientations, different colors can be observed under polarized light using an optical microscope [PET06, VAN84]. Posterior to the electrolytic polishing, each sample was connected to an anode while the study surface was dipped into the electrolyte (Fluoride acid HBF_4). The separation distance between the sample surface and the cathode was 4 cm and the anodization was carried out at room temperature. More details are showed in the Table 5.3.

Table 5.3. Specifications for anodization with Baker agent.

Electrolyte	Time [s]	Voltage [V]	Current density (A/cm^2)
50 ml (HBF_4) (48 %) **950 ml (H2O) (dest.)**	60	30	0.2

5.2 Aluminum alloy EN AW-6060

Cast and homogenized billets were provided by Otto Fuchs KG with a chemical composition resumed in the Table 5.4. According to the stoichiometric analysis this alloy contains 0.789 wt% of Mg_2Si and 0.19 wt% of Si excess.

Table 5.4. Chemical composition of aluminum alloy EN AW-6060 [wt%].

Al	Si	Fe	Cu	Mn	Mg	Cr	Zn	Ti
Balance	0.48	0.19	0.01	0.03	0.50	0.01	0.009	0.01

Plates were cut from billets with the above chemical characteristics and then turned to achieve plane surfaces (Fig. 5.2a, b). Moreover, small cylinders with diameter 7.8 mm and height 10.5 mm were extracted from those aluminum plates by means of wire erosion (Fig. 5.2c). Some extracted cylinders were transversal and lengthwise cut and prepared for metallographic analysis. Therefore, they were embedded, ground, and mechanical and chemical polished to finally be etched by means of anodization with barker agent.

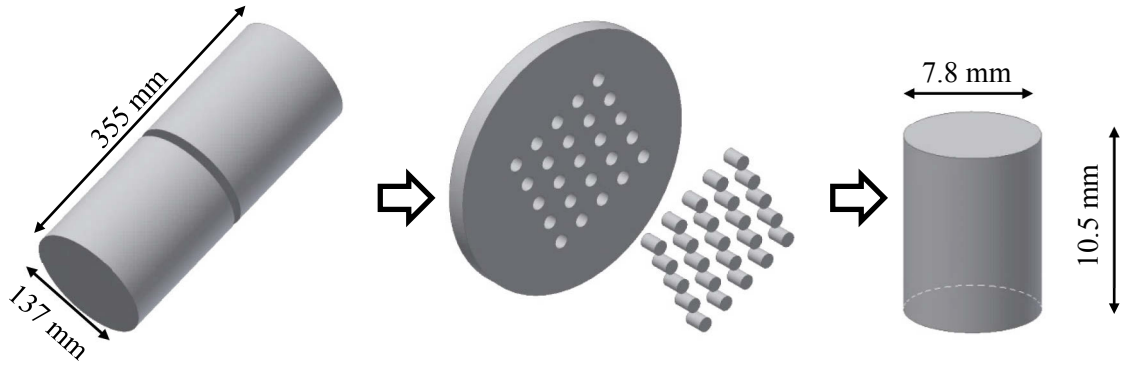

Fig. 5.2. Preparation of small specimens from billets of aluminum alloy EW AW-6060.
a) Cast and homogenized billet, b) sectioned plate, c) cylindrical sample.

Using polarized optical microscope the microstructure was studied and the average grain size determined. Moreover, the same samples were ground again until 4000 µm for hardness investigation applying a normal force of 0.1 HV (9807 mN).

5.3 Hot Compression test of aluminum alloy EN AW-6060

5.3.1 Preparation of hot compression samples

Small cylindrical samples were extracted from cast and homogenized aluminum alloy EN AW-6060 as explained above (Fig. 5.2). Two thermocouples were welded on the cylindrical surface of the sample to monitor and control the temperature during the test (Fig. 5.3). Furthermore, graphite paper was used to reduce the friction between the punches and the aluminum sample and also a nickel based anti-seize and lubricating compound (Thred Grad) to reduce the contact electrical resistance.

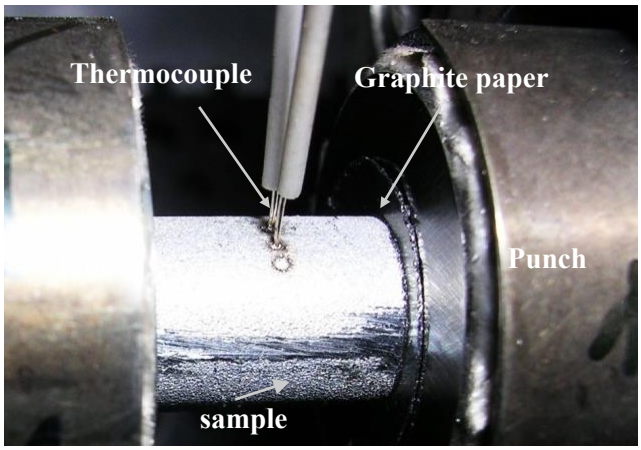

Fig. 5.3. Sample preparation and montage for hot compression test [SAN15].

5.3.2 Hot compression experiments

During the hot compression test a preheated cylinder is compressed a certain stroke by two punches at difference strain rate and temperature conditions in order to study the real stress response. The experiments were carried out in a thermo-mechanical deformation simulator (Gleeble System 3800) at the Extrusion Research and Development Center of TU Berlin. In each experiment the sample was heated by means of electrical resistance (joule effect) controlled and monitored by the Gleeble machine. Thus, samples were heated at a rate of 5 °C/s and then kept constant during 10 s at the test temperature before performing the compression step. Multiple compression tests were carried out at different temperature and strain rate conditions as is summarized in the Table 5.5. The samples were compressed until ca. 5.25 mm to achieve a strain of 0.5 mm/mm approximately, and immediately were quenched in water. The samples were identified with an alphanumeric code for posterior reference, thus for instance M13 represents the test at 400 °C and at 0.1 s^{-1} of strain rate, according to the table 5.5.

Table 5.5. Different temperature and strain rate conditions at the compression test.

Temperature [°C]	**Strain rate [s^{-1}]**				
	0.0005	0.01	0.1	1	10
300 °C	M1	M2	M3	M4	M5
350 °C	M6	M7	M8	M9	M10
400 °C	M11	M12	M13	M14	M15
450 °C	M16	M17	M18	M19	M20
500 °C	M21	M22	M23	M24	M25

5.3.3 Microstructural analysis after hot compression test

Using polarized light microscope the microstructure of the samples' middle planes was investigated. Additionally, all tested samples were ground ones again until 4000 μm in order to perform hardness measurements (0.1 HV) on center of the middle plane. Fig. 5.4a shows the sample position before compression, while the Fig. 5.4b depicts the hardness measure positions on the mid-plane of a tested cylinder.

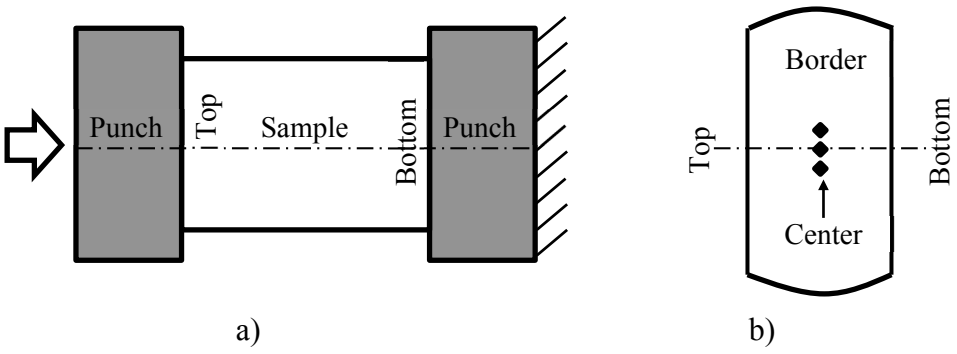

Fig. 5.4. Schematic representation of the hot compression test and compression sample.
a) Initial position, b) hardness measurement positions on the tested sample.

5.4 Friction investigation using the tribo-torsion-test

Friction experiments were carried out between the aluminum alloy EN AW-6060 and the hot working steel AISI H-13 (DIN 1.2344 X40CrMoV5-1) at high temperature, moderate speed and low pressure (10 MPa – 40 MPa). The trials were performed using the tribo-torsion-test at the Institute of Virtual Production IVP of the Swiss Federal Institute of Technology, ETH Zurich. The tribo-torsion-test (Fig. 2.12) was described in details in the section 2.3.5.2. During each friction experiment a small hole-cylinder (Fig. 5.5) was heated by means of an inductive heat coil and the temperature monitored by a thermocouple. The required temperature was achieved in 60 s and then kept constant for another 60 s. Later, the conic area of the sample was pushed against a rotating conic punch (AISI H-13) to generate the friction. The tension-compression machine (Baehr STD 810) records the needed torque (M) to rotate the punch against the aluminum sample, which is used to calculate the friction applying the Eq. 2.17. The sample has an internal (D_i) and external diameter (D_e) of 5 mm and 10 mm respectively, while the contact conic area has an inclination (ϕ) of 45 degree.

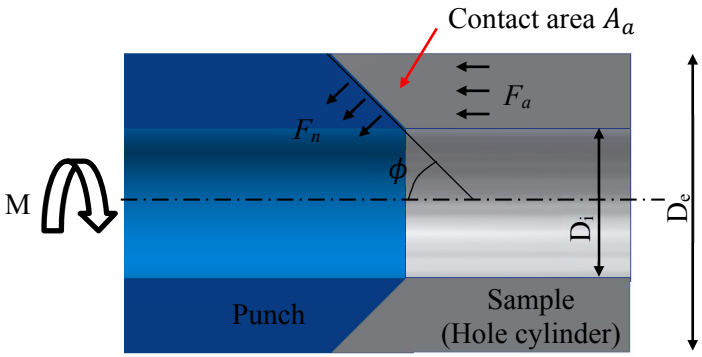

Fig. 5.5. Contact area between punch and sample during the tribo-torsion-test.

According to the geometrical configuration the friction contact area A_a can be calculated using the Eq. 5.1. Additionally, the axial force F_a and the normal force F_n (Fig. 5.5) can be related by the Eq. 5.2.

$$A_a = \frac{\pi}{4}\frac{\left({D_e}^2 - {D_i}^2\right)}{sin(\phi)} \quad \text{(Eq. 5.1)}$$

$$F_n = \frac{F_a}{sin(\phi)} \quad \text{(Eq. 5.2)}$$

Hence, the average normal pressure can be calculated dividing the normal force (Eq. 5.2) by the contact area (Eq. 5.1). From this relation can be derivated the required axial force to generate a particular normal pressure P during the friction tests (Eq. 5.3).

$$F_a = \frac{\pi}{4}P\left({D_e}^2 - {D_i}^2\right) \quad \text{(Eq. 5.3)}$$

Table 5.6 shows the temperature, axial force, normal pressure and speed conditions applied for all friction experiments. The normal pressure was varied from 10 MPa to 40 MPa in order to investigate the friction stress at slipping conditions as is reported in the literature [BEC14, HOR12]. Each friction condition was evaluated two times with the same sample, thus an unused sample was initially tested and afterwards the experiment repeated using the same sample at equal friction conditions.

Table 5.6. Boundary conditions during the tribo-torsion-tests.

Temperature T	**Friction Speed v**	**Axial Force F_a [N] / Pressure P [MPa]**			
[°C]	**[mm/s]**	590 / 10	1170 / 20	1760 / 30	2350 / 40
400	2.5	T1	T2	T3	T4
	10	T5	T6	T7	T8
500	2.5	T9	T10	T11	T12
	10	T13	T14	T15	T16

5.5 Friction investigation using the axial friction test (A)

5.5.1 Preparation of friction samples

Cylindrical samples of aluminum alloy EN AW-6060 were extracted prepared as explained in the section 5.2. Additionally, plates were sawed from a billet of hot working steel AISI H-13

(Fig. 5.6) and then turned until 15 mm of thickness. From these plates hollow cylinders were extracted by means of wire erosion. Special attention was given to the internal diameter (8 mm) in order to achieve a very small tolerance of ± 0.01 mm.

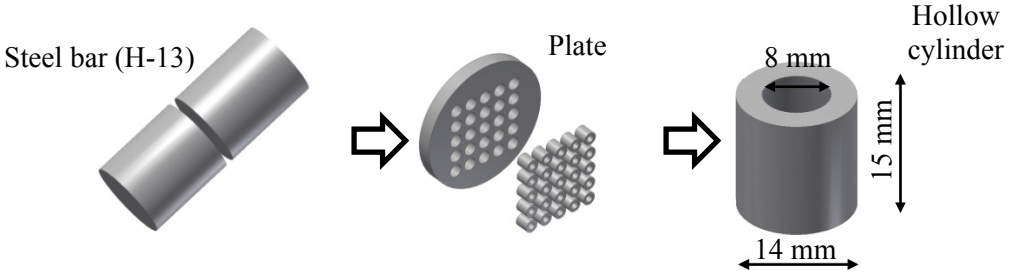

Fig.5.6. Preparation process of the hollow cylinder for the new axial friction test.

5.5.2 Axial friction test A. Mechanical and chemical behavior of the friction

Applying the axial friction test multiple friction tests were carried out at the Extrusion Research and Development Center of the Technical University of Berlin. The axial friction test was described and explained in details in the chapter 4. For every friction experiment an unused aluminum cylinder (Fig. 5.2c) and a steel hollow cylinder (Fig. 5.6) were used to keep constant the superficial and microstructural initial conditions. Furthermore, cylindrical punches and a friction length of 5 mm were applied for all friction experiments. Moreover, three main parameters were analyzed during the friction tests: temperature T, initial normal pressure P_s and the relative friction speed v summarized in the Table 5.7.

In order to reproduce sticking conditions between the aluminum and the hollow cylinder, the applied normal pressure was set higher than the flow stress. The normal pressure at the initial compression state P_s was calculated relating the axial stress and the aluminum flow strength at $\dot{\varepsilon} = 0.0005\ s^{-1}$ according to the Eq. 4.3. Moreover, the flow strength was estimated applying the called Zener-Hollomon empirical hyperbolic-sine relationship (Eq. 2.14 and 2.15), whose parameters (A=2.03E+14 S^{-1}, n=5.29, ΔH=201386 J/mol, α=0.0265) where determined in this work (section 6.2.2). The asterisk (*) represents those experiments where the cylinders were compressed initially at a certain force, but during the friction test the axial force dropped to zero, because Belleville springs were not used. This procedure was done for some conditions to evaluate the adhesive or chemical component of the friction force at different initial compression and temperature. After each friction test, the axial or compression force was reduced to zero and then the sample was separated from the hollow cylinder and quenched in water.

Table 5.7. Boundary conditions during the axial friction tests (A).

				Friction speed [mm/s]						
	F_a [N]	P_s [MPa]	$P_s/\bar{\sigma}$	**0.1**	**1**	**5**	**10**	**20**	**42**	**42***
300 °C	3900	20	0.4	A1	A2	A3	A5	A5	A6	A7
	7700	96	1.7	A8					A9	
	10800	158	2.8	A10	A11	A12	A13	A14	A15	A16
400 °C	1600	16	1.1	A17	A18	A19	A20	A21	A22	A23
	3150	48	3.2	A24					A25	
	4400	73	4.9	A26	A27	A28	A29	A30	A31	A32
500 °C	760	8	1	A33	A34	A35	A36	A37	A38	
	2100	34	4.4	A39	A40	A41	A42	A43	A44	A45

5.5.3 Microstructural analysis after friction experiments A

In order to investigate the friction boundary layer (Fig. 5.7a), microstructural analysis was carried out at the Department of Materials Science and Technology of the Technical University of Berlin. To reduce the number of case studies, 6 samples were analyses. Thus, the samples tested at low and high friction speed (0.1 mm/s and 42 mm/s) as well as at 300 °C, 400 °C and 500 °C were analyzed (A1, A6, A22, A27, A44 and A49 from Table 5.7). The selected samples were lengthwise sectioned and the mid-plane macroetched with Poulton agent (see Table 5.2) to observe the general deformation of the whole specimen. Additionally, the samples were etched using anodization with Barker agent and analyzed using polarized light microscope.

5.6 Friction investigation using the axial friction test (B)

5.6.1 Preparation of friction samples

The sample preparation was carried out identical as described in the section 5.2.

5.6.2 Axial friction test B. Influence of the punch configuration on the friction force

Three different punch configurations were tested to evaluate not only a possible friction force between punch and hollow cylinder, but also the effect of the different normal pressure distribution achieved using the convex punch (Fig. 5.7).

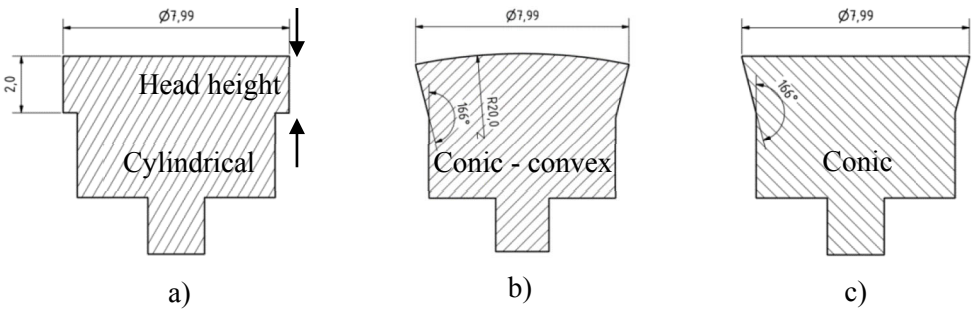

Fig. 5.7. Punch configurations tested with the axial friction test.
a) Cylindrical punch, b) conic-convex and c) conic punch.

Cylindrical, conic and conic with convex head punches were used to carry out friction experiments at 300 °C and a friction speed of 42 mm/s. Table 5.8 shows the boundary conditions for the 6 friction experiments (B1-B6). Two different procedures after finishing the friction test were applied to observed it influence on the specimen plastic deformation. Thus, the samples B1, B3 and B5 were separated from the hollow cylinder before quenching. On the other hand, the samples B2×, B4 × and B6 × were quenched together with the hollow cylinder, and later separated by means of a light axial force.

Table 5.8. Boundary conditions during the axial friction tests (B) at 42 mm/s and 300 °C.

		Friction Speed [mm/s]
	F_a **[N]**	**42**
Cylindrical	3900	B1 B2 ×
Conic-convex	3900	B3 B4 ×
Conic	3900	B5 B6 ×

5.6.3 Microstructural analysis after friction experiments B

The samples (B1-B6) were metallographic prepared as in section 5.5.3 and then etched by means of anodization using Barker agent. By means of polarized light microscope the microstructure of the friction boundary layer was analyzed.

5.7 Friction investigation using axial friction test (C)

5.7.1 Preparation of friction samples

The sample preparation was carried out identical to chapter 5.2.

5.7.2 Axial friction test C. Stick friction and effect on the microstructure

Additional friction experiments were performed to investigate the relationship between the friction stress and the microstructure evolution of the friction boundary layer at sticking conditions. Punches with conic configuration (Fig. 5.7) were used to improve the measurement of the friction force during the whole test. Moreover, Belleville springs were applied in all experiments to keep constant the axial compression force (pressure compensation). The sample and hollow cylinder were separated after quenching to minimize the extra plastic deformation during the extraction process. For a better estimation of the initial normal pressure during the compression step (Eq. 4.3), experimental values of flow strength at $\dot{\varepsilon} = 0.0005\ s^{-1}$ were applied (Table 5.5). The boundary conditions evaluated during the friction experiments are summarized in the Table 5.9.

Table 5.9. Boundary conditions during the axial friction tests (C).

				Friction speed [mm/s]			
	F_a **[N]**	P_s **[MPa]**	$P_s/\bar{\sigma}$	**0.1**	**1**	**10**	**42**
300 °C	12825	198	3.5	C1	C2	C3	C4
400 °C	3395	53	3.5	C57	C6	C7	C8
450 °C	2470	38	3.5	C9	C10	C11	C12
500 °C	1700	26	3.5	C13	C14	C15	C16

5.7.3 Microstructural and hardness analysis after friction experiments C

The samples tested high hydrostatic pressure ($P_s/\bar{\sigma}$= 3.5) and at a friction speed of 0.1 mm/s and 50 mm/s (C7-C10, C17-C20, C21-C24 and C31-C34) were subjected to microstructural and hardness analysis. Using LOM the microstructure of the samples' middle planes was investigated with special attention to the friction boundary layer (Fig. 5.8a). Additionally, the samples C17, C20, C31 and C34 were analyzed by means of electron backscatter diffraction EBSD in order to determine the grain size in the friction boundary layer (Fig. 5.8b). Moreover, the samples C7-C10, C17-C20, C21-C24 and C31-C34 were ground until 4000 µm to perform

hardness measurements (0.1 HV) at 100 µm, 300 µm, 500 µm, 700 µm, 1200 µm and 4000 µm from the border to the center (Fig. 5.8c).

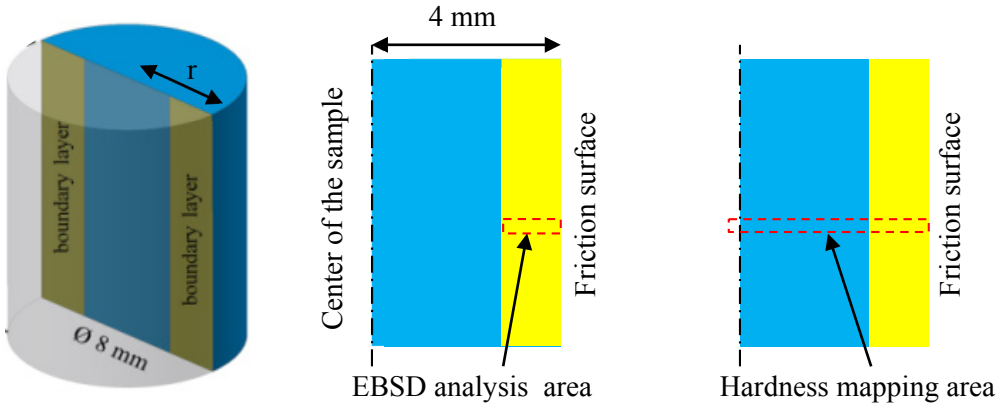

Fig. 5.8. Sample analysis after friction experiment C. a) Sample's middle surface, b) EBSD analysis area, c) hardness mapping area.

5.8 Friction evaluation using the Axial Friction test (D) and a grid pattern technique

5.8.1 Preparation of friction samples

Extruded profiles with lengthwise stripe grid pattern were provided by the Department of Engineering Design and Material NTNU Trondheim. Posteriorly, small cylinders with diameter 7.8 mm and height 8.1 mm were extracted from a selected extruded profile by means of wire-cut erosion. For each extrusion trial a billet of aluminum alloy AA6063 (similar mechanical properties to EN AW-6060) was filled with contrast material. Thus, pins of Al1.8Cu were inserted into radially drilled holes arranged in the mid-plane of the billet. Using this method, profiles with lengthwise grid pattern were produced. Fig. 5.9a shows the chosen profile after extracting the cylinders and macro etching with Tucker's agent. Additionally, an extracted cylinder was also etched to observe the contrast material on its lateral surface (Fig. 5.9b). Later, this sample was radially ground using a SiC abrasive grinding paper 800 µm, such a way that all the lateral marks were met by the new ground surface. The new surface was later etched with Tucker agent to reveal the original grid pattern (Fig. 5.9c). More details about this grid pattern technique are available in the literature [VAL88, VAL08].

a) b) c)

Fig. 5.9. Preparation of samples with internal grid pattern. a) Sample extraction from the extruded profile, b) etched friction sample, c) original grid pattern.

5.8.2 Axial friction test D. Material flow of the intern grid pattern

Friction tests were performed with the new axial friction tests using aluminum samples with radial grid pattern (Fig. 5.9c) in order to investigate the real material flow in the friction boundary layer. The experiments were done at 400 °C applying an initial compression force of 1600 N and using conic punches. Different friction speeds and lengths were tested (Table 5.9). After each friction test, the assembly sample-hollow cylinder was quenched in water and then carefully separated at room temperature.

Table 5.9. Boundary conditions during the axial friction tests (D).

		Friction speed [mm/s]		
	[mm]	**0.1**	**1**	**10**
400 °C	2	D1		
	3.5	D2		
	5	D3	D4	D5

5.8.3 Grid pattern analysis after friction experiments

Posteriorly, the sample were sectioned to reveal the internal grid pattern. Since the marks are not visible after friction test (Fig. 5.10a), the specimens were macroetched with Tucker agent (Fig. 5.10b). The external contrast marks were used as a reference to find the pattern plane. Thus, the cylinder was grinded carefully until the new surface intercepted all the contrast marks. The sample was not embedded, so the lateral surface was visible all the time. In order to reveal the final grid pattern, the specimens were etched again with Tucked agent (Table 5.2). Though the small size of the stripes cross section, it was possible to create planes containing most of the deformed contrast lines.

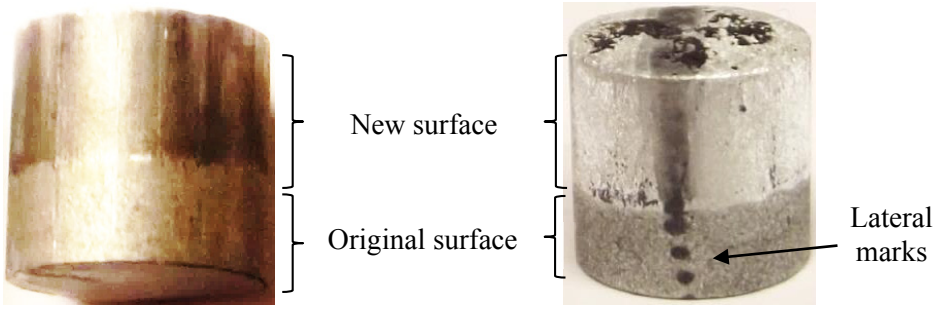

Fig. 5.10. Typical surface appearance of the samples with grid pattern after friction test. a) Without etching, b) after etching with Tucker agent.

5.9 Multi-hole extrusion with long and different inclinations of the bearing channels

5.9.1 Definition of extrusion parameters

Extrusion trials were performed at the Extrusion Research and Development Center (ERDC) of the Technical University of Berlin, applying an 8 MN SMS extrusion press. This extrusion facility allows determining not only the total extrusion force, but also the container and die force during the entire process. Fig. 5.11a depicts a schematic drawing of the extrusion press including the load cell distribution responsible for the force recording. The die force represents the magnitude needed to deform the billet as well as the friction generated in the die. Furthermore, the container force decreases continuously due to the reduction of the billet length producing the same decrease on the total force (Fig. 5.11b). Cast and homogenized billet of aluminum alloy EN AW-6060 with diameter 137 mm and length 355 mm were used. Each billet was heated at 460 °C using an inductive furnace and posteriorly and posteriorly extruded with a ram speed of 4 mm/s. Moreover the container (diameter 140 mm) and the die were preheated at 470 °C approximately. A discard of approximately 20 mm was set. Moreover the multi-hole die was preheated at 470 °C and the temperature was monitored with thermocouples placed in the bearing channel. Additionally, the length of the extruded profile was measured to calculate the relative product velocity.

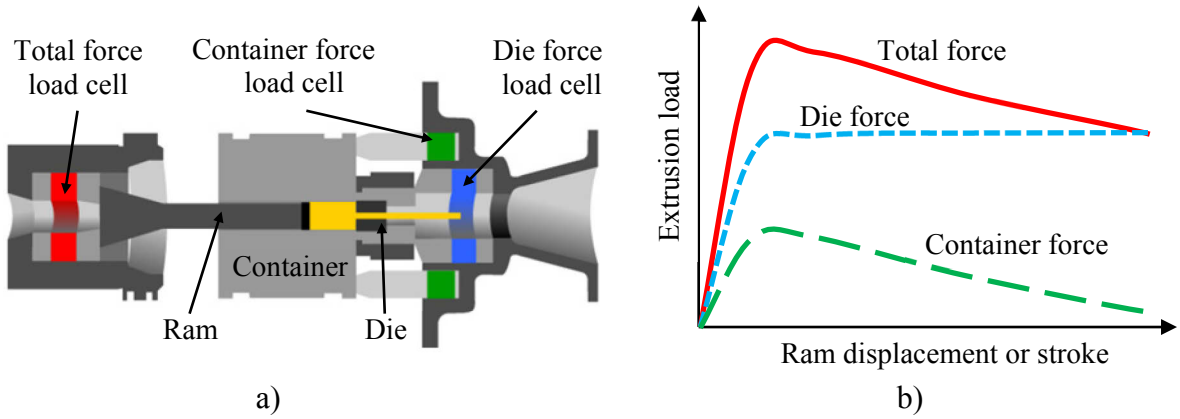

Fig. 5.11. Extrusion press force measurement at the ERDC TU Berlin.

a) Location of the load cells [MUE96], b) Typical force curves during direct extrusion.

5.9.2 Geometrical configuration of multi-hole dies

A multi-hole die with exchangeable inserts were applied for all experiments (Fig. 5.12a,b).

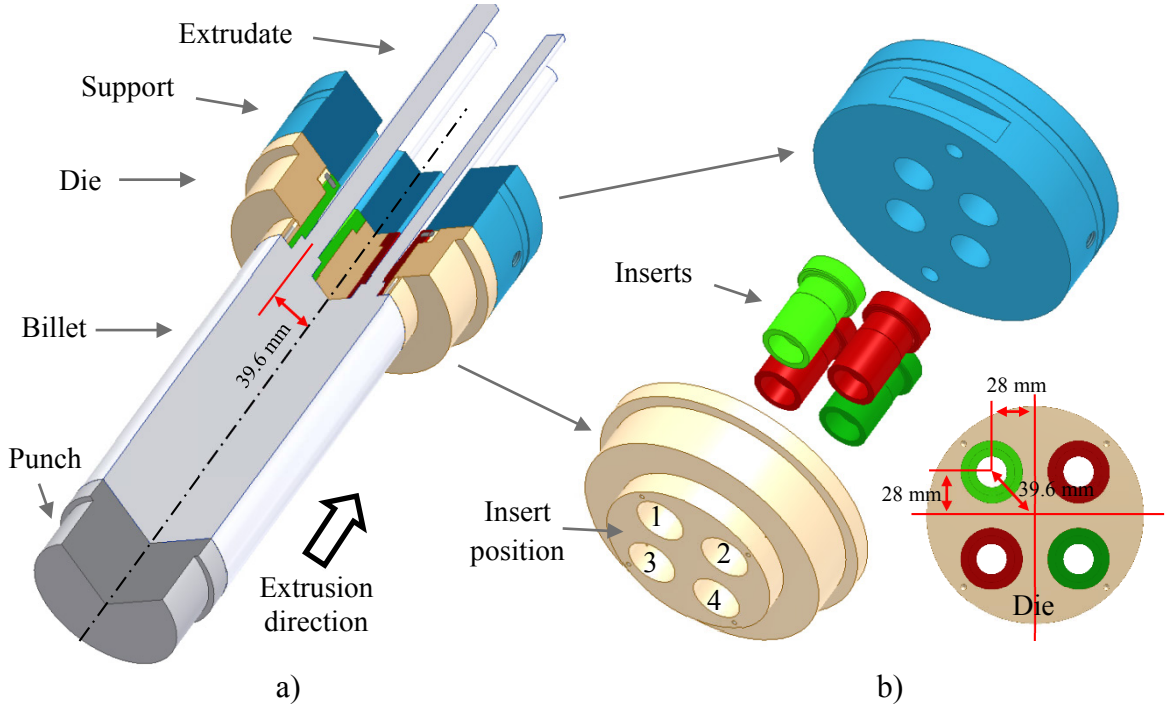

Fig. 5.12. Description of the multi-hole die. a) Arrangement of the multi-hole die during direct extrusion, b) assembly of the multi-hole die.

Unused inserts with different bearing channel inclinations were combined as showed in Fig. 13.a,b. In order to correct a possible influence of top-bottom position in the measured profile speeds, the inserts were pairwise positioned in the extrusion die and diagonally placed across from each other (Fig. 5.12b). Each insert was placed 28 mm vertically and horizontally from the center of the die or 39.6 mm radially from the die center (Fig. 5.12b).

The extrusion die and all inserts were fabricated by WEFA Inotec GmbH applying the hot working steel AISI H-13 which was hardened at 48-50 HRC. The length and the inlet diameter of all bearing channels were 20 mm (Fig. 5.13a). Additionally, four different geometries of the bearing channel were used: parallel (0°), +0.5° choked, +1° choked and -0.5° relief and combined to perform four experiments (Fig. 5.13b).

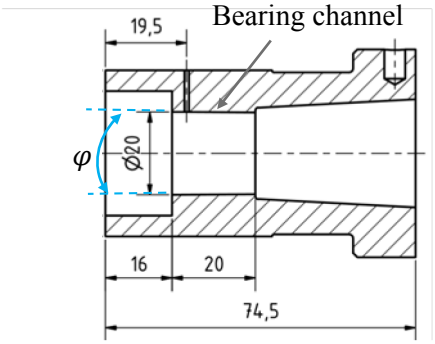

a)

Position		Bearing angle (φ)			
		Exp. 1	Exp. 2	Exp. 3	Exp. 4
1	Top left	0°	0°	0°	+0.5°
2	Top right	+0.5°	+1°	-0.5°	+1°
3	Bottom left	+0.5°	+1°	-0.5°	+1°
4	Bottom right	0°	0°	0°	+0.5°
Note: (+) choked and (-) relief					

b)

Fig. 5.13. Description of the extrusion inserts. a) Insert dimensions, b) inclination angle of the bearing channel and insert position for different experiments (Exp.).

5.9.3 Temperature in the bearing channel during the extrusion experiments

In each experiment thermocouples were placed in the bearing channels to measure and record the profile temperature during the whole extrusion process. Fig. 5.14a shows the thermocouple position (T1, T2, T3, T4) in the die and inserts. Small holes of diameter 1.1 mm were carried out in the extrusion die and each insert by means of wire erosion to allow the introduction of the thermocouples. Thus, thermocouples of diameter 1 mm were placed directly on the bearing land and fixed by means of screws (Fig. 5.14b).

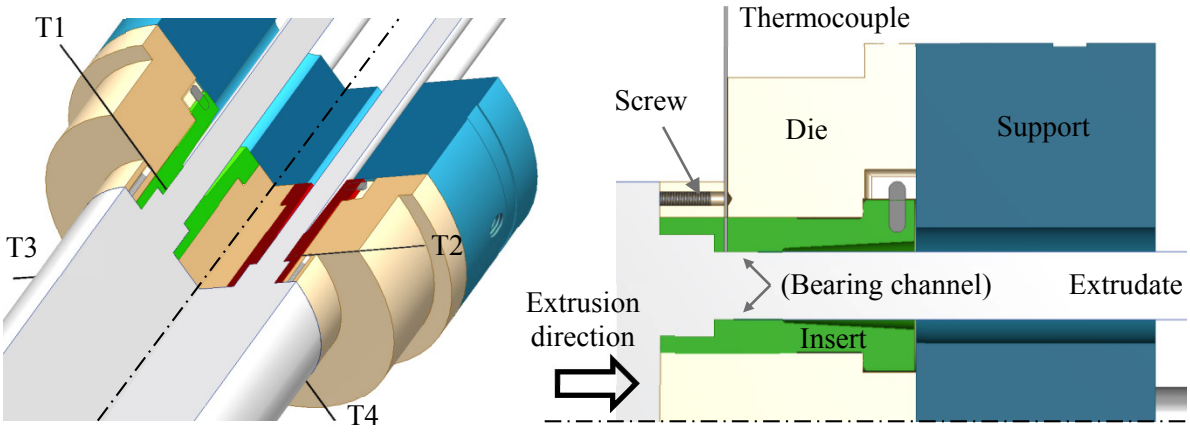

Fig. 5.14. Thermocouple in multi-hole die. a) Thermocouple arrangement in the multi-hole die, b) thermocouple position in the extrusion insert.

5.9.4 Analysis of the contact mechanisms and microstructure at the bearing channels

After each extrusion experiment the profiles were cut and the die assembly cooled in air at room temperature. The billet discard was not sheared as is common in industrial practice, but it was machined to avoid any relative movement between the workpiece and insert (Fig. 5.15a).

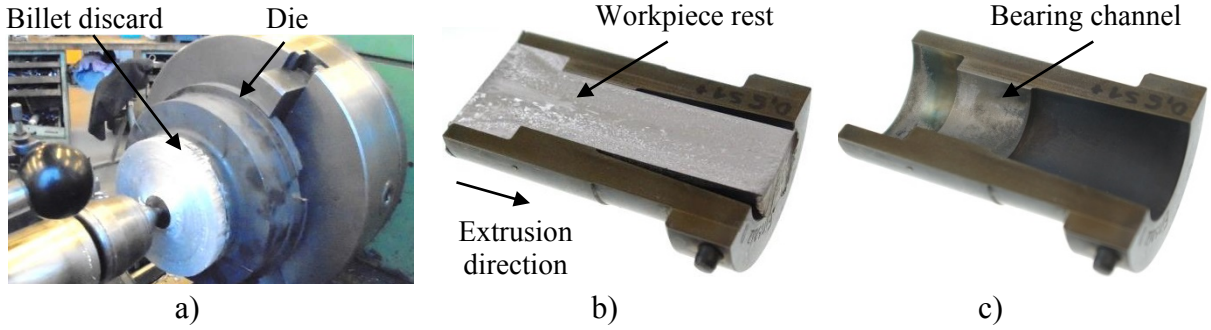

Fig. 5.15. Microstructural and contact analysis in bearing channel.
a) Machining of billet discard, b, c) cut insert with and without workpiece rest.

Posteriorly, the inserts were carefully extracted from the extrusion die pushing them toward the extrusion direction with a manual press. Furthermore, each insert (filled with aluminum) was identified and lengthwise cut by means of wire erosion. On one hand, the mid-plane of one half was ground and macroetched according to Poulton to investigate the microstructure inside the insert (Fig. 5.15b). One the other hand, the aluminum remained in the other half was carefully extracted to evaluate the contact area between both materials (Fig. 5.15c).

6 Experimental results

6.1 Microstructure of cast and homogenized aluminum alloy EN AW-6060

In order to describe the initial microstructure of the cast and homogenized aluminum alloy EN AW-6060, small cylindrical undeformed specimens (Fig. 5.2c) were analyzed by means of LOM. Fig. 6.1a shows a microstructure region of the cross section at the middle of a specimen. Uniform grain size of approximately 140 µm was observed across the sample's section, as well as a dendritic grain structure typical of the cast state (Fig. 6.1b).

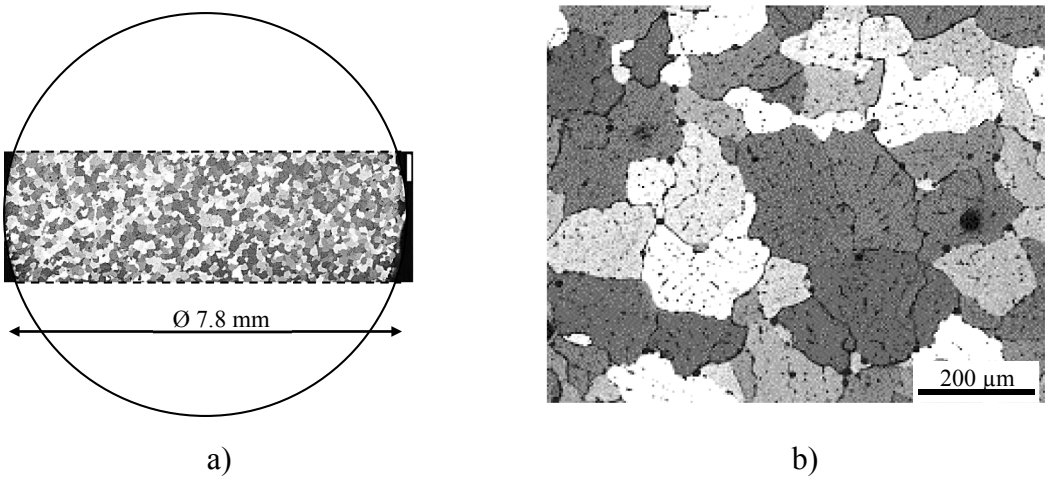

Fig. 6.1. Initial microstructure of the aluminum alloy EN AW 6060 (cast and homogenized). a) Crosswise section of the friction sample, b) dendritic structure of the initial state.

6.2 Hot compression test of aluminum alloy EN AW-6060

6.2.1 Temperature and strain rate influence on the flow stress of EN AW-6060

Fig. 6.2 depicts the stress response of the aluminum alloy EN AW-6060 at different temperatures and strain rates until a maximal strain of 0.5 mm/mm. As it has been reported in the literature, the curves show how the true stress behaves during the deformation at different temperatures and strain rates [ZEN44]. In the initial part of the deformation the stress increases rapidly until a certain critical strain, approximately 0.05 and 0.02 at 300 °C and 500 °C respectively. Posteriorly, with additional deformation the stress can increase or remain constant depending on the temperature and strain rate. Thus, at 300 °C (Fig. 6.2a) the true stress still increases with the strain, but decreases at very low strain rate (0.0005 1/s). At temperatures between 350 °C and 400 °C (Fig. 6.2b-c) the true stress experiments a slight variation at low strain rate, but

continues increasing at a deformation rate of 10 1/s. Moreover, at higher temperatures (450 °C – 500 °C) the true stress remains almost constant in the strain range from 0.02 to 0.5 mm/mm, and is only influenced by the strain rate (Fig. 6.2d,e).

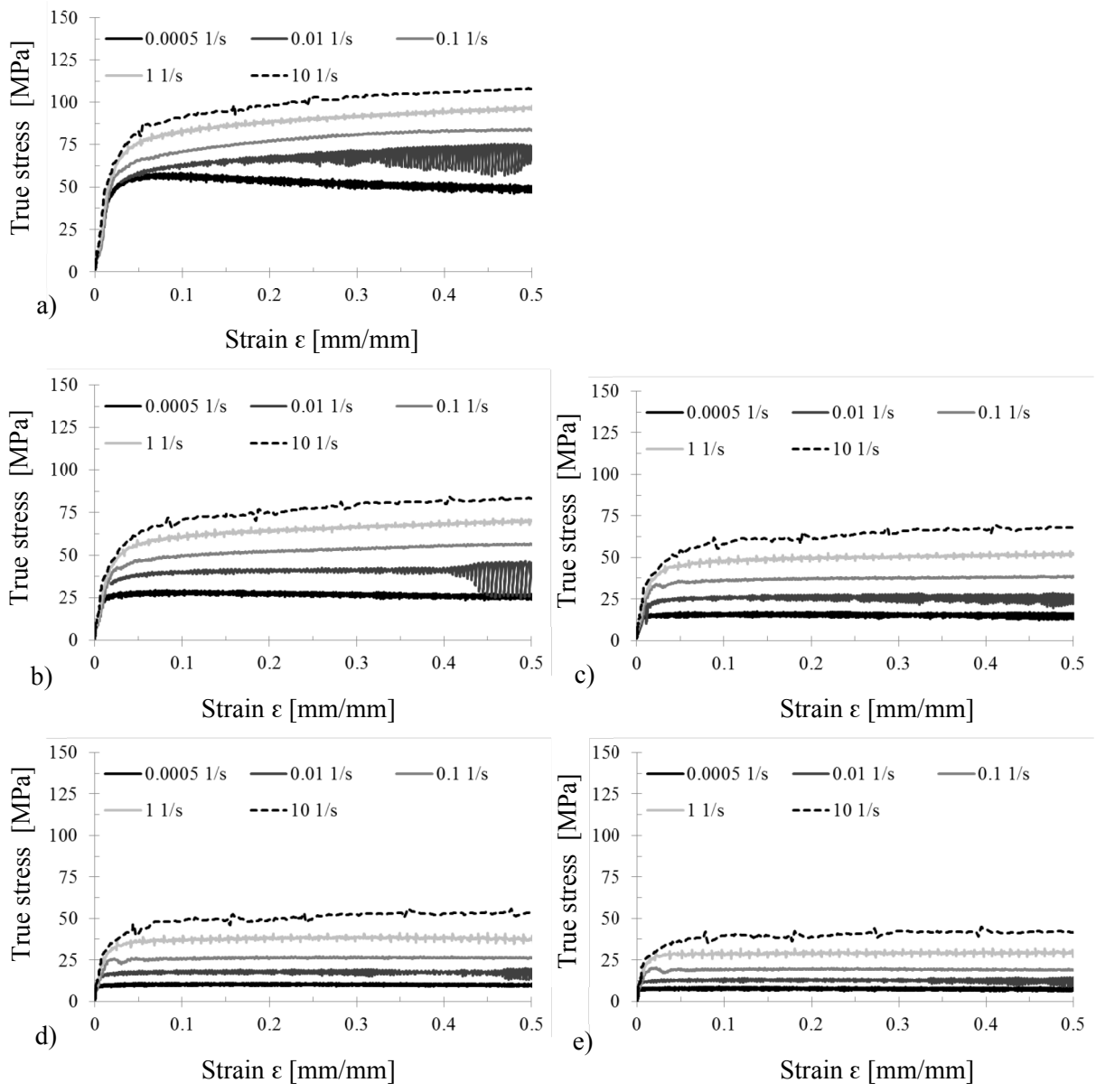

Fig. 6.2. True stress of the aluminium alloy EN AW-6060 meassured during hot compression test (ε_{max}=0.5). a) 300 °C, b) 350 °C, c) 400 °C, d) 450 °C and e) 500 °C.

6.2.2 Constitutive model of EN AW-6060

The temperature and strain rate dependence of the flow stress is expressed with the Zener-Hollomon equation (Eq. 2.14) [ZEN44]. Additionally, according to Sheppard and Wright (Eq. 2.15) the effective flow stress can be modelled estimating the material constants α, *n* and

A and the deformation activation energy ΔH. Steady state deformation conditions were considered at a strain of 0.5 mm/mm, taking thus the values of stress from the curves stress-strain (Fig. 6.2). The flow stress variation as a function of strain rate at different temperatures is plotted in the Fig. 6.3. The slope of the linear curves $\bar{\sigma}$ vs. $\ln(\dot{\varepsilon})$ (Fig.6.3) varies from 0.1660 to 0.2728, with an average of β'=0.2025. Moreover, the average of the slopes $\ln(\bar{\sigma})$ vs. $\ln(\dot{\varepsilon})$ (Fig. 6.3b) is ψ'=7.6350. Posteriorly, the stress multiplier $\alpha = \beta/\psi'$=0.0265 MPa^{-1} can be obtained [MCQ02].

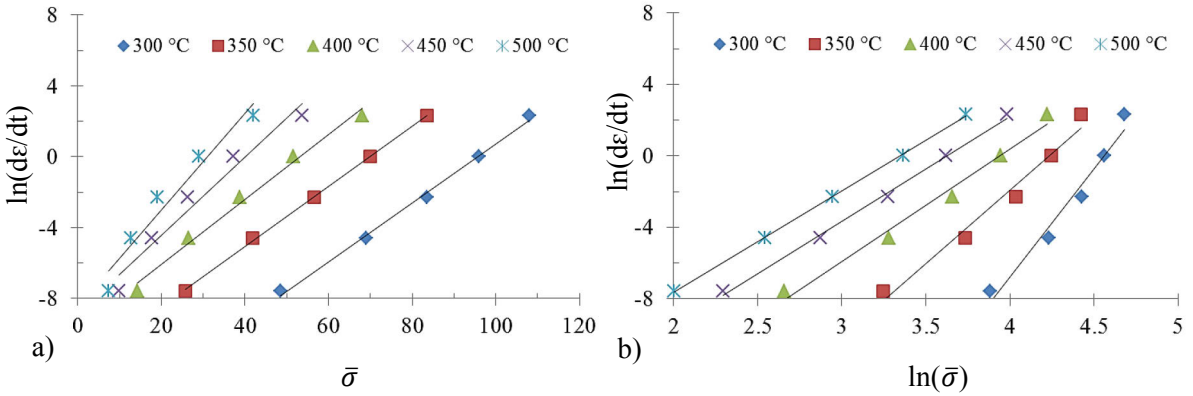

Fig. 6.3. Variation of the flow stress $\bar{\sigma}$ (a) and $\ln(\bar{\sigma})$ (b) as a function of strain rate.

Fig. 6.4a shows the flow stress variation adjusted by the multiplier α at constant temperature. This graphic makes clear the increase of the flow stress at higher rate of deformation. The slope of the linear curves $\ln(\sinh(\alpha\bar{\sigma}))$ vs. $\ln(\dot{\varepsilon})$ varies from 5.13 to 5.97, with an average of n=5.2945. Examining the flow stress at constant strain rate it is clear that it increases at lower temperatures as depicted in Fig. 6.4b. The average slope of $1000/T_k$ vs. $\ln(\sinh(\alpha\bar{\sigma}))$ was s=4.574. The calculated activation energy was $\Delta H = R \cdot n \cdot s = 201.386$ kJ/mol.

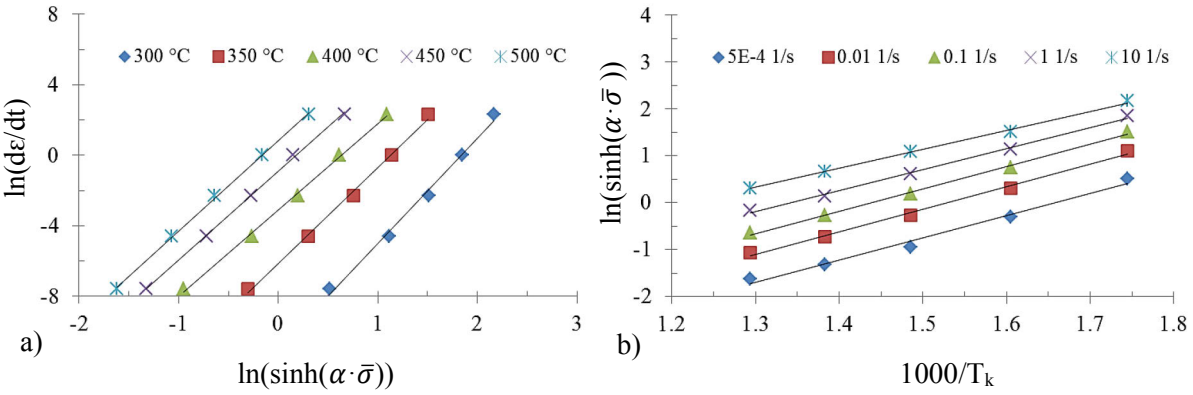

Fig. 6.4. Variation of flow stress at constant (a) temperature and (b) strain rate.

As was proposed by Zener and Hollomon [ZEN44], the isothermal stress-strain relation depends upon strain rate and temperature only through a single parameter Z. The results obtained

applying the hyperbolic-sine relationship and depicted in Fig. 6.5, corroborate this statement (ε=0.5).

The constant A of the Eq. 2.15 can be calculated A= exp(32.9) = 2.03E+14 1/s.

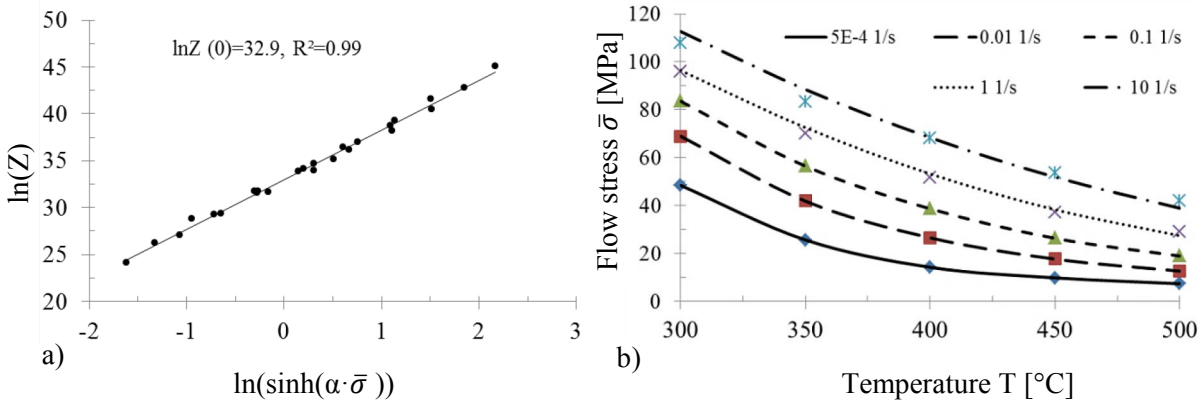

Fig. 6.5. Material behavior of EN AW-6060.

a) Linear relation ln(sinh(α·$\bar{\sigma}$)) vs ln(Z) and b) true flow stress at ε=0.5.

Fig. 6.6 illustrates the experimental (singular values) and calculated (lines) flow stress of the aluminum alloy EN AW-6060 at different temperatures and strain rates. Using the calculated material parameters (Table 6.1) similar experimental and modelled stress values can be achieved.

Table 6.1. Constitutive material constants of the aluminum alloy EN AW-6060 (ε=0.5).

Alloy	**Temperature [°C]**	**ΔH[kJ/mol]**	***n***	***A*[1/s]**	**α[MPa^{-1}]**
EN AW-6060	300 - 500	201.386	5.2945	2.03E+14	0.0265

6.2.3 Microstructure and hardness analysis after hot compression test

Posterior to the compression test the samples were immediately quenched in water in order to avoid additional change of the microstructure. During the uniaxial test the original grains were axially compressed and radially elongated. Fig. 6.6 shows LOM micrographs taken in the center of the axial mid-plane of samples tested at high temperature (300 °C, 400 °C, 500 °C) and at strain rates of 0.1 1/s and 10 1/s. In general, similar microstructure was developed in all samples, however little differences could be noticed at different temperatures. Grain dendritic structure as well as the original grain boundaries was clear observed at 300 °C. On the other hand, at 500 °C no dendritic grain structure was observed and the original grain boundaries were difficult to distinguish. Additionally, at 500 °C serrated grain boundaries and subgrains were identified.

As it was expected for high stacking fault energy alloys, no dynamic recrystallization took place during the compression test due to the low strain [MON02, PET03].

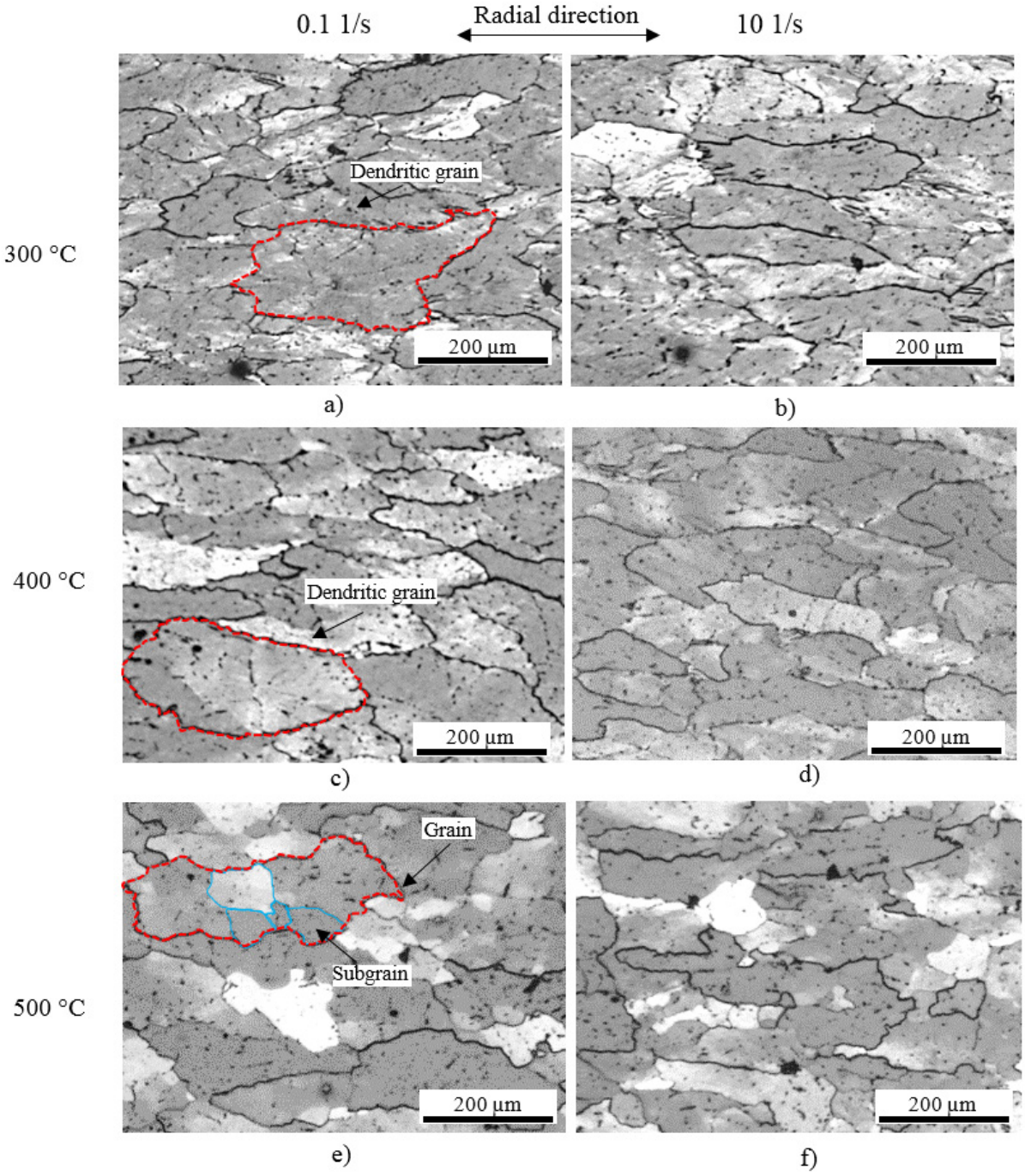

Fig. 6.6. LOM micrographs of aluminum alloy EN AW-6060 after hot compression test at 300 °C a) 0.1 1/s, b) 10 1/s, 400 °C c) 0.1 1/s, d) 10 1/s, and 500 °C e) 0.1 1/s, f) 10 1/s.

Micro hardness measurements were carried out in the mid-plane of all samples subjected to hot compression test, as described in section 5.3.3. Influence of the sample temperature and

compression strain rate on the hardness are resumed in Fig. 6.7. In general, higher hardness values were detected in samples compressed at higher temperatures and strain rates, moreover a nonlinear influence of theses parameters were also observed. For instance, increasing the strain rate from 0.0005 1/s to 10 1/s the hardness increased 34 % at 350 °C (from 37 HV to 49.5 HV) but only 3 % at 500 °C (from 55 HV to 57 HV). Additionally, it was observed that the temperature significant influences on the hardness at lower strain rate. Thus, the hardness was increased almost 50 % from 37 HV to 55 HV in samples compressed at 0.0005 1/s and temperature of 350 °C and 500 °C respectively. Nevertheless, the hardness in samples compressed at higher strain rate (10 1/s) was enlarged only 15 % (from 49.5 HV to 57 HV). Furthermore, the hardness values plotted at 300 °C obtained in samples compressed at 300 °C were clearly higher than at 350 °C and 400 °C and they did not follow the general tendency observed from 350 °C to 500 °C (Fig. 6.7).

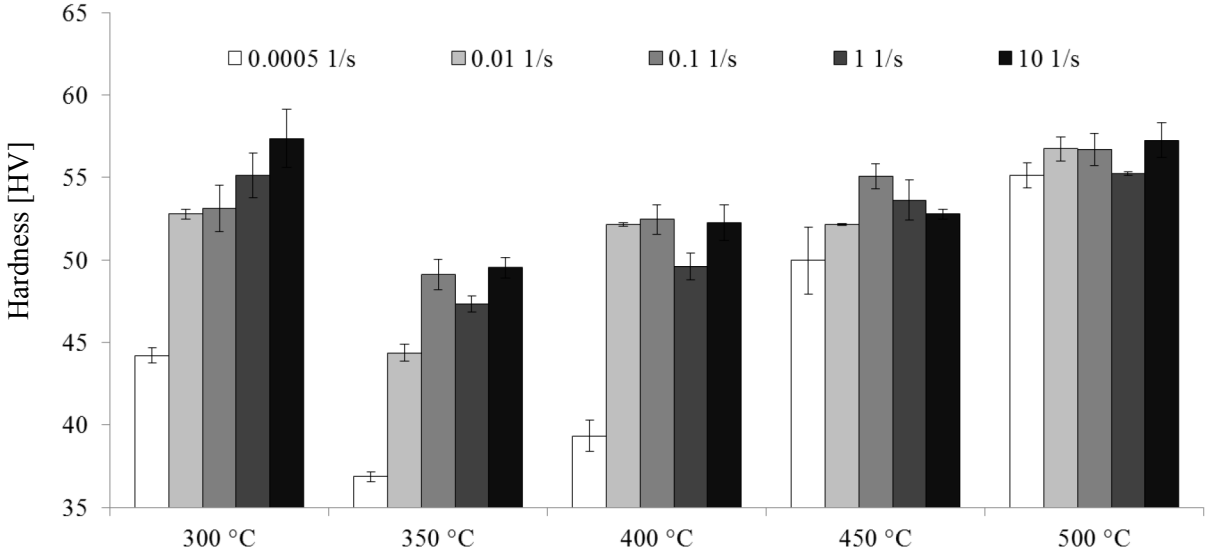

Fig. 6.7. Micro hardness of aluminum alloy EN AW-6060 after hot compression test.

6.3 Friction investigation using the tribo-torsion-test

The friction behavior between the aluminum alloy EN AW-6060 and the hot working steel H13 (DIN 1.2344) was investigated using the tribo-torsion-test, as explained in section 5.4. The friction experiments were carried out at 400 °C and 500 °C, friction speed of 2.5 mm/s and 10 mm/s and at low pressure (10 MPa – 40 MPa). Selected results of the friction torque are depicted in Fig. 6.8. A fluctuation of the measured torque, characteristic of this friction test,

could be observed in all friction experiments. The same oscillation behavior has been reported in the literature [HOR12]. During the first seconds of the friction test an unstable adhesive aluminum layer can be formed in between the aluminum and steel contact area. As a consequence, an alternating frictional torque is measured [BEC14], as could be observed at 400 °C, 40 MPa and friction speed of 2.5 mm/s and 10 mm/s (Fig. 6.8a,b). Due to this oscillation, an average of the friction torque was determined using the maximum and minimum values measured after approximately 200 s.

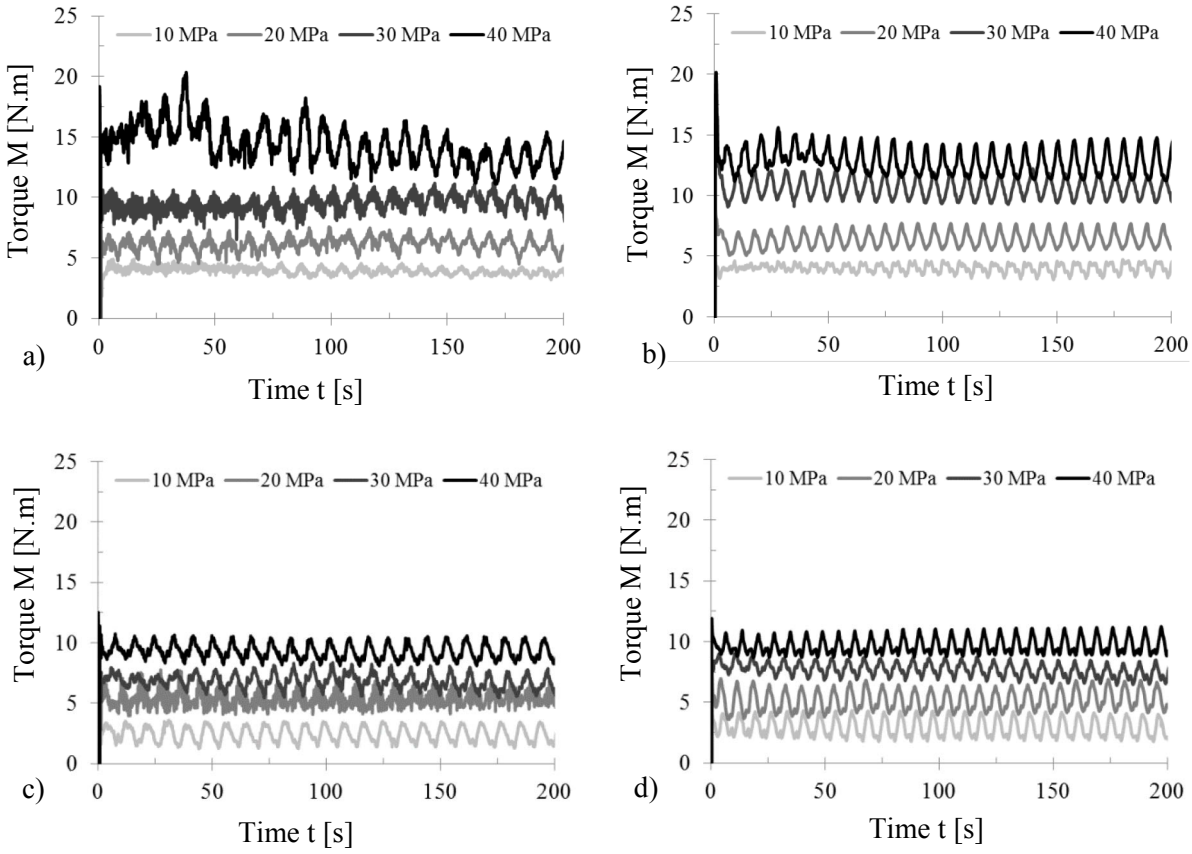

Fig. 6.8. Friction moment measured with the tribo-torsion-test at a) 400 °C and 2.5 mm/s, b) 400 °C and 10 mm/s, c) 500 °C and 2.5 mm/s, d) 500 °C and 10 mm/s.

Applying the Eq. 2.17 the average friction stress τ could be calculated. The influence of the pressure on the friction stress at two different speeds and temperatures is displayed in Fig. 6.10. It was observed, that the friction increased proportional to the normal pressure as suggested by Coulomb (section 2.3.6.1). Assuming an ideal linear behavior $\tau \alpha P$ and applying the Eq. 2.18 the Coulomb friction coefficients were calculated to μ=1.08 and μ=0.83 at 400 °C and 500 °C respectively. As expected, lower friction values were measured at higher temperature.

Moreover, under this pressure conditions the friction was only slightly influenced by the friction speed. Hence, the friction raised approximately 7 % after increasing the friction speed from 2.5 mm/s to 10 mm/s.

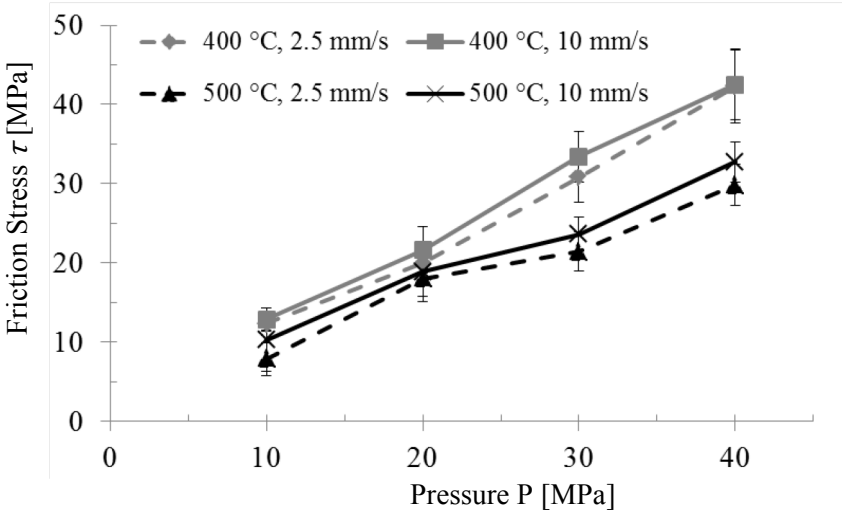

Fig. 6.9. Variation of friction stress at different temperature, speed and pressure.

6.4 Friction investigation using the axial friction test (A)

6.4.1 Mechanical and chemical behavior of the friction

Friction between aluminum alloy EN AW-6060 and the hot working steel AISI H-13 was also investigated by means of the new axial friction test. Unlike other methods, this technique allows the friction investigation at pressures higher than the material's flow stress, as well as at high friction speed. Due to the high pressure at high temperature, the asperities of both surfaces enter in intimate contact producing a high bonding force. The main idea of this friction experiment was to determine the force required to separate the friction pair at different temperatures (300 °C, 400 °C and 500 °C), speeds (0.1 mm/s – 42 mm/s) and initial normal pressures (Po). The results of selected friction experiments are depicted in Fig. 6.10. In the initial part of each curve, the friction force increased proportionally to the stroke (part I, Fig. 4.9). It is possible because at this point the friction surfaces have not experimented relative motion and the system responds according to the Hooke's law. However, after a certain friction force had been achieved, the slope of the curve changes in according with the friction and material behavior. Hence, the inflexion point between the two different slopes represents the friction force generated at the beginning of the dynamic friction process (F_{fa}). At 500 °C the curve's slopes remained almost

constant after the inflexion point (Fig. 6.10c.f), but at lower temperatures (300 °C and 400 °C) it increased, especially at higher friction speeds (Fig. 6.10a,b,c,d). In general higher friction forces were obtained when the experiments were carried out at higher speeds and lower temperatures.

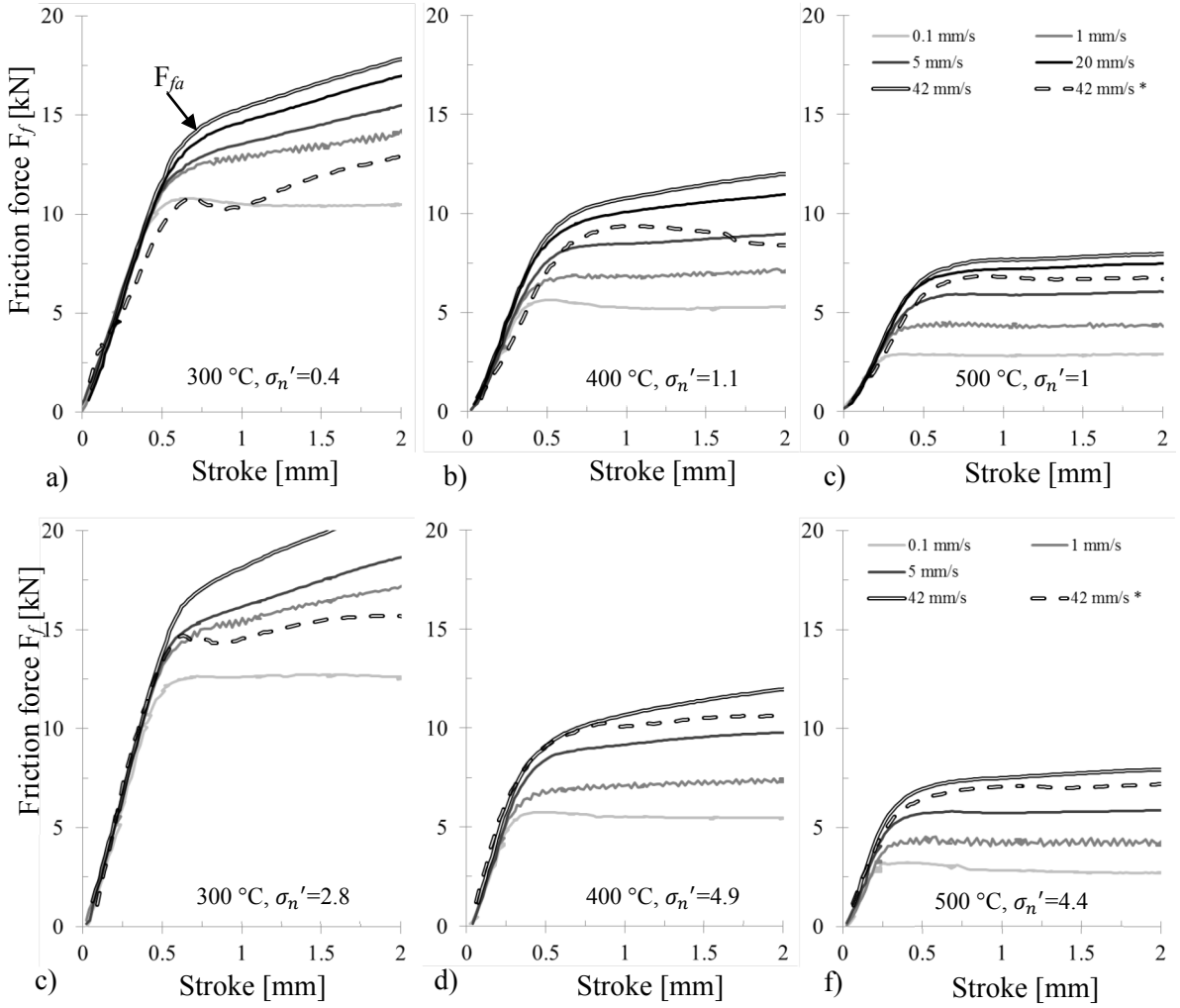

Fig. 6.10. Friction force between EN AW-6060 and AISI H13 measured with the axial friction test at a) 300 °C, $\boldsymbol{\sigma_n'}$=0.4, b) 400 °C, $\boldsymbol{\sigma_n'}$=1.1, c) 500 °C, $\boldsymbol{\sigma_n'}$=1, d) 300 °C, $\boldsymbol{\sigma_n'}$=2.8, e) 400 °C, $\boldsymbol{\sigma_n'}$=4.9 and f) 500 °C, $\boldsymbol{\sigma_n'}$=4.4. (* without Belleville springs)

The friction stress τ at the beginning of the friction process can be calculated dividing the friction force F_{fa} by the friction contact area $\boldsymbol{A_a}$ (Eq. 4.2). Fig. 6.11 shows the influence of the normalized normal stress $\boldsymbol{\sigma_n'}$ on the friction stress at different temperatures and speeds. It was found that the friction stress remains almost constant after a normalized normal stress of 1 at 400 °C and 500 °C, and 2.8 at 300 °C. Similar results were obtained by Wanheim and Bay

[WAN73, WAN78]. On the other hand, the friction speed played a very important role at different temperatures. Changing the speed from 0.1 mm/s to 42 mm/s the friction stress increased around 40 %, 80 % and 135 % at 300 °C, 400 °C and 500 °C respectively (Fig. 6.11).

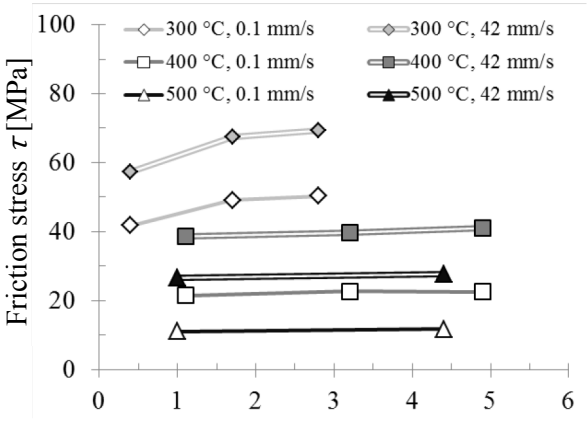

Fig. 6.11. Friction vs normalized normal stress at different temperatures and speeds.

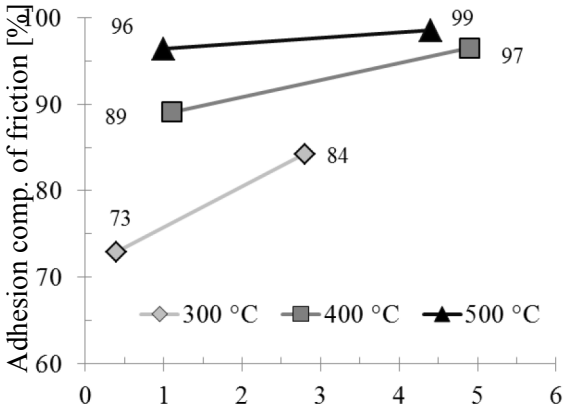

Fig. 6.12. Adhesion component of the friction stress at high speed (42 mm/s).

The experiments carried out at 42 mm/s were repeated without pressure compensation or Belleville springs (for more details see section 4.2). Thus, the friction pair was compressed with an initial pressure, but then it dropped to zero during the friction test. It means that the friction measured under these conditions was due to the adhesion between the friction pair. The results of these experiments were compared with those carried out with pressure compensation and presented in Fig. 6.12. The results show that the adhesion portion of the total friction force is higher at higher temperatures. At 500 °C almost the whole friction was due to the adhesion phenomenon. Additionally, at lower temperature the normal pressure played a more relevant role to increase the adhesion portion of the friction. Hence, at 300 °C an increment of the normalized normal pressure from 0.4 to 2.8 produced a significant increment of adhesion from 73 % to 84 % (Fig. 6.12).

The experimental results were also organized in Fig. 6.13 to enphasize the influence of the speed on the friction stress. A logarithmic tendency was found in all curves when the friction speed was varied from 0.1 mm/s to 42 mm/s. The friction stress incresed substantially from 0.1 mm/s to 10 mm/s calculating 32%, 57 % and 105 % at 300 °C, 400 °C and 500 °C respectively. However, increasing the speed from 10 mm/s to 42 mm/s, the friction incresed around 15 % at 400 °C and 500 °C.

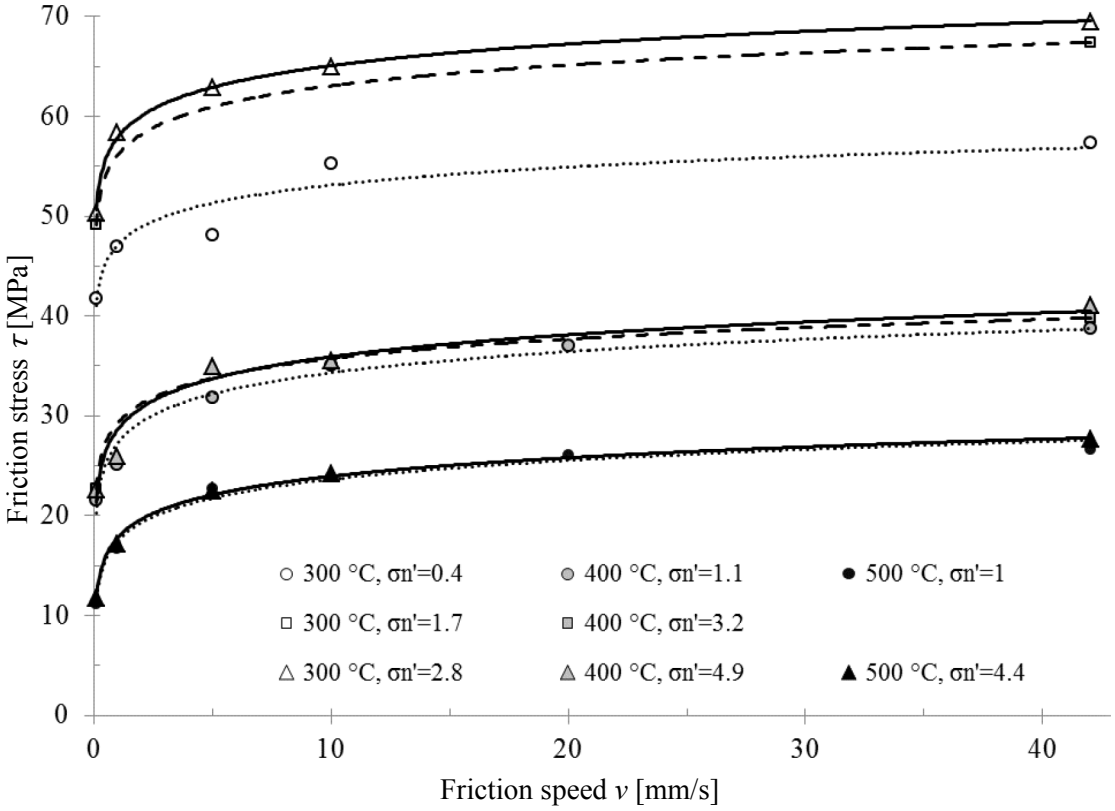

Fig. 6.13. Variation of the friction stress between EN AW-6060 and AISI H13 at different speed, temperatures and normalized normal stress.

6.4.2 Microstructural changes in the friction boundary layer

The internal microstructure of some friction specimens was analyzed after friction test as described in section 5.5.3. Fig. 6.14 shows the macrostructure of aluminum specimens tested at 300 °C, 400 °C and 500 °C and low and high friction speed. It was observed a deformed zone at the friction border of all samples as a consequence of high shearing during the friction test. On the other hand, the material in the center zone was only slightly deformed especially at the top and bottom side. Radially elongated grains were observed at the top side and radially compressed grains at the bottom side. This deformation pattern was more pronounced specially in the samples tested at high temperature and high speed (Fig. 6.14c-f).

The same samples were then metallographic prepared and analyzed with LOM to investigate the friction boundary layer. Fig. 6.15 depicts the micrograph of the entire friction boundary layer of the samples tested at 42 mm/s (Fig. 6.14d-f).

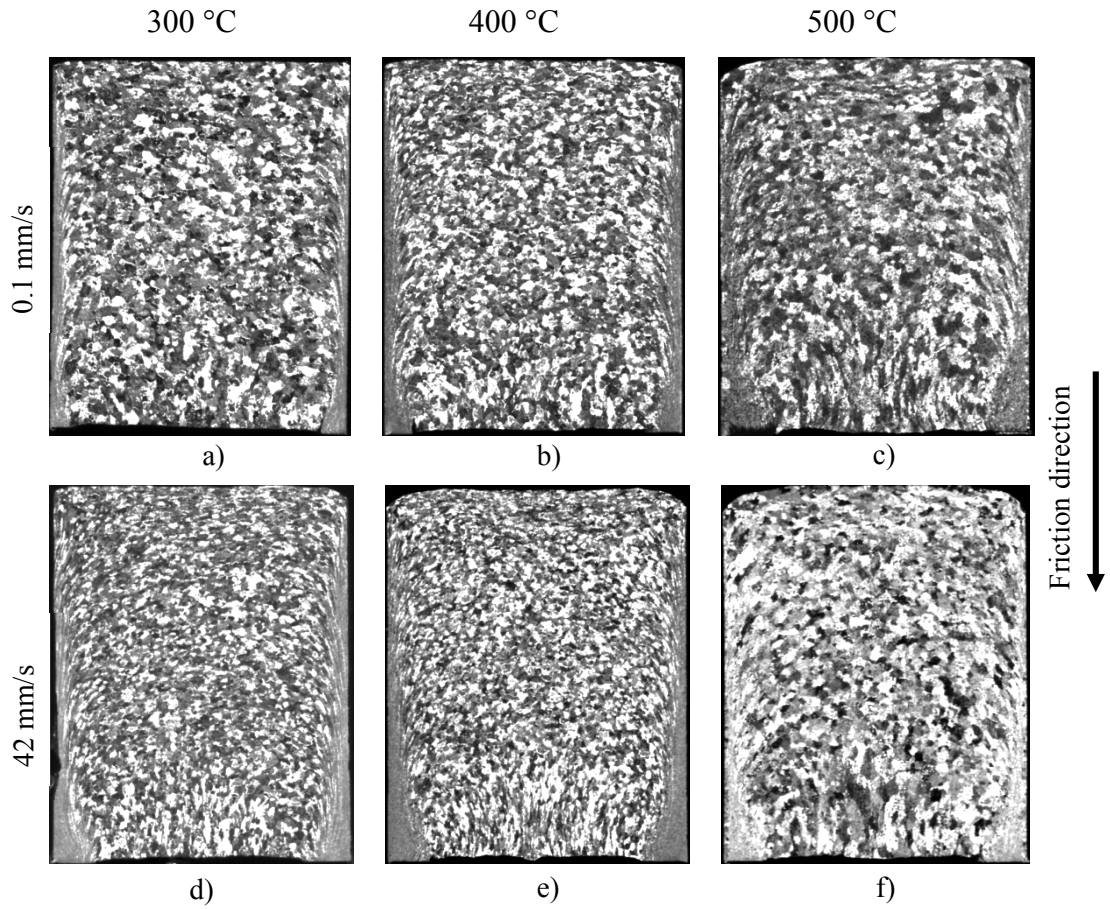

Fig. 6.14. Macrograph of aluminum specimens after friction tests at 0.1 mm/s, a) 300 °C, $\sigma_n{'}$=0.4, b) 400 °C, $\sigma_n{'}$=1.1, c) 500 °C, $\sigma_n{'}$=1, and at 42 mm/s, d) 300 °C, $\sigma_n{'}$=2.8, e) 400 °C, $\sigma_n{'}$=4.9 and f) 500 °C, $\sigma_n{'}$=4.4.

The areas with a severe shearing deformation initially observed in Fig. 6.14 are described in details in Fig. 6.15. A shear zone with a variable thickness *h* was clearly identified (Fig. 6.15a), which was divided into a low and a high shear deformation zone according to the grade of deformation. The low shear deformation zone was difficult to delimit because it is the transition section between the non-deformed and highly deformed grains. Nevertheless, the high shear deformation zone was well defined and characterized by grain refinement. Additionally, deformation zones were observed at the top edge and at the bottom corner of the samples generated during the friction test (Fig. 6.15a). Thus, the maximal deformed top edge was 3 % at 300 °C and 5 % at 500 °C of the total sample height.

Measurements revealed that the shear zone *h* increases with the temperature. Thus, *h* was approximately 1300 µm, 1500 µm and 1600 µm at 300 °C, 400 °C and 500 °C respectively (Fig. 6.15b-d).

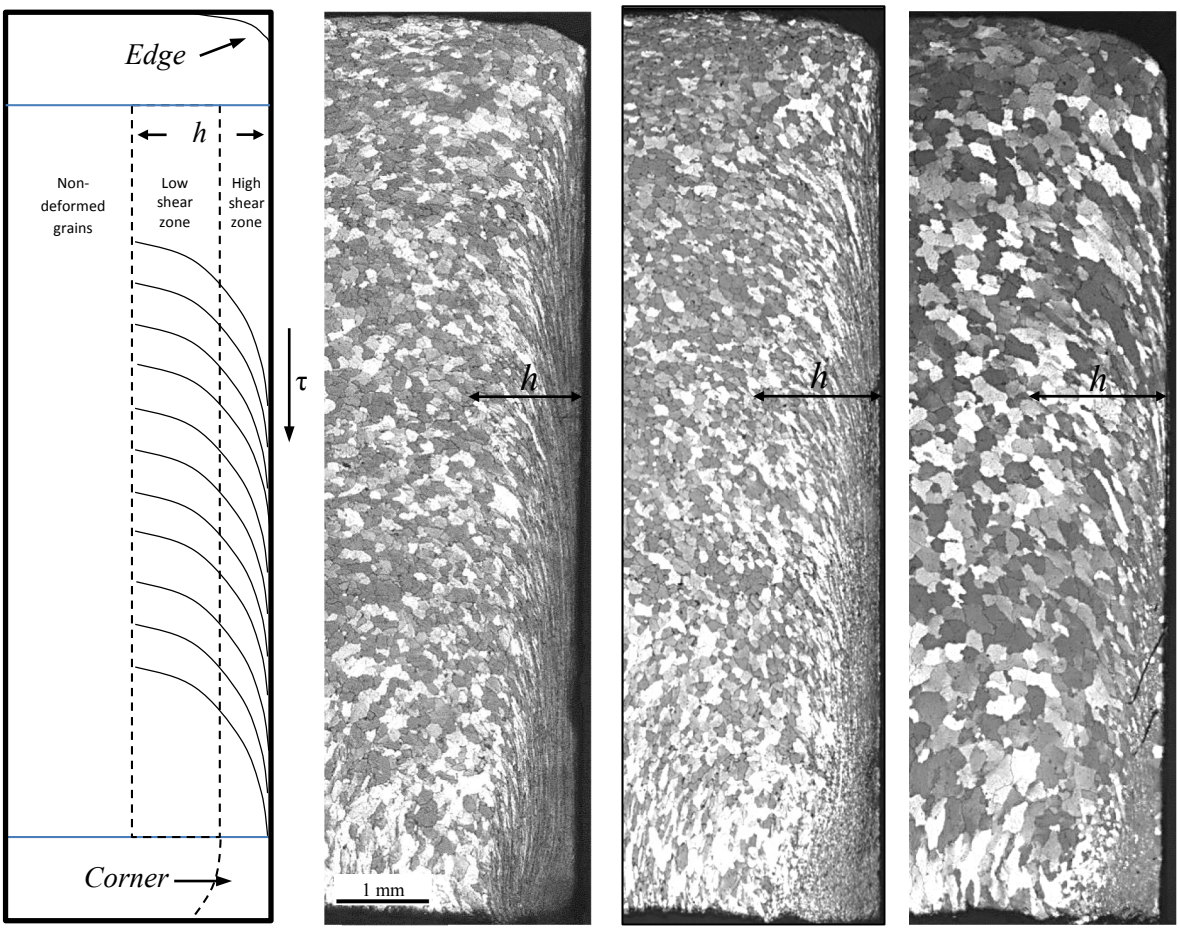

Fig. 6.15. Micrograph of the friction boundary layer after friction test at 42 mm/s. a) Shear zones in the boundary layer, b) 300 °C, σ_n'=0.4, c) 400 °C, σ_n'=1.1, d) 500 °C, σ_n'=1 [SAN14].

6.5 Friction investigation using the axial friction test (B)

6.5.1 Influence of the punch configurations on the friction force at high speed

In order to evaluate the influence of the punch configuration on the friction force, some friction experiments were carried out applying three different punch geometries. Thus, cylindrical, conic-convex and conic punches were used to measure the friction force at 42 mm/s, 300 °C and a normalize normal stress of σ_n'=0.4 (F_a=3900 N). Two experiments were carried out with each punch configuration to evaluate two different methods of sample extraction. In the first experiment the sample was separated from the hollow cylinder before quenching, and after quenching in the second experiment. The corresponding friction curves of the 6 experiments measured with the three different punches are depicted in Fig. 6.16. It was observed that all experiments had a similar friction response until the inflexion point. Only a small increment of

3% was measured using the conic-convex punch, whose difference with the conic punch was kept during the whole friction stroke. However, after the inflexion point a sustained increase in the friction force was generated by means of the cylindrical punch. These results demonstrated firstly the good reliability and reproduction of the initial friction condition as well as during the friction test. On the other hand, an extra friction force (ΔF_f) until 20 % was generated posterior to the inflexion point when cylindrical punches were used due to additional friction between the punch and the aluminum sticking layer on the hollow cylinder.

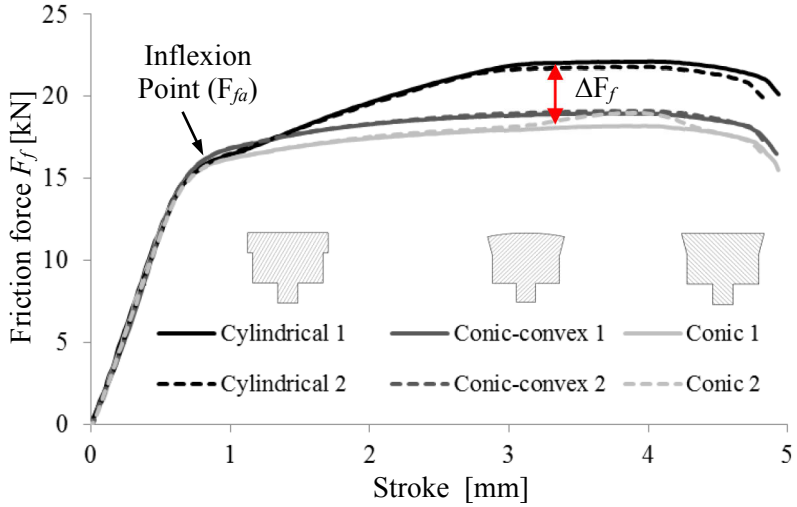

Fig. 6.16. Friction force between EN AW-6060 and AISI H13 at 300 °C and 42 mm/s applying different punch geometries.

6.5.2 Microstructural changes in the friction boundary layer

After friction experiments carried out in section 6.1.5, the microstructure of the whole friction boundary layer was analysed by means of LOM (Fig. 6.17). Some changes of the deformation patterns in the friction shear zone were found using different punch geometries and sample's extraction methods. The thickness of the high shear deformation zone was kept similar around 550 µm in all friction experiments. The punch geometry did not have a direct influence on the thickness or deformation of the friction shear zone. However, the conic-convex punch pruduced more distortion on the top and bottom side of the sample (Fig. 6.17c,d). On the other hand, the deformation at the bottom corner was reduced by means of extracting the sample from the hollow cylinder after quenching.

According to the deformation patterns observed in Fig. 6.17, an additional deformation of the friction shear zone was produced during the sample extraction at high temperature (before quenching), even though the hydrostatical pressure was completely reduced before extracting

the sample. Therefore, it is convenient to quench the sample and the hollow cylinder together and then separate each other. This extraction method will not modify the measured friction force but will provide a true microstructure state of the shear zone after the friction test.

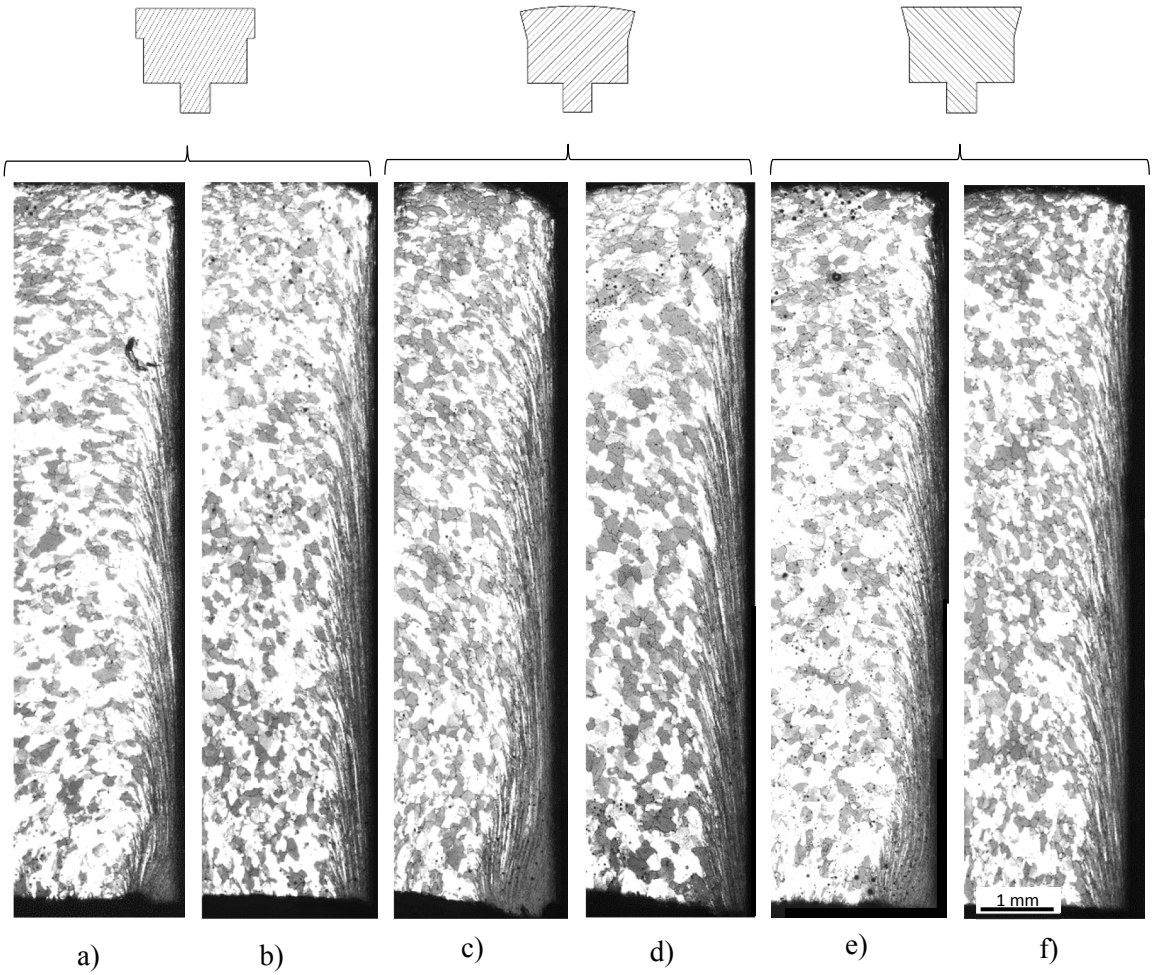

Fig. 6.17. Micrograph of the friction boundary layer of EN AW-6060 tested at 300 °C, 42 mm/s and $\boldsymbol{\sigma_n}'$=0.4 applying different punch configuration and sample extraction method. Using a,b) cylindrical punch, c,d) conic-convex punches and e,f) conic punches and sample extraction before and after quenching respectively.

6.6 Friction investigation using the axial friction test (C)

Considering the influence of the punch configuration on the friction measurement, as well as the sample extraction method on the friction shear zone, the friction experiments were repeated applying the best practices obtained in sections 6.4 and 6.5. Therefore, punches with conic geometry were used, and all samples were extracted from the hollow cylinder after quenching.

The main objective of this experimental trial was the measurement of the real friction force not only at the beginning of the plastic deformation (inflexion point) but also at the steady state and its relation with the microstructure of the shear zone.

6.6.1 Friction at sticking conditions

The experiments were performed at 300 °C, 400 °C, 450 °C and 500 °C to obtain a more detailed influence of the temperature on the friction stress. Moreover, Belleville springs and a normalized normal pressure of $\sigma_n{}'$=3.5 was applied to assure sticking conditions, as showed in Fig. 6.11 (see Table 5.9). Additionally, the friction stroke was 3.5 mm and a relative friction speed 0.1 mm/s, 1 mm/s, 10 mm/s and 42 mm/s. Fig. 6.18 depicts the linear increase of the friction force with the stroke until the inflexion point (point a, Fig. 6.19a), also showed in Fig. 6.10 and Fig. 6.16.

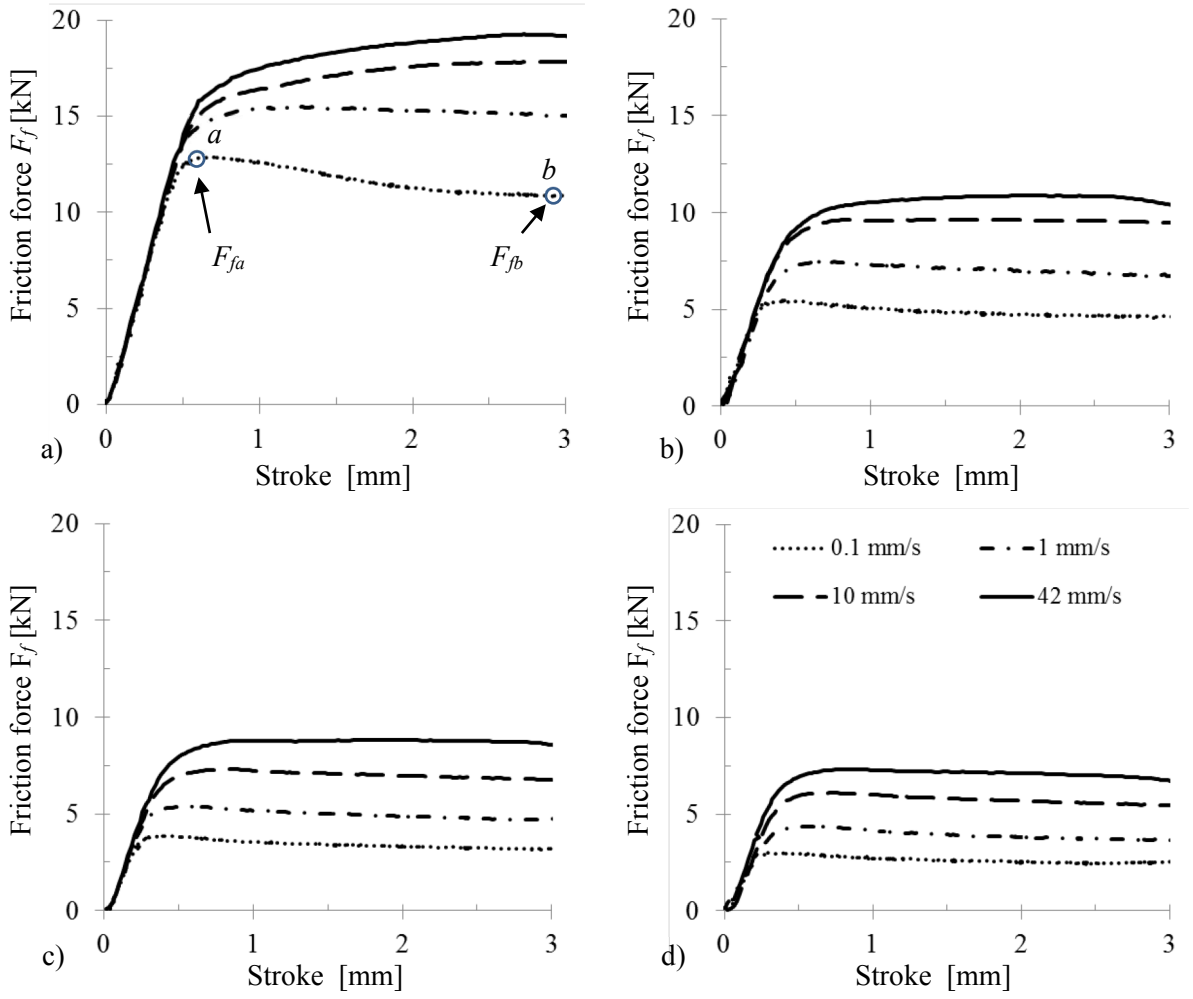

Fig. 6.18. Friction force between EN AW-6060 and AISI H13 measured with the axial friction test at $\sigma_n{}'$=3.5. a) 300 °C, b) 400 °C, c) 450 °C and d) 500 °C.

Posterior to the inflexion point *a*, the curves varied during the friction stroke until a quasi-steady state (point b, Fig. 6.18a) in dependence to the temperature and the speed. The measured friction force corresponds to the force required to deform the friction boundary layer at sticking conditions, but also decreased at low speed especially at 0.1 mm/s.

Fig. 6.19a resumes the calculated friction stress τ at the beginning of the plastic deformation τ_a (Point *a*) as well as at quasi-steady state τ_b (Point b). A logarithmic tendency of the friction stress in relation to the speed was observed in all curves. At 300 °C τ_b decreased 8 MPa at 0.1 mm/s, but it increased 13 MPa at 42 mm/s. However at 500 °C τ_b also increased with the speed but remained always lower than τ_a. Fig. 6.19b shows the ratio between the friction stress τ_a and τ_b at different temperatures and speeds. It was observed that the friction is increased at higher speed, however higher temperature reduces the effect produced by the speed. Friction values at steady state τ_b were lower than τ_a at lower speeds (v < 1 mm/s). At 0.1 mm/s the reduction of stress was around 15 % at temperatures between 300 °C and 450 °C, but 20 % at 500 °C. On the other hand, at high speed (42 mm/s) τ_b was 20 % higher than τ_a at 300 °C, only 5% at 400 °C and almost no variation was found at 450 °C and 500 °C (Fig. 6.19b). Additionally, a very low variation of the friction stress along the friction stroke (τ_b/τ_a ≈1) was also observed at 300 °C and 1 mm/s and 400 °C and 10 mm/s.

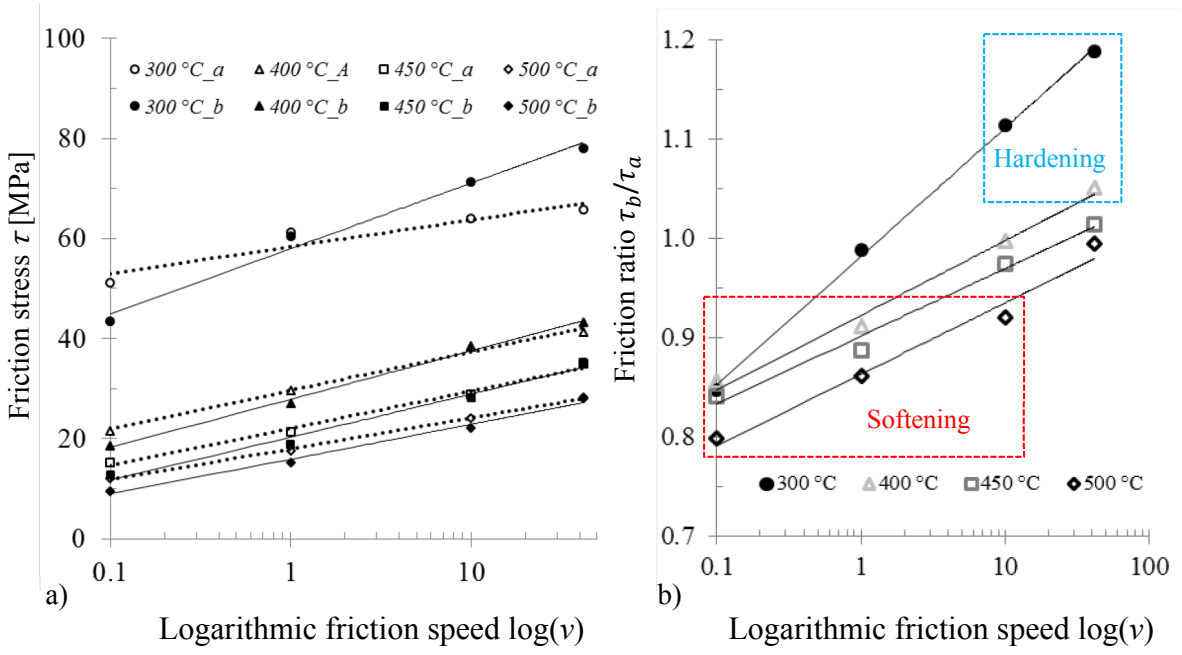

Fig. 6.19. Friction vs speed under sticking conditions, at friction beginning and steady state. a) Friction stress vs logarithmic speed and b) ratio τ_b/τ_a vs logarithmic friction speed.

6.6.2 Microstructural analysis of the friction boundary layer

Some samples tested in section 6.6.1 were analyzed by means of LOM to observe the microstructure evolution in the friction boundary layer. Fig. 6.20 compares the microstructure of the boundary layer before and after friction test at sticking conditions and high friction speed (42 mm/s). A homogeneous initial grain size of approximately 140 µm was observed in the lateral subsurface of an original sample (Fig. 6.20a). Similar to the previews results obtained in section 6.4.2 (Fig. 6.15) a zone of grain refinement or high shear deformation zone was developed behind the friction surface (Fig. 6.20b-d).

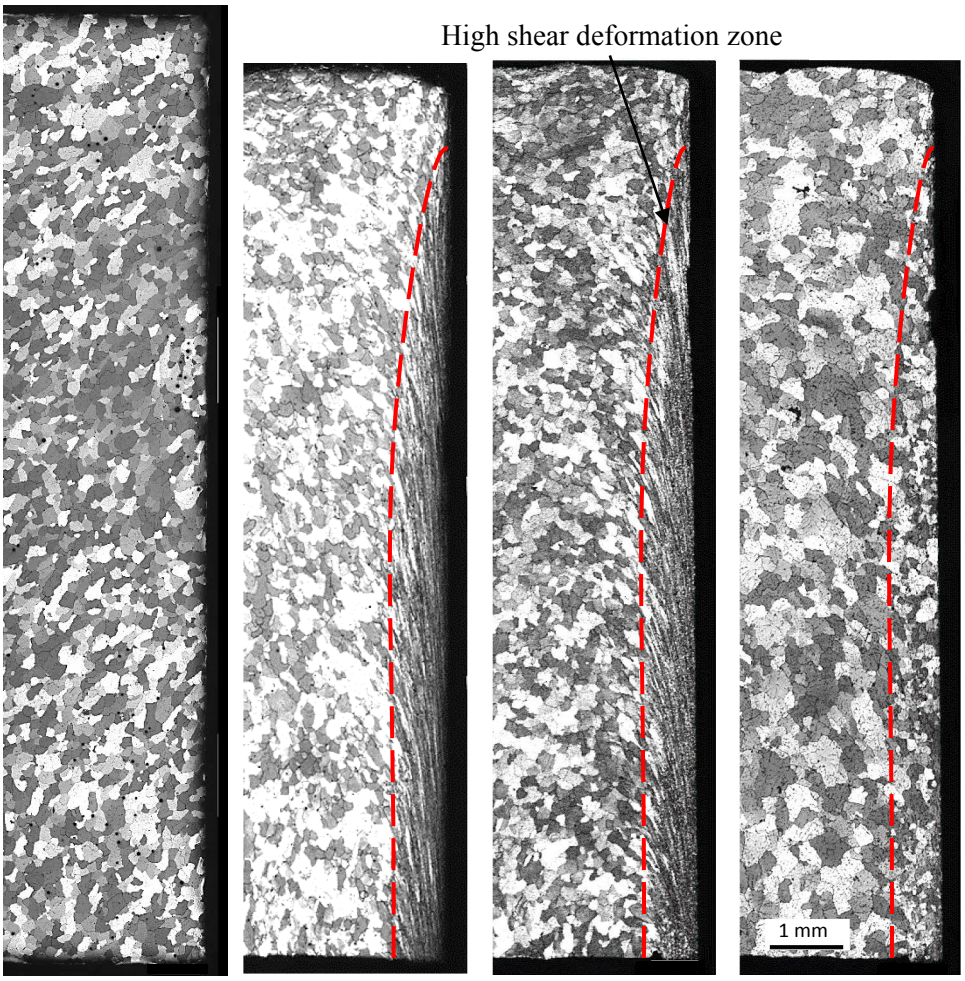

Fig. 6.20. Microstructural changes of the entire friction boundary layer after friction test at 42 mm/s and sticking conditions. a) Initial sample, b) 300 °C, c) 400 °C and d) 500 °C.

A reduction of the bottom corner and top edge deformation was achieved; however, the shear zone was not completely uniform detecting a reduction of the thickness of the shear zone at the

top side of the sample. On the other hand, the average grain size out of the shear zone remained almost constant at 300 °C and 400 °C, indicating concentrated deformation in the shear zone during the friction test. This effect was also observed at 500 °C, however a higher average grain size (200 µm) with maximal values of 400 µm was generated next to the shear zone (Fig. 6.20d). Fig. 6.22 illustrates the microstructure evolution in the middle of the shear zone, product of friction tests at different temperatures and friction speeds. The results showed the original and undeformed dendritic grains next to the shear zone at 300 °C and 400 °C (Fig. 6.21a,b,d,e,g,h). Moreover, the thickness of the shear zone was increased at higher speed at 300 °C and 400 °C. At 300 °C, the growth of the shear layer was accompanied by a high reduction of the grain size to 4 µm at 0.1 mm/s and less than 1 µm at 42 mm/s, also observed in Fig. 6.22a,d.

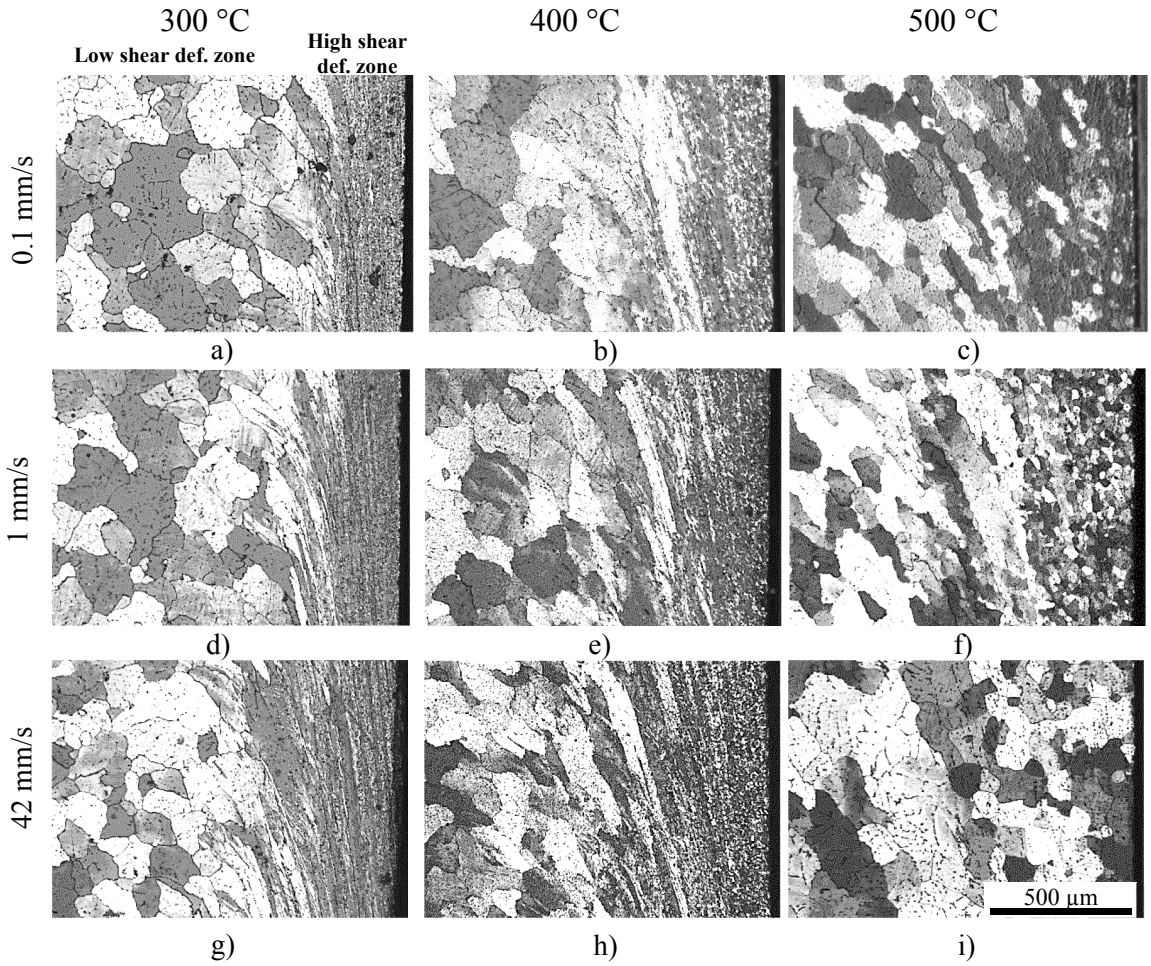

Fig. 6.21. Micrograph of the friction shear layer at sticking conditions.
a,b,c) 0.1 mm/s, d,e,f) 1 mm/s, g,h,i) 42 mm/s at 300 °C, 400 °C and 500 °C respectively.

At 400 °C a grain fragmentation was also observed in the shear zone, generating average grains size of 9 µm at 0.1 mm/s and 5 µm at 42 mm/s. Moreover, stretched grains with only few sub grains of thickness were observed at 0.1 mm/s (Fig. 6.22b) and even thinner at 42 mm/s (Fig. 6.22e). At 500 °C, the shear zone was characterized by the formation of new equiaxed grains with an average size of 30 µm and 70 µm at 0.1 mm/s and 42 mm/s respectively (Fig. 6.22c,f).

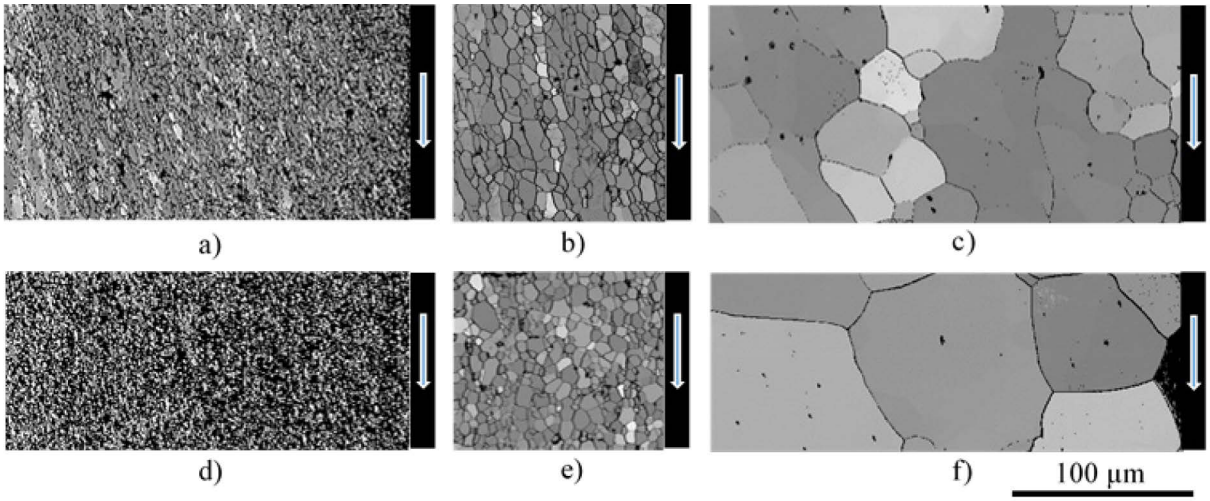

Fig. 6.22. Microstructure of the high shear deformation zone at the middle of the sample by means of EBSD. a,b,c) 0.1 mm/s, d,e,f) 42 mm/s, at 300 °C, 400 °C and 500 °C respectively.

6.6.3 Hardness analysis of the friction boundary layer

Selected samples tested at 300 °C, 400 °C and 500 °C and at a friction speed of 0.1 mm/s and 42 mm/s were subjected to hardness measurements. Fig. 6.23 depicts the hardness mapping carried out in the middle of the shear zone at multiple points situated at 100 µm, 300 µm, 500 µm, 700 µm, 1200 µm and 4000 µm from the border of the friction surface (more details in section 5.7.3). In general, a higher hardness was measured in samples tested at higher friction speed. Thus, a speed increase from 0.1 mm/s to 42 mm/s produced a hardness rise in the high shear layer of 10 %, 6 % and 2 % at 300 °C, 400 °C and 500 °C. Additionally, the results showed a hardness variation in the radial direction of the sample, especially in the friction boundary layer. In samples tested at 300 °C and 42 mm/s the harness increased progressively in the high shear deformation zone until a maximum of 13 % approximately (Fig. 6.23a). However, at 400 °C the hardness increment was only 5 % (Fig. 6.23b), while at 500 °C not important change in the radial direction was measured (Fig. 6.23c). The temperature also influenced the hardness even at 4000 µm, where a very low deformation was expected. Thus, the average hardness in

the center of the sample at 400 °C was 23 % lower than at 300 °C. However, at higher temperature (500 °C) the hardness was 6 % higher than at 300 °C possibly due to solid solution strengthening.

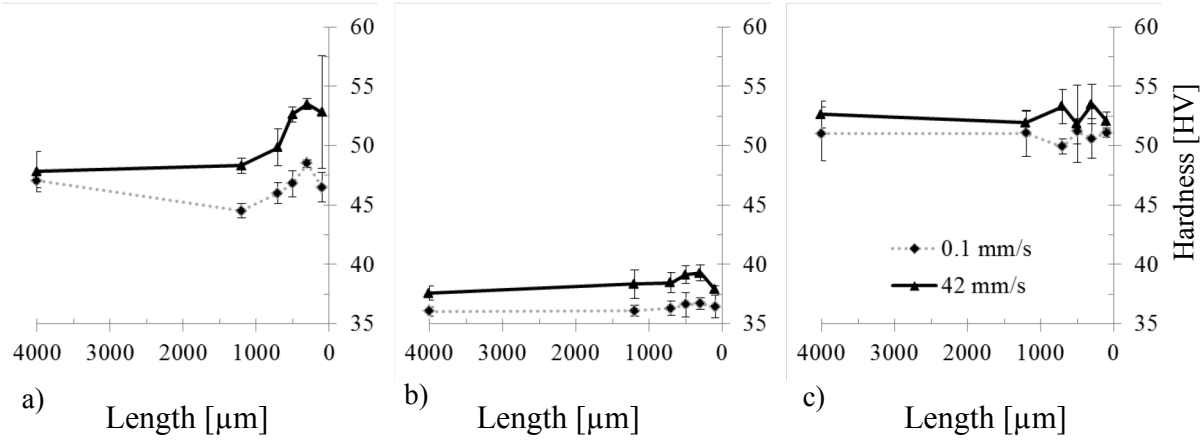

Fig. 6.23. Hardness mapping of the friction shear zone. a) 300 °C, b) 400 °C and c) 500 °C.

6.6.4 Thickness variation of the friction boundary layer at sticking conditions

The high shear deformation zone can be identified due to the strong microstructural changes produced during the friction test (Fig. 6.24). Thus the thickness of the high shear deformation zone at different temperatures and friction speeds was determined (Fig. 6.24). A thin high shear deformation zone of 230 µm was measured in samples tested at 300 °C and 0.1 mm/s. This thickness increased with the friction speed until a maximum of approximately 430 µm at 10 mm/s, which remained constant also at higher speeds (42 mm/s).

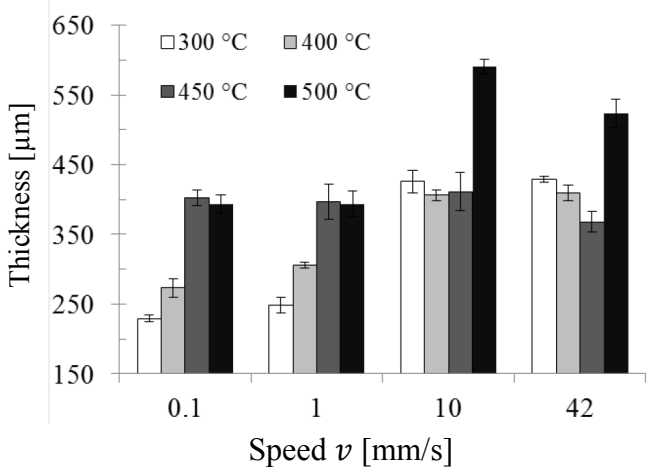

Fig. 6.24. Thickness variation of the high shear deformation zone at sticking friction.

At higher temperatures (450 °C and 500 °C) the thickness remained constant around 400 µm until 1 mm/s. At higher speeds (42 mm/s) the thickness was slightly reduced around 9 % at 450 °C, but increased 30 % at 500 °C (Fig. 6.25).

6.7 Friction investigation using the axial friction test (D) and a grid pattern technique

6.7.1 Friction experiments at different strokes and speeds

Additional to the friction tests performed with aluminum alloy EN AW-6060, a special friction trial was carried out applying the axial friction test. Friction experiments were performed using samples with radial contrast material extracted from extruded profiles provided by the Department of Engineering Design and Material NTNU Trondheim (more details in section 5.8). The main objective of these experiments was to reveal the real material deformation in the friction boundary layer and also investigate the friction contact mechanisms. Hence, cylindrical samples of aluminum alloy AA6063 with a radial grid pattern of A1.8Cu (Fig. 5.9) were subjected to friction experiments at 400 °C and $\sigma_n{}'$=1.1. On one hand, experiments were carried out at 0.1 mm/s whereas the stroke was set at 2 mm, 3.5 mm and 5 mm. On the other hand, the stroke was fixed at 5 mm and the speed was evaluated at 0.1 mm/s, 1 mm/s and 42 mm/s (Fig. 6.25). As was explained in previews sections, all curves had an initial straight with the same slope, because the whole system behaved elastically at the beginning of the test. In this initial part the friction interface sample-hollow cylinder experiences a strong junction force. The second part of the curve depicts the force required to separate plastically the junction. Similar friction force (4.2 kN) was measured at constant speed 0.1 mm/s and different strokes (Fig. 6.25), but higher friction values were measured at higher friction speeds. Moreover, in all tests the friction force decreased after overcoming the inflexion point or peak force.

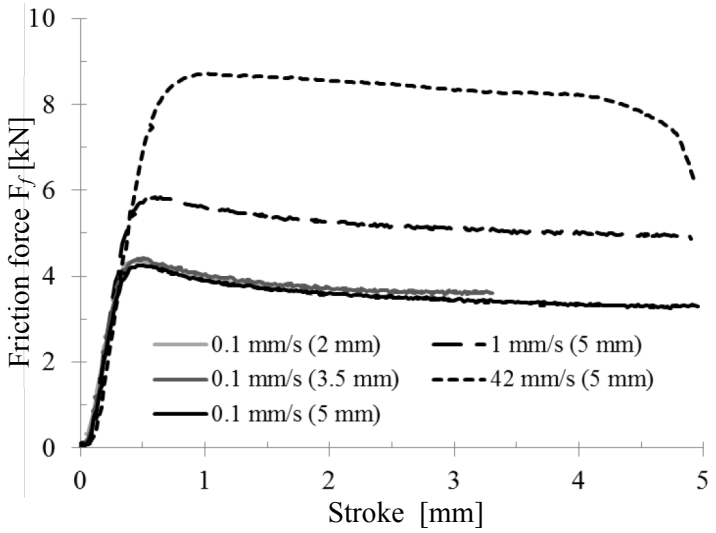

Fig. 6.25. Friction force between EN AW-6060 and AISI H13 measured with the axial friction test at 400 °C and $\sigma_n{}'$=1.1.

Since, the measured stroke contains an elastic part, it was subtracted to calculate the real friction length (*Fl*). Hence, the friction length was approximately 1.6 mm, 3 mm and 4.5 mm instead of 2 mm, 3.5 mm and 5 mm respectively when the friction tests were performed at 0.1 mm/s. Additionally, the elastic deformation of the mechanical assembly also increases at higher friction forces. Consequently, a small difference in the friction length could not be avoided at different speeds. Thus, the real friction length reached at 1 mm/s and 42 mm/s was 4.4 mm and 4.2 mm respectively.

6.7.2 Grid pattern analysis in the friction boundary layer

Fig. 6.26 shows the external (a-f) and internal (g-l) grid pattern of six selected samples tested at different friction conditions. Fig. 6.26a and Fig. 6.26g depict the external and internal contrast stripes at the compressed stage of the sample respectively. The lines 1-7 were identified to facilitate the description of the plastic deformation (Fig. 6.26g). The grid pattern contains four equidistant lines (1-4) in the top side of the sample. Moreover, a thick line (5) is located in the middle, whereas the lines 6 and 7 were numbered in the bottom side. Fig. 6.26b,c,d show new surfaces on the top side as a result of the friction, and therefore its height was the same to the friction length 1.6 mm, 3 mm and 4.5 mm respectively. The grid pattern reveal that the original friction surface was moved down without damage or relative movement between the contrast marks. The presented results demonstrate the perfect sticking contact mechanism generated

during the axial friction test. Therefore, the initial contact surface remained stick to the hollow cylinder and a severe shear deformation is generated in the subsurface (friction shear zone). During the friction test shear material was accumulated in the bottom side of the sample (Fig. 6.26h-g), pushing the material radially towards the center and consequently moving all stripes upwards (Fig. 6.26h-j).

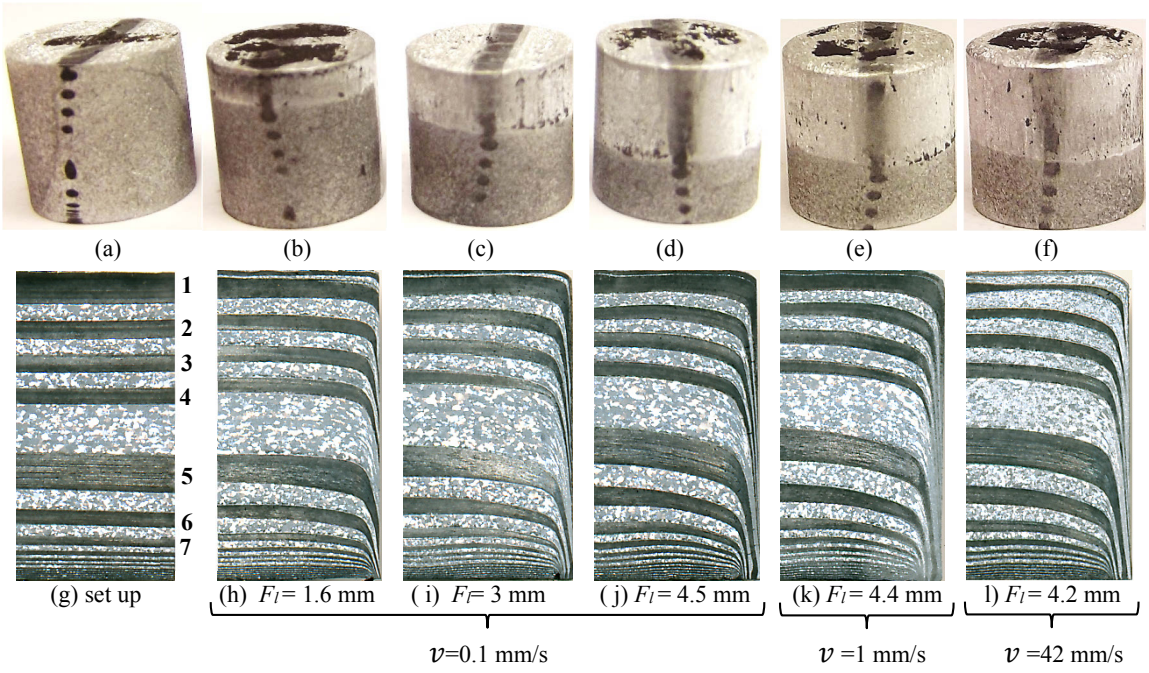

Fig. 6.26. Comparison of the external (a-f) and internal (g-l) grid pattern under stick friction.

6.8 New friction model

Based on the experimental results the influence of the normal pressure, speed and temperature on the friction stress was quantified. Friction experiments at low pressure were carried out by means of the *Tribo-torsion-test* in order to evaluate mainly the influence of the pressure as suggested by Coulomb [POP10]. Moreover, friction experiments under sticking conditions were performed applying the *Axial friction test* at $\sigma_n/\bar{\sigma}$=3.5. Fig. 6.27a and 6.27b depict the friction stress obtained with both methods at 400 °C and 500 °C respectively, specifying the results obtained with the Tribo-torsion-test with the letter (T). The experimental results show the friction increase with the normal pressure, but a very low influence of the speed (2.5 mm/s and 10 mm/s) at the same pressure range. On the other hand, the friction stress obtained at sticking contact and evaluated from 0.1 mm/s to 42 mm/s displayed a high dependence on the friction speed.

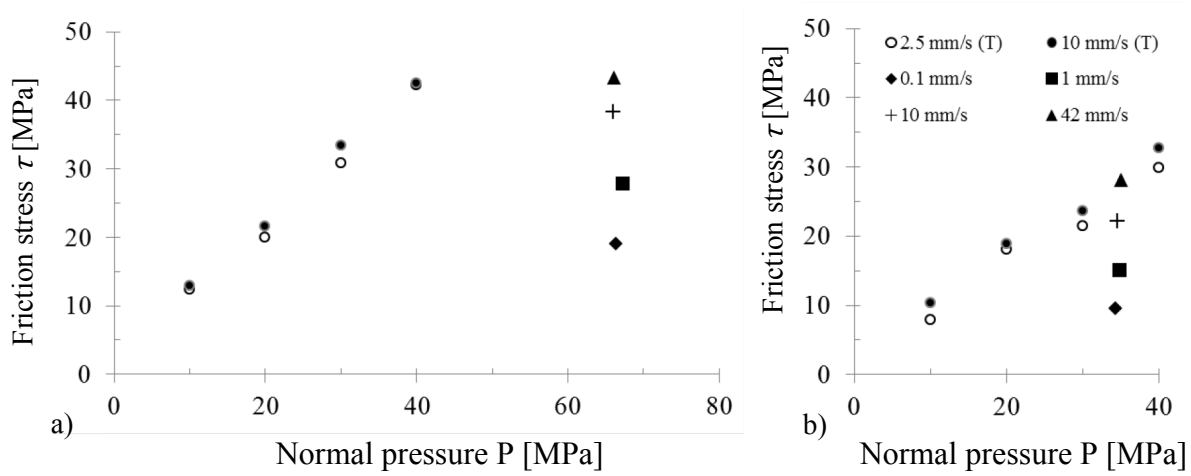

Fig. 6.27. Friction stress under slipping and sticking conditions at a) 400 °C and b) 500 °C.

The friction stress under sticking contact meassured by means of the *axial friction test* should be the maximal value possible at a specific relative speed and temperature, however higher values were achieved with the *tribo-torsion-test* under similar conditions. Due to the differences observed with both methods, the friction values meassured with the *tribo-torsion-test* were used only as reference to calulate the slope of the proportional relationship between friction and pressure (τ α P). Thus, the friction stress increases liniarly with the pressure as suggested by Coulomb, until a maximal value τ_{st} reached at sticking friction, which is also equivalent to the shear flow stress k (Fig. 6.28a).

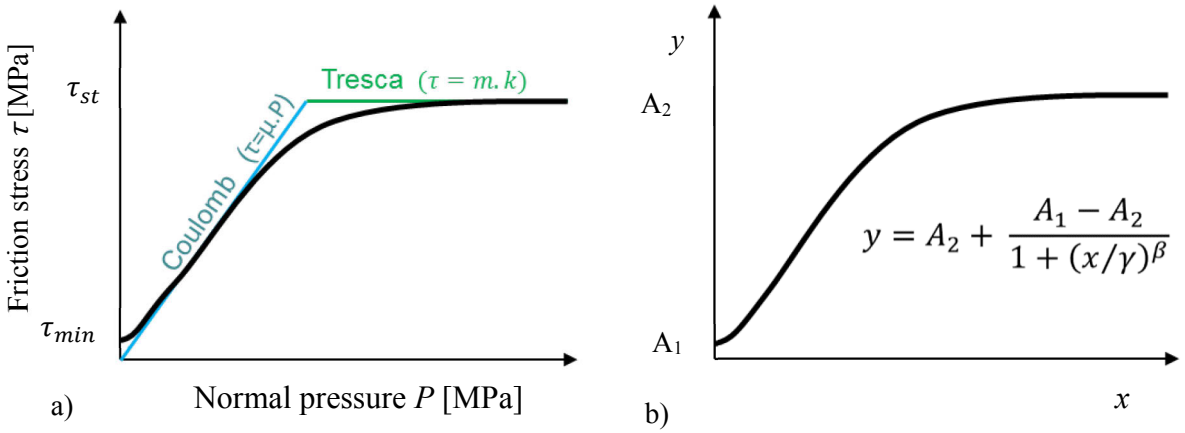

Fig. 6.28. Logistic function applied in a) the friction phenomena and b) general applications.

In order to reproduces mathematically this behavior, the logistic function was selected (Eq. 6.1). Hence, initially the variable y increases quickly as function of x, but once an inflexion point is achieved, it is followed by a horizontal asymptotic tendence (Fig. 6.28b).

$$y = A_2 + \frac{A_1 - A_2}{1 + (x/\gamma)^{\beta}} \quad \text{(Eq. 6.1)}$$

Replacing the boundary values A_1 and A_2 by the minimum τ_{min} and maximum friction value τ_{st} respectively, and introducing the pressure *P* as independent variable, the Eq. 6.1 can be rewritten to calculate the friction stress τ (Eq. 6.2). The minimum friction value is assumed as a small fraction of the maximal value ($\tau_{min} = f \cdot \tau_{st}$), thus an inferior friction limit can be stablished ($0<f\ll1$). Moreover, β and γ adjust the form and slope of the curve. A constant value is assigned to β, while γ is corrected by the tempertaure *T* (Eq. 6.3). Where γ_1 and γ_2 are constant.

$$\tau = \tau_{st} + \frac{\tau_{min} - \tau_{st}}{1 + (P/\gamma)^{\beta}} \quad \text{(Eq. 6.2)}$$

$$\gamma = \gamma_2 - \gamma_1 T \quad \text{(Eq. 6.3)}$$

According to Tresca, the friction at sticking conditions τ_{st} is equivalent to the shear flow stress *k*, and therefore it can be used to calculate the flow stress $\bar{\sigma}$ by means of the von Mises yield criterium (Eq. 6.4). Thus, applying the Zener-Hollomon relationship (Eq. 2.15 and 2.14) and the constants calculated for EN AW-6060 (Table 6.1), the average strain rate can be calculated for different friction speeds and tempertaures. Eq. 6.5 can be used to estimate the average strain rate $\dot{\bar{\varepsilon}}$ at temperatures from 400 °C to 500 °C, where v is the speed and *a* a variable modified by the tempertaure *T* and the constants a_o, *b* and *c* (Eq. 6.6). Moreover, the constant c_1 (1 mm^{-1}) was introduced to balance the dimensions of the Eq. 6.5.

$$\bar{\sigma} = k \cdot \sqrt{3} = \tau_{st} \cdot \sqrt{3} \quad \text{(Eq. 6.4)}$$

$$\dot{\bar{\varepsilon}} = a\left(e^{v/a} - 1\right)c_1 \quad \text{(Eq. 6.5)}$$

$$a = a_0 + be^{-T/c} \quad \text{(Eq. 6.6)}$$

Fig. 6.31a shows the variation of the average strain rate estimated with the new empirical equations Eq. 6.5 and 6.6. Additionally, Fig. 6.31b depicts a good agreement between the meassured and calculated shear stress or friction stress at sticking conditions.

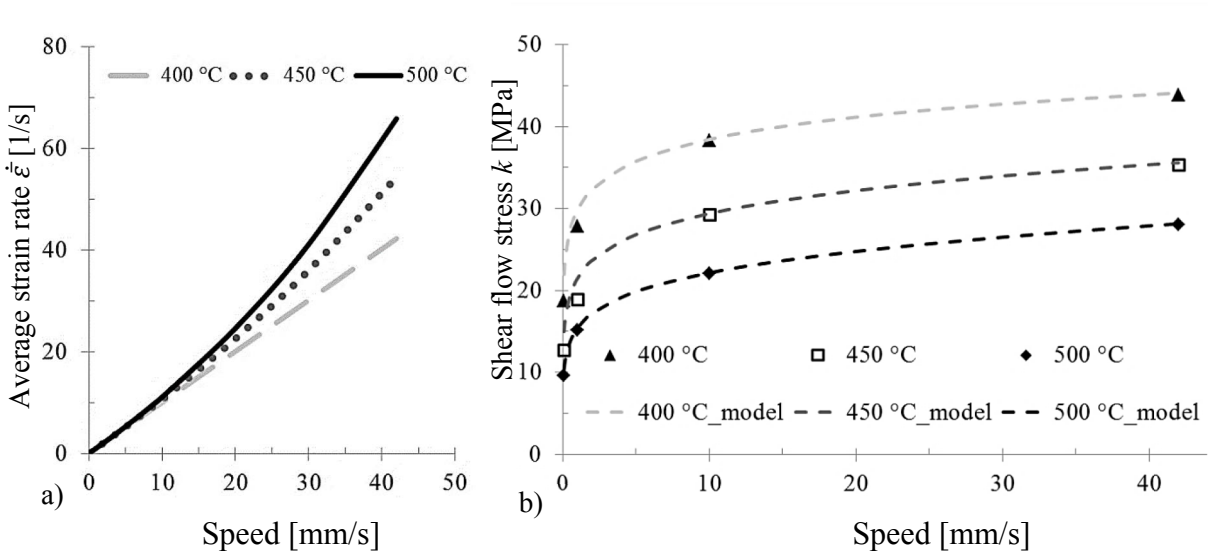

Fig. 6.29. Average strain rate under sticking friction. a) Influence of the speed and temperature on the average strain rate, and b) shear stress estimation based on Avg. strain rate.

Table 6.2 resumes the value of the constants needed to define the form and slope of the friction curve ($\gamma_1, \gamma_2, \beta, f$), as well as the average strain rate (a_o, b, c).

Table 6.2. Constants for the estimation of the friction stress and the average strain rate.

Friction stress (τ)				**Average strain rate ($\dot{\bar{\varepsilon}}$)**		
γ_1	γ_2	β	f	a_o	b	c
0.06	40	2.1	0.01	49.68	9.68E+19	10.59

Once the above constants are defined, the friction stress can be estimated at different combinations of pressure, speed and temperature as illustrated for instance in Figs. 6.30a and 6.30b for 400 °C and 500 °C respectively.

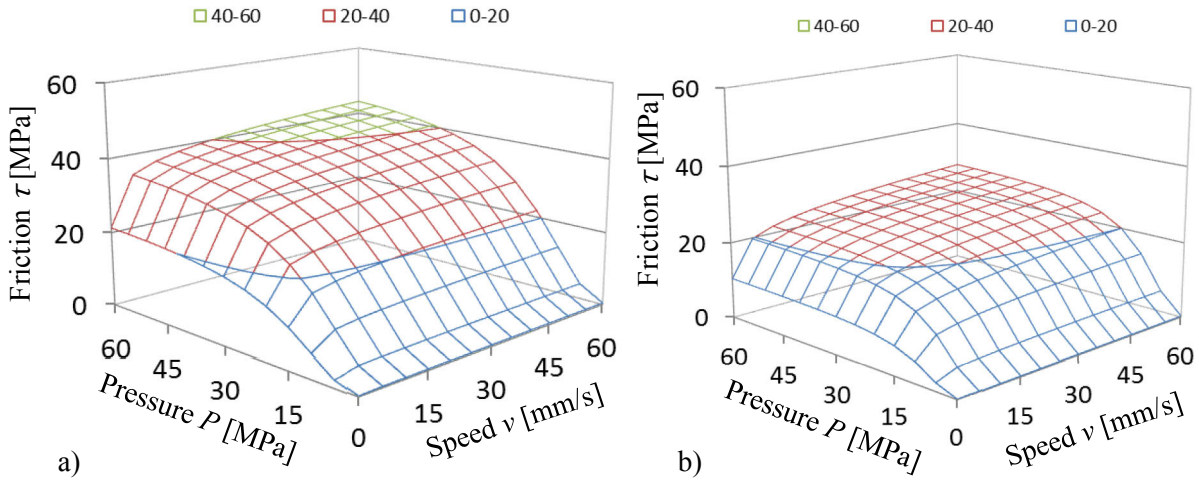

Fig. 6.30. New friction model at a) 400 °C and b) 500 °C.

6.9 Multi-hole extrusion with long and different inclinations of bearing channels

Numerous multi-hole extrusion trials have been performed to investigate the friction behavior inside the bearing channels [MUE96, HOR05, MUE12, DON15]. The results have demonstrated the highly sensitive of the product speed to the inclination angle in long bearing channels. Since, the material flows slower through channels with higher resistance, different friction conditions generate not only dissimilar product speed, but also changes of the temperature [MUE12] and the microstructure [OCK12]. Although, the great knowledge about the friction in aluminum extrusion and especially in multi-hole dies, its correct determination and thus the accurate prediction of the product speed still represents a big challenge. In order to investigate this complex phenomena multiple variables such as; extrusion force, bearing temperature and product speed were measured during multi-hole extrusion experiments. Additionally, the contact mechanisms in the bearing channel were analyzed evaluating the surface contact and the microstructure of the friction boundary layer inside the bearing channels.

6.9.1 Extrusion force and temperature applying different bearing angles

Extrusion experiments were carried out using four different die configurations. Special die inserts with long bearing channels (length 20 mm) and also different inclination angles were pairwised placed in a special extrusion die as explained in Fig. 5.12 and Fig. 5.13. Thus cylindrical (0° parallel), choked (+0.5° and +1°) and relief (-0.5°) bearing channels were applied to evaluate its effect on the relative product velocity (Fig. 5.13). Moreover, billets of EN AW-6060 preheated at 460 °C (diameter 137 mm and length 355 mm) were extruded applying a ram speed of 4 mm/s. The extrusion force distribution and the temperature evolution on the bearing

channel for selected experiments are shown in Fig. 6.31. Parallel 0° and +0.5° choked bearing channels were applyed in the experiment #1 (Fig. 6.31a) and 0.5° and 1° choked bearing channel in the experiment #4 (Fig. 6.31b). A temperature variation was detected during the whole extrusion process. At the first 25 mm of stroke a strong tempertaure increase of 6 % and 8 % was measured in the experiment 1 and 4 respectively. Posteriorly, the temperature continued increasing with different rates according to the bearing geometry. A high temperature diference of 15 °C between parallel 0° and +0.5° choked bearing was generated in the experiment 1, however only 5 °C between 0.5° and 1° choked bearing channels was observed in the experiment 4.

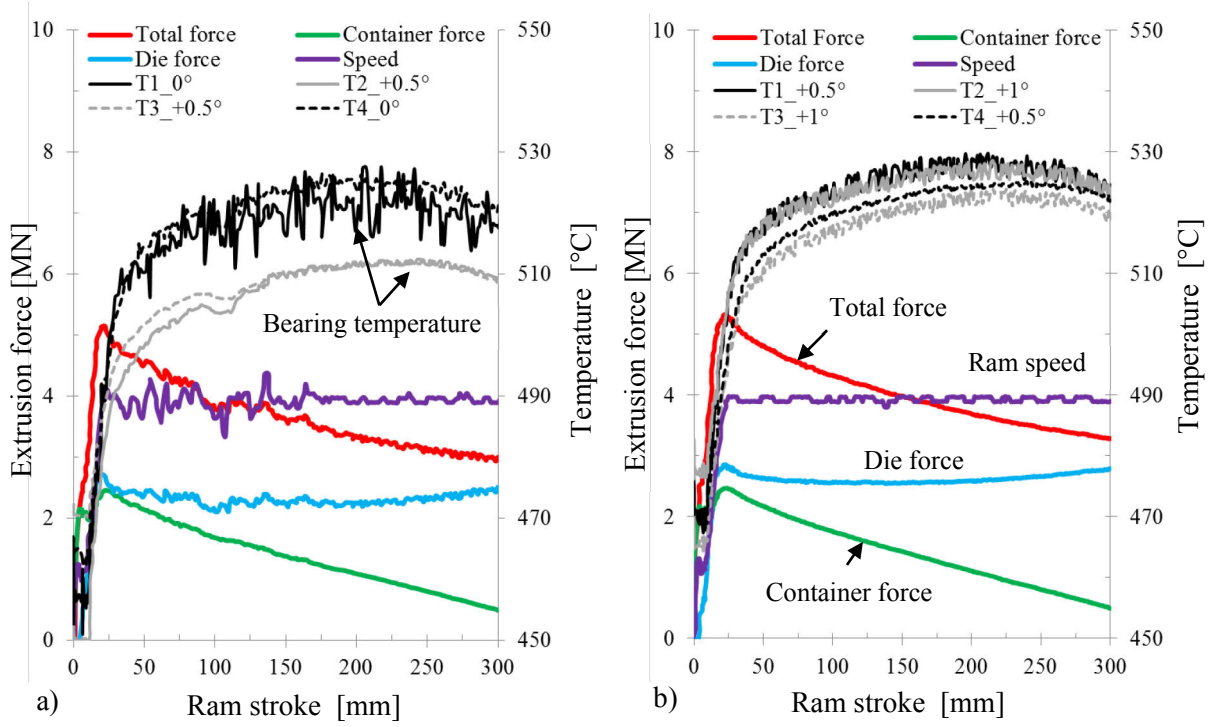

Fig. 6.31. Friction and deformation force during multi-hole extrusion of EN AW-6060 as well as temperature evolution on long bearing channels. a) 0° parallel and 0.5°choked bearing channels (Exp. 1), and b) 0.5° choked and 1° choked bearing channels (Exp. 4).

The experimental results also showed a little increase of the die force using inserts with higher choked angles. Thus, die force in the experiment 4 was 200 kN (8 %) higher than in the experiment 1. However, in the experiment 3 the die force was 300 kN (12 %) lower than the experiment 1 (Fig. 6.32). On the other hand, the container force remained constant around 2.5 MN, except in the experiment 3, where a shorter billet reduced the container force to 1.8 MN.

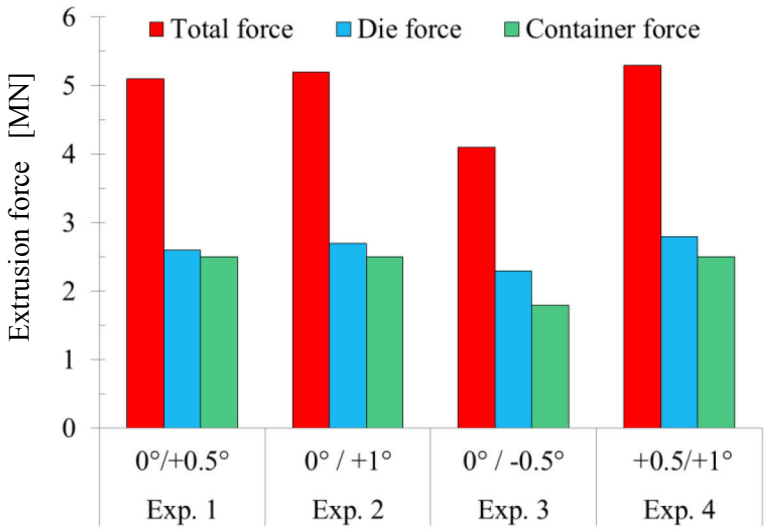

Figure 6.32. Peak force distribution during extrusion at different angle of bearing channel.

6.9.2 Influence of the channel angle on the product length and speed

Inserts with different angle inclinations generated dissimilar product length. Fig. 6.33 depicts the product length produced with each bearing channel and its position in the die for each extrusion experiment. Similar product lengths were observed in the pairwise inserts with the same geometrical configuration. Experiments 1 and 2 depicted equivalent results, detecting a very low influence of changing the bearing channel from +0.5° to +1° choked. The low influence on the product length using +0.5° or +1° could be also proven in the experiment 4, observing similar results. Moreover, larger rods were obtained with relief (-0.5°) than with the parallel bearings channels in the experiment 3.

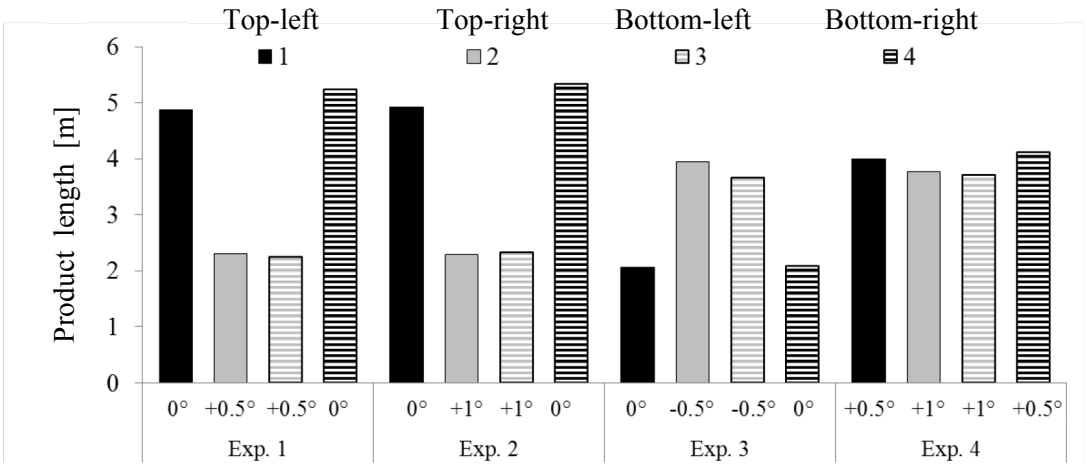

Fig. 6.33. Product length after multi-hole extrusion applying different bearing angles.

In order to compare quantitatively the effect of the two bearing angles used in each extrusion die, average product lengths were determined. For instance, the average product length produced applying parallel and +0.5° choked channels were 5060 mm and 2280 mm respectively (Fig. 6.33). From the average product length the product velocity (Fig. 6.34a) and also the normalized product velocity (Fig. 6.34b) were calculated. It was also observed, that an insert with a particular bearing angle generated different product lengths depending on the angle of the neighbour insert place in the same extrusion die. Thus, the normalized velocity on the parallel channel was 0.69 in the experiment 1, but 0.35 in the experiment 3. Similarly, the +1° choked channel caused a normalized speed of 0.3 and 0.48 in experiments 1 and 4 respectively.

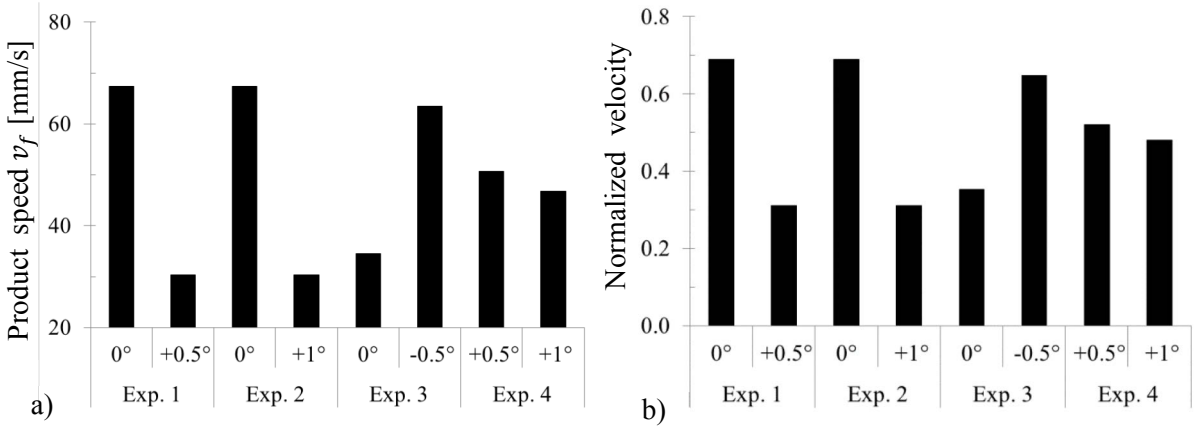

Fig. 6.34. Product velocity during multi-hole extrusion applying different bearing channel inclination. a) Product velocity and b) normalized product velocity.

6.9.3 Real contact area inside the bearing channel

The contact area between the aluminum alloy EN AW-6060 and the bearing channel AISI H-13 were investigated following the procedure explained in section 5.9.4. Only one billet was extruded through each die configuration to observe the bearing contamination caused by the contact with the extruded aluminum material. Fig. 6.35 depicts selected section of the bearing channels after extrusion experiments. The different color and surface roughness of the bearing channels revealed some information about the contact mechanisms. The inserts with choked bearing channels presented a black color area at the inlet side, in which the perpendicular ground marks could be also observed (Fig. 6.35b,d,g,h). According to previews similar experiments, this area could be an evidence of sticking friction [AKE85, VAL94]. Posterior to this dark zone, aluminum colored lines in the extrusion direction formed a thin layer on the bearing channel, characteristic of slipping friction. Moreover, in the parallel channels the area situated at the inlet

side presented two different appearances. In the experiments 1 and 3 (Fig. 6.35a,e) the inlet was covered with an adhesive aluminum layer and followed by aluminum stripes. Since, neither dark zones with visible ground lines nor aluminum stripes were observed, sticking or slipping friction could not be assumed. On the other hand, the parallel channel of the experiment 2 depicted a dark area at the inlet side brighter than the observed in choked channels (Fig. 35c). Additionally, the relief channel presented only light marks at the beginning and end of the bearing land (Fig. 6.35f). According to the color and surface topography observed in the bearing channels the length of the sticking and slipping zones can be presumed (Fig. 6.35). However, the surface appearance was not enough to identify the friction mechanisms presented on the inlet of the parallel channels applied in the experiments 1 and 3.

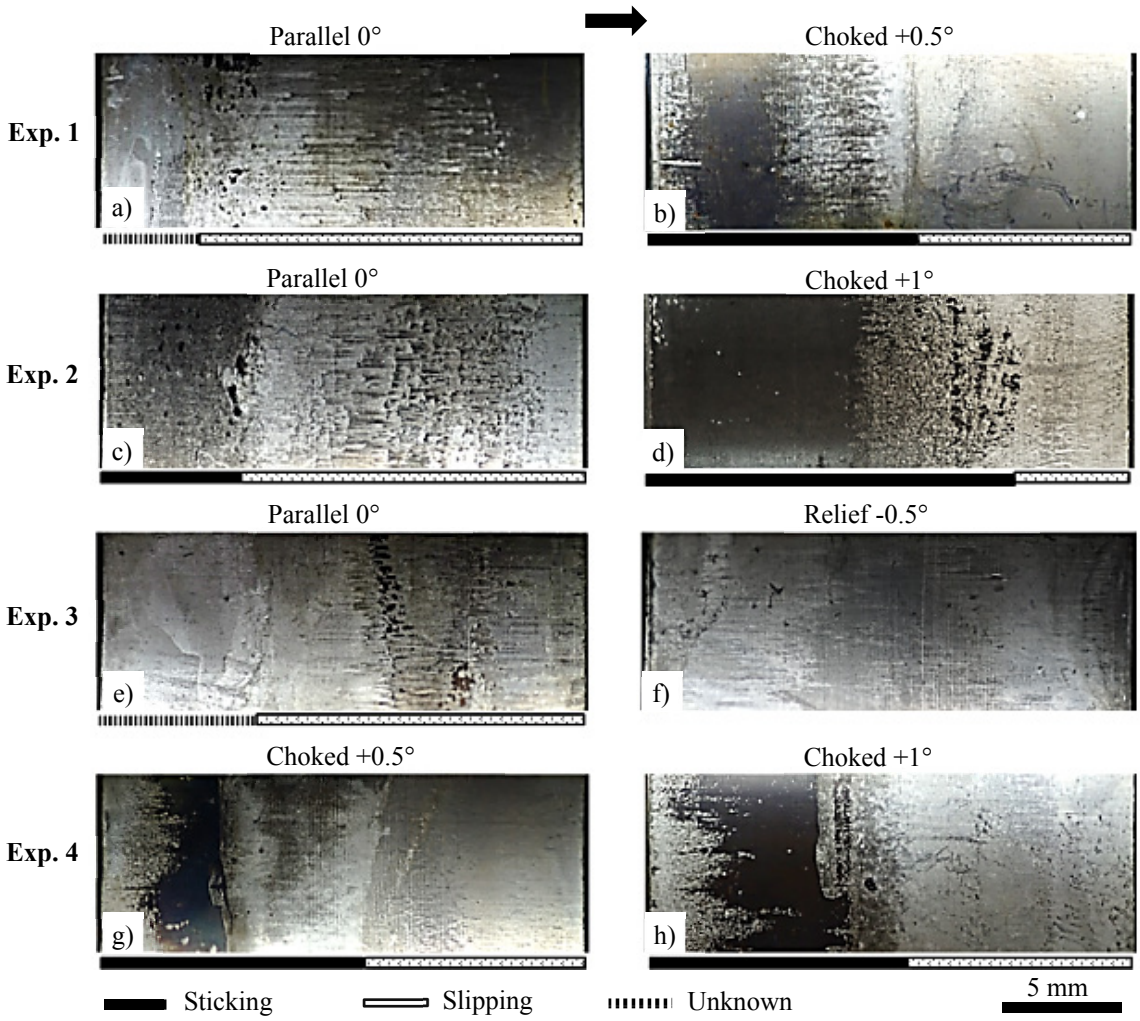

Figure 6.35. Surface of selected bearing channels after removal of aluminum rods.

6.9.4 Microstructure analysis of extrudates inside the bearing channel

Fig. 6.36 shows the microstructure of the aluminum rests remained in contact with the bearing channels of selected inserts applied in each extrusion trial.

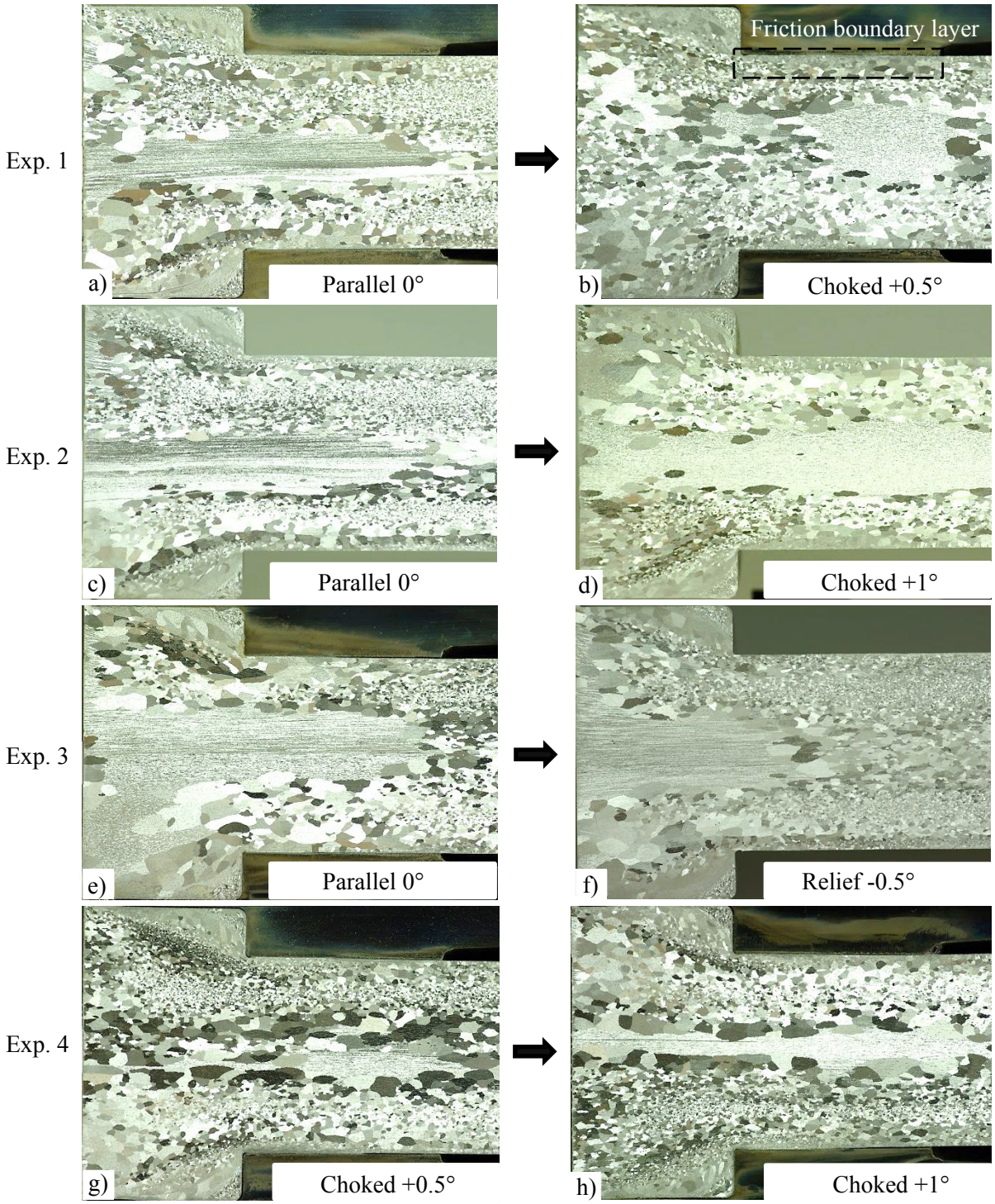

Fig. 6.36. Micrographs of selected aluminum rest remained in the bearing channels after multi-hole extrusion. a,b) Experiment 1, b,c) experiment 2, d,e) experiment 3 and f,g) experiment 4.

Since, the extrusion product and also the rest of aluminum remained inside the bearing channels were slowly cooled at room temperature, the microstructure could have changed by means of static recrystallization or grain growth. Therefore, the relative grain size inside the insert indicates different deformation history. The different microstructures present inside the inserts reveal the important effect of the speed, and temperature variation on the final microstructure, caused by small changes of the inclination angle in long bearing channels.

Fig. 6.37 depicts microstructural changes of the material in contact with the bearing channel. It was found that in choked bearing channels a grain refinament was produced in the sublayer which remained adhered to the dark area mentioned above. For instance, the first 14 mm of the subsurface in contact with the 1° choked bearing channel presented fine grains (Fig. 6.37a), that correspondes with the same length of the black area meassured on the contact surface (Fig. 6.35d). The same effect was observed in the first 11 mm of the 0.5° choked channel in the experiment 1 (Fig. 6.37b). Moreover, in parallel channels two different cases were obeserved.

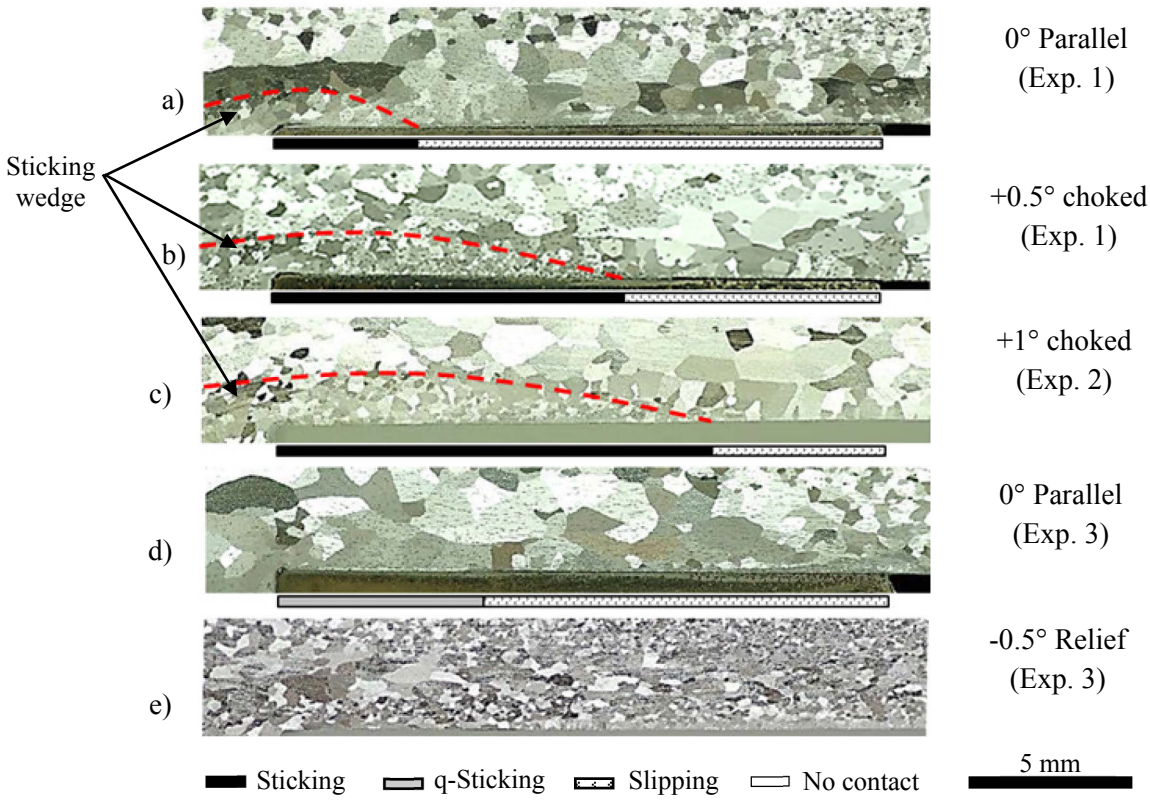

Fig. 6.37. Influence of the friction contact mechanism on the microstructure in the friction boundary layer inside the bearing channel.

On one hand, a grain refinement was detected in the first 4 mm of the parallel bearing channel of the experiment 1 (Fig. 6.37c). Thus, sticking conditions could have occurred in the inlet side, although no black aparence was observed in Fig. 6.35a. On the other hand, big grains were observed using a similar channel in the experiment 3. Since, no grain refinament was observed (Fig. 6.37d) and no scratched line pattern was present on the inlet side (Fig. 6.35e), neither perfect sticking nor sliding friction conditions took place on this contact area respectively. Hence, the normal pressure in the inlet of the bearing channel caused an intimate contact, however it was not enough to stick perfectly the two surfaces. This contact mechanism can be consideredd as *quasi-sticking* (q-sticking). The friction boundary layer in the relief channel depicted no additional deformation because any important interaction with the bearing land took place (Fig. 6.37e).

6.9.5 Friction mechanisms inside the bearing channels

According to the contact areas observed in the bearing channels and the microstructure evolution in contact with the bearing channel, the length of the real contact mechanism was determined. Fig. 6.38 illustrates the length of the sticking, q-sticking and slipping areas presented in the different bearing channels geometries.

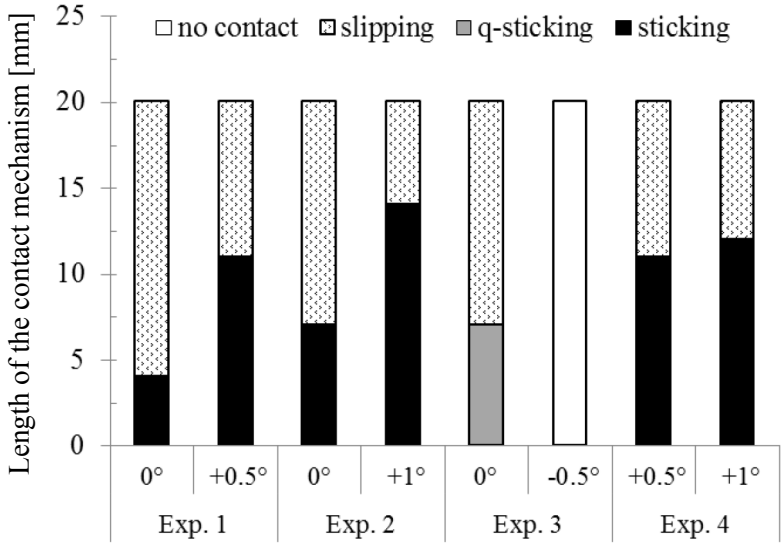

Fig. 6.38. Average length of the contact mechanism on the bearing channels.

7 Numerical analysis

Additional to the experimental investigation, the axial friction test and the multi-hole extrusion trials were numerically analyzed applying the software DEFORM™, which is based on the finite elements method (FEM). Moreover, the updated Lagrange approach was selected, which governs the response of the elements under plastic deformations. Thus, the mesh is modified during the deformation and remeshed in case of large distortions. This method leads to an approximate solution during each single step, allowing a continuous analysis during the whole process. The numerical simulation of the axial friction test provides more details about the internal plastic deformation and stress under severe and localized shearing. In addition, the influence of different friction boundary conditions inside the bearing channels can be simulated and compared with the experimental results. Especial emphasis is put on the product speed prediction through a multi-hole die applying the new friction model inside bearing channels with dissimilar inclination angles.

7.1 Numerical simulation of the axial friction tests

The new axial friction test was applied to investigate the friction behavior between the aluminum alloy EN AW-6060 and the hot working steel AISI H-13 (HRC 48-52) under high hydrostatic pressure. The new method allowed not only the determination of the friction stress under sticking conditions, but also the microstructural analysis of the friction boundary layer. Numerical simulations of the friction test can provide more information about the strain and strain rate distribution in the shear zone, which can be related with the observed microstructure. Since the measured force is related to the friction contact conditions, an accurate simulation of this process should introduce adequate friction assumptions. Sticking friction was expected between the sample and the hollow cylinder, however the friction conditions between the punches and the sample were unknown. Simulations of the axial friction tests D were used to find the adequate boundary conditions, which were validated with the intern grid pattern (Fig. 6.26). The axial friction test D were performed with samples extracted from extruded profiles of aluminum alloy AA6063 (Fig. 5.9), while the rest of the friction tests with cast and homogenized samples of EN AW-6060 (Fig. 5.2). Both alloys have similar thermo-mechanical properties, therefore they were simulated applying the same constitutive model obtained from hot compression tests (Table 6.1).

7.1.1 Axial friction test applying samples with internal grid pattern

21The simulation of the axial friction test applying specimens of aluminum alloy AA6063 with internal contrast material were performed at 400 °C and with a friction speed of 0.1 mm/s, 1 mm/s and 42 mm/s. In order to reduce the simulation time only a quarter model (Fig. 7.1a) was analyzed introducing planes of symmetry as showed in Fig. 7.1b,c. Additionally, three mesh windows were introduced with radius 2.5 mm, 3.7 mm and 4 mm (Fig. 7.1b) to define element sizes of 0.6 mm, 0.2 mm and 0.1 mm respectively (Fig. 7.1c). The simulations were carried out in two steps. First, the specimens were compressed with a speed of 0.005 mm/s until reaching an axial force of 400 N. During the upsetting the specimen reduces its height from 8.1 mm to 7.7 mm, and increases its diameter from 7.8 mm to 8 mm approximately. Posteriorly, the hollow cylinder was pulled down 5 mm at a constant speed, keeping constant the compression force (400 N).

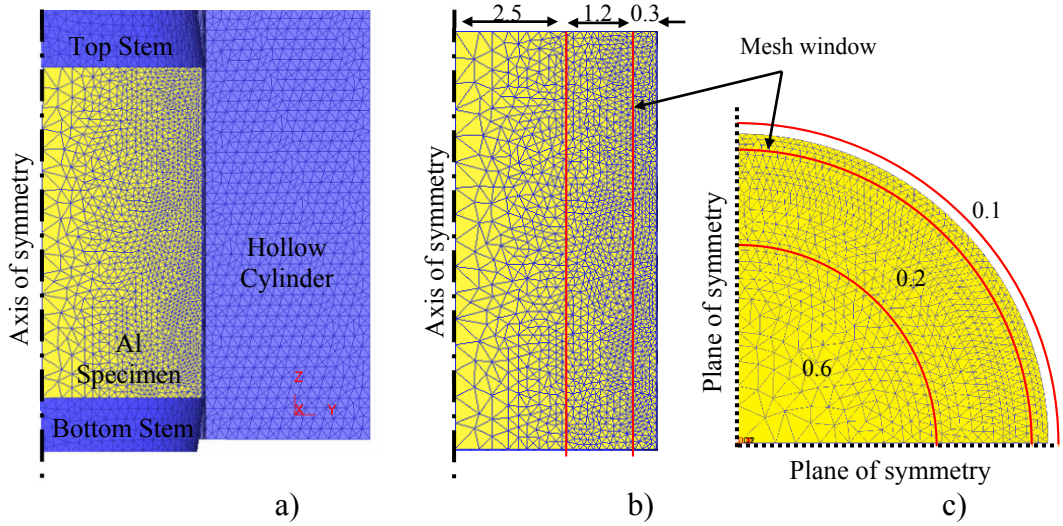

Fig. 7.1. Geometric model used in the axial friction test simulation. a) Components assembly, b) meshed specimen (mid-plane view) and c) meshed specimen (top view).

The specimens were simulated as a plastic material of EN AW-6060, due to the similar thermo-mechanical properties. Eq. 2.14 and Eq. 2.15 were applied to determine the relation between the flow stress, strain rate and temperature. The intern contrast material (grid pattern) was not simulated, because its yield stress is very similar to the sample material. Furthermore, the heat transfer coefficient between the specimen and the tools was set constant at 11 kW/m^{2}K. The Tresca friction model [WUT87] was selected to idealize the friction relation between the specimen and the tools. The grid pattern was set during the post-processing to compare with its deformation with the experimental results (Fig. 6.26). Multiple simulations were carried out

with different friction factors until finding similar deformation of the intern grid pattern (Fig. 6.26). During the compression the friction factors *m* were set at 0.3, 1 and 0.3 at the top, side and bottom of the specimen respectively. At the beginning of the compression is no contact between the specimen and the hollow cylinder, but posteriorly they contact during the upsetting with a friction factor of *m*=1. On the other hand, after the upsetting the specimen is in contact with the stems and the hollow cylinder. Hence, the friction factors were set at 0.3 at the top, 0.6 at the bottom, but sticking conditions at the lateral side. Since the hollow cylinder moves down with the sticking surface, a new contact surface is generated at the top side of the specimen which was simulated with a friction factor *m*=1. It is important to notice the particular difference between m=1 and "sticking" friction found in Deform 3D^{TM}. According to Tresca, the friction stress τ reaches the value of the shear flow stress *k* when *m*=1 (Eq. 2.22). Under this condition the surfaces in contact stick, producing a severe deformation of the subsurface of the softer material [VAL94, SAN14, SAN15]. Since the friction can not be higher than the shear stress, the friction factor should not be higher than 1. However, DEFORM 3D^{TM} allows using higher values of m to control the relative displacement between the nodes in contact. Thus, two surfaces can stick when "sticking" contact conditions or $m \geq 2$ are applied. In addition, the initial grid pattern (Fig. 5.9c) was introduced in the first step of the post-processing part as radial marks (grid flow net) to simulate its deformation during the compression and friction simulation (Fig. 7.2a). Fig. 7.2b depicts the mesh and the deformed grid pattern at the end of the compression simulation.

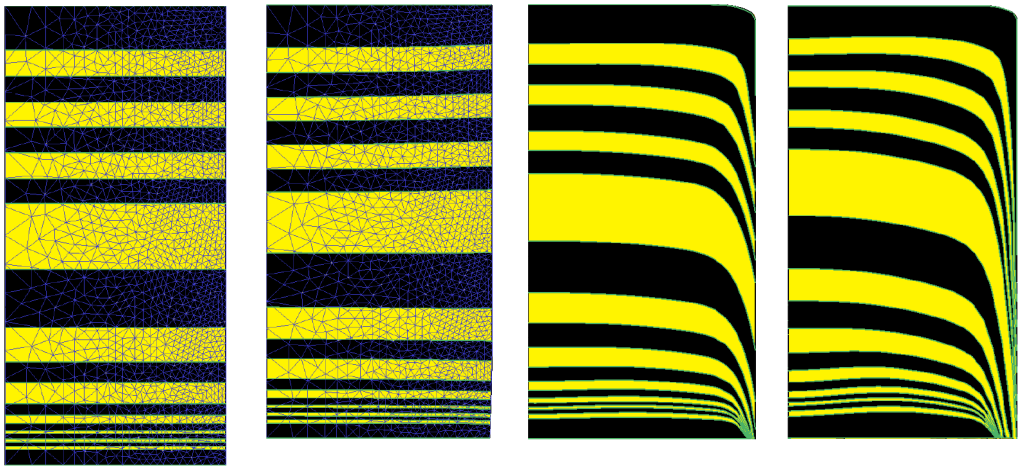

a) b) c) d)

Fig. 7.2. Friction test simulation with grid pattern at 400 °C and 0.1 mm/s. a) Initial state, b) compressed specimen, c) deformation at F_f= 1.6 mm and d) deformation at F_f= 4.5 mm.

A clear shear zone was observed at the friction subsurface during the test at 0.1 mm/s after a friction length of 1.6 mm (Fig. 7.2c) and 4.5 mm (Fig. 7.2d).

The numerical model provides additional information such as the thickness of the shear zone, the velocity and also the stress distribution at each step of the simulation (Fig. 7.3). The simulation results show the increase of the shear zone from 100 µm to 300 µm when the friction length (F_l) was changed from 1.6 mm (Fig. 7.3a) to 4.5 mm (Fig. 7.3d). Figs. 7.3b and 7.3e display the velocity vector at a friction length of 1.6 mm and 4.5 mm respectively. As expected the stick friction surface flows at 0.1 mm/s, however the surface with a friction factor m=1 flows with a lower speed (Fig. 7.3e). The velocity vectors indicate also a slow radial movement toward the friction surface at the top, but toward the center at the bottom side. Moreover, the two different friction conditions (sticking and m=1) influence the flow stress as showed in Figs. 7.3c and 7.3f generating a maximal value around 45 MPa.

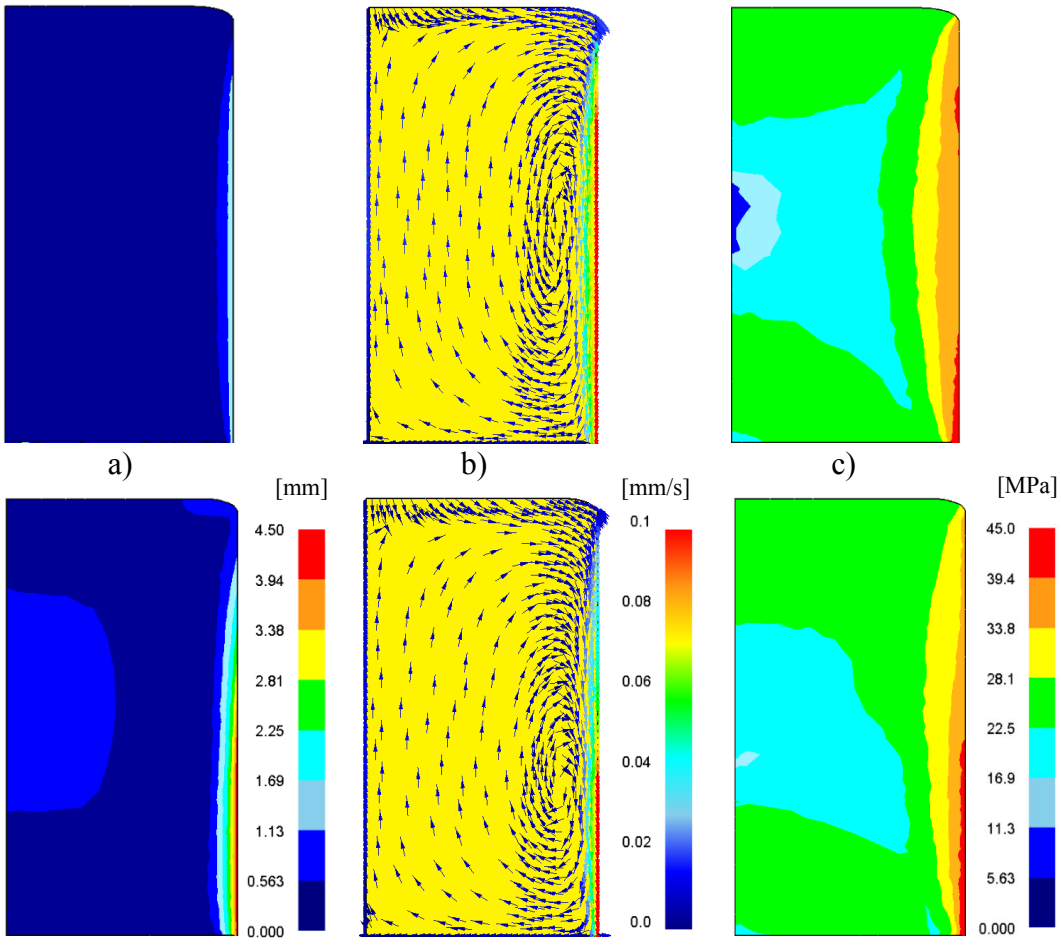

Fig. 7.3. Simulation results at 400 °C applying EN AW-6060. Displacement, velocity vector and effective stress at F_l =1.6 mm (a, b,c) and F_l = 4.5 (d, e, f) respectively.

Fig. 7.4 plots the simulated friction force at different friction speeds. Thus, the maximal friction force at 0.1 mm/s, 1 mm/s and 42 mm/s was 4.5 kN, 6.1 kN and 8.9 kN respectively.

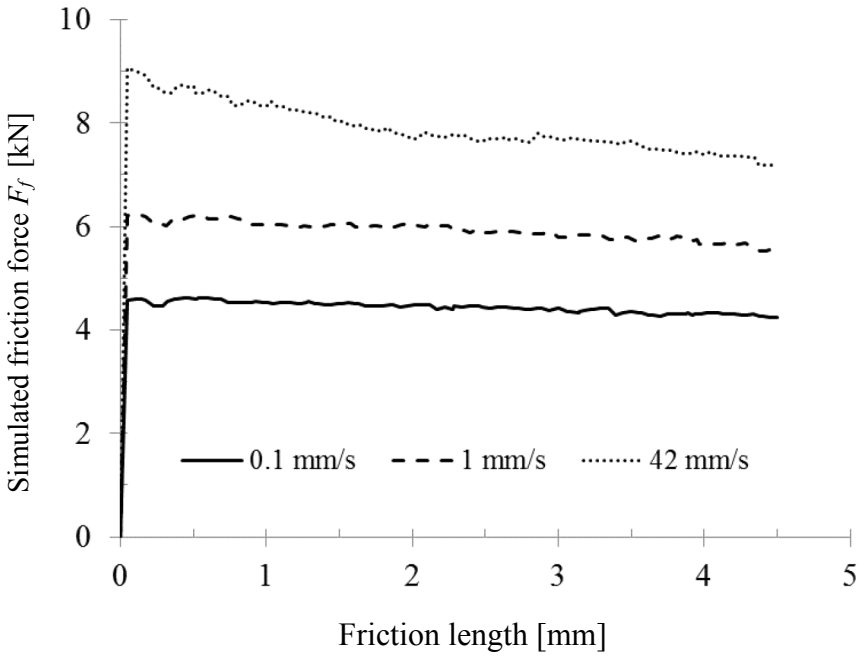

Fig. 7.4. Simulated friction force with contrast material at 400 °C (axial friction test D).

7.1.2 Axial friction test of aluminum alloy EN AW-6060

Similar to the numerical analysis performed in section 7.1.1, a quarter model and the same mesh windows were applied to simulate the friction test with specimens of aluminum alloy EN AW-6060. Furthermore, the specimen was simulated as plastic whereas the tools were considered as rigid solids. The material flow was simulated using the Zener-Hollomon relationship (Eq. 2.14 and 2.15), whose constants were calculated and resumed in the Table 6.1. Simulations at 400 °C were carried out as performed with specimens with internal grid pattern. During the first part of the simulation a specimen was compressed with a constant speed of 0.006 mm/s until the axial force reached almost 850 N, reducing thus the height from 10.5 mm to 9.9 mm, and increasing the diameter from 7.8 mm to 8 mm approximately. As used in the upsetting phase of specimens with internal grid pattern, the friction factors 0.3, 1 and 0.3 were applied at the top, side and bottom of the specimen. Posteriorly, the hollow cylinder was pulled down 3.5 mm with a constant speed, while the axial compression force (850 N) was kept constant. At the beginning of this simulation a friction factor of 0.3 at the top and 0.6 at the bottom side of the specimen were set, while “sticking” contact fixed the contact surface of the specimen and the hollow

cylinder. Additionally, *m*=2 was selected between both surfaces to generate sticking conditions at the new contact surface generated at the top side of the sample.

Fig. 7.5 depicts selected results at the mid-plane of the specimen (EN AW-6060) generated during the friction simulation at 400 °C, 0.1 mm/s and a friction length of 3.25 mm. The total displacement corroborates a maximal friction length of 3.25 mm of the initial stick friction surface, as well as a zone of high shearing in the friction subsurface (Fig. 7.5a).

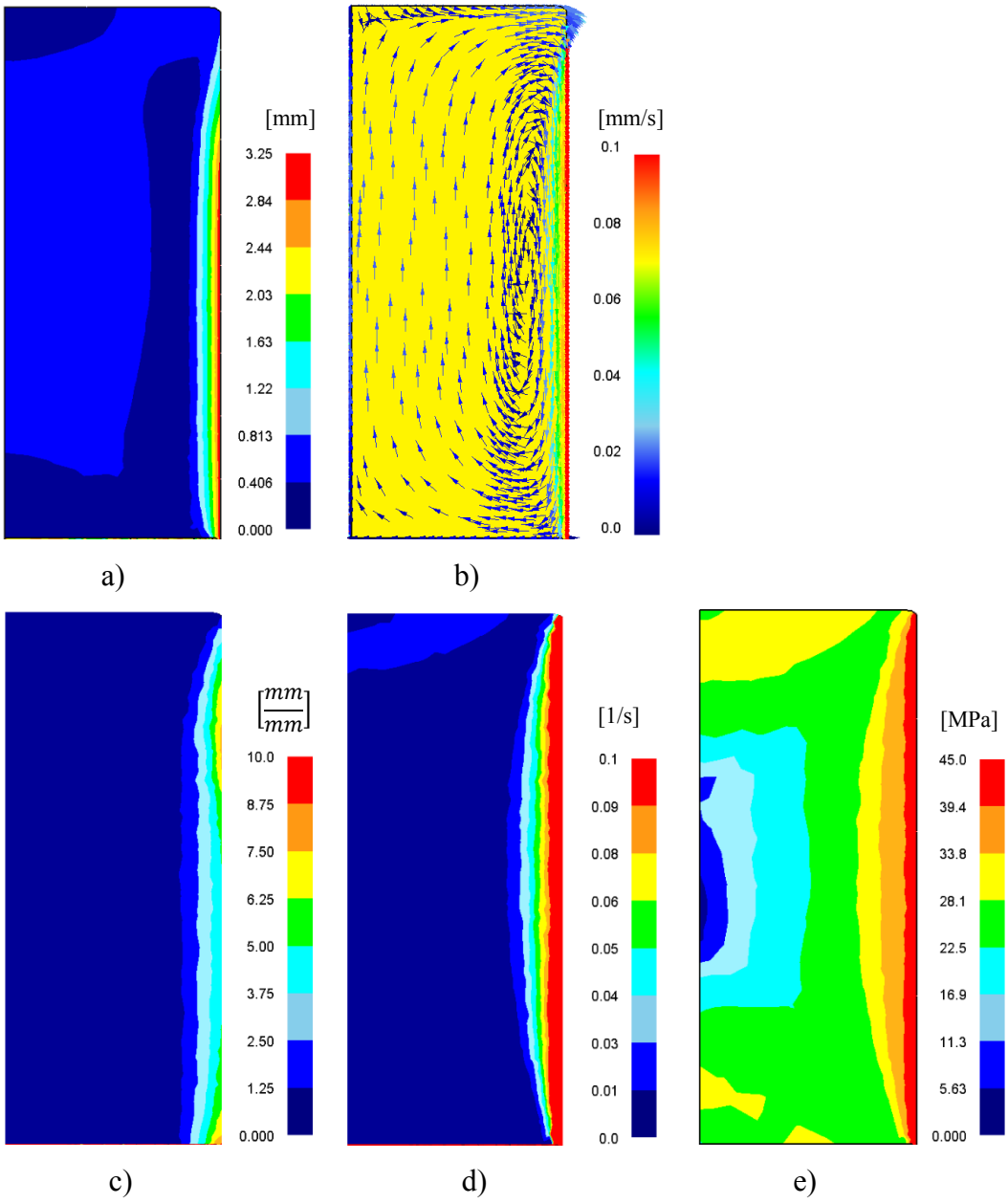

Fig. 7.5. Simulation results using EN AW-6060 at 400 °C, 0.1 mm/s and F_l =3.25 mm.
a) Displacement, b) velocity vectors, c) strain, d) strain rate and e) effective stress.

Moreover, the Fig. 7.5b shows a uniform speed of 0.1 mm/s of the whole friction surface, whom magnitude is quickly reduced to 0.03 mm/s in the first 350 µm toward the center of the specimen. On the other hand, a clear difference between the strain and strain rate distribution could be observed. Although the complete friction surface moved at the same velocity the strain was not uniform along the friction boundary layer, but lower at the top edge of the sample (Fig. 7.5c). At the middle (height of 5 mm) the strain was around 5 mm/mm, however at the top edge was progressively reducing until 0.5 mm/mm. The simulation results also showed a zone of around 280 µm behind the friction surface with a constant strain rate of 0.1 1/s (Fig. 7.5d) and an effective stress of 45 MPa approximately (Fig. 7.5e).

Simulations at 1 mm/s and 42 mm/s were also carried out at 400 °C. Fig. 7.6 illustrates the simulated evolution of the friction force at 0.1 mm/s, 1 mm/s and 42 mm/s.

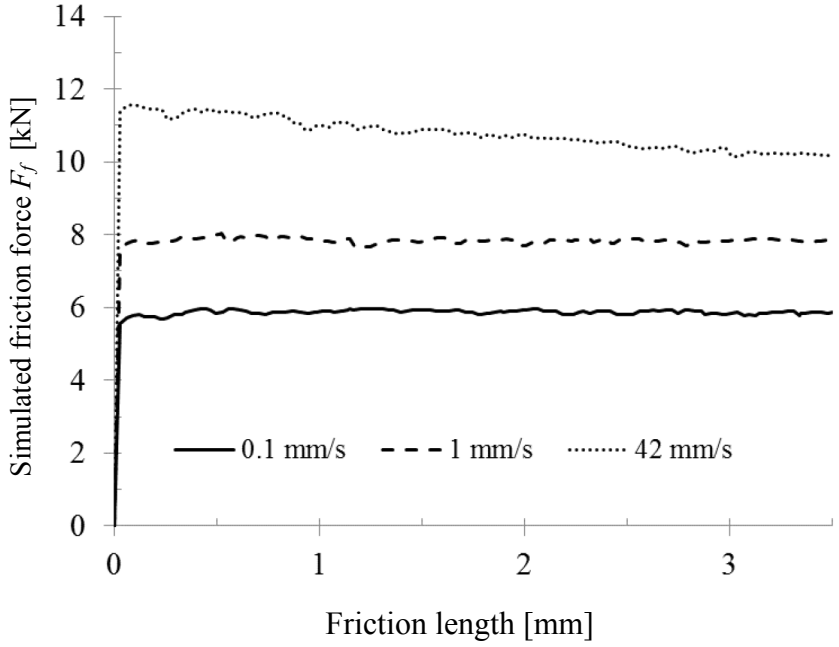

Fig. 7.6. Simulated friction force of EN AW-6060 at 400 °C (axial friction test C).

It was noticed that the predicted friction curves at 0.1 mm/s and 1 mm/s reached a maximal value of 5.7 kN and 7.7 kN respectively, and remained constant until the end of the simulation. Contrary to the friction force at low speed, the friction obtained at 42 mm/s was 11.5 kN at the beginning and gradually decreased until 10.1 kN at the end of the simulation.

7.2 Numerical analysis of the multi-hole extrusion process

Simulations of multi-hole extrusions applying long bearing channels with different inclination angles were conducted. The product velocity, extrusion force and temperature at the bearing channels were used to evaluate the simulations. The *Tresca* model was selected to define the friction behavior inside the bearing channels, assuming constant friction factors as well as a function derived from the new friction model (Eq.6.2).

7.2.1 Influence of different simulation criterion applied in the bearing channels

The FEM-based software DEFORM™ was used to simulate the extrusion experiments with multi-hole dies (Fig. 5.12 and 5.13). The geometric assembly consists of a billet set in a container, which is pushed by a ram at 4 mm/s towards the die (Fig. 7.7a). The tools (ram, container and die) were considered as rigid objects, while the workpiece (billet) as a plastic material (Fig. 7.7a). The Zener-Hollomon relationship (Eq. 2.14 and 2.15) was applied to model the flow stress of the aluminum alloy EN AW-6060, and whose constants are resumed in Table 6.1. The container and die temperature was set constant to 470 °C, and the ram to 450 °C. Besides, mesh windows were introduced to generate smaller elements inside the die during the discretization and remeshing.

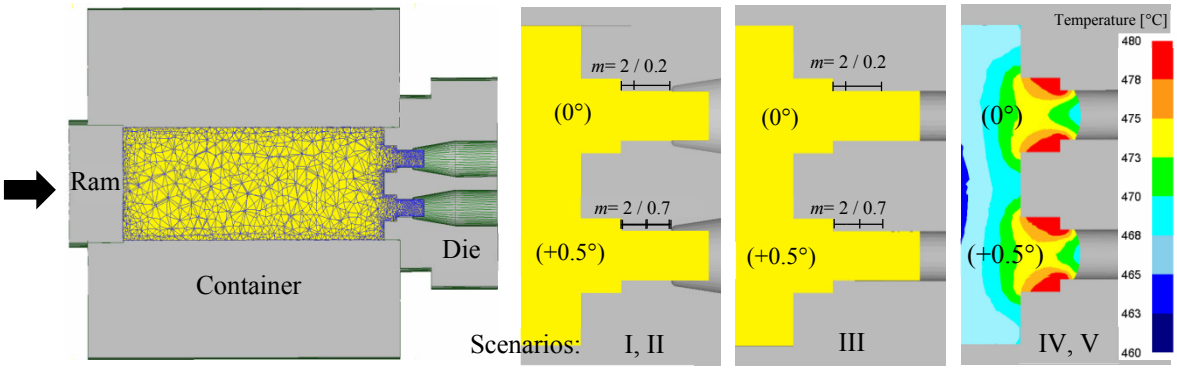

Fig. 7.7. Simulation conditions of experiment 1. a) Assembly model, b) filled die, c) filled die with elongated bearing channels and d) stage after simulation of the die filling.

Additionally, a friction factor m=2 was set at the container, face die and pockets to assure sticking contact. Due to the application of lubrication between ram and block the friction factor was m=0.8. A constant heat transfer coefficient of 7 kW/m^{2}K was applied between the billet and the tools [OCK12]. Before simulating all extrusion experiments, the experiment 1 (Fig. 5.13b) was evaluated for five different scenarios (Fig. 7.7). Thus, the influence of the initial domain

geometry, contact interaction and the friction conditions inside the bearing channels could be investigated (Table 7.2). In the **scenario I** the die was filled with the workpiece and the billet length reduced from 355 mm to 332 maintaining thus the same initial volume (Fig. 7.7b). The temperature in the whole billet was assumed at 460 °C. In addition, friction windows were used to define the length of the slipping and sticking areas inside the bearing channels as observed experimentally (Fig. 6.38). Hence, each bearing channel was divided into inlet and outlet area with different friction factors. Thus, m=2 was set at the inlet and m=0.2 and m=0.7 were set on the outlet of the parallel and +0.5° choked channels respectively (Fig. 7.7b). The **scenario II** has similar conditions as the scenario I, however the surfaces are forced to keep in contact with the bearing channels by means of activating the *non-separable* function (Table 7.2). In the **scenario III** the bearing channels were elongated but the same friction windows were used. In other words, the workpiece remains in contact with the long bearing channel, nevertheless the friction occurs only in the friction windows (Fig. 7.7c).

Table 7.2. Different scenarios applied to simulate the experiment 1.

Scenarios	Original Die	Filled Channels	Friction Windows	Non Separable	Elongated Channels	Simulated Upsetting	New Friction Model
I	✓	✓	✓				
II	✓	✓	✓	✓			
III		✓	✓	✓	✓		
IV			✓	✓	✓	✓	
V				✓	✓	✓	✓

Usually the extrusion process is simulated assuming filled dies because computing time can be saved as considered in the scenarios I, II and III. Nonetheless, in some cases ignoring the temperature development generated during the filling of the die could lead to inaccurate simulation results. For this reason, the **scenarios IV and V** start with a temperature distribution gained during a previews filling simulation (Fig. 77.d). Both scenarios differ in the friction condition inside the bearing channels. On one hand, in the **scenario IV** a constant friction factor m was assumed for each friction window as applied in the previews scenarios. On the other hand, in the **scenario V** the friction windows were omitted, instead of a function of the friction factor was applied on the whole bearing channels. Based on the Tresca friction model, the new function m was obtained dividing the estimated friction stress τ (Eq. 6.2) by the shear flow stress

(k) or friction at sticking conditions (τ_{st}). As shown in Eq. 7.1, the new relation $m(P,T)$ will be a function of the normal pressure P and the temperature T (Eq. 6.3).

$$m(P,T) = \frac{\tau}{k} \approx \frac{\tau}{\tau_{st}} = 1 + \frac{f-1}{1+\left(\frac{P}{\gamma}\right)^{\beta}} \qquad \text{(Eq. 7.1)}$$

Applying the Eq. 7.1 the friction factor was calculated for different temperatures (450 °C – 550 °C) and pressures (0 MPa – 80 MPa), and then integrated in the software as function data through a default friction function. Fig. 7.8 depicts the evolution of the friction factor as function of the normal pressure P and temperature T. The friction increases at higher pressure to posteriorly acquires a horizontal asymptotically tendency. Additionally, the temperature modifies the slope and the inflexion point of the curve. Hence, at higher temperature a lower normal pressure will be required to reaches the inflexion point of the curve.

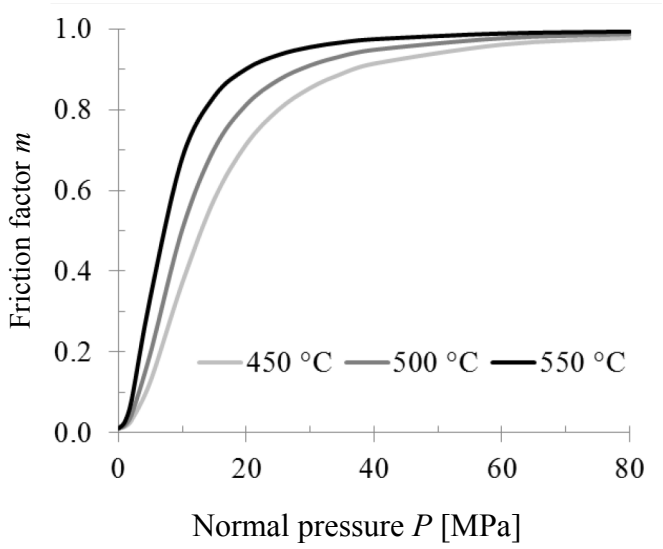

Fig. 7.8. Relation of the Tresca friction factor m as a function of the normal pressure P and temperature T.

Fig. 7.9 shows selected simulation results of the extrusion experiment 1, considering the five different scenarios (Table 7.2). Since the same friction conditions were applied in the container for all scenarios, a similar container force of 2.4 kN was obtained (Fig. 7.9a). Hence, the different boundary conditions only affect the simulated die force. The simulation results depict an average die force of 3.3 kN, 4.1 kN and 3.9 kN in the scenario I, II and III respectively. The die force was reduced to 3.6 kN including the heat generation during the die filling (scenario IV), however 2.9 kN was siulated applying the new friciton model (scenario V).

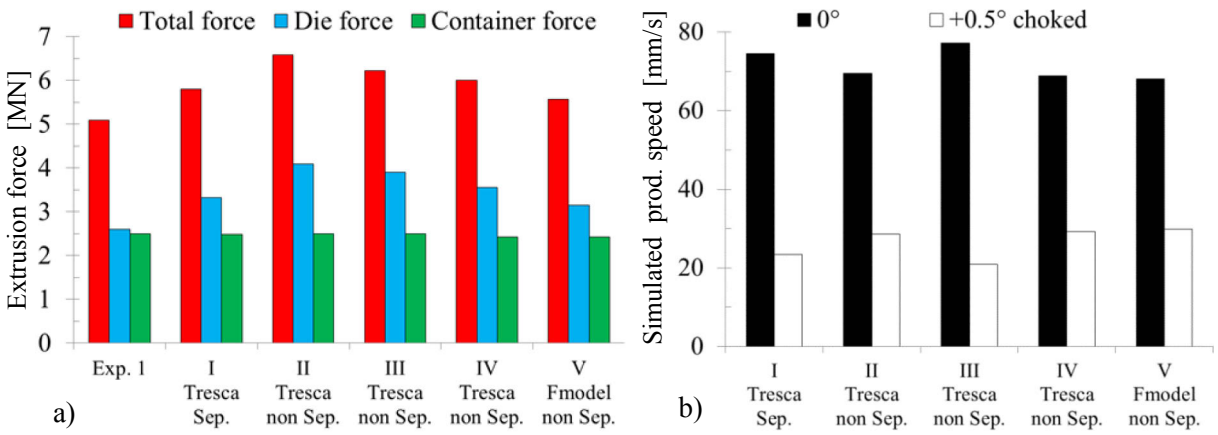

Fig. 7.9. Multi-hole extrusion simulation of the experiment 1, under different contact condition inside the bearing channels (scenarios). a) Die force and b) average product speed.

Different simulation conditions inside the bearing channels influenced not only the predicted die force, but also the product speed distribution. As depicted in Fig. 7.9b, the predicted speed ranges from 68 mm/s to 77 mm/s for parallel channels and from 21 mm/s to 30 mm/s for the +0.5° choked channels.

In addition, similar numerical results were observed inside the billet for all scenarios. Fig. 7.10 shows the simulated effective stress of the scenarios IV and V.

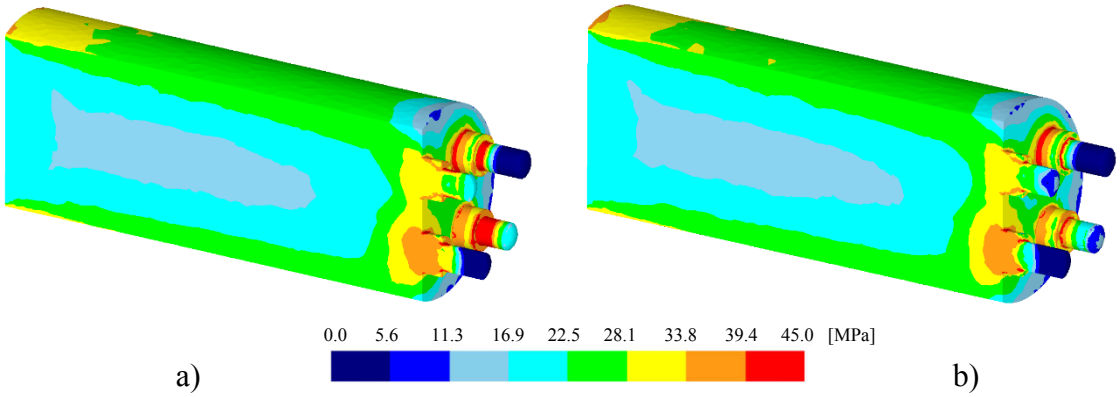

Fig. 7.10. 3D distribution of the simulated effective stress of the experiment 1 (stroke 2 mm), applying a) tresca friction model (IV) and b) the new friction model (V) in the bearing channel.

The billets were sectioned lengthwise at the middle of a parallel and +0.5° choked channel to observe the internal stress distribution. According to the results, 28 MPa was estimated in the shear zone, while 16 MPa in the center of the billet. Moreover, about 39 MPa and 33 MPa were calculated in the pockets where parallel and +0.5° choked channels respectively are located. On

the other hand, the stress distribution inside the bearing channels was highly influenced by the friction conditions analyzed in each scenario. Therefore more details of the simulation results present in this zone are displayed in the next section.

All extrusion trials were simulated applying the scenarios IV and V. The length of each contact area was taken from the experimental results (Fig. 6.38). Moreover, the friction factors were assumed as resumed in the Table 7.3. In the case of the scenario V, the same function $m(P,T)$ was applied in all bearing channels (Eq. 7.1).

Table 7.3. Tresca friction conditions applied in the bearing channels in all extrusion experiments.

Position	**Experiment 1**				**Experiment 2**				**Experiment 3**				**Experiment 4**			
	0°		***+0.5°***		***0°***		***+1°***		***0°***		***-0.5°***		***+0.5°***		***+1°***	
	L_c	m	L_c	m	L_c	m	L_c	m	L_c	m	L_c	m	L_c	m	L_c	m
Inlet	4	2	11	2	7	2	14	2	7	1	-	-	11	2	12	2
Outlet	16	0.2	9	0.7	13	0.3	6	0.9	13	0.3	-	-	9	0.7	8	0.7

L_c= Contact length, m= Friction factor.

7.2.2 Numerical results applying parallel and 0.5° choked bearing channels

Since the numerical results inside the billet were almost the same for all scenarios (Table 7.2), only the pockets and bearing channels were studied in details. Fig. 7.11 compares the effective stress, temperature and velocity inside the parallel and +0.5° choked channels of experiment 1, simulated for scenarios IV and V. Moreover, the length of the friction windows as well as the friction factors were added to the results obtained by the scenario IV. A high stress was observed in zones closed to surfaces fixed with friction factors m=2 (Fig. 7.1a,d). In addition, the same zones presented higher temperature than those analyzed with the scenario V (Fig. 7.11b,e). Similar product speed was predicted for both scenarios, delivering values 67±1 mm/s and 28±1 mm/s in the parallel and +0.5° choked channels respectively (Fig. 7.12c,f).

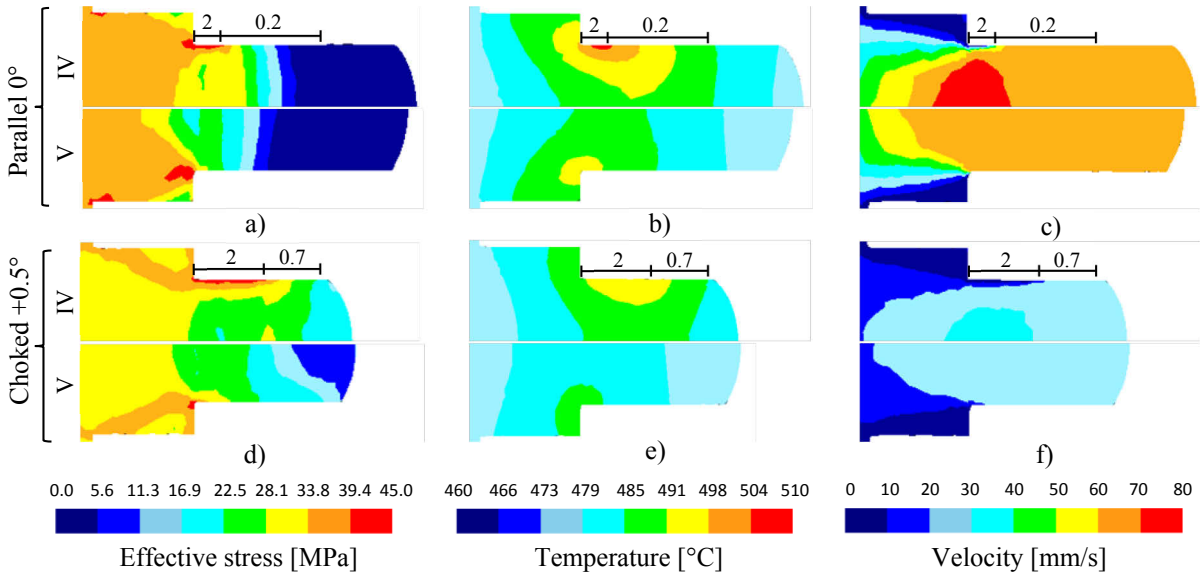

Fig. 7.11. Simulation results of the experiment 1, applying scenarios IV and V. a,d) Stress, b,e) velocity and c,f) temperature in parallel channels and +0.5° choked channels respectively.

7.2.3 Numerical results applying parallel and 1° choked bearing channels

The simulations of the experiment 2 (Fig. 7.12) showed comparable results to the experiment 1 (Fig. 7.12). Only small changes in the stress, temperature and velocity were observed inside the bearing channels, caused by different friction contact interactions. Thus, the simulated product speed for both scenarios was 71±1 mm/s in the parallel channels, whereas 27±1 mm/s in the +0.1° choked channels (Fig. 7.12c,f).

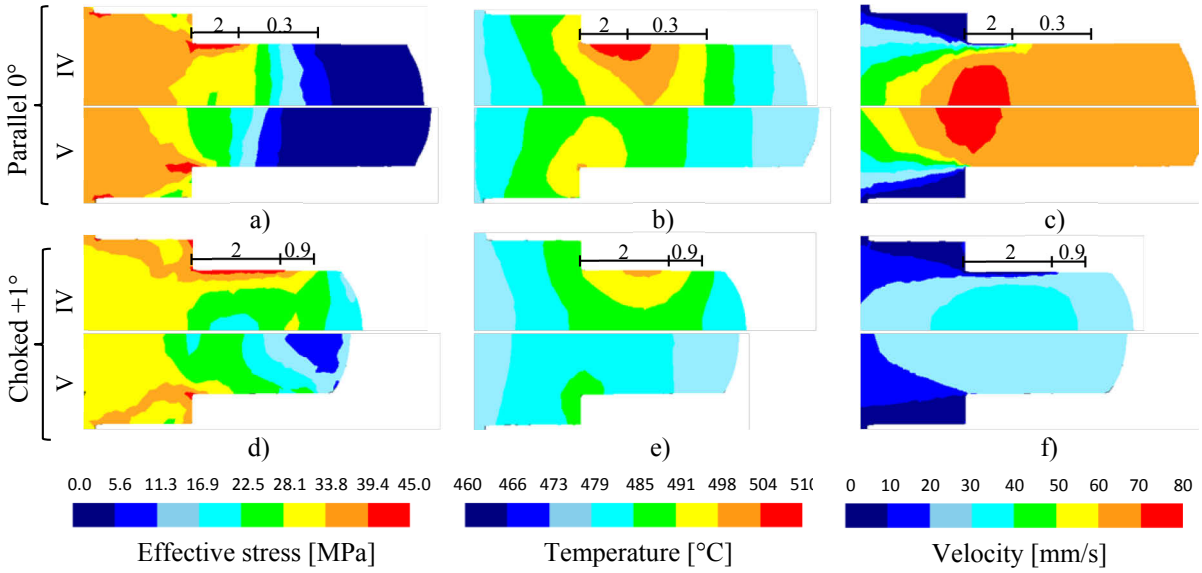

Fig. 7.12. Simulation results of the experiment 2, applying scenarios IV and V. a,d) Stress, b,e) velocity and c,f) temperature in parallel channels and +1° choked channels respectively.

7.2.4 Numerical results applying parallel and 0.5° relief bearing channels

The simulation results of the experiment 3 are depicted in Fig. 7.13. In order to simulate the relief channels, no contact was established between the workpiece and the 20 mm of bearing land as was observed in the experimental results (Fig. 6.34). As observed in the experimental results (Fig. 6.37d and Fig. 6.38) sticking contact was omitted in the parallel channels, and therefore the friction factor was m=1 (Fig. 7.13a,b,c). Similar stress (Fig. 7.13a,d) and temperature distribution (Fig. 7.13b,e) were achieved applying the scenarios IV and V, however relevant differences on the product speed were observed. Applying the scenario IV the product speeds were about 31 mm/s and 67 mm/s in parallel and relief channels respectively. Nevertheless, considering the scenario V the speed in parallel channels was 25 % higher (41 mm/s), while 15 % lower (57 mm/s) in the relief channel.

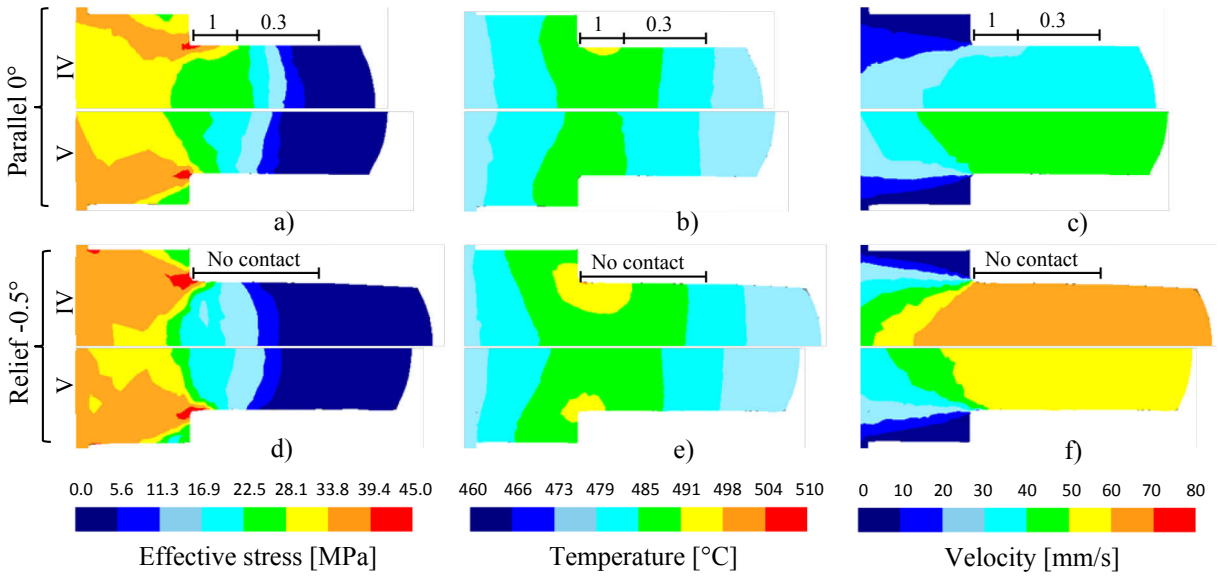

Fig. 7.13. Simulation results of the experiment 3, applying scenarios IV and V. a,d) Stress, b,e) velocity and c,f) temperature in parallel channels and -0.5° relief channels respectively.

7.2.5 Numerical results applying 0.5° and 1° choked bearing channels

The experiment 4 was also simulated applying the scenarios IV and V and the numerical results are resumed in Fig. 7.14. The geometrical difference between the choked channels was 0.5° that represents an alteration of 100 % of the inclination angle. Although this significant variation, similar simulated results were detected in both channels. For the scenario IV, the same friction factors were assumed in both channels and the single difference was the length of the friction windows (Table 7.3). A clear variation of the stress and temperature in the friction boundary

layer was noticed considering the scenarios IV and V. Applying sticking conditions (m=2) the stress increased until 45 MPa, however using the new function (scenario V) the stress varied between 22 MPa and 39 MPa (Fig. 7.14 a,d). Additionally, the maximal temperature in the scenario IV was 10 °C higher than in the scenario V (Fig. 7.14 b,e). Furthermore, the predicted product speed for both scenarios was 51±1 and mm/s 47±1 mm/s in the +0.5° and +1° choked channels respectively (Fig. 7.14c,f).

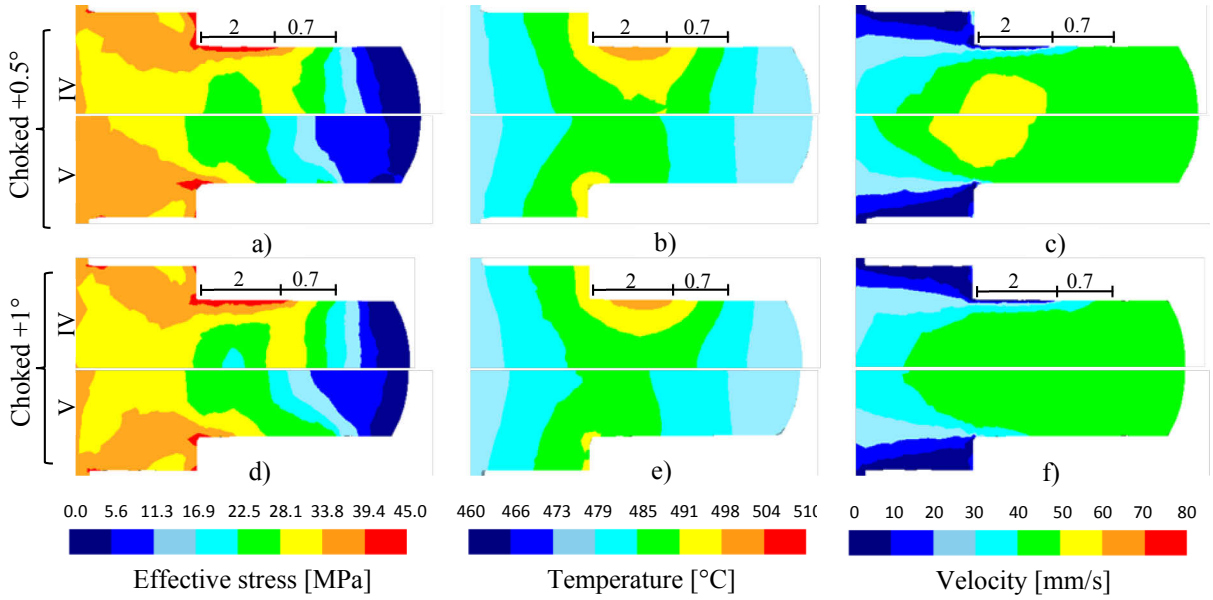

Fig. 7.14. Simulation results of the experiment 4, applying scenarios IV and V. a,d) Stress, b,e) velocity and c,f) temperature in +0.5° and +1° choked channels respectively.

8 Discussion

The experimental and numerical results presented in the two previous chapters are discussed and evaluated in the following. First, the results of the hot compression tests, friction experiments and hot extrusion of the aluminum alloy EW AW-6060 are discussed. As explained in section 2.3.5, there are several methods to measure the friction, however only few of them allow to realize an accurate friction investigation under extrusion conditions. Therefore, the friction experiments were performed with two different methods. The influence of the low normal pressure was investigated by means of the tribo-torsion-test. Moreover, the friction behavior under high normal pressure could be investigated applying the new developed axial friction test, which is explained in detail in chapter 4. Four series of friction experiments (test A, B, C and D) were performed with the axial friction tests as explained in Table 5.1. In the test A the influence of the normal stress, speed and temperature, as well as the mechanical and chemical interactions at the beginning of the test was investigated. The test B evaluated the influence of the punch configuration on the friction force at 300 °C and 42 mm/s. The test C determined the sticking friction at different temperatures and speeds. Finally, the test D was performed applying specimens with internal grid pattern in order to reveal the real plastic deformation at the friction boundary layer. Combining, the results acquired with the tribo-torsion-test and the axial friction test C a new friction model for extrusion process was developed.

In addition, the numerical simulations about the axial friction test and the multi-hole extrusions depicted in chapter 7 are also discussed.

8.1 Hot compression test

The appropriate determination of the flow stress at different temperatures, strain and strain rate is very important to simulate accurately the extrusion force and material flow during the extrusion process. Additionally, the shear stress and thus the flow stress is closed related to the friction during extrusion. The torsion test and compression test are commonly applied to study the flow stress in extrusion. The torsion test allows large strains (0-25 mm/mm) [PET03], however important radial gradients of strain and strain rate in the specimen can not be avoid [MCQ02, MIS06]. Moreover, in the compression test the deformation is more uniform, but only a relatively low strain can be achieved (0-1.5 mm/mm) [MON00]. According to the literature [SHE99], in hot deformation of aluminum alloys the strain has a minor influence on the flow

stress. Hence, the flow stress determined through hot compression test is assumed to be constant at larger deformations or strains. Hot compression tests of the aluminum alloy EN AW-6060 were carried out until 0.5 mm/mm of strain to investigate the flow stress at different temperatures (300 °C-500 °C) and strain rates (0.0005 1/s – 10 1/s). During plastic deformation heat is generated, which can change the local temperature. However the compression tests were performed keeping a constant temperature. Additionally, strain rate was set constant during each test.

8.1.1 Influence of the temperature, strain and strain rate on the flow stress of EN AW-6060

According to the experimental results depicted in Fig. 6.2, the true stress measured during the hot compression test depends on the temperature, strain and strain rate. As it was expected for aluminum alloys, the true stress increased at higher strain rates and lower temperatures [ZEN44]. The stress increased rapidly at the beginning of the strain until a critical value. Afterward, it grow up or remained constant depending on the temperature and strain rate. During plastic deformation the stored energy is increased due to multiplication and interaction of dislocations. As a result a higher stress has to be applied to continue the deformation (strain hardening). This mechanism explains the initial growing of the stress observed in all the curves. On the other hand, the dislocation movements are facilitated in materials with high stacking fault (HSF) energy such as aluminum alloys. Thus, the dislocations are rearranged in a lower energy configuration and eventually annihilated, process known as dynamic recovery (DRV) [HUM04]. Hence, the flow stress is increased by strain hardening and decreased by DRV. Since, both processes occur simultaneously their effect competes to define the flow stress as observed in Fig. 6.2. At 300 °C the flow stress increased due to the strain hardening effect until 0.05 mm/mm approximately. At this strain the stored energy was enough to activate the DRV, which decelerated the growing flow stress. However, the flow stress continued increasing for strain rates from 0.01 1/s to 10 1/s, because the strain hardening overcome the effect of the DRV (Fig. 6.2a). A more rapid deformation reduces the effect of the DRV because there is less time for annihilation of dislocations. In other words, a faster generation of dislocations occurs at higher strain rates, producing a higher stress, as observed at 300 °C and 350 °C (Fig. 6.2a,b).
At temperatures higher than 450 °C (Fig. 6.2d, e) the strain seems to have no more influence on the flow stress, which remained almost constant after the critical strain value. For materials with high stacking fault (HSF) energy the mobility and annihilation of dislocations is accelerated at

higher temperatures. For that reason, the effect of the DRV balance the strain hardening generating a more stable stress at 450 °C and 500 °C (Fig. 6.2d,e).

8.1.2 Constitutive model of EN AW-6060

The constitutive model of the aluminum alloy EN AW-6060 is required to estimate the flow stress at any deformation condition of temperature, strain and strain rate. The stress-strain curves obtained by means of hot compression tests provided the flow stress in a wide range of temperature (300 °C – 500 °C), strain rate (0.0005 1/s – 10 1/s) and until 0.5 mm/mm of strain (Fig. 6.2). The deformation could have been carried out until 2 mm/mm of strain, but after 0.5 mm/mm the measurements can be influenced by the barrel effect of the specimen. According to the results showed in Fig. 6.2, the strain has less influence on the flow stress at temperatures higher than 450 °C. Assuming constant flow stress at strains higher than 0.5 mm/mm, the strain effect can be neglected in the material model. This consideration is often assumed to model the material behavior of aluminum alloy for hot extrusion [SHE99]. In this case, the Zener-Hollomon relationship (Eq. 2.14) and the Eq. 2.15 can be applied to build the constitutive model. Thus, the proportionality between the temperature-compensated strain rate Z (Zener-Hollomon parameter) and the flow stress $\bar{\sigma}$ was confirmed (Fig. 6.5a), where Z increases at a higher strain rate and lower temperature. After the material constants were calculated (Table 6.1) the experimental and modeled flow stress were compared (Fig. 6.5b), observing good agreement at ε =0.5 mm/mm, especially at higher temperatures. Since, the selected material model $\bar{\sigma}(\dot{\varepsilon},T)$ does not include the influence of the strain on the flow stress calculation, strain hardening effect can not be predicted. Hence, inaccurate flow stress values could be obtained at temperatures lower than 350 °C and strains higher than 0.5 mm/mm (Fig. 6.2a,b).

8.1.3 Microstructure and hardness after hot compression test

After each hot compression experiment the specimen was immediately quenched in water to avoid possible changes of the microstructure subsequently to the deformation. Thus, static recovery (SRV), static recrystallization (SRX) and static grain growth (GG) can be neglected. Fig. 6.7 depicts the micrographs of the specimens tested at different temperatures (300 °C, 400 °C and 500 °C) and strain rates (0.1 1/s and 10 1/s). Significant changes of the microstructure was not generated, because of the low strain (0.5 mm/mm). The original grain boundaries were observed and thus radial stretched grains were detected. During the test the specimen's height was reduced and simultaneously the diameter increased. Therefore, the grains

present at the initial state (Fig. 6.1b) were stretched radially and simultaneously forced to reduce the height. Dendritic structure and the original grain boundaries could be observed at 300 °C (Fig. 6.6a). The increasing flow stress observed in Fig. 6.2a suggests the strain hardening as the main mechanism of deformation at 300 °C. A similar microstructure was observed at 400 °C. However, the slight serrated appearance of the grain boundaries (Fig. 6.6c) and the more stables stress-strain curves (Fig. 6.2c) suggest the beginning of the grain fragmentation and DRV. At 500 °C, the dendritic grain structure was not identified, and the serrated grain boundaries as well as the sub grains were easier distinguished (Fig. 6.6e). At high temperature the dislocation movements are facilitated particularly for materials with high stacking fault energy. Hence, the dislocations are arranged themselves in walls forming subgrains as observed in Fig. 6.6e. The serrated grain boundaries as well as the sub grains at 500 °C indicate that dynamic recovery (DRV) overcome the strain hardening as explained in section 8.1.1. Similar results obtained by means of hot torsion test are found in the literature [PET03]. According to this investigation, the subgrains and the serrated appearance should be observed until a strain of about 1 mm/mm. In addition, Vicker hardness tests were performed, which results are resumed in Fig. 6.7. The hardness measurements can give additional information about the mechanical properties, where larger hardness values are related to a higher strength. The material resistance is also associated with its previous thermo-mechanical history. Thus, the obtained results are not only influenced by the mechanisms of deformation such as strain hardening and dynamic recovery explained above, but also by the eventual occurrence of solid solution strengthening during quenching. When the working temperature approaches or exceeds the solvus temperature (Fig. 2.5), the second phases (Mg_2Si and Si) dissolve into the matrix forming a solid solution. During a rapid cooling, the solid atoms remain into the matrix restricting the dislocation movements, and therefore increasing the strength and hardness at room temperature. Considering the stoichiometric analysis of the applied aluminum alloy (Mg 0.5%), it contains an excess of 0.789 wt. % of Mg_2Si and 0.19 wt. % Si. For this content of magnesium silicide the solvus temperature is around 430 °C approximately (Fig. 2.5).

The experimental results (Fig. 2.5) depict a nonlinear hardness behavior ad different temperature and strain rate. At low temperatures the strain rate had more influence on the hardness than at higher temperatures. Increasing the strain rate from 0.0005 1/s to 10 1/s, the hardness was increased in 30 % and 34 % at 300 °C and 350 °C respectively. However, at 450 °C and 500 °C only a hardness rising of 6 % and 4% was observed respectively. This behavior is due to the

significant strain hardening present at 300 °C and 350 °C, also observed in the stress-strain curves (Fig. 6.2a, b). At higher temperatures dislocations are easier annihilated by means of DRV reducing the hardening effect as found comparing the hardness results at 300 °C and 350 °C.

Since the strain hardening effect produced by the high dislocation density is reduced at higher temperatures, a lower strength and thus hardness would be expected at higher temperatures. Contrary, the experimental results showed greater hardness values at 400 °C, 450 °C and 500 °C (Fig. 6.8). The hardness improvement obtained from 400 °C was due to the solid solution strengthening mentioned above. Similar results have been reported in the literature [GAR04]. Moreover, a general hardness increase from 400 °C to 500 °C was also noticed. Increasing the work temperature the atomic diffusion in the crystalline lattice is facilitated producing a more significant strengthening effect after quenching.

8.2 Tribo-torsion-test

The slipping friction under extrusion conditions is a very complicated phenomena, because many variables such as temperature, speed, normal pressure, surface condition interact simultaneously and change also with the time. In the bearing channel, the workpiece (softer material) slides at high temperature against a hard surface generating slip-stick contact (Fig. 2.8b). The contact occurs between the asperities of both surfaces, reducing thus the real contact area [POP10, WUT87]. The asperities can slide or stick according to the adhesion and mechanical interactions. Due to the low flow stress at high temperature, asperities of the softer material deform plastically at low normal pressure. Moreover, the contact asperities form weld junctions due to the high adhesion force, which are continuously built and sheared [BOW50]. During this process the initial surface topography alters randomly and thus the real contact area, making more difficult its prediction [HOR14]. Eventually, the die land is contaminated creating and intermittent thin layer, which interact with the extrudate during the extrusion [ROO12]. The die contamination has been observed in different friction experiments such as pin on disc (Fig. 2.11a) [MAH84], block on disc (Fig. 2.11d) [PEL07] and low pressure friction test (Fig. 2.13b) [SUN12]. Additionally, trials with the ball on disc test have shown the significant wear track created on the specimen a high temperature (Fig. 2.11b) [WAN10].

In general, the friction stress can be measured dividing the friction force by the contact area, however the unknown real contact area leads to wrong friction estimations. It seems to be an

easy task, but the unknown real contact area makes it a big challenge. Even, when the test method can reproduce similar friction conditions, the friction stress can be only calculated applying the nominal or apparent contact area. Since, the apparent contact area is higher than the real contact area, in theory the estimated friction stress will be lower than the real one. On the other hand, the measured friction force can be altered due to unwanted contact of metallic parts that generate extra friction. Thus, the estimated stress based on experimental measurements has a certain inaccuracy related to the configuration and method applied.

In order to investigate the slipping friction between the aluminum alloy EN AW-6060 and the hot working steel (AISI H13), experiments were carried out with the tribo-torsion-test (Fig. 2.12). The investigation was performed at the Institute of Virtual Production IVP of the Swiss Federal Institute of Technology, ETH Zurich, where this method was developed [KAR10, HOR12]. The mean objective of this study consisted to reproduce similar slipping conditions present in the bearing channel during hot extrusion. Thus, the trials were done at high temperature (400 °C and 500 °C) and also applying a low normal pressure varied from 10 MPa to 40 MPa. Additionally, the slipping speed was set at 2.5 mm/s and 10 mm/s, which was the maximal available speed.

Selected curves of the torque measured during the friction tests are presented in Fig. 6.8. The curves were characterized by permanent oscillations also reported in the literature [HOR12, BEC14]. The periodic oscillations of the curves were observed during the whole test and under different conditions of temperature, speed and pressure. Therefore, this variation could be related to the rotation movement of the assembly. Between the external diameter of the punch and the inner diameter of the outer tool is a gap of about 10 µm to 25 µm at room temperature (Fig. 2.12a). Additionally, there is a very fine tolerance (H7) between the punch and the inner tool. This separations are very important to avoid the contact between the tools, while the test is carried out. A small buckling effect, an unexpected thermal dilatation or non-concentric position of the tools could cause the contact between them and generate an additional torque (friction). Considering the maximal and minimal values at a time of 200 s an averaged torque was calculated for each curve. Moreover, the Eq. 2.17 was applied to calculate the average friction stress presented in Fig. 6.9. According to the experimental results the friction increased proportionally with the pressure in the range 10 MPa to 40 MPa. The friction increased about 130 % from 10.3 MPa to 42.5 MPa when the pressure was varied from 10 MPa to 40 MPa at 400 °C and 10 mm/s. The proportionality between the pressure and the friction was proposed

by Coulomb (Eq. 2.18). It is widely accepted that the real contact area grows at a higher normal force (pressure), because more asperities comes in contact [WUT87]. A higher number of asperities in contact will be sheared during the movement, resulting in a higher friction. At 500 °C the friction increased 12 % less than at 400 °C, at the same speed and pressure range. At a higher temperature the asperities have a lower flow stress, and therefore a lower pressure is required to compress them. As a result the pressure has a more influence on the friction at low temperature than at higher temperatures.

Considering the shearing of the junctions during the friction and the strain rate-dependence observed in Fig. 6.2, a higher friction should be expected when the speed is increased. At low pressure this effect could not been noticed due to the low real contact area. However, a more significant effect of the speed on the friction should be observed at high pressure. The experimental results showed low influence of the speed on the friction under low pressure. Thus, the friction raised about 7 % changing the speed from 2.5 mm/s to 10 mm/s, but the effect produced by the speed was not increased at higher pressures. Limited information can be found about the speed influence on the friction at high temperature. Most of the studies are focused on the pressure, surface condition, temperature and time. Experiments carried out with the same method (tribo-torsion-test) showed also the low influence of the speed [BEC14]. Coulomb was more radical and proposed that the slipping friction is independent to the speed [DOW97]. These assumptions can not be established to all boundary conditions, because his investigations were carried out in a limited range of low pressure and temperature. In extrusion conditions the high temperature and pressure dramatically change the boundary conditions. Another aspect could explain the low influence of the speed in the tribo-torsion-test and all rotational friction tests. When two surfaces experiment large relative rotation both suffer a milling process that generates detached particles moving and rotating in between the friction planes. Hence, a combination of shearing and milling take place in the intermediate layer. Due to the presence of many detached particles in the slipping friction contact [ROO12], the shear mechanism can be reduced and thus the effect of the speed on the friction stress.

The microstructure of the friction specimens could not be analyzed, because they could not be extracted from the friction assembly. The specimen is confined between the outer and inner tools (Fig. 2.12a) and additionally fixed with three screws to avoid rotation. After each friction trial, the tools and specimen seem to be welded. To extract the specimen, the mentioned assembly is etched, modifying thus the friction surface and the boundary layer.

8.3 Axial friction test A

It is accepted that under very high pressure the friction stress is equivalent to the shear flow stress as suggested by Tresca [AKE85, WUT87]. Under high normal force more asperities become in contact, and the real contact area is similar to the apparent area (Fig. 2.8c). The total junction force is higher than the local shear flow stress of the softer material, and both surfaces suffer stick while a severe shearing occurs in the subsurface layers. Local deformation of the microstructure under the friction surface has been observed in specimens subjected to friction tests [DAU73, DAU80, MEN08]. The strong deformation occurs after a prolonged friction time at high normal pressure. According to the experimental results, it can be assumed that the friction is high enough to deform the subsurface. However the results can not demonstrate 100 % of sticking friction. Friction under sticking conditions has been also observed inside the extrusion container and also in the inlet zone of choked bearing channels [VAL94, ABT96].

The boundary conditions needed to generate sticking conditions are difficult to determine. There are sophisticated testing devices available to study the friction at high pressure [HOR12, OCK12, WID12], however the reproduction of sticking friction and the posterior evaluation of the friction boundary layer has not been demonstrated.

The new axial friction test (Fig. 4.3) was developed to determine pressure required to generate sticking friction at different temperatures and speeds. Additionally, this method was defined to allow a rapid extraction of the specimen for subsequent microstructure analysis.

The axial friction test A involve the first friction experiments carried out with this new method. Therefore a widely range of temperature (300 °C – 500 °C), pressure and speed (0.1 mm/s – 42 mm/s) was evaluated. As was explained in section 5.5.2, each specimen must be plastically compressed inside the hollow cylinder (Fig. 4.1) to generate the initial friction contact. A very slow compression velocity was applied (0.005 mm/s) to reduce the strain hardening during the upsetting. The initial axial compression force was determined applying Eq. 4.3 and the flow stress measured by means of the hot compression tests at a strain of 0.5 mm/mm (Fig. 6.2). Thus, the specimens were complete set up at the different hydrostatic and thermic conditions evaluated in this work.

8.3.1 Influence of the pressure, temperature and speed on the friction

Selected friction experiments performed with the new axial friction test are depicted in Fig. 6.10. The curves show the evolution of the friction force F_f during the stroke of the hollow cylinder

(Fig. 4.1). Since the contact only occurs between the specimen and the hollow cylinder, the friction force is the force measured during the axial relative movement between the aluminum specimen and the hollow cylinder. In order to obtain reliable friction measurements, additional contact areas such as between punch and hollow cylinder have to be avoided. A gap of 5 µm between both parts was applied to reduce the steel-steel contact, and also avoid the flow of aluminum. Friction tests at different temperatures and high pressure were performed without aluminum specimen to measure the intrinsic friction of the device, showing low friction values (0.01 kN to 0.02 kN).

The friction curves are characterized by a rapid increase of the friction force at the beginning of the stroke (part I, Fig. 4.9). The high stroke values and the similar slope at different speeds suggest that the forces and deformations of the part I correspond to the elastic deformation of the device. At the beginning of the stroke the friction surfaces remain stick until the applied force is higher than the friction resistance and a relative movement take place. Thus, the first part of the curve is not the result of friction behavior, but the elastic response of the device during the static friction. When the applied force overcome the static friction resistance F_{fa} (Fig. 6.10a), begins the plastic response of the friction junction (Part II, Fig. 4.9). At 300 °C the friction force increased with the stroke particularly at higher speeds, however at 500 °C the stroke did not influence the dynamic friction response. Considering that the friction stress at sticking conditions is equivalent to the shear flow stress, the variation of the second part of the curve should be related to the microstructure evolution at different deformation conditions. Based on the experimental results obtained by means of hot compression tests (Fig. 6.2), the growing friction values at 300 °C could be related to the strain hardening effect at low temperature. Moreover, the DRV at 500 °C would explain the low influence of the stroke (strain) on the friction at high temperature. The friction increase at 300 °C and 400 °C was kept with a constant slope until approximately 3 mm of stroke. This large and constant growing tendency was influenced by the punch configuration, as was explained in section 6.5. Since the evolution of the friction curve was altered by external causes, only the initial value of the plastic deformation (F_{fa}) was considered to the friction analysis. Thus, the F_{fa} was divided by the apparent contact area (geometric area) after upsetting (Eq. 4.2) to calculate the friction stress. Fig. 6.11 presents the influence of the normalized normal stress σ_n' or normalized pressure on the friction at different temperatures and speeds. According to the results, a normalized normal stress of 2.8 was necessary to achieve a stable friction value at 300 °C. In other words, the

pressure applied against the friction surface was 180 % higher than the flow stress. It means that under this hydrostatic condition the apparent and real contact area were very similar and an additional compression will not increase the friction. On the other hand, the friction was slight influenced after a normalized normal stress of 1 at 400 °C and 500 °C. The experimental results showed that sticking conditions can be reproduced with a normalized normal stress of 3.

The friction under high pressure is dominated by the shearing of the real contact area. The results showed, lower friction stress at higher temperatures, due to the reduction of the flow stress and therefore the shear flow stress. Contrary to the results obtained with the tribo-torsion-test, the friction results were high influenced by the speed. Fig. 6.13 emphasizes the speed influence on the friction stress. A logarithmic tendency of the friction stress was observed when the speed was increased from 0.1 mm/s to 42 mm/s. It is due to the viscoplastic response of the friction junction. The sticking friction test can be compared with a shear test, where the aluminum alloy will have the similar strain-rate dependence observed in Fig. 6.2. The temperature-compensated strain rate Z (Zener-hollomon parameter) has the same behavior. The Eq. 2.14 predicts higher value of Z when the strain rate is increased. As proposed by Zener and Hollomon (Eq. 2.14) [ZEN44] the strain rate has a more distinctive on the flow stress and thus on the friction stress at higher temperature. Hence, a variation of the speed from 0.1 mm/s to 42 mm/s leads a friction increase of 32 %, 57 % and 105 % at 300 °C, 400 °C and 500 °C respectively.

8.3.2 Influence of the pressure and temperature on the mechanical and chemical interaction

Some additional experiments were carried out with the axial friction test to evaluate the adhesion effect at different temperatures and pressures. For this purpose no Belleville springs were applied. Thus, the specimen was initially compressed but the axial compression force was drop to zero before the friction stroke. Hence, the mechanical component of the junction was retired, and the friction was only due to the molecular adhesion.

Experimental results can be observed in Fig. 6.10 denoted with dotted lines. Additionally, Fig. 6.12 depicts the estimated adhesion component of the friction stress in percentage. As was expected, most of the friction at high temperature is due to the adhesion phenomena. At 500 °C, the adhesion interaction represented about 95 % of the total friction stress. However, a lower adhesion influence was observed at lower temperatures. According to the literature a stronger adhesion effect is expected in intermetallic contacts at high temperatures, due to the higher interatomic bonding energy possibly caused by diffusion process [WUT87].

8.3.3 Change of the microstructure in the friction boundary layer

Based on the high friction stress and the asymptotic tendency obtained with the axial friction test A at higher normal pressures (Fig. 6.11) sticking friction can be assumed. However, to demonstrate this hypothesis the microstructure of some tested specimens were analyzed. First the small aluminum cylinders were sectioned lengthwise at the mid-plane, ground and macroetched with Poulton agent. Selected macrographs of specimens tested at 300 °C, 400 °C and 500 °C at 0.1 mm/s and 42 mm/s are presented in Fig. 6.14. The results showed a thin shear zone at the lateral borders of all cylinders, resulted from the high friction stress at sticking conditions. It was also observed a thickness variation of the boundary layer. At the top side the zone is very thin, but it becomes considerably thicker at the bottom side. Moreover, at 300 °C the sample tested at 42 mm/s presented a thicker shear zone than at 0.1 mm/s possible due to the larger distortion energy at a higher strain rate. Consequently, the same specimens were metallographic prepared and analyzed by means of LOM to obtain more details about the shear zone. Fig. 6.15 depicts the friction boundary layer of the whole specimens tested at high speed (42 mm/s), where the different deformation areas can be better recognized. Although the top and bottom sides were compressed during the whole test, they showed dissimilar deformation pattern. At the top side the grains were radially elongated toward the border reducing thus the height. Similar grain structure was found after hot compression tests (Fig. 6.7). Moreover, at the bottom side the grains were radially compressed and therefore elongated vertically. This effect was produced, because part of the sheared subsurface is dragged to the bottom border forcing thus the flow toward the center of the sample. Due to dragging effect of the subsurface, the top edge of the samples were deformed in the friction direction. A local height variation of 3 % and 5 % were measured at 300 °C and 500 °C respectively. The effects of the dragging deformation will be discussed with numerical simulations of the axial friction test presented in section 8.9.1. As a result of the friction test the contact subsurface suffered a strong shearing clear visible in Fig. 6.15. The grain deformation allows the identification of a high and a low shear deformation zone (Fig. 6.15a). The high shear deformation zone is localized at the border of the specimens, and can be identified on the higher grain refinement. The zone with smallest grain size was subjected to the highest strain and strain rate. Next to the high shear deformation zone elongated grains in the friction direction were observed (low shear deformation zone). This area was also sheared during the friction tests but with a lower strain generating a higher grain size. The thickness of the total shear zones h was also sensible to the friction temperature. Thus, at 300 °C

the thickness of the shear zone was 1300 µm for samples tested at 42 mm/s. However, at 500 °C *h* increased about 20 %. Due to the reduction of the flow stress at higher temperatures, a thicker zone is deformed during sticking friction.

The micrographs suggest that the significant plastic strain and strain rate is concentrated in the high shear deformation zone. Therefore the friction stress is determined by the plastic response of this thin layer.

8.4 Axial friction test B

The friction curves obtained with the axial friction test A (Fig. 6.10) showed a significant friction growing during the plastic deformation at 300 °C and 400 °C. The origin of this behavior was not clear and for that reason only the friction values at the beginning of the relative movement (F_{fa}) was taken into account. In order to evaluate the effect of the punch configuration on the friction force, three different configurations were applied. Thus, friction experiments were performed with cylindrical, conic-convex and conic punches applying the same friction device and keeping constant the temperature (300 °C), stroke (5 mm) and compression force (3900 N). On the other hand, the high adhesion detected in the first experiments (Fig. 6.12) suggested that an additional deformation of the friction boundary layer during the extraction of the sample could occur. For that reason, the friction experiments were repeated applying a different extraction procedure. In the axial friction test A the specimen and the hollow cylinder were separated at high temperature (before quenching). However, in the axial friction test B the separation was done after quenching. The change of the extraction procedure do not influence the friction force, but the final microstructure of the shear zone.

8.4.1 Influence of the punch configuration on the measured friction force

The friction curves measured applying different punch configurations are depicted in Fig. 6.16. As was mentioned above, each punch was tested two times at 300 °C and 42 mm/s. The difference between both experiments was the extraction procedure of the samples. In the first test the samples were extracted at high temperature and then quenched in water. These experiments were plotted with continuous lines. In the second test the samples were extracted after quenching (dotted curves). Similar force evolution was observed for all six experiments during the elastic part of the curve (part I). The results demonstrate the good reproduction of the initial friction conditions such as temperature, compression force, contact area and the same procedure of the friction device. The friction force at the beginning of the plastic movement F_{fa}

was almost the same applying either cylindrical or conic punches. The similar friction values are due to the comparable contact area generated at the compression step of the friction test. Additionally, it verifies that the friction between the punch and the hollow cylinder can be neglected. Furthermore, a little increase of 3 % was obtained with the conic-convex punches, which was kept constant until the end of the test. A convex head of the punch (Fig. 5.7b) could produce a more uniform distribution of the radial force and the contact friction area. However, in this case the high compression force was enough to generate a full upsetting and full contact area. Hence, a superior friction force was measured because the height of the contact area was higher than those generated with flat punches (Fig. 5.7a, c). After the inflexion point similar and asymptotic curves were measured with the conic (Fig. 5.7c) and conic-convex (Fig. 5.7b) punches. Applying the cylindrical configuration the friction force increased linear and continuously the following 2 mm of stroke and then stabilized analogous to the other curves. It was found that the friction difference obtained with the cylindrical punch was due to the interaction between the aluminum stick layer (Fig. 8.1a) and the lateral surface of the punch (Fig. 5.7a). At the beginning of the friction test the punch has only contact with the bottom side of the sample (Fig. 8.1b). Nonetheless, when the shear flow stress of the friction boundary layer is overcome (inflexion point) the plastic deformation begins. Consequently, the stick aluminum layer moves with the hollow cylinder and interacts with the lateral area of the punch (Fig. 8.1c).

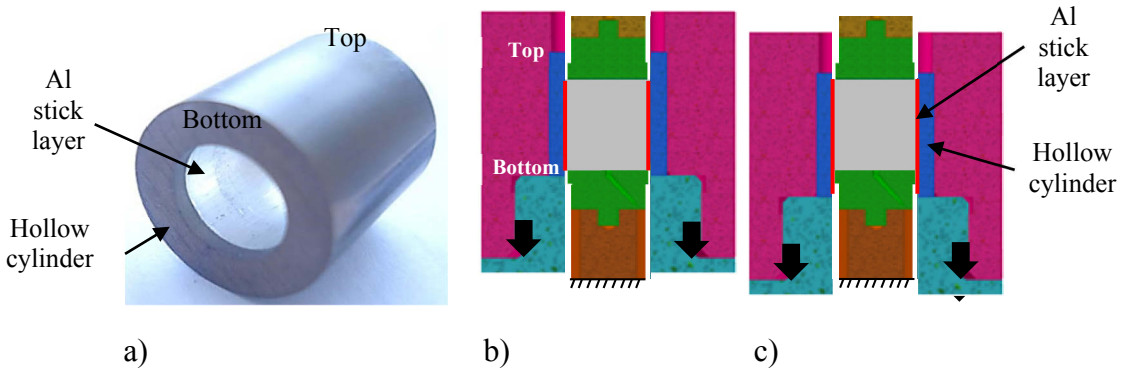

Fig. 8.1. Effect of the cylindrical punch configuration of the friction force. a) Aluminum stick layer, (b) initial and (c) final configuration of the friction components.

The friction increased linearly along 2 mm of stroke approximately due to the increasing contact with the 2 mm (height) of the cylindrical head (Fig. 5.7a). The extra friction observed applying a cylindrical punch at 300 °C was 20 % approximately. Applying a conic punch configuration

the lateral area of the punch head is reduced, and therefore extra friction is neglected. Hence, the friction measured using conic punches indicates the real evolution of the shear stress of the boundary layer.

8.4.2 Influence of the specimen's extraction method on the final microstructure

When the friction tests with different punch configurations (axial friction test B) were accomplished, the samples were quenched in water to avoid static alteration of the microstructure. Two different procedures were applied to remove the samples. Thus, the hot samples were removed from the hollow cylinder and then quenched. The other procedure consisted of removing the sample after quenching. Fig. 6.17 compares the micrographs of the six tested samples. As was observed in Fig. 6.15, a zone of severe shearing was distinguished at the border of the samples, but no relevant microstructural changes was noticed in the rest of the specimen. It indicates that the measured friction force is the force necessary to deform plastically the shear zone. The results also showed a clear difference on the shear zone as a consequence of the extraction method. When the samples are removed before quenching, the high residual adhesion and the low flow stress allow an extra deformation of the shear zone. Thus, during the separation more material is dragged to the bottom and is accumulated in the corner. This behavior was observed in all samples removed at 300 °C (Fig. 6.17a,c,e). The same deformation pattern was detected at 400 °C (Fig. 6.15c) and 500 °C (Fig. 6.15d). On the other hand, a more uniform thickness of the shear zone was distinguished in specimens removed at room temperature (Fig. 6.17b,d,f). During quenching both materials are rapidly cooled and the change of the temperature is accompanied with variation of the geometrical dimensions due to the thermal dilatation. Since the coefficient of thermal dilatation of the EN AW-6060 (24 mm/mm°C) is almost twice of the hot working steel AISI H13, both components suffer different shrinkage. Thus, the weld junctions created between the aluminum and steel are broken spontaneously during quenching. Hence, the samples are easily removed after quenching the assembly (sample-hollow cylinder) and no extra deformation is caused in the surface or shear zone.

8.5 Axial friction test C

The axial friction test A allowed the estimation of the boundary conditions to reproduce sticking friction between the aluminum alloy EN AW-6060 and the hot working steel AISI H13. Moreover, the axial friction test B showed the influence of the punch configuration on the

measured friction force. Additionally, an appropriate method was found to avoid extra deformation of the shear zone during the sample extraction.

The axial friction test C incorporates the best practice developed with the previous experiments to measure accurately the sticking friction during the whole stroke and analyze its relation with the microstructure of the shear layer. Moreover, the experiments were carried out at 300 °C, 400 °C, 450 °C and 500 °C, as well as 0.1 mm/s, 1 mm/s, 10 mm/s and 42 mm/s of relative speed. Since all experiments were performed applying conic punch configuration, the measured friction force corresponds to the force required to deform plastically the shear zone.

8.5.1 Influence of the temperature and speed on the sticking friction

Under sticking friction the high junction force avoid relative movement between the contact surfaces. Thus, when the applied shear stress is higher than the shear flow stress of the softer material a severe shear occurs in the subsurface layer. This condition could be reproduced applying the axial friction tests (Fig. 6.15). A strong shearing was observed in the friction boundary layer with a σ_n'=0.4 at 300 °C (Fig. 6.15b) and σ_n'≈1 at 400 °C and 500 °C (Fig. 6.15c,d). It is an evidence of the high junction force between both surfaces, however it not enough to demonstrate full sticking friction. Full sticking friction can be confirmed when the friction force does not increase under higher normal pressures, as reported in Fig. 6.11. Based on these experimental results sticking friction can be assured at σ_n'>3.5.

Fig. 6.18 shows the friction evolution under sticking conditions at different temperatures and speeds. As reported in the axial friction test A and B, the initial growing slope indicates the elastic deformation of the device. Moreover, the plastic deformation of the friction boundary layer begins in the inflexion point designated with the letter *a* (Fig. 6.18a). During the plastic deformation the friction force changed depending on the microstructure evolution, however a steady state was observed after approximately 3 mm of stroke. According to the experimental results the friction force increases at higher speeds and lower temperatures. The sticking friction test can be considered as a shear experiment, where the measured force is product of the plastic response of the viscoplastic material. Thus a higher speed generates a larger strain rate of the shear zone and therefore increasing flow stress and shear flow stress, in concordance with the Zener-Hollomon parameter (Eq. 2.14). Additionally, a lower temperature reduces the flow stress and thus the friction. The friction values at the initial plastic deformation F_{fa} and at the quasi-steady state F_{fb} were divided by the contact area to calculate the friction stress. Fig. 6.19a compares the friction stress at low and high deformation (stroke) at different speeds and

temperatures. In general, during the test the friction increased at low temperatures and high speeds (high Z), but decreases at high temperatures and low speeds (low Z). This variation is due to the microstructural changes suffered during high plastic strain. At 300 °C the hardening effect overcome the DRV and it is increased with the speed due to the faster generation and multiplication of dislocations at higher strain rates (Fig. 6.18a, Fig. 6.19a). Hardening effect ($\tau_b/\tau_a > 1$) was identified during experiments carried out at high speed and low temperature. For instance, at 300 °C hardening of 20 % and 10 % were generated at 42 mm/s and 10 mm/s of speed respectively.

On the other hand, at higher temperatures the friction stress or shear flow stress was reduced due to the softening effect in the shear layer (DRV and gDRX), which will be discussed in detail in the section 8.5.2. A friction reduction (softening) of about 20 %, 14 % and 8 % was observed at 500 °C at 0.1 mm/s, 1 mm/s and 10 mm/s respectively. Moreover, a balance between strain hardening and dynamic recovery was observed at 300 °C at 1 mm/s, 400 °C at 10 mm/s and 500 °C at 42 mm/s. Thus, the friction test give additional information about the plastic behavior at large deformation, which could not be evaluated by means of the hot compression test.

The reduction of the shear flow stress can be also caused by local temperature increase, generated at large deformations. During the friction tests a temperature variation around +5 °C to +8 °C was measured at the top side of the sample (Fig. 4.1), which is equivalent to a flow stress reduction of 4 %. The temperature evolution of the friction boundary layer could not be measured, however similar values are expected due to the high thermal conductivity of the aluminum.

8.5.2 Microstructural and hardness evolution of the boundary layer under sticking friction

Sticking conditions were reproduced by means of the axial friction test C, applying a normalized normal stress of $\boldsymbol{\sigma_n}'$=3.5 (Fig. 6.18). Moreover, the samples were quenched and then removed from the hollow cylinder to avoid plastic deformation during the extraction procedure. Consequently, the samples were metallographically prepared and analyzed with LOM. Selected micrographs are depicted in Fig. 6.20. A shear zone could be identified at the friction subsurface, which presented some differences comparing to those obtained in the axial friction test A (Fig. 6.15). In the test C, the thicker shear zone located at the bottom side was reduced for the different temperatures evaluated (Fig. 8.2). It was found that a thicker shear zone is produced in the bottom corner due to the extra deformation caused during the sample's extraction at high

temperature. Thus, the microstructure of the shear zone obtained with the friction test C was not affected or modified by the sample extraction process.

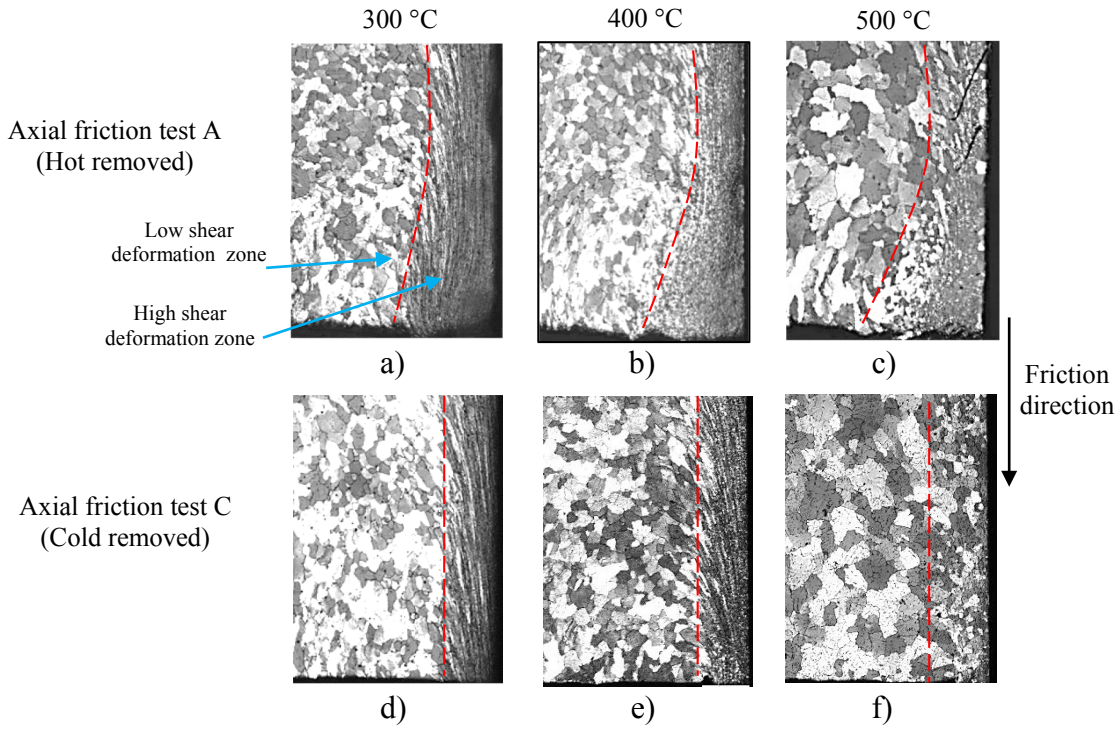

Fig. 8.2. Shear deformation at the bottom corner after friction test A at a) 300 °C, b) 400 °C and c) 500 °C and friction tests C at d) 300 °C, e) 400 °C and f) 500 °C (42 mm/s).

Micrographs of the shear zones taken at the middle of the samples are depicted in Fig. 6.21. The grain structure of the low shear deformation zones could be observed for different tested temperatures and friction speeds. Elongated grains with dendritic structures were observed in the low shear deformation zones. It can be assumed that the friction stress (sticking condition) will be defined by the plastic response of the high shear deformation zone. Therefore, this region was studied in detail. Fig. 6.22 shows the microstructure of the high shear deformation zones obtained by means of EBSD. A very fine grain size was created at 300 °C, with 4 µm at 0.1 mm/s (Fig. 6.22a) and less than 1 µm at 42 mm/s approximately (Fig. 6.22b). During the severe shearing the original grains are stretched and the grain boundaries of the grain are approached each other. Due to the strong deformation the interaction and multiplication of dislocations is expected leading strain hardening effect. EBSD-maps of the friction subsurface (300 °C, 0.1 mm/s) shows the low shear deformation zone with stretched grains (left), as well as the high shear deformation zone (right) (Fig. 8.3a). The low angle grain boundaries (LAGBs < 5°) are indicated by red lines and the high angle grain boundaries (HAGBs >15°) by dark black lines.

High fragmentation of the initial grains can be observed in the high shear deformation zone. Small elongated grains (HAGBs >15°) are distinguished with high number of subgrains (LAGBs < 5°) (Fig. 8.3b). Base on the high shear and the presence of small grains with HAGBs >15° would suggest continuous dynamic recrystallization (CDRX) and gDRX as the main deformation mechanisms [MCQ99, GEE04].

Friction stress measurements (Fig. 6.18a) and hardness mapping (Fig. 6.23a) confirm the existence of strain hardening. Thus, the friction stress was increased 20 % at 300 °C and 42 mm/s, whereas the hardness of the same sample was increased circa 12 % in the high shear deformation zone.

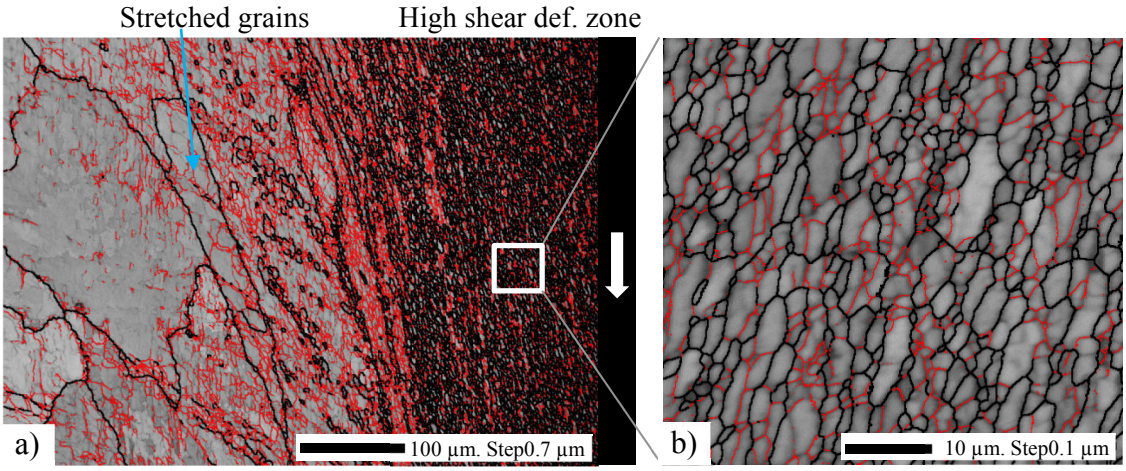

Fig. 8.3. EBSD-maps of friction subsurface generated at 300 °C and sticking friction speed of 0.1 mm/s (HAGBs >15°, LAGBs < 5°). a) Shear zone and b) from the high shear def. zone.

Micrographs of the samples tested at 400 °C (Fig. 6.21b,e,h) showed also elongated grains with dendritic structure in the low shear deformation zone. However, EBSD of the high shear deformation zone revealed small equiaxed grains with an average grain size of 9 µm at 0.1 mm/s and 5 µm at 42 mm/s (Fig. 6.22b,e). It is assumed that the grains are stretched and the grain boundary angle is increased continuously during the high strain. Fig. 8.4 shows the formation of small equiaxed grains with large number of high angle boundaries (HAGBs >15°) that suggests the presence of geometric dynamic recrystallization (gDRX) [DON08, KAY10, MCQ99, NEG16]. Additionally, hot torsion tests of a similar aluminum alloy suggested gDRX after a strain of 3 mm/mm [PET03]. At high temperature the dislocation movements are facilitated particularly for materials with high stacking fault energy. Thus the dislocations are easier annihilated by means of DRV. Since, the sticking friction is directly related to the plastic

response of the high shear deformation zone, DRV could reduce the shear flow stress and thus the friction stress. It explains the friction decrease (15%) during the friction test at 0.1 mm/s (6.19b) and also the general reduction of the hardness at 400 °C (Fig. 6.23b). Moreover, the softening effect is reduced at higher friction speed (strain rate) because dislocations are generated faster than they can be annihilated [MCQ75]. Therefore, the hardness was slightly increased at 42 mm/s (6.23b).

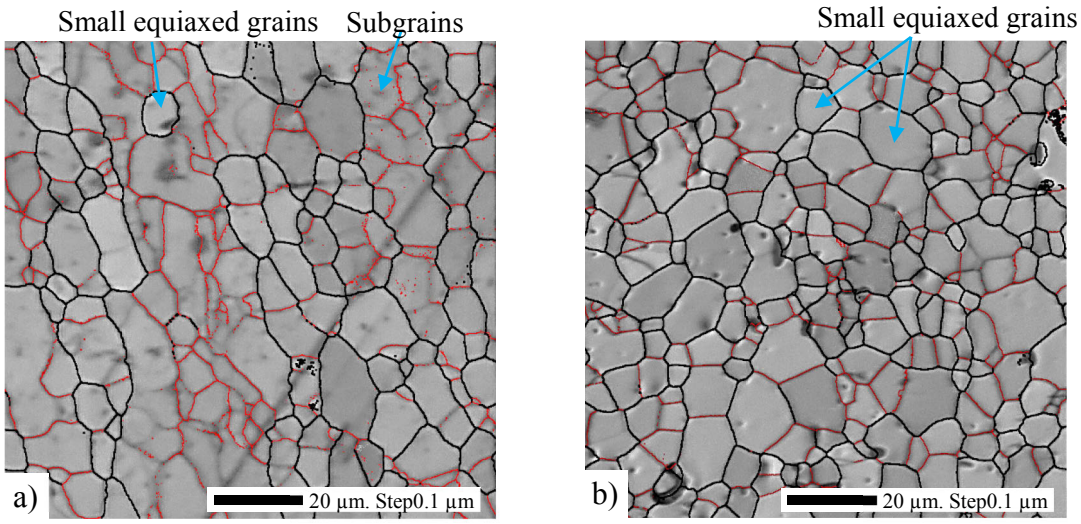

Fig. 8.4. EBSD-maps of the high shear deformation zone generated at 400 °C and sticking friction speed of a) 0.1 mm/s and b) 42 mm/s. (HAGBs >15°, LAGBs < 5°).

In addition, the high shear deformation zone of samples tested at 500 °C was also investigated by means of EBSD (Fig. 6.22c,f). The microstructure revealed large grains with average size of 30 µm and 70 µm in specimens evaluated at 0.1 mm/s and 42 mm/s respectively. Due to the high stacking fault energy at 500 °C gDRV or also called grain dividing (gDRV) is also expected [MCQ10]. During the deformation at 500 °C large number of dislocations are annihilated reducing the effect of the strain hardening and facilitating a more efficient process of dynamic recovery. At high temperatures a more rapid annihilation occurs and the steady-state balance is achieved at a larger subgrain size [MCQ75]. It could explain the larger grain size at higher temperatures (Fig. 8.3b, Fig. 8.4a, and Fig. 8.5a). The accompanied softening consequence could be also confirmed by the friction reduction of 20 % during the friction test at 500 °C and 0.1 mm/s (Fig. 6.19b). Furthermore, larger grains with less number of subgrains obtained at 500 °C and 42 mm/s (Fig. 8.5b) suggest that static recrystallization (SRX) could occur before quenching. Static changes of the microstructure should not happened because the samples were

quenched. However, as it has been observed experimentally SRX can occurred in only few seconds after the hot deformation [GEE05]. When the stored energy as well as the temperature are still enough to overcome the critical values static recrystallization can be generated. Fig. 8.5b shows static recrystallized grains which could have grown before quenching. Moreover, subgrains were also observed suggesting that the static recrystallization was not finished [MCQ04].

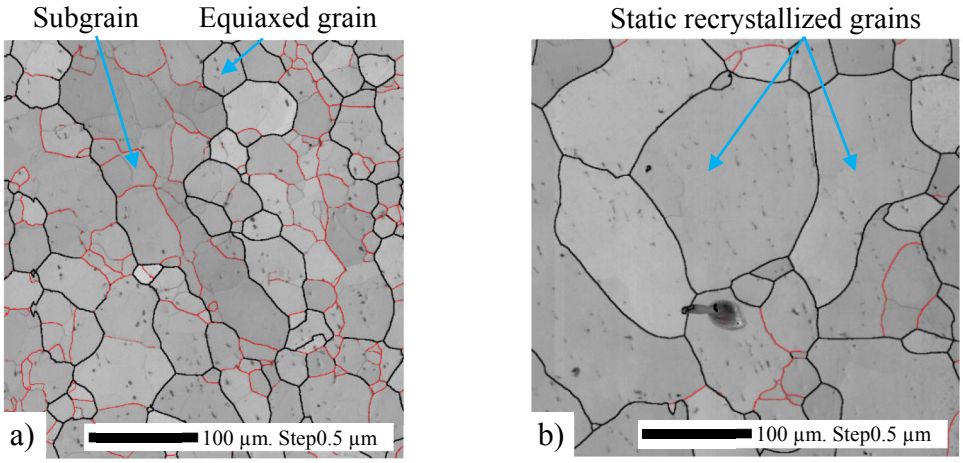

Fig. 8.5. EBSD-maps of the high shear deformation zone generated at 500 °C and sticking friction speed of a) 0.1 mm/s and b) 42 mm/s. (HAGBs >15°, LAGBs < 5°).

As it was discussed in section 8.1.3, a higher hardness was measured in samples tested at 500 °C due to the solid solution strengthening. According to the stoichiometric balance of the aluminum alloy (Mg 0.5 %), the excess of Mg2Si (0.789 wt. %) and Si (0.19 wt. %) are dissolved at 430 °C approximately (Fig. 2.5). Thus, at 500 °C the second phases (Mg2Si and Si) diffuse in the crystalline lattice. The solid atoms remain into the matrix (solid solution) during a rapid cooling and impose lattice strains on the surrounding atoms (base metal). Hence at room temperature the dislocation movements are restricted improving the strength and hardness at room temperature [GAR04]. Since the solid solution strengthening overcome the effect of the strain hardening in the shear zone, similar hardness was observed in the radial mapping (Fig. 6.23c).

8.5.3 Thickness evolution of the high shear deformation zone under sticking conditions

The influence of the temperature and friction speed on the thickness variation of the high shear deformation zone can be observed in Fig. 6.24. Based on the friction results and the microstructure evolution, the high shear deformation zone is subjected to strain hardening and DRV simultaneously. These deformation mechanisms can explain some of the thickness

variations of the shear zones. At low temperatures (300 °C and 400 °C) the strain hardening overcome the DRV and this strengthening effect influence the thickness of the shear zone. According to the results at low temperature, the thickness increased more than 80 % at 300 °C and almost 50 % at 400 °C when the speed was varied from 0.1 mm/s to 42 mm/s respectively. At low speed a thin layer is sheared during the friction stroke as observed in Fig. 6.21a, but its thickness increases at higher speeds. It is supposed that during the friction at a higher speed the subsurface is subjected to a higher strain rate leading to a local hardening. Since the subsurface is strengthened more adjacent softer material is sheared during the friction stroke, increasing the thickness of the shear zone. On the other hand, the effect of the strain hardening is lower at high temperatures (450 °C and 500 °C) producing a minor influence on the thickness variation of the high shear deformation zone (Fig. 6.24).

8.6 Axial friction test D

8.6.1 Physical modelling of the specimen deformation applying internal grid pattern

Based on the friction results obtained with the axial friction test (Fig. 6.11) and the severe shearing observed in the friction subsurface (Fig. 6.20) sticking conditions could be reproduced. However, the real deformation of the contact surface and the deformation path in the friction boundary layer was still unknown. Additional axial friction tests were carried out applying samples with radial grid patterns in order to make clear the real deformation behavior.

The samples were extracted from an extruded profile of AA6063 with similar mechanical properties to the EN AW-6060. Moreover, the radial contrast alloy (Al.8Cu) had similar mechanical properties to the base material as well. The initial height of the new samples was 8.1 mm, while in the axial friction tests A, B and C was 10.5 mm. Therefore, the measured friction forces of the test A, B and C (Fig. 6.10, Fig. 6.16 and Fig. 6.18) and D (Fig. 6.25) can not be directly compared. However, all results can be compared dividing the friction force by the corresponding contact area (friction stress). Fig. 8.6 depicts the friction stress of both alloys tested at 400 °C (Tests C vs D). The experimental results demonstrate the similar mechanical properties (shear flow stress) of the EN AW-6060 and the AA6063 (with internal grid pattern) applied in this work.

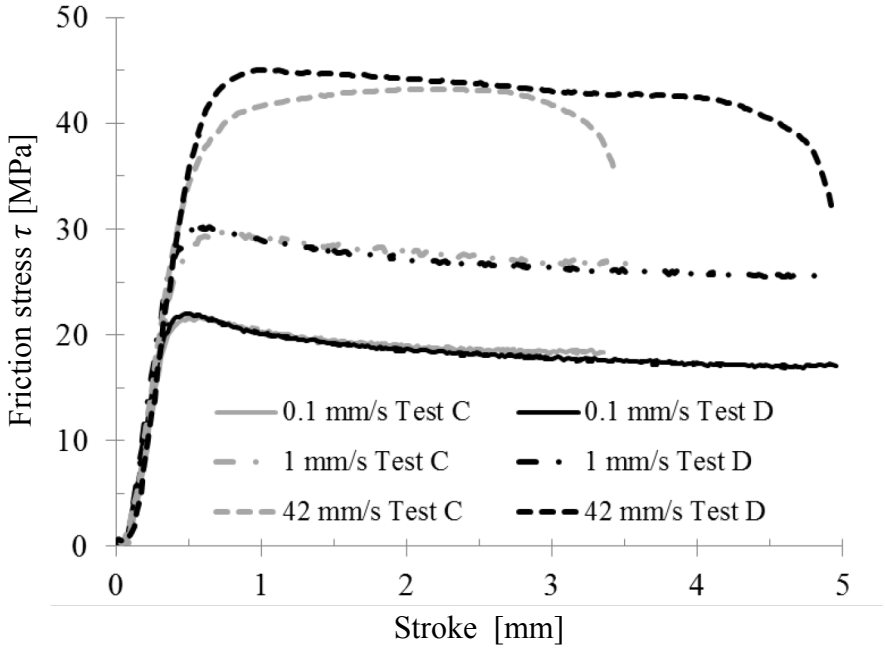

Fig. 8.6. Friction stress comparison applying the aluminum alloys EN AW-6060 (Test C) and AA6063 (Test D), measured with the axial friction test at 400 °C.

The lateral marks (dark circles) and intern contrast material made visible the real friction behavior under sticking conditions (Fig. 6.26). As was expected fully sticking friction could be successfully reproduced by means of axial friction test. During the test the friction subsurface is sheared and most of the plastic deformation is concentrated in a thin region called high shear deformation zone, as it was also observed in previous experiments (Fig. 6.15, Fig. 6.17, and Fig. 6.20). The results indicated that this method can be considered as a shear test and could be used to investigate the plastic response and microstructural evolution under high temperature, strain and strain rate.

During the test the specimen remains static and the hollow cylinder is axially moved. Fig. 8.7 shows the same axial relative movement, but illustrates a static die and a moving sample to imitate a similar sticking friction such us inside the extrusion bearing channel. It was detected, that during the movement the whole contact area remains adhered (stick) to the die forming an aluminum stick layer. The initial contact area (Fig. 6.26a) is dragged (sheared) and a new surface is generated (Fig. 8.7). Fully sticking was demonstrated, since the relative displacements of the lateral marks (6.26b,c,d) were the same to the friction length measured during the friction test (Fig. 6.25).

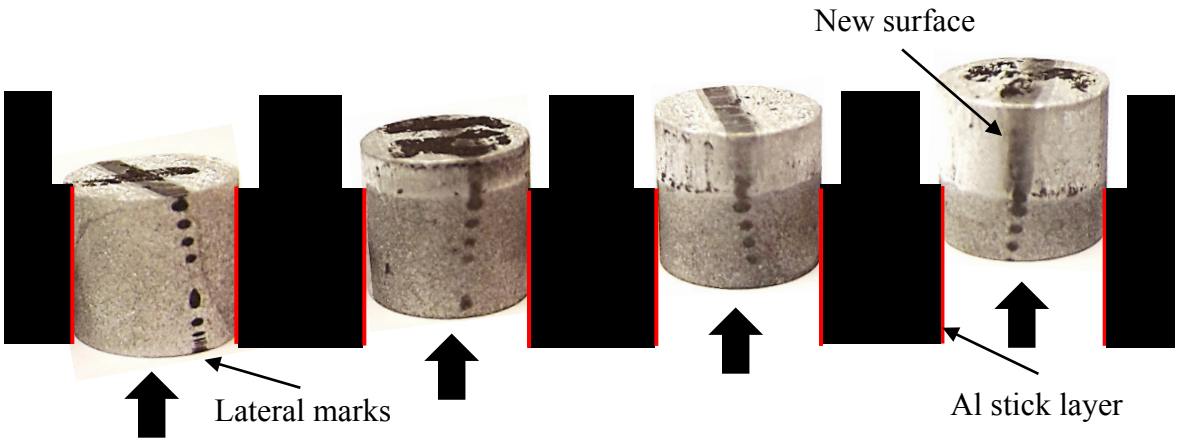

Fig. 8.7. Illustration of the sticking friction inside an extrusion bearing channel applying lateral contract marks.

8.7 New friction model

As it was experimentally validated the friction increases linearly with the normal pressure but remains constant at a very high normal pressure ($\boldsymbol{\sigma_n' > 3.5}$). Therefore, a combination of the Coulomb (Eq. 2.18) and Tresca (Eq. 2.22) friction laws seems to be a good commitment, as proposed by Wanheim and Bay (Eq. 2.24) [WAN73, WAN78] and posteriorly modified by Lin (Eq. 2.25) [LIN03]. Unfortunately, these equations require an unknown friction factor *m* which may change under friction conditions such as temperature and pressure. Sticking and slipping occur along the extrusion bearing channel as it has been reported in the literature [ABT96, AKE85, MUE96, THE92, VAL94, VAL96]. Therefore, an appropriate friction model for extrusion process should accurately reproduce the slipping as well as the sticking behavior. In order to achieve this goal a suitable friction test and the adequate mathematical formulation have to be selected. Slipping friction can be studied by means of several methods (Fig. 2.11, Fig. 2.12), but the modelling of the real contact area represents a very complicated task. On the other hand, under sticking conditions the real and apparent contact area should be similar, however there are difficulties to reproduce sticking friction. The friction simulation is more complicated inside the bearing channel because the real contact length of the friction mechanisms are unknown and vary with the extrusion parameters and the die configurations. Abtahi proposed an empirical friction model to estimate separately the sticking (Eq. 2.26) and slipping friction (Eq. 2.27) in the extrusion bearing channel [ABT95, ABT96]. Based on Abtahi's results Saha suggested a similar formulation (Eq. 2.28) [SAH98]. Both approaches

require the good prediction of the length of both friction mechanisms inside the bearing channel as well as the assumption of correct friction factors. Due to the complex friction behavior exponential equations with several constants have been recently proposed to reproduce friction in extrusion. The complexity of these formulations makes difficult the implementation in commercial FEM-codes as is the case of Eq. 2.32 [OCK12]. Other equations (Eq. 2.35) has been evaluated in house developed codes [BEC14]. These formulations incorporate a closed relationship between the friction stress and the flow stress. Therefore the friction estimation also depends on the correct simulation of the flow stress or shear flow stress (Eq. 2.23) in the friction boundary layer. The flow stress can be calculated with the temperature and strain rate $\bar{\sigma}(T, \dot{\varepsilon})$ (Eq. 2.14, Eq. 2.15). However, the strain rate calculation is also influenced by the mesh size, thus a lower strain rate will be determined with a coarse mesh. For that reason, the shear flow stress is calculated based on the flow tress and the strain rate distribution obtained in the simulation [HOR14].

Based on the friction results obtained with the tribo-torsion-test (Fig. 6.19) and the axial friction test C (Fig. 6.19a) an empiric friction model was developed. The tribo-torsion-tests (at low pressure) provided mainly the linear relation between the normal pressure and the friction stress. Thus, higher friction values were measured with increasing normal pressures. At larger normal pressures the number of asperities in contact (weld junctions) increases, thus a higher force have to be applied to separate or shear the greater real contact area. On the other hand, the maximal values of the friction stress (sticking friction) were determined with the axial friction test under different speeds and temperatures. The friction measured using the tribo-torsion-test was slightly higher compared to those determined by the axial friction test (Fig. 6.28). It could have been caused by additional friction between punch and outer and inner tools during the tribo-torsion-tests (Fig. 2.13). Due to these differences the results at low normal pressure were used as a reference to construct the slope of the curve friction-pressure (Fig. 6.29a). A logistic function (Eq. 6.1) was selected to fit the experimental results due to the simple formulation and few variables. Moreover, the pressure *P* was introduced as independent variable and the sticking friction was set to the maximal value of the curve (Eq. 6.2). Sticking friction (shear flow stress) in steady state was measured with the axial friction test C (Fig. 6.19) and demonstrated with the axial friction test D. For that reason the flow stress of the high shear deformation zone can be calculated applying the von Mises yield criterion (Eq. 6.4). Furthermore, an average strain rate $\dot{\bar{\boldsymbol{\varepsilon}}}$ was derived with the Eq. 2.14 and 2.15 applying the new constitutive constants (Table 6.1).

Due to its dependence to the relative speed and temperature an empiric formulation was constructed to the average strain rate (Eq. 6.5 and Eq. 6.6). Hence, the friction under sticking conditions can be estimated, if the temperature, speed and constitutive constants ($\Delta H, n, A, \alpha$) are known.

In addition, the slope of the friction curve is defined by the constant β and the variable γ, which is also modified by the temperature (Eq. 6.3). The friction results showed a greater slope of the curve at higher temperatures, since a lower pressure is needed to reach sticking friction at higher temperatures. The friction estimation at 400 °C and 500 °C under different combinations of pressure and speeds are depicted in Fig. 6.30.

8.8 Multi-hole extrusion applying different inclinations of bearing channels

Different bearing angles origins dissimilar friction interactions inside the bearing channels [AKE85]. In multi-hole extrusion the material flows faster through channels with less resistance (friction), therefore friction variations in the channels generate dissimilar product speeds. Several extrusion experiments have verified the significant influence of the bearing angle on the product speed during multi-hole extrusion [DON15, HOR05, MUE96, MUE12]. Additionally, physical simulations applying contrast materials have demonstrated the presence of sticking and slipping regions along long bearing channels [VAL96, VAL10]. Although the large number of experiments the relation between bearing angle, friction mechanisms and speed distribution has not been fully understood.

Extrusion trials of aluminum alloy EN AW-6060 were carried out applying a four-hole die (Fig. 5.12) with interchangeable inserts (Fig. 5.13a). Homogenized billets were preheated to 460 °C, while the container and die at 470 °C. The inlet diameter and length of the bearing channels was 20 mm. Moreover, -0.5° relief, 0° parallel, +0.5° and +1° choked bearing channels were applied (Fig. 5.13b). During the extrusion trials the extrusion forces (Fig. 5.11) and the bearing temperature were measured. Moreover, the product length was also measured to evaluate the effect of the friction in the bearing channels. Since bearing channels with different inclinations were applied dissimilar friction behavior and then different product length were obtained. In addition, the inserts and the filled aluminum were also analyzed to investigate the friction mechanisms, the contact lengths, as well as the microstructural changes in the friction boundary layer.

Based on the experimental results obtained in this work, the intimate relationship between the bearing angles, friction mechanisms, die force, temperature and product speed is discussed.

8.8.1 Influence of the bearing angle on the extrusion force, temperature and product speed

Thanks to the load cells installed in the extrusion machine (Fig. 5.11) and the thermocouples placed in the bearing channels (Fig. 5.14) the evolution of the extrusion force and product temperature could be recorded during the whole process. Fig. 6.31 depicts the extrusion diagrams of the experiment 1 applying parallel and +0.5° choked channels (Fig. 6.31a) as well as the experiment 4 applying +0.5° and +1° choked channels (Fig. 6.31b). In the first 25 mm of ram stroke approximately, the billet is set up inside the container and forced to fill the pockets and bearing channels. Due to the sum of the billet deformation mainly produced in the shear and primary zones (Fig. 2.3a) as well as the friction with the container and bearing channels the extrusion force increases until a peak (Fig. 6.31). Experimental and numerical experiments suggest that the peak of the extrusion force is reached when the workpiece fills the bearing channel [MIS00].

Changes of the bearing angle cause small variation of the friction force, which is usually not distinguished in the total extrusion force. Moreover, the measurement of the die force allows its better recognition. Particular arrangement of the load cells allowed measuring the container and die force separately (Fig. 5.11a). The die force involves the force needed to deform plastically the billet in the primary and shear zones as well as the friction generated in the bearing channels. Therefore, the friction force in bearing channels can not be measured directly. Furthermore, the relative friction force in the bearing channels can be obtained comparing the die force from different extrusion trials. The die forces at the moment of the extrusion peak were 2.6 MN, 2.7 MN and 2.8 MN in the experiments 1, 2 and 4 respectively (Fig. 6.32). According to the experimental results the bearing friction force increased 100 kN when the bearing angle was changed from parallel to +0.5° choked (Exp. 2 / Exp.4) and also from +0.5° to +1° choked (Exp. 1 / Exp.2). On the other hand, an opposite tendency was detected applying relief channels (Fig. 2.9c). A lower die force (2.3 MN) was measured applying parallel and -0.5° relief channels possible due to the reduction of the friction contact in the bearing channel. The mentioned force differences remained almost constant during the extrusion trials indicating stable friction conditions inside the bearing channels. Thedja suggested that adhesion layer on the bearing

channel suffers significant changes, however this variation was detected after several extrusion trials [THE92].

Based on the results, it is clear that a higher friction or flow resistance is generated with choked channels, however a lower friction with relief bearing channels. Similar tendency was also found by Akeret [AKE85].

The experimental results showed a substantial temperature increase during the die filling. Thus, the bearing temperature varied from 470 °C to 490 °C and 500 °C in the experiments 1 and 4 respectively. Later, the temperature continued growing with different gradients to find a quasi-steady-state (Fig. 6.31). In the experiment 1, the maximal temperatures were 525 °C in the parallel channels and 510 °C in the +0.5° choked channels. More than 90 % of the deformation work is transformed in heat. Since all the generated heat can not be transferred to other bodies or dissipated to the surrounding at the same generation rate the local temperature increases [LIE11]. The plastic deformation in the primary and shear zones together with the significant friction in the bearing channel can produce enough heat to increase the bearing temperature as observed in Fig. 6.31. The temperature magnitude measured in the bearing channel can be influence by deviations of the initial billet and die temperature or even fluctuations of the ram speed. Additionally, small temperature variations can be also caused by the contact instability between the workpiece and the thermocouple. Despite all this, a clear difference of 15 °C was measured between parallel and +0.5° choked channels (Exp. 1) possibly caused due to the higher speed gradient of 45 % (Fig. 6.34a). The faster products are subjected to a higher deformation rate (strain rate) and therefore larger heat rate. Furthermore, in the experiment 4, the low speed difference (8 %) in +0.5° and +1° choked channels, originated also a low temperature variation between the products (rods). The constant temperature difference observed in the friction experiments suggests stable relative speed and friction conditions.

Similar product length were extruded through inserts with the same configuration placed in the same die. It suggests comparable and stable friction conditions inside the pair inserts with the same angle. Furthermore, the product length was not completely related to the angle of the bearing channel, but to the insert combination in the die. Thus, the profile length was around 2.2 m with +0.5° choked channels in experiment 1, but 4 m in experiment 4 (Fig. 6.33). The length and speed of the profiles are linearly related, because the four rods were extruded at the same time. In experiments 1 and 2, the profile speed in parallel channels was almost 70 mm/s, but 30 mm/s in the choked channels. Nevertheless, in the experiment 3 the speed in parallel

channels was 35 mm/s and faster through relief channels (65 mm/s). As observed in experiments 1 and 2, choked angles higher than +0.5° have a very low influence on the length and product speed. The same effect was observed in the experiment 4 detecting only a product speed variation of 8 % applying +0.5° and +1° choked bearing channels. The most significant influence on the length and product speed was observed when the bearing angle was changed from -0.5° relief to +0.5° choked. Similar results are also reported in the literature [AKE85]. According to experimental results, there should be a relationship between the inclination angle from -0.5° to +0.5° and the resistance against the material flow through the bearing channels. The results also showed that choked channels higher than +0.5° generate higher friction forces inside the bearing channels due to the larger sticking zones. However it has a very low influence in the final product speed, because the speed distribution is also influenced by the friction behavior inside the other channels.

8.8.2 Analysis of the friction mechanisms inside the bearing channels and its relation with the microstructure in the friction boundary layer

Based on the extrusion results a significant friction variation was detected when the bearing angle was changed from -0.5° relief to +0.5° choked (Fig. 6.32). Since all the bearing channels had the same initial diameter (20 mm) and were equidistant radially placed the different flow resistances must be caused by a different friction behavior on the bearing land. As was observed by Akeret [AKE85] choked channels generate high extrusion resistance (high friction) than parallel channels. Moreover, the friction is decreased applying relief channels. Several experimental investigations have demonstrated the relation between the bearing angle and the friction mechanisms. Thus, in relief channels the bearing length is almost zero, therefore a minimum friction is expected. In parallel channels slipping friction prevails and the bearing land is contaminated with a thin layer [ABT96, MUE96, THE92]. Furthermore, a combination of sticking and slipping friction has been reported inside choked and long bearing channels [MUE96, VAL94, WEL96].

In order to investigate the relation between the bearing angle and the friction behavior inside the bearing channels the appearance of the bearing areas (Fig. 6.35) as well as the microstructure of the friction boundary layer (Fig. 6.37) were analyzed. Based on the surface topography and color the sticking and slipping areas were distinguished. In general, black areas and perpendicular ground lines indicate sticking conditions, while aluminum colored areas with stripes in the

extrusion direction suggest slipping friction. Figs. 8.8a,b show the mentioned black area in the pocket as well as at the inlet region of a +0.5° choked bearing channel. According to the literature this zone corresponds to the iron oxide layer formed during the die preheating step [VAL94].

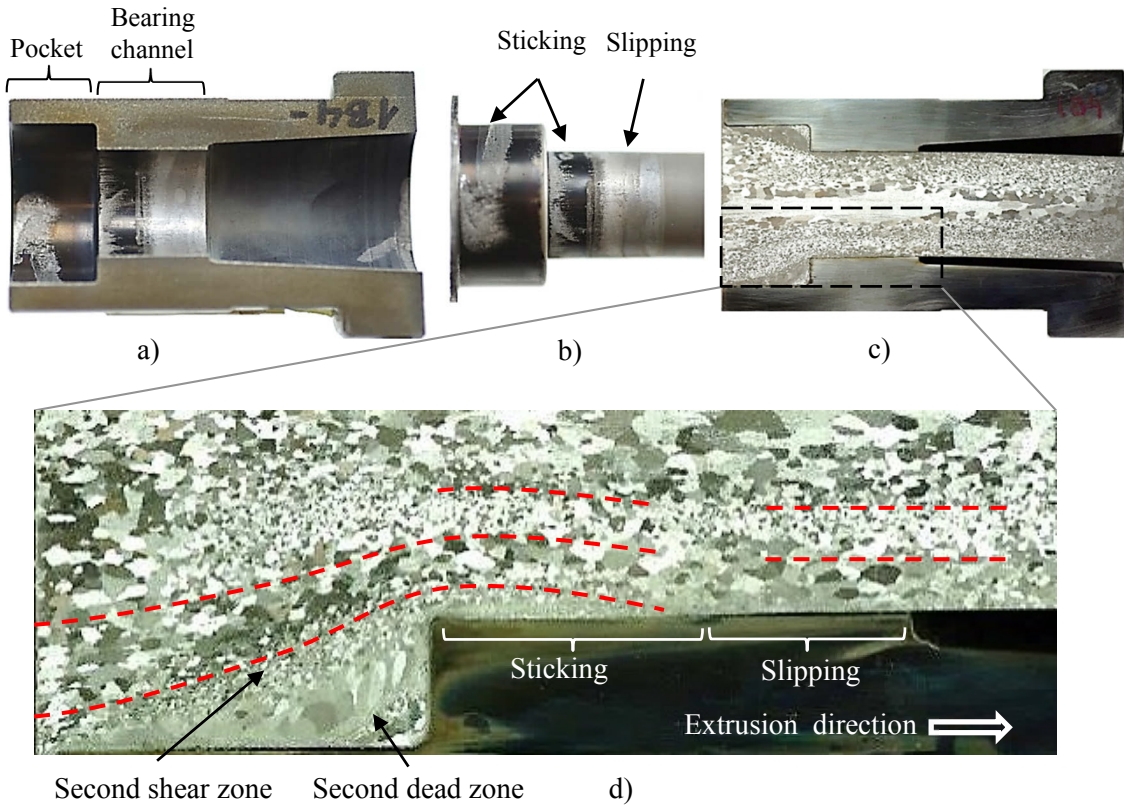

Fig. 8.8. Choked insert +1° applied in experiment 4. a) Inner appearance after lengthwise cutting, b) extracted aluminum rest from the insert, c) macroetching of the aluminum rest inside the insert and d) microstructure and schematic material flow inside the insert.

It can be presumed that during the die filling the aluminum is pressed against the pocket surface with a high pressured enough to maintain fixed both surfaces and avoid slipping until the end of the extrusion process. Due to the intimate contact between both surfaces and the diffusion effect the oxide layer as well as the grounding marks of the pocket surface are also observed in the aluminum rest after the separation Fig. 8.8b.

The sticking friction in the pocket produces a second dead zone illustrated in Figs. 8.8c,d. As a consequence, the workpiece is sheared toward the center of the channel as illustrated in Fig. 8.8d. Due to the cone flow effect caused by the second dead zone the material is radially pressed against the inlet surface of the bearing channel. The radial pressure is increased in

choked channels generating sticking contact. The presence of the dark black region at the inlet of the choked channels suggests that the workpiece does not slip on the bearing inlet, but the subsurface is sheared progressively to contact the bearing land. Fig. 8.9 illustrates the evolution of the sticking friction contact at the inlet of a choked bearing channel. When the workpiece contacts the inlet of the choked bearing channel both surfaces are fixed due to the strong adhesion at high temperature and normal pressure (a in Fig. 8.9). Thus, the friction subsurface is sheared and forced to flow above the sticking surface (b in Fig. 8.9). Due to the significant radial pressure, this process continues building the whole sticking area (c in Fig. 8.9). The large local deformation of the friction subsurface produces a grain refinement which can be clear distinguished in Figs. 6.37a,b,c (sticking wedge) and Fig. 8.8d. Even in choked channels, the radial pressure is reduced toward the end of the channel leading to slipping conditions (d in Fig. 8.9).

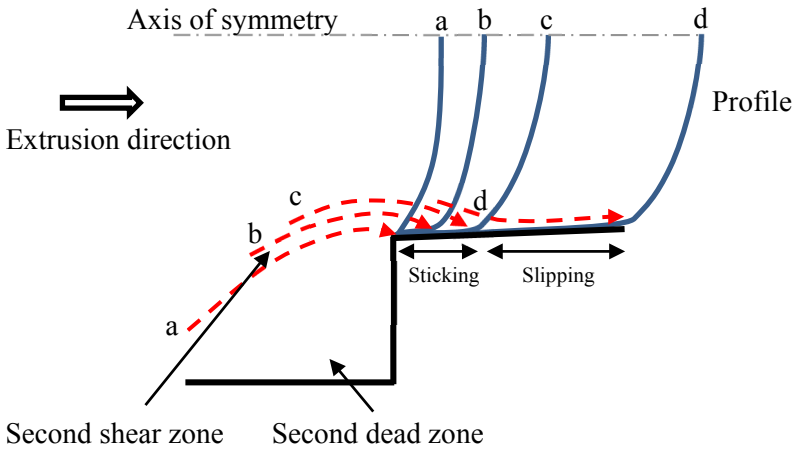

Fig. 8.9. Material flow during sticking contact formation.

Based on this assumption the surface of the extruded profile is formed by material that flows above the sticking wedge and then slides against the slipping zone. Extrusion experiments applying intern grid pattern also confirmed sticking and slipping friction and the inlet and end side of choked channels respectively [VAL90].

Sticking regions were observed at the inlet of all choked channels (Fig. 6.35b,d,g,h) that explains the relation between the choked channels and the friction force. Choked channels lead a higher friction resistance due to the formation of a sticking region in the entrance of the channels. The results also showed that higher choked channels are related to longer sticking zones and thus higher friction forces (Fig. 6.38). For instance, increasing the angle of the choked channels from

+0.5° to +1° generated 100 kN extra of die force (Fig. 6.32) and 3 mm longer of sticking length (Fig. 6.35b,d). Moreover, in experiment 4 the sticking length in +1° choked channels was longer than in +0.5° choked channels producing also a higher die force than the rest of the experiments. Although longer sticking lengths are found with higher choked angles its magnitude will be influenced by the friction behavior of the neighbor channel. The observed slipping zones following the sticking regions (Fig. 6.35b,d,g,h) were covered by a smooth adhesion layer with aluminum stripes in the extrusion direction. Due to the weak surface interaction lower friction forces are expected in the slipping zones.

In addition, the parallel bearing channels were also investigated. The three parallel channels applied in the experiments 1, 2 and 3 presented diverse scenarios (Fig. 6.35a,c,e). Experiment 2 showed sticking conditions at the inlet (dark zone) of the parallel channels followed by slipping layer with a scheme of lamellar current also reported in the literature [THE92]. An aluminum color layer covered the inlet of the parallel channels in experiments 1 and 3, followed by rough aluminum stripes in the extrusion direction (Fig. 6.35a,e). Since, neither black color nor stripes could be distinguished at the inlet side of the mentioned channels, sticking or slipping behavior could not be assumed. Subsequent microstructural analysis of the friction boundary layer revealed a grain refinement at the inlet of parallel channels in experiment 1 (Fig. 6.37a). It indicates a strong adhesion possibly comparable with sticking conditions. It can be assumed that the dark zone was not observed in this case, because the oxide layer was removed progressively and eventually sticking friction took place. On the other hand, the coarse microstructure in the parallel channel of experiment 3 (Fig. 6.37d) did not give evidence of sticking conditions. Since no sticking or slipping friction can be confirmed analyzing the contact surface and the subsurface microstructure an intermediate condition could be assumed. Hence, both surfaces could be pressed with a significant pressure to avoid slipping, but not enough to generate fully sticking friction, which can be referred as quasi-sticking friction.

It is true that the length of the sticking region influences directly the friction force, nevertheless its magnitude does not always define the product speed distribution. Thus, in the experiments 1 and 4 the +0.5° choked channels have the same sticking length (11 mm), however the products flowed at 30 mm/s and 50 mm/s respectively (Fig. 6.35b,g). This speed difference is not only caused by the friction interaction in both slipping zones, but also the friction response in the neighbor channels. This effect could be also noticed comparing the die forces, friction behaviors and product speed of friction trials 1 and 2. Thus, a higher die force was measured in experiment

2 increasing from +0.5° to 1° the choked channels. However similar product speed distribution was obtained, because the friction difference between parallel and choked channels did not change. Since the workpiece acts as a parallel system in multi-hole extrusions the material flow inside a bearing channel will influence the flow distribution in the rest channels. Higher speed was obtained with +0.5° choked channel in experiment 1 because more material flowed through the neighbor parallel channels (Fig. 6.35a). Thus, the distribution of the product speed in multi-hole extrusion will not depend on a particular friction condition in a bearing channel, but on the differences between all channels resistances.

8.9 Analysis of the numerical simulations

8.9.1 Simulation of the axial friction test D (internal grid pattern)

Numerical simulations of the axial friction test D (with contrast material) were carried out in order to determine the suitable friction boundary conditions between the sample and the tools. The FEM model was validated comparing the simulated (Fig. 7.2) and the experimental grid patterns (Fig. 6.26). Before starting the simulations the initial geometrical configuration of the grid pattern was analyzed. Thus, the thickness and position of each contrast stripe was measured and reproduced in the numerical model (Fig. 8.10a). Subsequently, the upsetting was simulated and compared to the real results. Fig. 8.10b shows similar experimental and numerical results. A graphite paper was introduced between the sample and punches in order to decrease the friction, however a complete friction reduction is not possible. For that reason the top lines 2 and 3 were bent slightly upward and the bottom lines 5, 6 and 7 downward (Fig. 8.10b). This effect was properly simulated applying a friction factor m=0.3 between the sample and punches. The simulated axial compression force was 1600 N as it was applied experimentally. The experimental and simulated results depict a small variation of the sample diameter at the bottom side (Fig. 8.11). It suggests that the sample is not fully compressed at σ_n'=1.1 forming a small gap in the bottom corner. This small difference in the friction contact could explain the minor friction difference obtained at the beginning of the friction tests (400 °C, 0.1 mm/s) applying a σ_n'=1.1 and σ_n'=3.2 (Fig. 6.11).

Since the hollow cylinder moves upward with the bottom punch during the upsetting, the lateral friction surface is dragged in the same direction generating thus a good contact. Therefore any gap was observed at the top side of the sample. The small gap observed at the bottom corner disappears in the first step of the friction simulation, because the friction subsurface is forced to

move downward against the bottom punch. The mentioned gap at the bottom corner was not observed during simulations of the upsetting step at σ_n'=3.5.

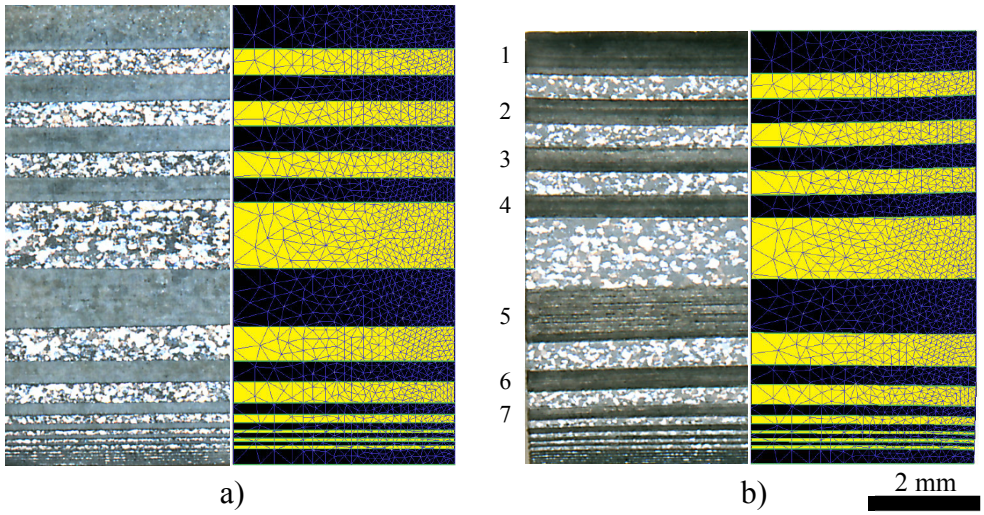

Fig. 8.10. Experimental and simulated intern grid pattern at the a) initial state and b) after upsetting at 400 °C in the axial friction test D.

The final deformation of the grid pattern obtained after upsetting (Fig. 8.10b) was the initial state of the friction test. After several simulations the deformation of the intern grid pattern could be reproduced applying friction factors of 0.3 and 0.6 at the top and bottom side of the sample. A higher friction factor was required in the bottom contact possibly due to the stronger interaction at higher normal pressure. It is assumed that the higher contact pressure increases the friction force between the sample and the bottom punch.

Sticking contact was assumed between the initial contact area between the sample and the hollow cylinder. Moreover, m=1 was set to the rest of the new contact area originated progressively at the top side of the sample. It was assumed that the new surface does not fully stick to the hollow cylinder due to the relative low normalized normal stress (σ_n'=1.1). For that reason a velocity variation was generated along the friction surface (Fig. 7.3e).

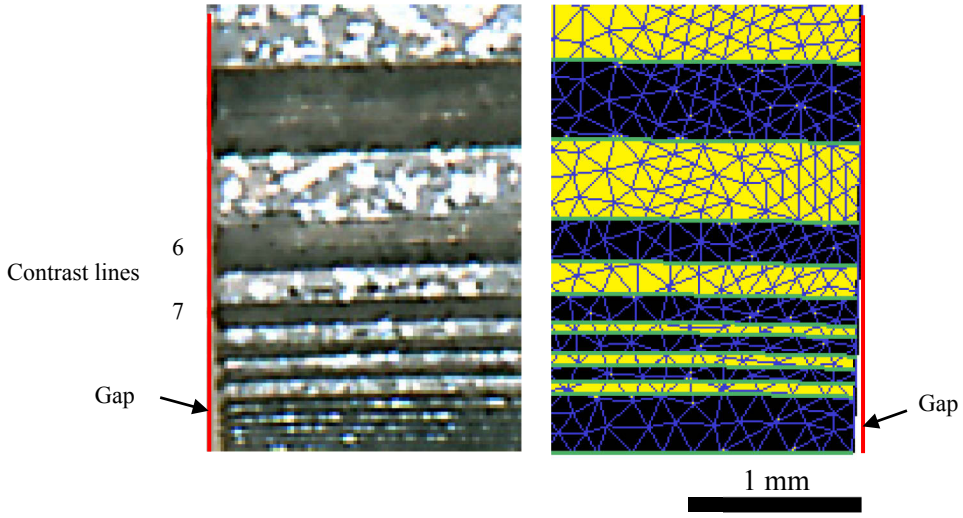

Fig. 8.11. Experimental and simulated sample deformation at the bottom side after upsetting at 400 °C and $\sigma_n{}'$=1.1.

Fig. 8.12 shows a good agreement between experimental and numerical deformation of the internal grid pattern. Thus, the complex material flow inside the tested samples could be successfully reproduced until 1.6 mm and 4.5 mm of friction length. A thickness difference was observed between the experimental and simulated lines 5, 6 and 7 in Fig. 8.12a. The mentioned contrast lines could not be cut in the middle of the circumference due to their small thickness, and therefore they appear to be thinner than the simulated.

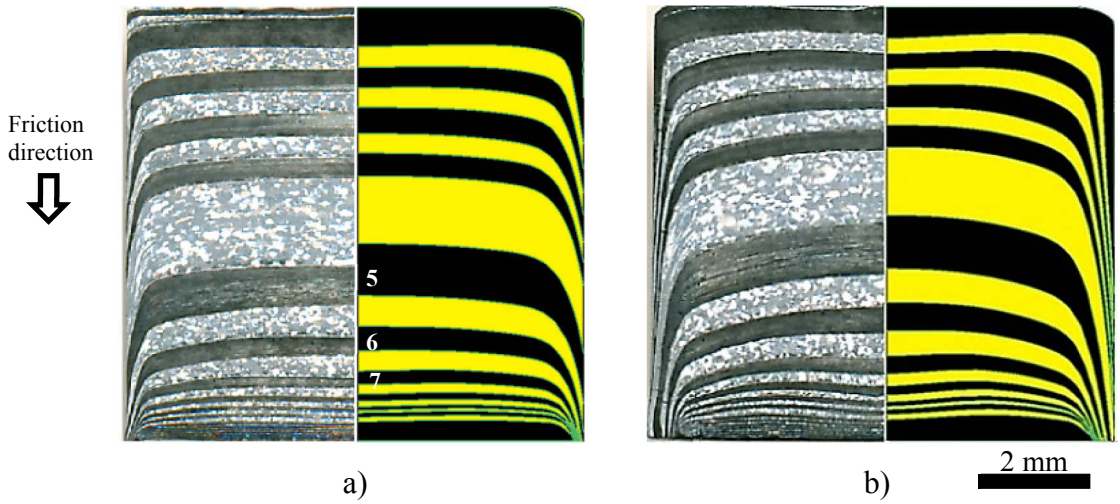

Fig. 8.12. Experimental and simulated intern grid pattern deformed by means of the axial friction tests D at 400 °C and 0.1 mm/s. After a friction length of a) 1.6 mm and b) 4.5 mm.

8.9.2 Simulation of the axial friction test C

Once the friction boundary conditions were validated for the simulation of the axial friction test D (with intern grid pattern) similar friction conditions can be assumed to the simulation of the friction test C. Since a significant higher normalized normal stress ($\boldsymbol{\sigma_n}'$=3.5) was applied in the axial friction test C, it is expected that the new surface placed on the top side of the sample also stick to the moving hollow cylinder. For that reason the whole friction surface moved at the same speed during the friction stroke (Fig. 7.5b). Nonetheless, a dissimilar displacement and strain distribution was detected along the friction boundary layer (Fig. 7.5a,c). Lower values were observed at the top corner, but higher and stable values toward the bottom side. The strain variation does not influence the stress calculation because the constitutive model is only sensible to the strain rate and temperature $\{\overline{\boldsymbol{\sigma}}(\dot{\boldsymbol{\varepsilon}}, \boldsymbol{T})\}$. However, the strain rate was concentrated in a thin shear zone along the whole lateral friction surface (Fig. 7.5d), which defined the magnitude of the shear flow stress (Fig. 7.5e). The calculated shear stress in the thin layer (40 MPa-45 MPa) corresponds to the experimental value obtained by the friction measurements (Fig. 8.6). It suggests that the sticking friction measured with the axial friction test is equivalent to the numerically calculated shear stress of the thin shear layer.

Numerical simulations can also reproduce the material flow during plastic deformation. Fig. 7.5b shows the velocity vectors inside the sample during the axial friction tests at a speed of 0.1 mm/s. The direction and color of the arrows indicate the average velocity direction and speed magnitude respectively. The results show how the stick layer moves with the same speed as the hollow cylinder. On the other hand, the rest of the sample flows with a very slow speed, but with an interesting flow direction. Moreover, the friction subsurface placed on the bottom corner is permanently divided. A thin stick layer flows through the gap between the punch and hollow cylinder and the rest of the workpiece is radially pressed toward the sample center (Fig. 8.13b). The axial material flow in the center of the sample explains the progressive upward movement of the contrast lines showed in Fig. 8.12a,b).

Based on the simulated material flow observed at the top of the sample the initial friction boundary layer is deformed homogeneously and therefore experiments the same displacement and strain. However, the new surface created at the top corner is formed with the material flowing from the center of the sample. That is the reason why the displacement and strain distribution is reduced upward the top corner (Fig. 7.5a,c).

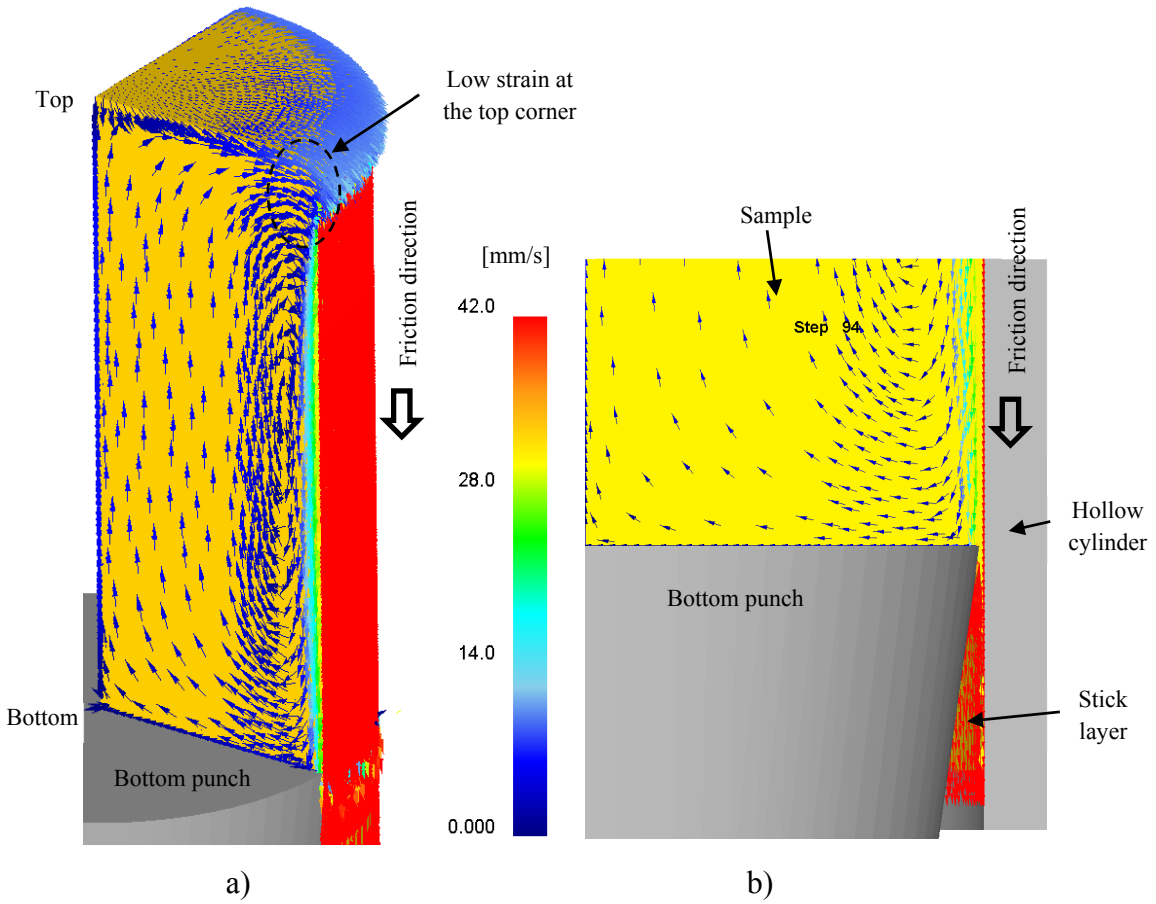

Fig. 8.13. Velocity vector during friction test at 400 °C and 42 mm/s.
a) A quarter model of the sample and b) velocity distribution at the bottom side.

Simulation of the microstructure was not carried out, however the simulation results could be used to identify the high shear deformation zone. Clear microstructure changes in the friction boundary layer allowed the recognition of the high shear deformation zone (Fig. 6.20). According to the literature a minimum strain of 3 approximately is required to obtained equiaxed grains during hot deformation of aluminum [PET03]. Thus, the strain distribution on the shear zone can be used to predict the high shear deformation zone. Fig. 8.14a depicts the strain distribution of a sample tested at 400 °C and 42 mm/s. The lines with different colors illustrate the layers with the same strain. The results showed that a strain in the range from 3 to 4 corresponds to the same thickness of the high shear deformation zone observed in the experimental experiments (Fig. 8.14b).

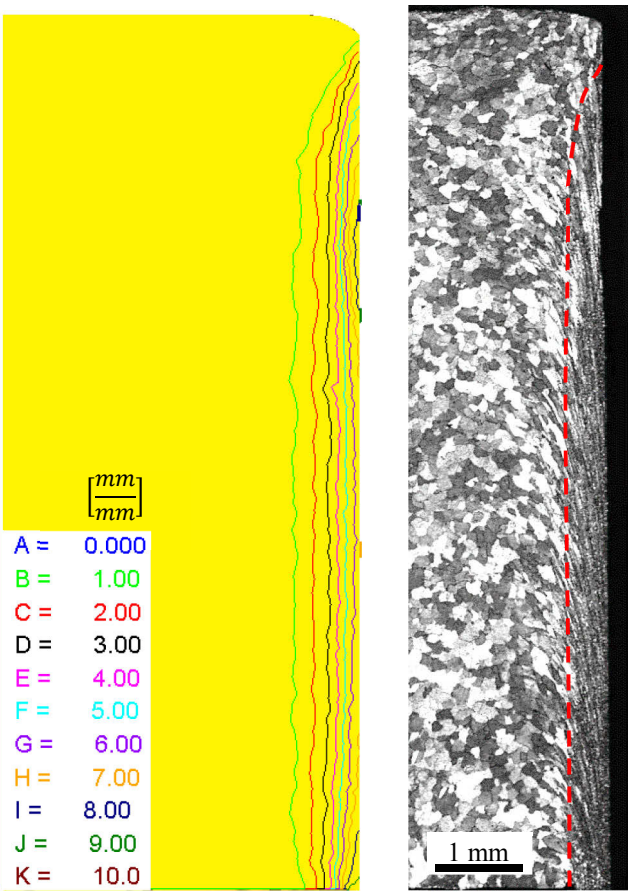

a) b)

Fig. 8.14. Recognition of the high shear deformation zone in samples tested at 400 °C and 42 mm/s by means of a) strain simulation and b) microstructural analysis (LOM).

In addition, the evolution of the experimental and simulated friction force was also compared at 400 °C for the speeds 0.1 mm/s, 1 mm/s and 42 mm/s (Fig. 8.15). The simulated values are illustrated with black curves (Sim), while the experimental values with gray lines (Real). The real curves show the characteristic initial straight slope of the elastic deformation of the whole system. Moreover, the numerical results do not reproduce this effect since the tools were simulated as rigid parts (no elastic deformation). The curves are analyzed comparing the friction magnitudes at the beginning and at the end of the curves. At the beginning of the test similar experimental and numerical values were obtained at 0.1 mm/s and 1 mm/s with a difference of 6 % approximately. The simulated friction force at 42 mm/s was 10 % higher than the experimental value. This higher difference could have been caused due to a higher estimation of the shear flow stress at 42 mm/s. Since the constitutive model is not sensible to the strain, the flow stress is always estimated at ε=0.5. Fig. 6.2c shows that the flow stress increases

progressively with the strain at higher strain rate. Moreover, the experimental and numerical values change during the friction test. At a slow speed (0.1 mm/s and 1 mm/s) the simulated friction remains almost constant, due to the insignificant variation of the contact area and the temperature. However, the progressive reduction of the real friction values until a quasi-steady state could be caused by the softening effect such as DRV and gDRX (Fig. 19b). Softening effect can not be reproduced with the applied material model, therefore the difference at the end of the curves was 20 % at 0.1 mm/s and 15 % at 1 mm/s. Moreover, at high friction speed (42 mm/s) the simulated friction force continuously reduces due to the higher temperature generated during the higher strain rate. On the other hand, the experimental friction force increased slightly due to the strain hardening effect. More accurate simulation results can be obtained incorporating the strain effect in the constitutive model $\{\overline{\boldsymbol{\sigma}}(\dot{\boldsymbol{\varepsilon}}, \varepsilon, \boldsymbol{T})\}$.

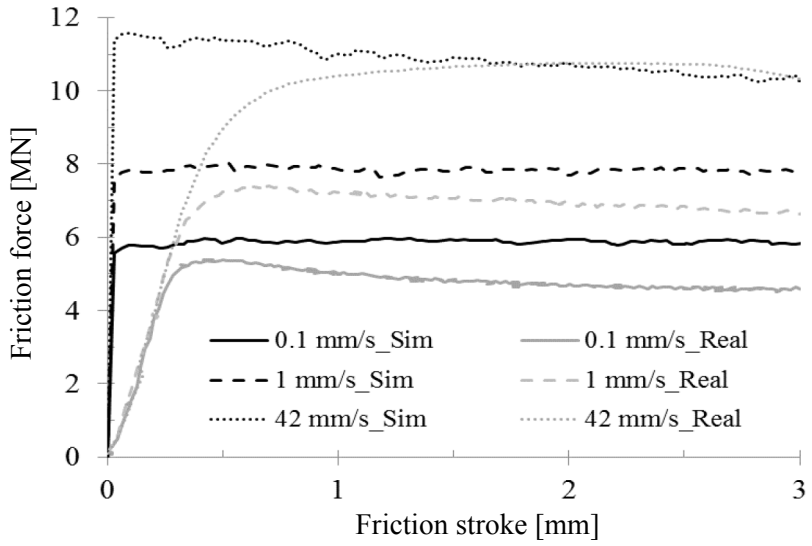

Fig. 8.15. Experimental and simulated friction force between EN AW-6060 and AISI H-13 at 400 °C (sticking conditions – test C).

8.9.3 Simulation of the multi-hole extrusion under different friction conditions inside the bearing channels

Multi-hole extrusion trials were numerical analyzed applying the FEM-based software DEFORM^{TM}. Four different die configurations were used as described in Fig. 5.13b. Thus inserts with -0.5° relief, 0° parallel and +0.5° and +1° choked bearing channels were applied. Sticking contact was set between the workpiece and container as well as with the die face. In order to introduce the friction conditions inside the bearing channels the well-known Tresca

friction model was applied (Eq. 2.22). On one hand different friction factors (*m*) where assumed based on the experimental observations (Table 7.3). Thus, sticking and slipping zones were defined inside the bearing channels. On the other hand no friction factor was assumed, but it was defined by the local normal pressure and temperature according to the Eq. 7.1, which was derived from the new friction model (Eq. 6.2). Moreover, additional variables such as the contact criterion (*separable* or *non separable*) as well as the initial condition of the workpiece were also analyzed.

Fig. 7.9 compares the experimental and simulated results at the peak of the extrusion curve of the experiment 1. The simulated container force was well predicted with only 2 % of difference to the real value. It indicates that the applied material model reproduces properly the real flow stress at the billet contact surface (Fig. 7.10).

During the die filling the billet is compressed about 20 mm with a ram speed of 4 mm/s approximately. Due to the slowly and marginally extrusion stroke the billet experiments low strain (Fig. 8.16a) and strain rates (Fig. 8.16b) comparing to the material filling the die. The strain (Fig. 8.16c) and strain rate (Fig. 8.16d) distribution of the billet subsurface can be better observed reducing to 1 the scaling of the colorbar.

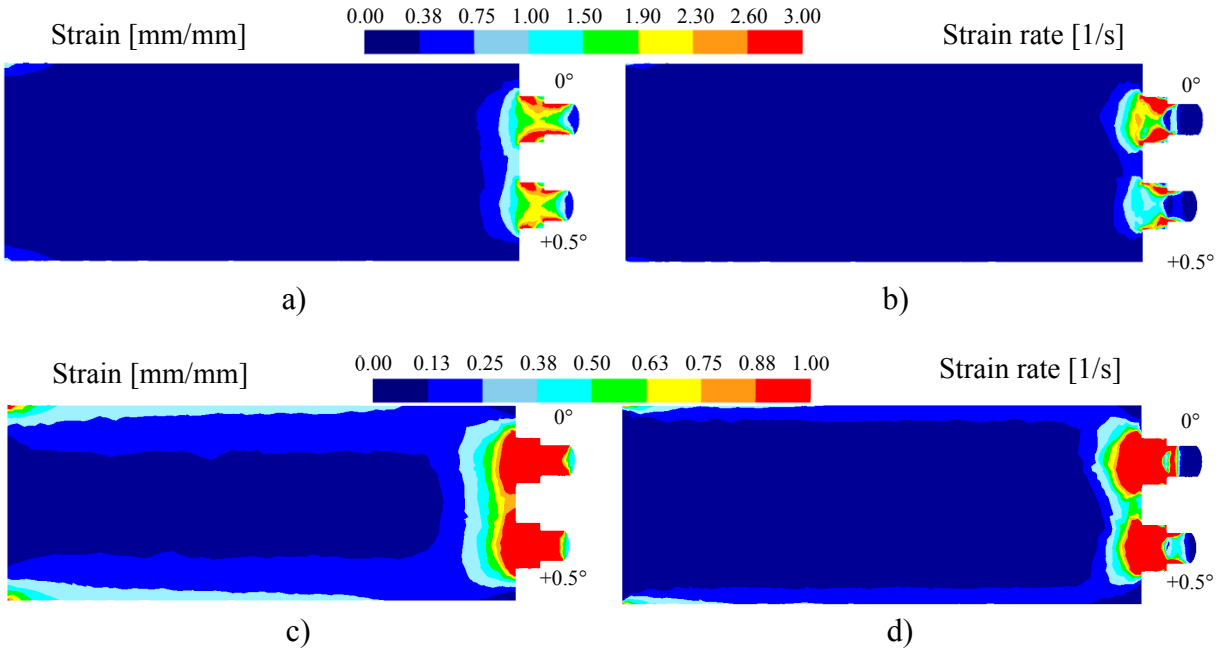

Fig. 8.16. Strain and strain rate distribution at the extrusion peak in the experiment 1. Strain distribution in the range from a) 0 - 3 and b) 0 - 1 as well as strain rate in the range from a) 0 - 3 1/s and b) 0 - 1 1/s.

The results shows that the friction subsurface of the billet is subjected to a maximal strain of 0.5 mm/mm and strain rate of 0.25 1/s at the peak extrusion. These strain and strain rate values are in the range of those evaluated with the hot compression test (Fig. 6.2). Therefore a good estimation of the flow stress is estimated applying the Garofalo or Zener-Hollomon relationship as observed in Fig. 7.9.

As it was noticed in the experimental extrusion trials a dissimilar product speed is caused due to the particular friction interactions inside different bearing angles. The prediction of the product speed distribution and the die force is a complex task, because the friction condition inside one channel is related not only to the bearing configuration and the extrusion parameters, but also to the friction behavior in the neighbor channel. It is known that inside long bearing channels sticking and slipping zones take place [VAL94, MUE96], nevertheless the length of those zones can not be accurately determined. Numerical benchmark of similar multi-hole extrusions has demonstrated the significant influence of the friction modelling on the simulated results [HOR05, DON15]. Even if the friction mechanisms and their interaction length are known as it was determined experimentally in this work (Fig. 6.35), correct friction factors have to be assumed to predict the product speed and die force accurately. Additionally, modelling contact criterion and model simplifications can also influence the numerical results.

Based on the friction mechanisms experimentally observed, the bearing channels were divided into inlet and outlet zones. Table 7.3 resumes the length and the friction factors assumed in each zone. Moreover, the experiment 1 was simulated under five different scenarios described in Fig. 7.7 and Table 7.2. In the first three scenarios (I, II and III) a filled die was simulated assuming an initial workpiece temperature of 460 °C. Furthermore, *separable* contact was set in the scenario I. It means that the elements are allowed to separate from the die land. Fig. 8.17a depicts the contact area at the beginning of the simulation. The results showed that after the first simulation step significant number of element lost the contact in the bearing channel (Fig. 8.17b) probably due to the reduction of the radial or normal pressure. This problem remains during the whole simulation and reduces the die force as well as influences the product velocity distribution.

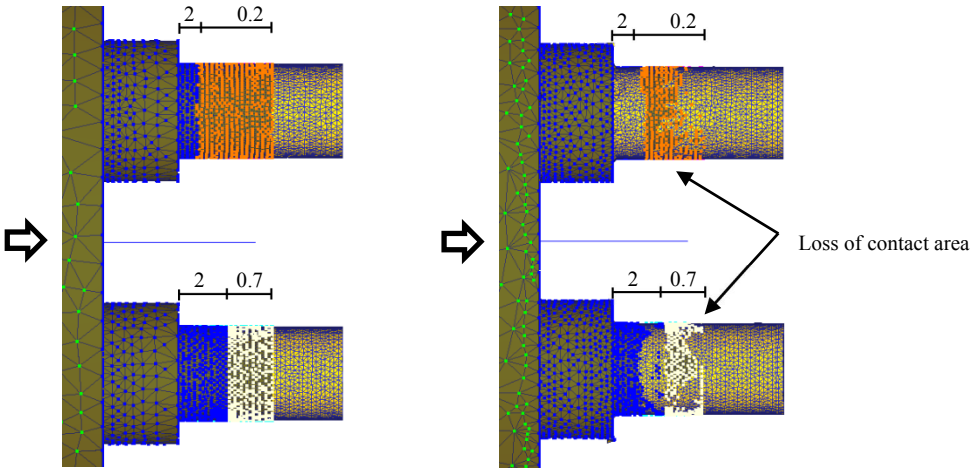

Fig. 8.17. Contact area between the workpiece and die in the simulation of the experiment 1 under scenario I. a) Initial contact area and b) contact area after the first simulation step.

A more stable contact area was achieved applying *non separable* contact conditions and for that reason was applied for the scenarios II, III, IV and V. The die force estimated with the scenario II was 28 % higher than in the scenario I (Fig. 7.9a). Moreover, when the elements are forced to contact the die land additional force has to be applied to separate the contact nodes from the end of the bearing channel. This extra friction force was 14 % approximately, and can be reduced introducing a longer bearing but keeping the same friction area by means of friction windows (Scenario III, Fig. 7.7c).

Due to the significant strain and strain rate observed in the primary deformation zone and inside the die a local temperature increase is expected. This effect could be accompanied by a reduction of the flow stress and thus the die force. The die filling was simulated in the scenario IV obtaining a maximal temperature increase of 20 °C inside the die (Fig. 7.7d) and a die force reduction of 7 % (Fig. 7.9). In the scenario V the friction factor is defined as a function of the contact pressure and temperature (Eq. 7.1). This function allows a variation of the fiction factor from 0 to 1. However, in DEFORM^{TM} means that sticking conditions ($m \geq 2$) can not be reproduced. For that reason the estimated die force was 12 % lower than in the scenario IV.

The scenario IV is considered the best condition to reproduce the multi-hole extrusion of the experiment 1. A good prediction of the product speed was achieved applying the scenarios V and IV, however overestimated die forces where observed. The die force estimated with the scenario IV (3.5 kN) was almost 40 % higher than the experimental value (2.5). This variation

could be caused because softening effects in the primary deformation zone and inside the die can not be reproduced with the Garofalo relationship. The applied material model was based on the results obtained by means of hot compression tests with a maximum strain of 0.5. On the other hand, as it has been reported in the literature [PET03] and confirmed during the sticking friction tests (Fig. 6.19b, Fig. 8.14) gDRX take place during the aluminum deformation at high temperature and high strain. Since high strains (2-3) were estimated inside the pockets and the bearing channels at the peak of the extrusion (Fig. 8.16) the softening effect could have caused the significant reduction of the experimental die force. The scenarios IV and V were also applied to simulate the extrusion experiments 2, 3 and 4. Fig. 8.18 compares the experimental and simulated results. Similar to the experiment 1, overestimated die forces were numerically determined. The values obtained with the scenario V (new friction model) were lower than the scenario IV, because no sticking could be simulated. An improved calculation of the die force should be achieved including the softening effects in the constitutive model.

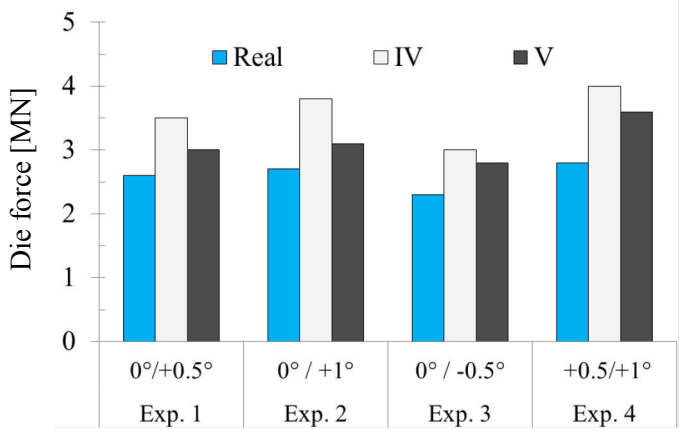

Fig. 8.18. Experimental and simulated (scenarios IV and V) die force of the extrusion trials.

Figs. 7.11-14 show the simulated distribution of the effective stress, temperature and velocity inside the die, applying the scenarios IV and V. In general higher stress was produced inside the pocket at a higher flow velocity, because the material is subjected to a higher strain rate. On the other hand, the choked bearing channel depicted higher stresses than the parallel caused by the stronger friction conditions. Different friction scenarios (IV and V) generated similar stress distribution in the pocket area. Nevertheless, higher stress distribution was observed in the bearing channel applying the Tresca friction model. Since the contact nodes can be moved applying a friction factor of m=1 no sticking was reproduced using the new friction model ($0 \leq m \leq 1$). Nonetheless, severe shearing was forced by applying sticking contact (m=2) and this explains the increase of stress and thus the die force. As a consequence of the sticking scenario

the estimated temperature on the thermocouple position was higher than in the scenario V and very close to the experimental value. Although the relevant different of the mentioned boundary conditions similar product speed was estimated, because it does not only depend on the local friction magnitude, but on the relative friction between channels (Fig. 8.19)

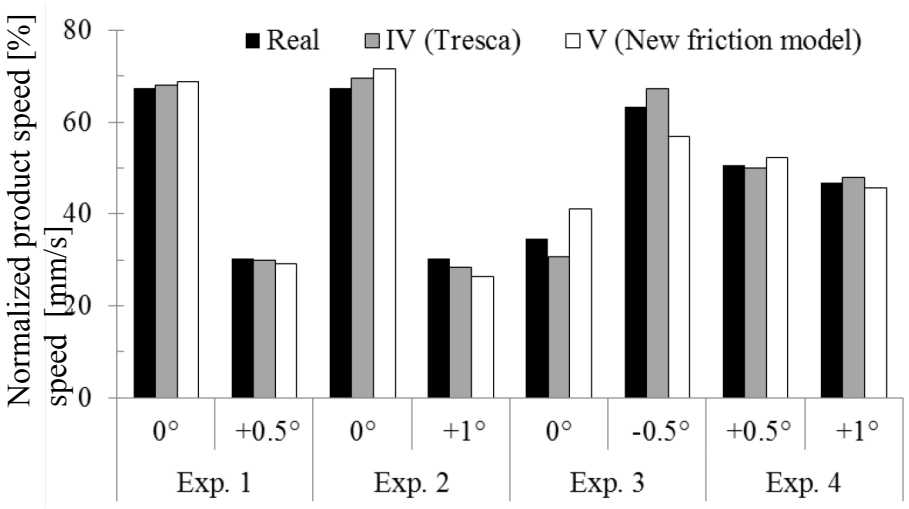

Fig. 8.19. Experimental and numerical product speed applying different combination of bearing angles and friction conditions.

Similar experimental product speed distribution was well predicted by means of numerical simulations. A maximal deviation of 4 % was estimated applying constant friction factors in different friction zones (Table 7.3). However, this method can not be used in the practice, because the real friction mechanisms and their contact interction lengths are unknown. In addition, a maximal deviation of 6 % was obtained with the new friction model (scenario V). Since, the friction factor was not assumed constant, but it was calculated based on the local pressure and temperature, this method is suitable to the friction simulation inside bearing channels. Thus, during the iterative simulation process the normal pressure distribution inside the bearing channel is estimated and the local friction factor defined. As a consequence higher normal pressures generate larger friction resistance and therefore higher effective stress (Fig. 7.8). Fig. 8.20 depicts the pressure and effective stress distribution of the workpiece surface inside the die obtained at the extrusion peak of the experiment 1 applying the new friction model. The simulation estimates not only higher pressure inside the +0.5° choked channel, but its variation along the bearing channel (Fig. 8.20a). Since the friction is related to the normal pressure (Eq. 7.8) a higher resistance and effective stress is caused at higher normal pressures (Fig. 8.20b). Additionally, the pressure and stress distribution illustrates different zones with

different colors, which have also similar lengths to those recognized experimentally inside the bearing channels (Fig. 6.35a,b). Thus, the length of the sticking and slipping zones can be also estimated inside long bearing channels applying the new friction model.

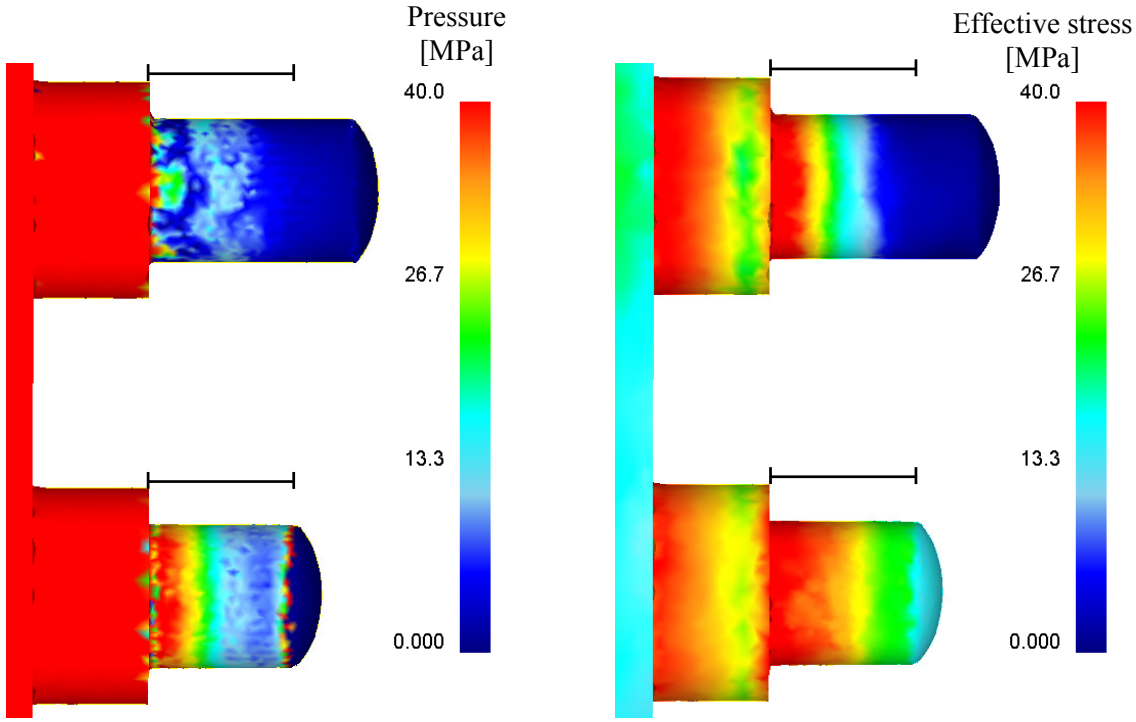

a) b)

Fig. 8.20. Numerical simulation of the extrusion experiment 1 applying the new friction model (scenario V). Numerical distribution of the a) normal pressure and b) effective stress.

Fig. 8.21 compares the simulated effective stress distribution and the length of the friction mechanisms observed inside the bearing channels of the experiment 1. The results show maximal stress (35-40 MPa) at the sticking zones detected experimentally. Moreover, a stress reduction was detected in the slipping zones caused by the reduction of the normal contact pressure.

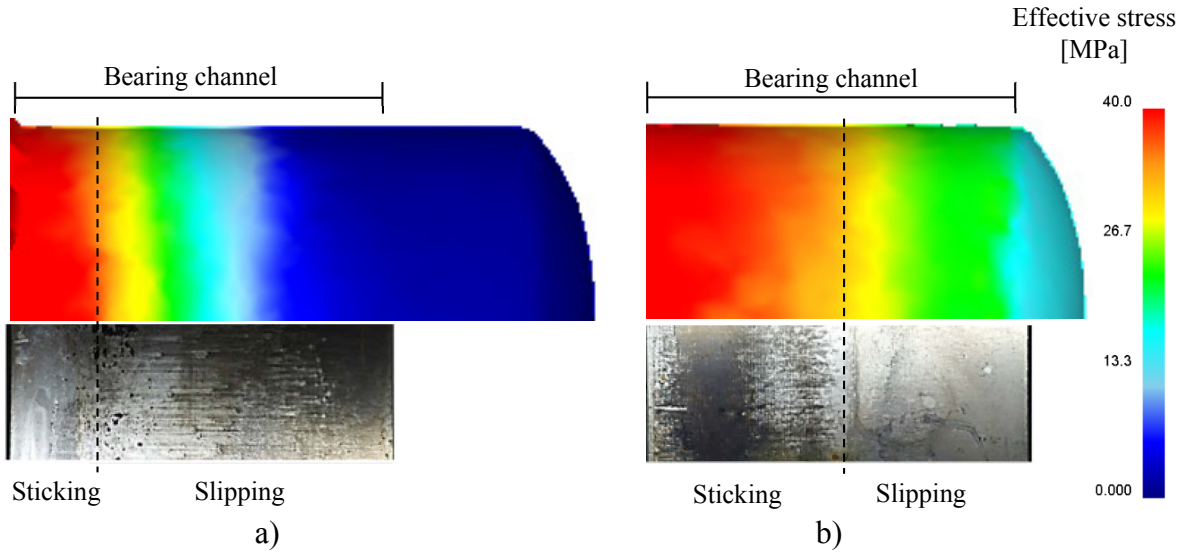

Fig. 8.21. Simulated effective stress distribution and surface appearance inside the a) parallel and b) +0.5° choked bearing channels.

9 Conclusions

In the present work the friction in hot extrusion of the aluminum alloy EN AW-6060 was investigated. The study combined experimental and numerical investigations in order to improve the understanding of the friction phenomena and its modelling in multi-hole extrusion processes. To achieve this goal the study was divided into different phases. First, the thermo-visco-plastic response of the EN AW-6060 was evaluated by means of hot compression tests ($\varepsilon \leq 0.5$). Furthermore, the friction between EN AW-6060 and the hot working steel AISI H-13 was experimentally investigated. Slipping conditions were studied using the tribo-torsion-test. In order to reproduce sticking conditions a new friction device (axial friction test) was developed. Thus, the sticking friction and the microstructure in the friction boundary layer were successfully developed. Based on the experimental results a new empirical friction model was developed. Moreover, experimental and numerical multi-hole extrusion trials were carried out applying -0.5° relief, 0° parallel and +0.5° and +1° choked bearing channels. Additionally, simulations of the axial friction tests were also accomplished.

Compression tests confirmed the viscoplastic behavior of the EN AW-6060. As it can be reproduced by the Zener-Hollomon parameter Z higher stress were obtained at lower temperatures and higher strain rate (high Z), but lower stress at higher temperatures and lower strain rates (low Z). Microstructure analysis revealed deformed grains with the original grain boundaries and dendritic structure at 300 °C and 400 °C. However, serrated grain boundaries as well as subgrains were observed by means of LOM at 500 °C. The simultaneous effect of the strain hardening and dynamic recovery (DRV) is expected to explain the observed plastic behavior. At lower temperatures (300 °C and 350 °C) the strain hardening overcome the DRV influence obtaining thus a higher stress. At higher temperatures (450 °C and 500 °C) the strain hardening is balanced by a more efficient DRV. According to the results the strain in the range $0.05 < \varepsilon \leq 0.5$ has a very low influence on the stress at temperatures higher than 450 °C. Applying the Garofalo or Zener-Hollomon relationship (ΔH=201.386 kJ/mol, n=5.2945, A=2.03E+14 1/s and α=0.02665 MPa^{-1}) the experimental stress values at ε=0.5 were well estimated.

Slipping friction investigated using the tribo-torsion-test showed a linear relation between the friction stress and normal pressure. Thus, the friction stress increased proportionally with the pressure from 10 MPa to 40 MPa at 400 °C and 500 °C. The stress-pressure ratio or friction coefficient (μ) was 1 and 0.8 at 400 °C and 500 °C respectively. The relative speed had a low

influence on the friction stress in the studied pressure range, possibly due to movement and rotation of detached particles of aluminum between the friction planes, which reduce the shearing effect at higher speeds.

The friction investigation under high pressures ($P/\bar{\sigma}>3$) and a wide range of temperatures (300 °C-500 °C) and speeds (0.1 mm/s – 42 mm/s) could be achieved applying the new friction device. Moreover, full sticking conditions could be reproduced by the new friction device applying a normalized normal stress of 3.5. Full sticking friction was validated by means of friction force measurements, microstructure analysis and internal grid pattern technique. At 500 °C, the adhesion interaction represented about 95 % of the total friction stress, possibly due to the higher molecular diffusion at high temperatures. Microstructural analysis of the friction boundary layer revealed a high shear deformation zone at the friction subsurface characterized by a structure grain refinement. Numerical simulations validated with intern grid pattern, suggested that the high shear deformation zone is closed related to the strain generated during the sticking friction test. At 400 °C and 42 mm/s the shear zone could be well reproduced from a strain of 3. Moreover, the simulated strain reached a maximal value of 8 at the friction surface after approximately 3 mm of sticking friction length. The evolution of the measured friction force corresponds to the force needed to deform plastically the high shear deformation zone. Thus, the sticking friction test is comparable to a shear test and therefore the sticking friction stress is equivalent to the shear flow stress. Hence, the sticking friction depends on the deformation mechanism and microstructure evolution of the high shear deformation zone. A high fragmentation of the initial grains was observed at 300 °C generating an average grain sizes of 4 µm at 0.1 mm/s and even smaller at 42 mm/s. At 400 °C, an average grain size of 9 µm and 5 µm were detected in samples tested at 0.1 mm/s and 42 mm/s respectively. The presence of small equiaxed grains with large number of large high angle grain boundaries (HAGBs>15) confirmed geometric dynamic recrystallization (gDRX). Grains with higher average size were observed in samples tested at 500 °C due to the most efficient effect of the DRV. At low speed (0.1 mm/s), equiaxed grains (30µm) with high angle grain boundaries (HAGBs>15) were also observed, suggesting gDRX. Moreover, static recrystallized grains (70 µm) were distinguished in samples tested at 42 mm/s. According to the experimental results the EN AW 6060 experimented a relevant softening effect (>10%) during large strains at high temperature (450 °C and 500 °C) and low deformation rate ($\dot{\varepsilon}<10$ 1/s). This effect was not observed during hot compression tests due to the very low strain ($\varepsilon \leq 0.5$).

Changes in the bearing angles generated a low variation of the extrusion force, but a great influence on the product speed distribution. The most significant influence on the length and product speed was detected when the bearing angle was changed from -0.5° relief to +0.5° choked. A higher friction force was generated applying higher choked channels (+1°), however it had a very low influence on the product speed because the flow distribution is defined by the friction combination of all channels. Choked channels generated higher friction or flow resistance than parallel channels, due to the formation of a sticking zone at the inlet of the channel. Additionally, higher choked channels are related to longer sticking zones, but it has not a direct influence on the speed distribution. The sticking zones are followed by slipping regions, which generate lower friction resistance. Sticking zones were identified by the presence of iron oxide layer on the bearing channel and the filled aluminum material as well as a localized grain refinement in the friction subsurface. In parallel channels the contact surface appearance and numerical simulations suggested a lower normal pressure than in choked channels. Due to the lower pressure the iron oxide layer is progressively removed, but the workpiece is eventually adhered under sticking or quasi-sticking conditions on the bearing channel.

A lower temperature inside the bearing channels was estimated using the new friction model, because sticking friction was not reproduced. Since sticking conditions could not be reproduced in DEFORM^{TM} with the estimated friction factor ($0 \leq m \leq 1$) the lower deformation work led to a lower heat generation. Simulated container force was well predicted with the Garofalo or Zener-Hollomon relationship, because the deformation conditions of the billet surface ($\varepsilon \approx 0.5$ mm/mm, $\dot{\varepsilon} \approx 0.25$ 1/s, $T \approx 460$°C) were inside the range studied during the hot compression tests. Nevertheless, the estimated die force was higher than the measured because the mentioned material model could not reproduced the softening effect at large strains (2-3) caused inside the pocket and bearing zones. The distribution of the product speed in the studied multi-hole extrusion trials could be successfully simulated applying the new friction model. Thus, the new friction model is suitable to the friction simulation inside bearing channels, since any friction factor was assumed, but it was calculated based on the local pressure and temperature.

10 References

[ABT95] S. Abtahi. Friction and Interface Reactions on the Die land in Thin-Walled Extrusion. Doctoral Thesis NTNU Trondheim (1995)

[ABT96] S. Abtahi, T. Welo and S. Støren. Interface Mechanisms on the Bearing Surface in Extrusion. Proc. of the 6th Int. Aluminium Extrusion Tech. Seminar. (1996) Vol. 2, pp. 125-131.

[AKE81] R. Akeret. Influence of Shape and Die Design on Metal Flow, Extrusion Load and Speed. In (Conference Report) Extrusion Scientific and technical Development, Garmisch-Partenkirchen 1982, Ed. G. Lang et al., Deutsche Gesellschaft für Metallkunde, (1981) pp. 191-207.

[AKE83] R. Akeret. Einfluß der Querschnittsform und der Werkzeuggestaltung beim Stranpressen von Aluminium. Teil I: Vogänge in der Umforzone. Aluminium. (1983) Vol. 59, No.9, pp. 665-669.

[AKE83] R. Akeret. Einfluß der Querschnittsform und der Werkzeuggestaltung beim Stranpressen von Aluminium. Teil II: Die Reibung im Presskanal. Aluminium. (1983) Vol. 59, No.10, pp. 745-750.

[AKE85] R. Akeret. Einfluß des Neigungswinkels und des Länge der Lauffläche auf die Reibung im Preßkanal. Aluminium. (1985) Vol. 61, No.3, pp. 169-172.

[AKE88] R. Akeret and W. Strehmel. Control of Metal Flow in Extrusion Dies. Proc. of the Fourth Int. Aluminium Extrusion Tech. Seminar. (1988) Vol. 2, pp. 357-367.

[ASM93] ASM Metals Reference Book. ASM International, third edition, OH 44073-0002 Materials Park, 1993.

[AST00] Standard Test Method for Macroetching Metals and Alloys. Annual book of ASTM Standars, E 340-00, Vol 03.01, pp. 1-11.

[AVI83] B. Avitzur. Handbook of Metal-Forming Processes. Wiley-Interscience, New York, 1983.

[BAU06] M. Bauser, G. Sauer and K. Siegert. Extrusion. Second Edition, ASM International, Ohio, 2006.

[BEC14] C. Becker, P. Hora, J. Maier and S. Mueller. Experimental Investigations of Friction Carried out with the Tribo-Torsion-Test and Frictional Modelling. Key Engineering Materials. (2014) Vol. 585, pp. 25-32.

[BEH09] B. Behrens, M. Alasti, A. Bouguecha, T. Hadifi, J. Mielke and F. Schäfer. Numerical and experimental investigations on the extension of friction and heat transfer models for an improved simulation of hot forging processes. 12th ESAFORM Conference on Material Forming. (2009) pp.

[BEN66] R. Benzing, V. Hopkins, M. Petronio and F. Villforth. Friction and Wear Devices - A Survey. Wright-Patterson Air Force Base, Ohio. (1966)

[BIN22] E. Bingham. Fluidity and Plasticity. McGraw-Hill. (1922) New York.

[BIR07] L. Birta and G. Arbez. Modelling and simulation. Springer-Verlag, London (2007).

[BJO99] T. Bjoerk, J. Bergstroem and S. Hogmark. Tribological Simulation of Aluminium Hot Extrusion. Wear. (1999) Vol. 224, pp. 216-225.

[BLA81] P. Blau. Mechanisms for Transitional Friction and Wear Behavior of Sliding Metals. Wear. (1981) Vol. 72, pp. 55-66.

[BOW50] F. Bowden and D. Tabor. The Friction and Lubrication of Solids. Oxford Univ. Press. (1950)

[BUC08] B. Buchner. Investigation of the friction in closed-die warm forging of aluminium alloys. Doctoral Thesis (2008) University of Leoben, Austria.

[BUD11] R. Budynas and J. Nisbett. Shigley's Mechanical Engineering Design. Ninth Edition, Mc Graw Hill, New York, 2011.

[BUR94] D. Buryta, R. Sowerby and I. Yellowley. Stress Distributions on the Rake Face During Orthogonal Machining. Int. J. of Machine Tools and Manufacture. (1994) Vol. 34. pp. 721-739.

[BUS92] A. Buschhausen, K. Wainmann, J. Lee and T. Altan. Evaluation of Lubrication and Friction in Cold Forging Using a Double Backward-Extrusion Process. J. of Materials Processing Technology. (1992) Vol. 33, pp. 95-108.

[CAM13] A. Camacho, A. Torralvo, C. Bernal and L. Sevilla. Investigation of Friction Factors in Metal Forming of Industrial Alloys. Procedia Engineering. (2013) Vol. 63, pp. 564-572.

[CHA06] J. Chakrabarty. Theory of Plasticity. Third Edition, Elsevier Bitterworth-Heinemann, Oxford, 2006.

[CHA79] J. Challen and P. Oxley. An Explanation of the Different Regimes of Friction and Wear Using Asperity Deformation Models. Wear. (1979) Vol. 53, pp. 229-243.

[CHE78] C. Chen and S. Kobayashi. Rigid Plastic Finite Element Analysis of Ring Compression. Application of Numerical Methods for Forming Processes. (1978) Vol. 28, pp. 163-174.

[CHE85] L. Chen and D. Rigney. Transfer during Unlubricated Sliding Wear of Selected Metal Systems. Wear. (1985) Vol. 105, pp. 47-61.

[CLO90] M. Clode and T. Sheppard. Formation of the Die Lines During Extrusion of AA6063. Mat. Sci. And Techn. (1990) Vol. 6, pp.755-763.

[CLO92] M. Clode. Material Flow and Microstructural Development During Extrusion of AA6063. Proc. of the 5th Int. Aluminium Extrusion Tech. Seminar. (1992) Vol. 2, pp. 79-99.

[COC62] M. Cocks. Interaction of Sliding Metal Surfaces. J. Appl. Phys. (1962) Vol. 33, pp 2152-2161.

[DAU73] J. Dautzenberg and J. Zaat. Quantitative Determination of Deformation by Sliding Wear. Wear. (1973) Vol. 23, pp. 9-19.

[DAU80] J. Dautzenberg. The Role of Dynamic Recrystallization in Dry Sliding Wear. Wear. (1980) Vol. 60, pp. 401-411.

[DEF12] Deform, Deform v10.2.1. Integrated 2D3D System manual. Deform, Ohio 2012.

[DON08] M. Schikorra, L. Donati, L. Tomesani and A. Tekkaya. Microstructure Analysis of Aluminium Extrusion: Prediction of microstructure on AA6060 alloy. J. of Mechanical Processing Technology. (2008) Vol. 201, pp. 156-162.

[DON15] A. Selvaggio, L. Donati, B. Reggiani, M. Haase, C. Dahnke, M. Schwane, L. Tomesani, A.E. Tekkaya. Scientific Benchmark 2015: Effect of choking and bearing length on metal flow balancing in extrusion dies. To be published in Materialstoday: Proceedings 2015.

[DOW97] D. Dowson. History of Tribology. Second Edition, Professional Engineering Publishing. (1944) ISBN 1-86058-070-X.

[DUA03] X. Duan and T. Sheppard. Simulation and Control of Microstructure Evolution During Hot Extrusion of Hard Aluminium Alloys. Materials Science and Engineering A. (2003) Vol. 351, pp. 282-292.

[DUE68] W. Duerrschnabel. Der Materialfluss beim Strangpressen von NE-Metallen. Metall. (1968). Vol. 22, I: pp. 426-437, II: pp. 995-998, III: pp. 1215-1219.

[FLI00] I. Flitta and T. Sheppard. On the Mechanics of Friction During the Extrusion Process. Proc. of the Seventh Int. Aluminium Extrusion Tech. Seminar. (2000) Vol. 1, pp. 197-203.

[FLI03] I. Flitta and T. Sheppard. Nature of Friction in Extrusion Process and its Effect on Material Flow. Materials Science and Technology. (2003) Vol. 19, pp.19.

[FLI05] I. Flitta and T. Sheppard. Material Flow During the Extrusion of Simple and Complex Cross-Sections Using FEM. Journal of Materials Science and technology. (2005) Vol. 21, pp. 648-656.

[GAR04] R. Garrett, J. Lin and T. Dean. An Investigation of the Effects of Solution Heat treatment on mechanical Properties for AA6xxx Alloys: Experimentation and Modelling. International Journal of Plasticity. (2004) Vol. 21, pp. 1640-1657.

[GEE04] W. Geertruyden and W. Misiolek. Analysis of Peripheral Coarse Grain Recrystallization in 6XXX Aluminium Alloy Extrusion. Proc. of the Eighth Int. Aluminium Extrusion Tech. Seminar. (2004) Vol. 1, pp. 107-113.

[GEE05] W. Geertruyden, H. Browne, W. Misiolek and P. Wang. Evolution of surface recrystallization during indirect extrusion of 6xxx aluminum alloys. Metallurgical and Materials Transactions A. Vol. 36A, pp. 1049-1056.

[GLA81] R. Glardon and I. Finnic. A Review of the Recent Literature on the Unlubricated Sliding Wear of Dissimilar Metals. Trans. ASME, J. Mater. Technol. (1981) Vol. 103, pp. 333-340.

[GOT05] G. Gottstein. Physical Foundations of Material Science. Springer, Berlin, 2005.

[HIL50] R. Hill. The Mathematical Theory of Plasticity. Clarendon Press, Oxford 1950.

[HIN79] E. Hinton and D. Owen. An Introduction to Finite Element Computations. Pineridge Press Ltd., U.K 1979

[HOR05] P. Hora, C. Karadogan and L. Tong. Numerische Modellierung thermischer und tribologischer Randbedingungen. Conference Proceedings: Extrusion Zurich (2005)

[HOR05] P. Hora st al.: Extrusion Zuerich 2005, Proceedings of the Extrusion benchmark 10.-11. March 2005, Institute of Virtual Manufacturing, ETH Zuerich.

[HOR12] P. Hora, M. Gorji and J. Maier. Analyzing the Tribological Phenomena in Hot Extrusion Process by using New Torsion-Tribo Test. Proc. of the 10th Int. Aluminium Extrusion Tech. Seminar. (2012) Vol. 1, pp. 461-470.

[HOR12] P. Hora, M. Gorji and B. Berisha. Modeling of Friction Phenomena in Extrusion Processes by Using a New Torsion-Friction Test. Key Engineering Materials. (2012) Vol. 491, pp. 129-135.

[HOR14] P. Hora, C. Becker, L. Tong. J. Maier and S. Mueller. Advanced frictional models for extrusion applications. Key Engineering Materials. (2014) Vol. 585, pp. 41-48.

[HUM04] F.J. Humphreys and M. Hatherly. Recrystallization and Related Annealing Phenomena. Second Edition, Oxford, 2004.

[IM02] Y. Im, J. Cheon and S. Kang. Determination of Friction Condition by Geometrical Measurement of Backward Extruded Aluminum Alloy Specimen. J. of Manufacturing Science and Engineering. (2008) Vol. 124, pp.409-415.

[JAV06] M. Javadi and M. Tajdari. Experimental Investigation of the Friction Coefficient Between Aluminium and Steel. Materials Science-Poland. (2006) Vol. 24, No. 2/1, pp. 305-310

[JOH58] W. Johnson, P. Mellor and D. Woo. Extrusion Trough Single Hole Staggered and Unequal Multi-hole Dies. Journal of the Mechanics and Physics of Solid. (1958) Vol. 6, pp. 203-222.

[JOH85] K.L. Johnson. Contact Mechanics. Cambridge University Press, Cambridge, 1985.

[JOO02] M. Bakhshi-Jooybari. A Theoretical and Experimental Study of Friction in Metal Forming by the Use of the Forward Extrusion Process. J. of Materials Processing Technology. (2002) Vol. 125-126, pp. 369-374.

[KAI03] S. Kailas and P. Menezes. Coefficient of Friction and Material Transfer Studies of an Al-Mg Alloy Pin on EN8 Steel Flat Using inclined Scratch. Proceedings of International Seminar on Metal Forming. (2003) pp. 124-143.

[KAI09] S. Kailas, P. Menezes and Kishore. Influence of Surface Texture and Roughness Parameters on Friction and Transfer layer formation During Sliding of Aluminium Pin on Steel Plate. Wear. (2009) Vol. 267, pp. 1534-1549.

[KAM12] M. Kammler, T. Hadifi, M. Nowak and A. Bouguecha. Experimental and Numerical Investigation on Metal Flow during Direct Extrusion of EN AW-6082. Key Engineering Materials. (2012) Vol. 491, pp.137-144.

[KAN11] S. Kang, K. Lee and Y. Lee. Evaluation of interfacial friction condition by Boss and Rib Based on Backward Extrusion. Int. J. of Mechanical Sciences. (2011) Vol. 53, pp. 59-64.

[KAR05] C. Karadogan, F. Vanini, L. Tong and P. Hora. State of the Art and Potential Development of Digital Extrusion Modeling. Light Metal Age. (2005) Vol. 63, pp. 40-43.

[KAR07] C. Karadogan, L. Tong and P. Hora. An Improved Modelling of Friction for Extrusion Simulations. 10th ESAFORM Conference on Material Forming. (2007) pp. 1325-1330.

[KAR10] C. Karadogan, R. Grueebler and P. Hora. A New Cone-Friction Test for Evaluating Friction Phenomena in Extrusion Processes. Key Engineering Materials. (2010) Vol. 424, pp. 161-166.

[KAY10] T. Kayser, B. Klusemann, H. Lambers, H. Maier and B. Svendsen. Characterization of Grain Microstructure Development in the Aluminium Alloy EN AW-6060 During Extrusion. Materials Science and Engineering A. (2010) Vol. 527, pp. 6568-6573.

[KEM67] A. Kemppinen. Die Pick-up Formation Investigated. Metals. (1967) Vol.2, pp.60.

[KIK88] S. Kikuchi and M. Sukimoto. Analysis of Metal Flow and Recrystallization Behavior in Extrusion and Application of the Results to Commercial Production. Proc. of the Fourth Int. Aluminium Extrusion Tech. Seminar. (1988) Vol. 2, pp. 343-355.

[KOB89] S. Kobayashi, S. Oh and T. Altan. Metal Forming and the e Element Method. Oxford University Press. 1989.

[KRA90] A. Krausz, J. Dickson, J. Immarigeon and W. Wallace. Constitutive Laws of plastic Deformation and Fracture. Kluwer Academic Publishers. Netherlands 1990.

[LAN81] G. Lang. Abschätzung der Reibung im Preskannal beim direkten und indirekten Strangpressen von Al99,6. Aluminium. (1981) Vol. 57, No. 12, pp. 791-796.

[LAN84] G. Lang. Reibung im Presskanal beim Direkten und Indirekten Strangpressen von AL99.6, AlMgSi0.5 und AlZn4.5Mg1. Aluminium. (1984) Vol. 60, No.4, pp. 266-268.

[LAN84] G. Lang. Determination of the Die Land Friction in the Direct and Indirect Extrusion of A199.6, AlMgSi0.5 and AlZn4.5Mg1. Aluminium. (1984) Vol. 57, No.12, pp. 791-796.

[LEF92] M. Lefsta, O. Reiso and V. Johnsen. Flow of the Billet Surface in Aluminium Extrusion. Proc. of the 5th Int. Aluminium Extrusion Tech. Seminar. (1992) Vol. 2, pp. 503-517.

[LEV97] A. Levanov. Improvement of Metal Forming Processes by Means of Useful Effects of Plastic Friction. Journal of Material Processing Technology. (1997) Vol. 72, pp. 314-316.

[LI03] Q. Li, C. Smith, C. Harris and M. Jolly. Finite Element modelling Investigations Upon the Influence of Pocket Die Designs on Metal Flow in Aluminium Extrusion Part II. Effect of Pocket Geometry Configurations on Metal Flow. Journal of Materials Processing Technology. (2003) Vol.135, pp. 197-203.

[LI03] Q. Li, C. Smith, C. Harris and M. Jolly. Finite Element modelling Investigations Upon the Influence of Pocket Die Designs on Metal Flow in Aluminium Extrusion Part I. Effect of Pocket Angle and Volume on Metal Flow. Journal of Materials Processing Technology. (2003) Vol.135, pp. 189-196.

[LIB10] W. Libura, A. Rękas and D. Leśniak. Numerical Analysis of Four-Hole Extrusion of Aluminium Alloys. Key Engineering Materials. (2010) Vol. 424, pp. 173-179.

[LIB92] W. Libura and J. Zasadzinski. The Strain Gradient Effect on Microstructure and Properties of Extruded Aluminium Alloys. Proc. of the 5th Int. Aluminium Extrusion Tech. Seminar. (1992) Vol. 2, pp. 485-494.

[LIE11] J.H. Lienhard IV, J.H. Lienhard V. A Heat Transfer Textbook. Fourth Edition, Phlogiston Press, Cambridge, 2011.

[LIN03] X. Lin, H. Xiao and Z. Zhang. Research on the Selection of Friction Models in the Finite Element Simulation of Warm Extrusion. Acta Metallurgica Sinica. (2003) Vol. 16, No. 2, pp. 90-96.

[LIN84] S. Lingard, K. Fu and K. Cheung. Some Observations of the Wear of Aluminium Rubbing on Steel. Wear. (1984) Vol. 96, pp. 75-84.

[LUN95] J. Lundberg. Influence of Surface Roughness on Normal-Sliding Lubrication. Tribol. Int. (1995) Vol. 28, pp. 317-322.

[LUP05] R. Lupoi and F. Hosman. Under Surface Pressure Sensing Technique for the Evaluation of Contact Stresses. J. of Materials Processing Technology. (2005) Vol.164-165, pp. 1537-1543.

[MA10] X. Ma, M. Rooij and D. Schipper. Modelling of Contact and Friction in Aluminium Extrusion. Wear. (2010) Vol. 43, pp. 1138-1144

[MA10] X. Ma, M. Rooij and D. Schipper. A Load Dependent Friction Model for Fully Plastic Contact Conditions. Wear. (2010) Vol. 269, No. 11, pp. 790-796.

[MA11] X. Ma. Surface Quality of Aluminium Extrusion Process. PhD thesis, Twente University. 2011.

[MA12] X. Ma, M. Rooij and D. Schipper. Friction Conditions in the Bearing Area of an Aluminium Extrusion Process. Wear. (2012) Vol. 278-279, pp. 1-8

[MAH82] S. Mahdavian, Y. Mai and B. Cotterell. Friction, Metallic Transfer and Debris Analysis of Sliding Surfaces. Wear. (1982) Vol. 82, pp. 221-232.

[MAH84] S. Mahdavian and Y. Mai. Further Study in Friction, Metallic Transfer and Wear Debris of Sliding Surfaces. Wear. (1984) Vol. 95, pp. 35-44.

[MAL64] A. Male, M. Cockcroft. A Method for the Determination of the Coefficient of Friction of Metals Under Conditions of Bulk Plastic Deformation. Journal of the Institute of Metals. (1964) Vol. 93, pp. 38-45.

[MCQ02] H. McQueen and N. Ryan. Constitutive analysis in hot working. Materials Science and Engineering A322 (2002) Pp. 43-63.

[MCQ75] H. McQueen and J. Jonas. Plastic Deformation of Materials. Treatise on Material Science and technology. (1975) Vol. 6, Akad. Press, New York. pp. 393-493.

[MCQ75] H. McQueen and W. Tegart. The deformation of metals at high temperatures. Scientific American (1975) Vol. 232, issue 4. pp. 116-125.

[MCQ99] S Gourdet and H. McQueen. High temperature deformation of 6060 aluminum alloy. ibid. 326, pp 575-582.

[MCQ10] H. McQueen. Mechanisms in creep and hot working to high strain; microstructural evidence: inconsistencies. Part I: substructure evolution; grain interactions. Metall. Sci. technol. (2010) 28, 12-21.

[MEN06] P. Menezes, Kishore and S. Kailas. Effect of Roughness Parameter and Grinding Angle on Coefficient of Friction when Sliding of Al-Mg Alloy over EN8 Steel. Trans. ASME: J. Tribol. (2006) Vol. 128, pp. 697-704.

[MEN08] P. Menenzes, Kishore and S. Kailas. Subsurface deformation and the Role of Surface Texture - A Study with Cu Pins and Steel. Sadhana. (2008) Vol. 33, Part 3, pp. 191-201.

[MER77] G. Merk and S. Naess. Die Pick-up formation in Aluminium Extrusion. Z. Metallkde. (1977) Vol. 68, No.10, pp. 683-687.

[MIS06] W. Geertruyden, W. Misiolek and P. Wang. Grain structure evolution in a 6061 aluminium alloy during hot torsion. Materials Science and Engineering A419 (2006) Pp.105-114.

[MIS00] A. Bandar, L. Negvesky and W. Misiolek. Physical and Numerical Modeling of Billet Upsetting. Proc. of the 7th Int. Aluminium Extrusion Tech. Seminar. (2000) Vol. 1, pp. 159-166.

[MIT04] B. Mitchell. An Introduction to Materials Engineering and Science. Wiley-Interscience, New Jersey, 2004.

[MOE05] T. Moe. Pressure and Strain Measurement During Hot Extrusion of Aluminium. Doctoral Thesis NTNU Trondheim (2005)

[MON00] S. Gourdet and F. Montheillet. An experimental study of the recrystallization mechanism during hot deformation of aluminium. Materials Science and Engineering A283 (2000) 274-288.

[MON02] S. Gourdet and F. Montheillet. Effects of dynamic grain boundary migration during the hot compression of high stacking fault energy metals. Acta Materialia 50 (2002) 2801-2812.

[MOR02] T. Mori, T. Takatsuji, K. Matsuki, T. Aida, K. Murotani and K. Uetoko. Measurement of Pressure Distribution on Die Surface and Deformation of Extrusion Die in Hot Extrusion of 1050 Aluminium Rod. J. of Mat. Processing Techn. (2002) Vol.130-131, pp. 421-425.

[MUE04] M. Klaus. Fundamental of Extrusion Technology. Giesel Verlag, Iserhagen, 2004.

[MUE12] S. Mueller, J. Muehlhause, J. Maier and P. Hora. Experimental and numerical Analysis of the Friction Condition in the Die Bearing During Aluminium Extrusion. Key Engineering Materials. (2012) Vol. 491, pp. 113-119.

[MUE96] K. Mueller and J. Wegener. Direct Extrusion of AA 6060 Trough Dies With Coated Bearing Length. Proc. of the 6th Int. Aluminium Extrusion Tech. Seminar. (1996) Vol. 2, pp. 147-153.

[NAJ04] A. Najafizadeh and R. Ebrahimi. A New Method for Evaluation of Friction in Bulk Metal Forming. J. of Materials Processing Technology. (2004) Vol. 152, pp. 136-143.

[NAK97] T. Nakamura, N. Bay and Z. Zhang. FEM simulation of Friction Testing Method Based on Combined Forward Rod-Backward Can Extrusion. J. of Tribology Transactions of the ASME. (1997) Vol. 119, pp. 501-506.

[NAK98] T. Nakamura, N. Bay and Z. Zhang. FEM simulation of Friction Testing Method Based on Combined Forward conical can-Backward straight can extrusion. J. of Tribology Transactions of the ASME. (1997) Vol. 120, pp. 716-723.

[NAU91] P. Nautiyal and J. Schey. Effects of Surface Roughness on Friction and Metal Transfer in Lubricated Sliding of Aluminium Alloy Against Steel Surfaces. Wear. (1991) Vol. 140, pp. 37-51.

[OCK12] A. Ockewitz, D. Sun, F. Andrieux and S. Mueller. Simulation of Hot Extrusion of an Aluminium Alloy with Modeling of Microstructure. Key Engineering Materials. (2012) Vol. 491, pp. 257-264.

[ORO43] E. Orowan. The Calculation of Roll Pressure in Hot and Cold Flat Rolling. Proc. Inst. Mech. Eng. (1943) Vol. 150, pp. 140.

[PAR04] N. Parson, S. Barker, A. Shalanski and C. Jowett. Control of Grain Structure in Al-Mg-Si Extrusions. Proc. of the Eighth Int. Aluminium Extrusion Tech. Seminar. (2004) Vol. 1, pp. 11-21.

[PAR96] N. Parson, W. Fraser and C. Pelow. Surface Defects on 6XXX Alloy Extrusions. Proc. of the 6th Int. Aluminium Extrusion Tech. Seminar. (1996) Vol. 1, pp. 57-67.

[PEA60] E. Pearson and R. Parkins. The Extrusion of Metals. 2nd. Edition. Chapman and Hall LTD, London, 1960.

[PED98] B. Post-Pedersen, T. Wanheim and N. Bay. Verification of a Friction Test for Warm and Hot Forming. Proceed. Of Int. Conf. On Forming Techn.. (1998) pp. 253-261.

[PEL07] M. Pellizzari, M. Zadra and A. Molinari. Tribological Properties of Surface Engineered Hot Work Tool Steel for Aluminium Extrusion Dies. Surface Engineering. (2007) Vol. 23, No 3, pp. 165-168.

[PET03] T. Pettersen, B. Holmedal and E. Nes. Microstructure development during hot deformation of aluminium to large strains. Metallurgical and materials transactions A. Vol. 34A, (2003) pp. 2737-2744.

[PET06] G. Petzow. Metallographisches, Keramographisches, Plastographisches Ätzen. Berlin-Stuttgart: Gebrüder Borntraeger, 2006.

[POP10] V. Popov. Contact Mechanics and Friction. Springer, Heidelberg, 2010.

[RIG84] D. Rigney, L. Chen and M. Naylor. Wear Processes in Sliding Systems. Wear. (1984) Vol. 100, pp. 195-219.

[ROO12] M.B. de Rooij, A.J. den Bakker and R.J. Werkhoven. Surface Quality Prediction in Aluminium Extrusion. Key Engineering Materials. (2012) Vol. 491, pp. 27-34.

[ROW91] G.W. Rowe, C.E.N. Sturgess, P. Hartley and I. Pillinger. Finite-Element Plasticity and Metalforming Analysis. Cambridge University Press, New York, 1991.

[RUP82] D. Ruppin und K. Mueller. Untersuchungen zur Scherreibung beim Warmstrangpressen von Aluminiumwerkstoffen - Einfluß geometrischer Bedingungen und Rueckwirkungen der Reibungsverhaeltnisse auf den Materialfluß. Aluminium. (1982) Vol. 58, No.12, pp. 725-729.

[SAH00] P. Saha. Aluminium Extrusion Technology. ASM International. OH, 2000.

[SAH04] P. Saha. Use of Tribology to Improve Performance and Quality in Aluminium Extrusion. Proc. of the Eighth Int. Aluminium Extrusion Tech. Seminar. (2004) Vol. 2, pp. 277-287.

[SAH98] P. Saha. Thermodynamics and Tribology in Aluminium Extrusion. Wear. (1998) Vol. 218, pp. 179-190

[SAN14] V. Sanabria, S. Mueller and W. Reimers. A new high speed friction test for extrusion processes. Key Engineering Materials. (2014) Vol. 585, pp. 33-39.

[SAN14] V. Sanabria, S. Mueller, S. Gall, W. Reimers. Investigation of Friction Boundary Conditions during Extrusion of Aluminium and Magnesium Alloys. Key Engineering Materials. (2014) Vols. 611-612, pp. 997-1004.

[SAN14] V. Sanabria, S. Mueller and W. Reimers. Microstructure evolution of friction boundary layer during extrusion of AA 6060. Procedia Engineering (2014) Vol. 81, pp. 586-591.

[SAN15] V. Sanabria, S. Mueller and W. Reimers. Friction modelling in long bearing channels during multi-hole extrusion of aluminium alloy. Materials Today: Proceedings 2 (2015) 4820-4828.

[SAR83] L. Sargent, W. Milz and R. Atkinson. The Effect of Aluminium Transfer upon the Friction Between Aluminium Alloys and Steel. Lubr. Eng. (1983) Vol. 39, pp. 706-711.

[SCH07] M. Schikorra, L. Donati, L. Tomesani and A. Tekkaya. Microstructure Analysis of Aluminium Extrusion: Grain Distribution in AA6060, AA6082 and AA7075 Alloys. J. of Mechanical Science and Technology. (2007) Vol. 21, pp. 1445-1451.

[SCH08] M. Schikorra, L. Donati, L. Tomesani and A. Tekkaya. Extrusion Benchmark 2007 - Benchmark Experiments: Study on Material Flow Extrusion of a Flat Die. Key Engineering Materials. (2008) Vol. 367, pp. 1-8.

[SCH83] J. Schey. Tribology in Metalworking: Friction, Lubrication and Wear. ASM International, Metals Park, OH 1983

[SEL72] C.M. Sellars and W. Tegart. Hot Workability. Int. Met. Rev. 17. (1972) pp. 1-24.

[SHE04] T. Sheppard and Z. Peng. Simulation of Multi-Hole Die Extrusion. Materials Science and Engineering A. (2004) Vol. 367, pp. 329-342.

[SHE04] T. Sheppard and Z. Peng. Application of FEM to Modelling of Multi-Hole Die Extrusion. Proc. of the Eighth Int. Aluminium Extrusion Tech. Seminar. (2004) Vol. 2, pp. 93-105.

[SHE79] T. Sheppard and D. Wright. Deformation of Flow Stress: Part 1 Constitutive Equation for Aluminium Alloy at Elevated Temperatures. Met. Tech. (1979) Vol 5, pp-194-201.

[SHE88] T. Sheppard and M. Clode. The origin of Surface Defects During Extrusion of AA6063 Alloy. Proc. of the Fourth Int. Aluminium Extrusion Tech. Seminar. (1988) Vol. 2, pp. 329-341.

[SHE99] T. Sheppard. Extrusion of Aluminium Alloy. Kluwer Academic Publishers, Dordrecht, 1999.

[SOF01] H. Sofuoglu, H. Gedikli and J. Rasty. Determination of Friction Coefficient by Employing the Ring Compression Test. Transactions of the ASME. (2001) Vol. 123, pp. 338-348.

[SOF02] H. Sofuoglu and H. Gedikli. Determination of Friction Coefficient Encountered in Large Deformation Processes. Trobology International. (2001) Vol. 35, pp. 27-34.

[STA73] H. Staph, P. Ku and H. Carper. Effect of Surface Roughness and Surface Texture on Scuffing. Mech. Mach. Theor. (1973) Vol. 8, pp. 197-208.

[STO05] M. Stoudt, J. Hubbard and S. Mates. Evaluating the Relationships Between Surface Roughness and Friction Behavior During Metal Forming

[SUN12] D. Sun, A. Kailer, F. Andrieux and A. Ockewitz. Determination of Friction Behavior in Extrusion Processes with a New Experimental Method. Proc. of the 10th Int. Aluminium Extrusion Tech. Seminar. (2012) Vol. 1, pp. 471-479.

[SUN96] M. Sundqvist, T. Bjoerk, S. Hogmark and I. Srinivasan. Tribological Evaluation of Surface Treatments for Extrusion Dies. Proc. of the 6th Int. Aluminium Extrusion Tech. Seminar. (1996) Vol. 1, pp. 1-4.

[TAJ06] M. Tajdari and M. Javadi. Experimental Investigation of tha Friction Coefficient Between Aluminium and Steel. Materials Science-Poland. (2006) Vol. 24, No. 2/1, pp. 305-310.

[TAJ06] M. Tajdari and M. Javadi. A new Experimental Procedure of Evaluating the friction Coefficient in Elastic and Plastic Region. J. of Materials Processing Technology. (2006) Vol. 177, pp. 247-250.

[THE92] W. Thedja, K. Mueller and D. Ruppin. Tribomechanical Process on the Die Land Area During Extrusion of AA6063 Alloy. Proc. of the 5th Int. Aluminium Extrusion Tech. Seminar. (1992) Vol. 1, pp. 467-474.

[THE93] W. Thedja, K. Mueller and D. Ruppin. Die Vongänge im Preßkanal beim Warmstrangpressen von Aluminium. Teil I: Strangoberflächen-reuheit und Haftschicht auf der Matrizenlauffläche. Aluminium. (1993) Vol. 69, No.6, pp. 543-547.

[THE93] W. Thedja, K. Mueller and D. Ruppin. Die Vongänge im Preßkanal beim Warmstrangpressen von Aluminium. Teil II: Reibung im Preßkanal und Matrizenverschleiß. Aluminium. (1993) Vol. 69, No.7, pp. 649-653.

[TOK76] M. Tokizawa, K. Dohda and K. Murotani. Mechanism of Friction at the Interface Between Tool Surface and Metals in Hot Extrusion of Aluminium Alloy. Effect of Dies and Extrusion Temperature. Bull. Japan Soc. Of Prec. Eng. (1976) Vol. 10, No.4, pp.145-150.

[TOK88] M. Tokizawa and N. Takatzuji. Effect of the Die Condition and Billet Composition on the Surface Characteristics of the Extruded 6063 Aluminium Alloy. Trans. Jap. Inst. of Met. (1988) Vol. 29, No.1, pp.69-79.

[TUN88] C. Tuncer and T. Dean. Surface Stress Measurement Techniques in Metal Forming. International Journal of Machine Tools and Manufacture. (1988) Vol. 28. pp. 417-428.

[VAL08] H. Valberg. Experimental Techniques to Characterize Large Plastic deformations in unlubricated Hot Aluminium Extrusion. Key Engineering Materials. (2008) Vol. 367, pp. 17-24.

[VAL10] H. Valberg. Analysis of Metal Flow of Aluminium Trough Long Choked Die Channels. Key Engineering Materials. (2010) Vol. 424, pp. 145-152.

[VAL10] H. Valberg. Applied Metal Forming; Including FEM Analysis. First Edition, Cambridge University Press, New York, 2010.

[VAL88] H. Valberg. Surface Formation in Al-extrusion (Direct Extrusion). Proc. of the 4th Int. Aluminium Extrusion Tech. Seminar. (1988) Vol. 2, pp. 309-319.

[VAL88] H. Valberg. Physical Simulation of Metal Extrusion by Means of Model Materials. Proc. of the 4th Int. Aluminium Extrusion Tech. Seminar. (1988) Vol. 2, pp. 321-327.

[VAL90] H. Valberg. Metal Flow in Direct Axisymmetric Aluminium Extrusion. Processings of the Int. Conf. On Dev. In Form. Techn. (1990) pp. 1.11-1.37.

[VAL92] H. Valberg. Metal Flow in the Direct Axisymmetric Aluminium Extrusion. J. of Mat. Processing Technology. (1992) Vol. 31. pp. 39-55.

[VAL92] H. Valberg and T. Loeken. The Formation of the Outer Surface Layers of the profile in Direct and Indirect Extrusion. Proc. of the 5th Int. Aluminium Extrusion Tech. Seminar. (1992) Vol. 2, pp. 529-550.

[VAL94] H. Valberg and T. Malvik. An Experimental investigation of the Material Flow Inside the Bearing Channel in Aluminium Extrusion. Int. J. of Materials and Product Technology. (1994) Vol. 9, Nos 4/5/6, pp. 428-463.

[VAL96] H. Valberg and T. Malvik. Metal Flow in Die Channels of Extrusion Investigated by an Experimental Grid Pattern Technique. Proc. of the 6th Int. Aluminium Extrusion Tech. Seminar. (1996) Vol. 2, pp. 17-28.

[VAL96] H. Valberg. A Modified Classification System for Metal Flow Adapted to Unlubricated Hot Extrusion of Aluminium and Aluminium Alloys. Proc. of the 6th Int. Aluminium Extrusion Tech. Seminar. (1996) Vol. 1, pp. 95-100.

[VAL96] H. Valberg. Metal Flow in Two-Hole Extrusion. Proc. of the 6th Int. Aluminium Extrusion Tech. Seminar. (1996) Vol. 1, pp. 113-124.

[VAN84] G. Vander Voort. Metallography, principles and practice. Mc Graw hill 1984.

[WAN09] L. Wang, J. Cai, J. Zhou and J. Duszczyk. Characteristics of the Friction Between Aluminium and Steel at Elevated Temperatures During Ball-on-disc Tests. Tribol. Lett. (2009) Vol. 36, pp. 183-190.

[WAN10] L. Wang, Y. He, J. Zhou and J. Duszczyk. Effect of Temperature on the Frictional Behavior of an Aluminium Alloy Sliding Against Steel During Ball-on-disc Tests. Tribology International. (2010) Vol. 43, pp. 299-306.

[WAN10] L. Wang, Y. He, Y. Zhang, J. Cai, J. Zhou, J. Duszczyk and L. Katgerman. Modeling of Double Action Extrusion - A Novel Extrusion Process for Friction Characterization at the Billet-Die Interface. Tribology International. (2010= Vol. 43, pp. 2084-2091.

[WAN10] L. Wang, J. Zhou and J. Duszczyk. Friction in Double Action Extrusion. Key Engineering Materials. (2010) Vol. 424, pp. 153-160.

[WAN12] L. Wang and H. Yang. Friction in aluminium Extrusion – Part 2: A Review of Friction Models for Aluminium Extrusion. Tribology International. (2012) Vol. 56, pp. 99-106.

[WAN12] L. Wang. Modelling of friction for high temperature extrusion of aluminium. Doctoral Thesis Technische Universiteit Delft (2012)

[WAN12] L. Wang, J. Zhou, J. Duszczyk and L. Katgerman. Friction in aluminium Extrusion – Part 1: A Review of Friction testing techniques for Aluminium Extrusion. Tribology International. (2012) Vol. 56, pp. 89-98.

[WAN73] T. Wanheim. Friction at High Normal Pressure. Wear. (1973) Vol. 25, pp. 225-244

[WAN78] T. Wanheim and N. Bay. A Model for Friction in Metal Forming Processes. Ann. CIRP. (1978) Vol. 27, pp. 189-193

[WAN92] F. Wang and J. Lenard. An Experimental Study of Interfacial Friction-Hot Ring Compression. J. of Engineering Materials and Technology. (1992) Vol. 114, pp. 13-18.

[WEL96] T. Welo, S. Abtahi and I. Skauvik. An Experimental and Numerical Investigation of the Thermo-Mechanical Conditions on the Bearing Surface of Extrusion Dies. Proc. of the 6th Int. Aluminium Extrusion Tech. Seminar. (1996) Vol. 1, pp. 101-106.

[WID12] F. WiderØe and T. Welo. Conditions for Sticking Friction Between Aluminium Alloy AA6060 and Tool Steel in Hot Forming. Key Engineering Materials. (2012) Vol. 491, pp. 121-128.

[WUT87] W. Wuttke. Tribophysik, Reibung und Verschleiß von Metallen. Hanser, Muechen, 1987.

[YON04] T. Yoneyama and M. Takahashi. Measurements of Pressure and Friction on the Container Surface During Aluminium Hot Extrusion. Proc. of the Eighth Int. Aluminium Extrusion Tech. Seminar. (2004) Vol. 1, pp. 39-45.

[YON04] Determination of Friction Condition by Geometrical Measurement of Backward Extruded Aluminum Alloy Specimen

[ZEN44] C. Zener and J.H. Hollomon. Effect of Strain Rate upon Plastic Flow of Stress. J. Appl. Phys. (1944) Vol 15, pp. 22-32.

[ZHO09] G. Fang, J. Zhou and J. Duszczyk. FEM Simulation of Aluminium Extrusion Through Two-Hole Multi-Step Pocket Dies. Journal of Materials Processing Technology. (2009) Vol. 209, pp. 1891-1900.

[ZIE00] O. Zienkiewicz and R. Taylor. The Finite Element Method. Butterworth-Heinemann. 5th Edition, Oxford 2000.

[ZIE77] W. Ziegler and G. Hartmann. Strangpressen von Leichtmetall: Axialkräfte messen im Fuhrungskanal. Maschinenmarkt. (1977) Vol. 83, pp. 2034-2036.